Modelling and correction of the non-linear transverse dynamics of the LHC from beam-based measurements

Ewen Hamish Maclean

Hertford College, University of Oxford

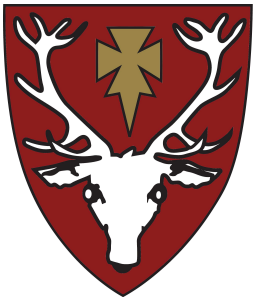

Thesis submitted in fulfilment of the requirements for the degree
of Doctor of Philosophy at the University of Oxford

Trinity 2014

Modelling and correction of the non-linear transverse dynamics of the LHC from beam-based measurements

Ewen Hamish Maclean

CERN Supervisor: Dr Rogelio Tomás

Oxford Supervisor: Prof Riccardo Bartolini

John Adams Institute for Accelerator Science,
Department of Particle Physics,
University of Oxford,
Denys Wilkinson Building,
Keble Road, Oxford, OX1 3RH, UK

This work was funded by the European Organization for Nuclear Research (CERN) and the John Adams Institute for Accelerator Science. It was supported by Hertford College, University of Oxford.

Abstract

The non-linear beam dynamics of a circular accelerator, such as the Large Hadron Collider, can have a significant impact on its operation. In order to avoid limitations on the performance reach of the accelerator, and ensure machine protection, it is vital that the beam dynamics are well understood and controlled. This thesis presents the results of studies of non-linear beam dynamics undertaken on the Large Hadron Collider at CERN, during the 2010 to 2013 period. It sets out to quantify the understanding of the non-linear beam dynamics through the comparison of beam-based measurements to simulation, and where able and appropriate seeks to explain deviations of measurement from the model, and define corrections for relevant aspects of the dynamics.

The analyses presented in this thesis represent considerable advances in the understanding of the LHC beam dynamics which should allow for an improved operation of the machine in the coming years.

Personal acknowledgments

I owe a significant debt of gratitude to the large number of people over the years without whom this thesis would not have come to fruition. Firstly I wish to offer a huge thanks to Dr Rogelio Tomás, who has been my supervisor at CERN since July 2011. Rogelio has been an incredible source of support throughout these studies. To do him full justice would extend these acknowledgments by several pages at least, so for now I shall simply say that I am, as ever, grateful for his considerable effort throughout the last few years, his tireless guidance, and his infectious enthusiasm for beam dynamics. I would also like to thank Dr Frank Schmidt who was my CERN supervisor from July 2010 until July 2011, and Dr Riccardo Bartolini, who has been my supervisor back in Oxford, for the invaluable assistance they have provided.

I would like to thank my parents for all the assistance they have given me over the years. It would have been impossible for me to reach this stage without their continual support and encouragement, not to mention tolerance. Without them I doubt I would have made it through high school, let alone all the way to a Doctoral Thesis. Thank you. A substantial thank you also goes to my sister Elizabeth who was based in Geneva during the second half of my time at CERN. The company, the baking, and the support was greatly appreciated. Many thanks go to my God-parents George and Sylvia, to my Granny, my Aunts and Uncles, my cousins, indeed to the whole extended family for their backing and encouragement.

To Clara there is little more I can say, than simply to thank you for how wonderful you have been. I cannot picture the last few years without you. You've been a huge source of support throughout my studies and I couldn't have done it without you. I must also thank you for putting up with my indenture to the LHC MD schedule: we'll make it to Venice eventually!

Nick Shipman is one of the least organized people I have ever known. It terrifies me therefore that I am now thanking him for finding me somewhere to live. Twice. Nick has been a fantastic friend and a tireless source of assistance whenever it was needed. My experience over the last few years would have been far poorer was it not for him. That said Nick: I am never, ever, letting you make duck pancakes in my kitchen again.

It has been a long process to arrive at this stage, and I would like to thank everyone who has had the misfortune of having to try and educate me on the way. Many thanks to Doctors George Doucas and Nicolas Delerue who supervised my MPhys project and who first introduced me to the field of accelerator physics. Thanks also go to George for convincing me to apply to Hertford College and Oxford during an undergraduate open day, which is a decision I have never regretted. To my undergraduate tutors at Hertford College: Robin Devenish, George Doucas, James Ferrando, Andy Higginbotham, Rhiannon Jones, Halim Kusumaatmaja, John Morton, Pat Roche, and Gassan Yassin a huge thanks is owed. I'd also like to thank all of my teachers at Earlston High School and St. Boswells Primary for their dedication and effort, in particular I would like to thank Mr Rae and Mr Wierter for always taking extra time to foster an interest in physics, to Mr Clark and Ms Flemming (particularly for the extra effort they made to ensure I was able to study maths in my final year of high school), to Mr McIvor and Mr Westgarth for keeping science exciting (read: explosive), to Ms Kitchener for the immense amount of work she put into both her teaching and her extra curricular societies, and to Miss Ross for the encouragement she gave from primary school onwards.

I have really enjoyed my time as a D.Phil student, and that is down to a wide range of people with whom I have shared the experience. Some have already been mentioned but a big thanks should also go to the UK students out at CERN on LTA for helping to keep Geneva fun, to Kat and Dave for their company and for teaching me a bit about wine (apologies to Kat for not making it to more of her classes!), and to my various room-mates over the last three years: Nick, Stefan, Clara, Giaccomo, and Kaspen (Kara + Espen). Many thanks also go to the Tanner society (the Hertford College physics society) and to my friends from Oxford for for keeping trips back to the Home Institute fun. Many thanks to my friends at home for making my intermittent trips back to The Borders memorable.

The studies undertaken in this thesis would have been impossible without the continual support of the members of the Optics Measurement and Correction team and the ABP group at CERN. In particular I would like to thank Glenn Vanbavinckhove and Maria del Carmen Alabau-Pons for the training and assistance they provided when I was first starting out, and Massimo Giovannozzi for the broad support he has lent to the studies presented in this thesis. Tobias Persson and Yngve Levinsen have not only been of invaluable assistance throughout my thesis, but also good friends. Many thanks to you both for numerous fruitful discussions (and the beer). It seems that all optics studies on the LHC are performed at around $2\,\mathrm{am}$, so many thanks to everyone in the OMC for making the late night measurements both successful and enjoyable.

The work presented in this thesis was funded by the European Organization for Nuclear Research (CERN) and the John Adams Institute for accelerator science (JAI), and has been supported by Hertford College, University of Oxford. I would like to thank these institutions for facilitating the studies presented in this thesis.

Ewen Hamish Maclean

Declaration

All work presented in this thesis is my own except where indicated. This thesis has not been submitted for any other qualification. Where the analyses presented herein have been reported previously, a summary of the references is provided below.

At the core of this thesis lie beam-based measurements performed on the Large Hadron Collider at CERN. The LHC, together with it's associated injector chain, is an immensely complex instrument. The successful resolution of any such experiment clearly relies on the contribution of the enormous team of accelerator specialists at CERN. In particular it would be impossible to perform many of the measurements presented in this thesis individually, and the assistance of my fellow members of the Optics Measurement and Correction (OMC) team at CERN during these measurements has been vital. Academic acknowledgments following this declaration have endeavored to credit all those who contributed.

Chapter 1 introduces the relevant theoretical framework for this thesis. No original contributions are presented.

Chapter 2 provides an overview of the LHC accelerator, the physical system studied in this thesis. No original contributions are presented.

Chapter 3 presents original studies of the LHC linear optics. Studies into the modelling of the linear optics were performed in collaboration with Dr M.C. Alabau Pons, Dr F. Schmidt and Dr R. Tomás. The results presented reflect contributions from all individuals. These results have previously been reported in a CERN internal note [1] and at the International Particle Accelerator Conference (IPAC) 2011 [2]. Measurement and correction of the linear LHC optics in 2012 was performed in collaboration with the LHC Optics Measurement and Correction team. The results reported reflect contributions from all members of the team. The author played a leading role in the measurements and corrections presented. Further details are provided in the chapter abstract. The results of the 2012 commissioning have previously been presented at the LHC Beam Operation Committee (LBOC) [3] and reported

in the peer reviewed literature [4].

Chapter 4 presents original studies of the non-linear dynamics of the LHC at injection. Except where explicitly indicated, these analyses were performed independently by the author with the assistance of members of the OMC team and Beam physics department at CERN. Further details are provided in the academic acknowledgments. The studies of non-linear chromaticity presented in this chapter have previously been reported as a CERN Internal Note [5] and at the International Particle Accelerator Conference (IPAC) 2011 [6]. Studies of the amplitude detuning, non-linear coupling, and dynamic aperture have previously been reported as a CERN Internal Note [7] and in the peer reviewed literature [8]. The content of this chapter was also presented at the 2013 LHC Optics Measurement and Correction Review [9].

Chapter 5 presents original studies of the influence of Landau octupoles on the LHC tune, first order chromaticity, and linear coupling. This analysis was performed independently by the author with the assistance of members of the OMC team and Beam physics department at CERN. Further details are provided in the academic acknowledgments. These results have previously been reported as a CERN Internal Note [10], at the International Particle Accelerator Conference (IPAC) 2013 [11], and at the 2013 LHC Optics Measurement and Correction Review [9].

Chapter 6 presents original studies of non-linear errors in the LHC insertions. This analysis was performed independently by the author with the assistance of members of the OMC team and Beam physics department at CERN. Further details are provided in the academic acknowledgments. The analysis presented in this chapter has previously been reported at the 2013 LHC Optics Measurement and Correction Review [9].

Ewen Hamish Maclean

Academic acknowledgments

Chapter 3

The studies presented in this chapter were collaborative efforts. Many people contributed to the results presented. Studies of the simulated beta-beat were performed together with Maria del Carmen Alabau-Pons, Frank Schmidt and Rogelio Tomás. Commissioning of the 2012 LHC optics was performed in collaboration with the CERN Optics Measurement and Correction (OMC) team. The entire OMC team, past and present, should be thanked for their efforts in developing and maintaining the LHC optics tools and for their collaboration in the studies presented in this chapter. Particular acknowledgments go to Rogelio Tomás, Glenn Vanbavinckhove, Tobias Persson, Piotr Skrowronski, Yngve Levinsen, Tomas Bach, Rama Calaga and Rayouchi Miyamoto and Massimo Giovannozzi with whom the 2012 commissioning was performed in collaboration. The assistance of the OP team, and the EICs on shift during the optics commissioning was also essential for the successful completion of the measurements. A huge thanks is offered to everyone involved in these studies.

Chapter 4

Rogelio Tomás, Tobias Persson, and Frank Schmidt have been closely involved in the experiments described in this Chapter, both through their assistance performing measurements, and through their invaluable consultations during the analysis. To them I am greatly obliged. Particular thanks must also go to the past and present members of the Optics Measurement and Correction team for the continuous support and development of BPM data analysis tools, to Massimo Giovannozzi for the support he has provided to these experiment programs, to Jan Uythoven, Alain Antoine and Rodolphe Rosol for their preparation of the MKA hardware, Rudiger Schmidt and Markus Zerlauth for their assistance regarding machine protection, S. Redaelli for his assistance regarding collimation, Verena Kain for her assistance with regard to the MKA software, Ezio Todesco and Walter Venturini for their invaluable consultations regarding various aspects of the MCDO, Eva Calvo Giraldo for performing the BPM rephasing and for consultations in regard to the BPM non-linearity, Ana Guerrero for assistance with the use of the wirescanners, the EIC for the measurements: Alick Macpherson,

and to Glenn Vanbavickhove for providing vital training and assistance in regard to the optics measurements. Finally the studies described in this Chapter would not have been successful was it not for the assistance of the members of the OP group on shift during the experiments, not to mention the continual efforts of the entire Acc-Tec sector at CERN which ensures the successful operation of the LHC.

Chapter 5

The measurements and analysis presented in this chapter have benefited from the support of many people. Particular thanks should go to Rogelio Tomás for his assistance throughout these studies, to Tobias Person for many fruitful discussions in regard to the coupling dependency, to Jorg Wenninger for his advice in regard to the orbit logging performed by YASP, to Ralph Steinhagen for the consultations regarding the LHC BBQ, to Massimo Giovannozzi for his assistance in regard of the BPM misalignments, and to Guilia Papotti who as EIC ran a Q' vs MO powering measurement analysed in this chapter. Thanks should also go to the past and present members of the CERN OMC team for the development of essential optics measurement tools and for performing AC dipole measurements analysed in this chapter.

Chapter 6

There are many people to whom thanks is owed for their contribution to these studies. Rogelio Tomás has been very closely involved with these studies and should be thanked for his continual support and valuable advice in regard to the analysis. Many thanks also go to Tobias Persson and Massimo Giovannozzi who have also been closely involved, both for their invaluable assistance in performing the measurements presented, and for their consultations with respect to the analysis. Particular thanks also go to the LHC aperture measurement team for allowing parasitic observations during the aperture measurements. Similarly thanks go to John Jowett for allowing the test of the IR2 crossing angle reversal to be used for these studies, and for the assistance he rendered in regard to the reproduction of the Alice internal and external crossing angles in MAD-X. Thanks also go to Gabriel Müller for assisting in the extraction of the trim history data for the aperture measurements. Furthermore none of these measurements would have been possible without all the members of the OMC team, past and present who have contributed to the optics tools, measurements, and corrections which were utilized in these studies. Finally thanks go to all the EICs and operations personnel who assisted with the measurements described in this note.

Ewen Hamish Maclean

“ Kick higher! Kick higher! . . . Just don’t quench the triplet. . . ”

Contents

Introduction

Since its inception around the 1930s the particle accelerator has come to infuse many aspects of our society. As examples, accelerators in various forms are either already utilized in, or being developed for, the fields of medicine, industry, defence, power generation, and scientific research [12, 13, 14, 15, 16].

High energy physics (HEP), the study of the fundamental constituents of matter, is one such field, which has pushed the boundaries of accelerator science throughout the 20th and 21st centuries. The European Organization for Nuclear Research (CERN) currently hosts the Large Hadron Collider (LHC), the highest energy and most technologically advanced particle accelerator yet constructed, which provides data for experiments at the forefront of HEP research. In order to achieve an optimal performance of the accelerator however, an understanding of the dynamics of the particle beams as they travel through the machine is essential.

The focus of this thesis is the single-particle transverse dynamics of hadron colliders, specifically of the Large Hadron Collider at CERN. Within the field of single-particle transverse dynamics, *transverse* refers to the plane of motion transverse to the direction of travel of the particle beam, while *single-particle* indicates that interactions between particles in the beams are neglected. Multi-particle effects are beyond the scope of this thesis. In particular the author has studied the modelling and correction of the non-linear dynamics in the Large Hadron Collider, using beam-based measurements. The linear dynamics has also been considered, both as a prerequisite to the non-linear studies, and as an essential contribution to the operation of the machine.

Chapters 1 and 2 briefly introduce the field and provide on overview of the Large Hadron

Collider. Chapter 3 presents results of beam-based correction of the linear optics[1] in the accelerator. Attention then turns to the non-linear dynamics, and Chapters 4, 5 and 6 present the results of three analyses of different aspects of the non-linearity in the machine. Chapter 4 describes the analysis of non-linear dynamics at injection (the state of the machine at which beam is introduced into the accelerator), and presents the results of measurement and correction of the non-linearities, together with comparisons to simulation. Chapter 5 discusses observations of unexpectedly large shifts to specific beam properties which were correlated with changes in the powering of non-linear elements, and presents an explanation for the effects. Chapter 6 is concerned with non-linear errors in specific elements of the machine which are significant sources of non-linearity in collision (the state of the machine where data is produced for the HEP experiments). First measurements and corrections of these errors are presented.

The non-linear dynamics of particle accelerators is a field of rich phenomenology, which lies at the forefront of modern accelerator science. The Large Hadron Collider is arguably the largest, most complex accelerator built to date, and represents a new and exciting dynamical system for study. Furthermore, in order to achieve the best possible performance of the LHC (and in doing so advance the research of the HEP community) the beam dynamics must be well understood, in order that it can be effectively controlled. The analyses presented in this thesis represent significant steps forwards in the understanding and correction of the LHC beam dynamics.

[1] A specific magnetic state of the machine is normally termed an *optics*, due to the similarity of the beam dynamics with the field of optics as it pertains to the transport of light through a system of lenses.

Chapter 1

Theories of beam dynamics pertaining to transverse single-particle motion in the Large Hadron Collider

Beam dynamics is a field of accelerator science which is significant for the design, operation, performance, and protection of an accelerator. In this section an overview is given of the theories of beam dynamics which are relevant to the material presented in this thesis. The chapter begins with a description of the linear dynamics, then progresses to deal with aspects of the non-linear dynamics, concluding with a discussion of the luminosity.

1.1 Linear beam dynamics

The linear beam dynamics of an accelerator is, in the first instance, concerned with the bending and focusing of the beams such that they remain within the aperture of the machine. Bending forces are supplied by dipole magnetic fields, while focusing is typically performed with the use of quadrupole magnets. Within the linear approximation non-linear magnetic fields are ignored and the beam dynamics is described by linear differential equations. Figure 1.1 illustrates the Frenet-Serret coordinate system most often applied when dealing with the linear beam dynamics.

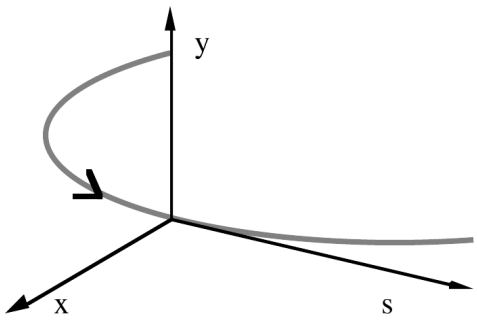

Figure 1.1: Coordinate system for linear accelerator optics [17].

The coordinate system travels with the particle, along a reference trajectory defined by an 'ideal' particle. s is the curvilinear coordinate. A local radius of curvature, $\rho(s)$, is also defined, which depends on the magnetic field and therefore varies around the ring. The transverse phase space is defined by (x, x', y, y'), where x and y are the transverse displacements of the particle relative to the reference trajectory. The coordinates x' and y' are the divergent angles in the x and y planes, the prime denoting differentiation with respect to s.

To first approximation, the dipoles in a circular accelerator define an ideal orbit for a particle having the reference momentum, p_0. This orbit passes through the magnetic center of all elements and closes in upon itself after a single revolution. An orbit which closes in upon itself is termed a *closed orbit*. In practice dipolar errors around the ring, together with a variety of other effects, will act to distort the real closed orbit from the ideal designed orbit. Furthermore, particles within the beam are distributed in amplitude (the beam occupies a finite area in (x, x', y, y') phase space). The closed orbit defines the path of a particle with zero amplitude within the beam, in practice the particles within the beam oscillate about the closed orbit as a consequence of the focusing forces present in the machine. In the LHC this focusing is provided predominantly by quadrupole magnets.

Quadrupolar fields acting on charged particles displaced from the central axis provide a restoring (focusing) force proportional to the displacement in one transverse plane, while simultaneously providing a divergent (defocusing) force in the other. A quadrupole which is focusing in the horizontal plane but defocusing in the vertical is referred to as a *focusing quadrupole*. Likewise a quadrupole which is defocusing in the horizontal plane but focusing in the vertical is referred to as a *defocusing quadrupole*. Utilizing an alternating arrangement of focusing and defocusing quadrupoles, referred to as a FODO lattice, a net focusing is obtained [18]. Figure 1.2 illustrates magnetic fields in an idealized dipole and quadrupole, together with the forces exerted on a positively charged particle travelling into the page.

In a circular accelerator such as the LHC the focusing due to the quadrupoles is periodic in s, with a period of at most the accelerator circumference. Motion in the transverse plane is therefore described by Hill's equation, Eq.(1.1), where $k(s)$ is a periodic coefficient

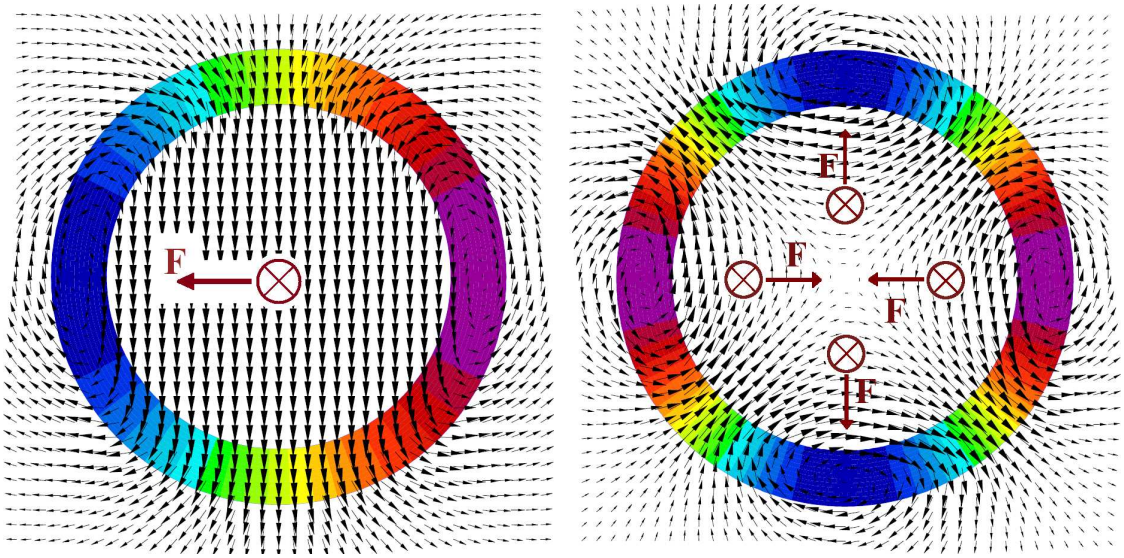

(a) Idealized dipole **(b)** Idealized quadrupole

Figure 1.2: Magnetic fields and forces in an idealized dipole (having a $\cos(\phi)$ current distribution in the circular coil) and an idealized focusing quadrupole (having a $\cos(2\phi)$ current distribution in the circular coil). Current in the dipole and quadrupole coils are indicated in colour. Forces exerted by the magnet on a positive charge travelling into the page are illustrated. Adapted from [19].

describing the restoring force due to the distribution of focusing fields around the ring.

$$z'' \mp k(s)z = 0 \qquad z = x, y \quad z' = \frac{\mathrm{d}z}{\mathrm{d}s} \tag{1.1}$$

Solutions to Hill's equation take the form of Eq.(1.2),

$$\begin{aligned} x &= \sqrt{\beta_x(s)\epsilon_x}\cos\left(\phi_x(s) + \phi_{x0}\right) \\ y &= \sqrt{\beta_y(s)\epsilon_y}\cos\left(\phi_y(s) + \phi_{y0}\right) \end{aligned} \tag{1.2}$$

where ϵ is the emittance of a particle, and is a constant of the motion at a given energy. $\beta(s)$ is the *beta-function* of the accelerator, which describes the variation of the oscillation envelope around the ring. In a collider such as the LHC, it is usual to denote the beta-functions at the Interaction Points (where the beams are made to collide) by the symbol β^*.

Particles oscillate about the closed orbit within the envelope defined by the beta function

and emittance. The number of these *betatron oscillations* per revolution around the accelerator is known as the *tune*, $Q_{x,y}$. The tune is defined in Eq.(1.3), where $\Delta\phi_{x,y}$ is the total betatron phase advance undergone by a particle during one complete revolution around the accelerator ring.

$$Q_{x,y} = \frac{1}{2\pi}\Delta\phi_{x,y} = \frac{1}{2\pi}\oint \frac{\mathrm{d}s}{\beta_{x,y}} \tag{1.3}$$

Figure 1.3 shows a tracking simulation of a particle undergoing such *betatron oscillations* in the LHC Arc12. Dipole errors were added which have distorted the closed orbit away from the ideal path.

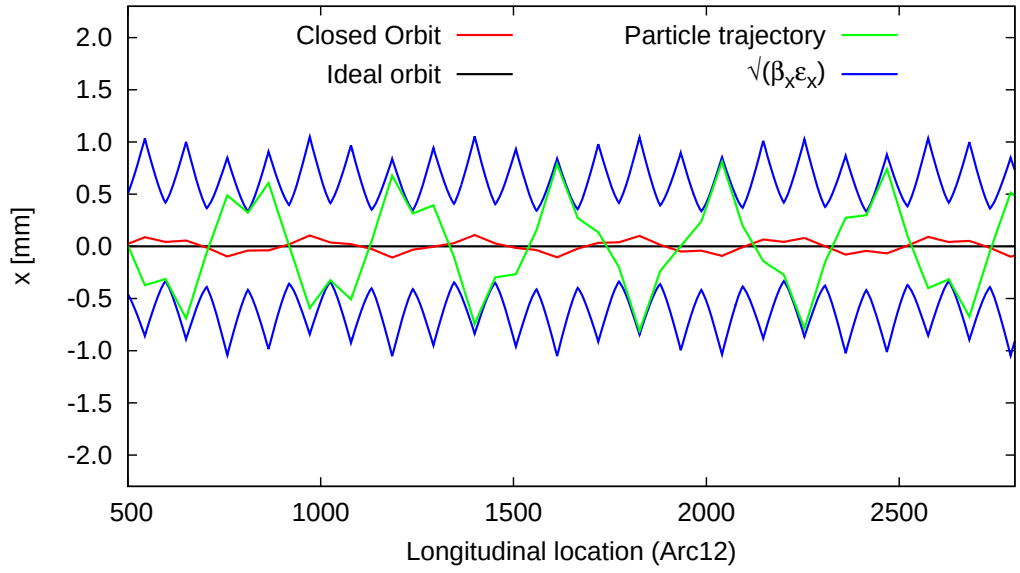

Figure 1.3: Tracking simulation in LHC Arc12 of a particle undergoing betatron oscillations.

Analogously to the beta-function, the *gamma-function*, $\gamma(s)$, describes the envelope of oscillations in x' and y'. The beta and gamma functions are related by the *alpha-function*:

$$\alpha_{x,y} = -\frac{1}{2}\frac{\mathrm{d}}{\mathrm{d}s}\beta_{x,y}(s) = \sqrt{\gamma_{x,y}(s)\beta_{x,y}(s) - 1} \tag{1.4}$$

Within the linear approximation all particles follow elliptical trajectories in x, x' and y, y' phase space. The equation of the ellipse, Eq.(1.5), is defined by the $\alpha(s)$, $\beta(s)$, and

$\gamma(s)$ functions together with the emittance.

$$\gamma_z(s)z^2 + 2\alpha_z(s)zz' + \beta_z(s)z'^2 = \epsilon \quad \text{where } z = x, y \tag{1.5}$$

Figure 1.4 shows schematically the phase space ellipse.

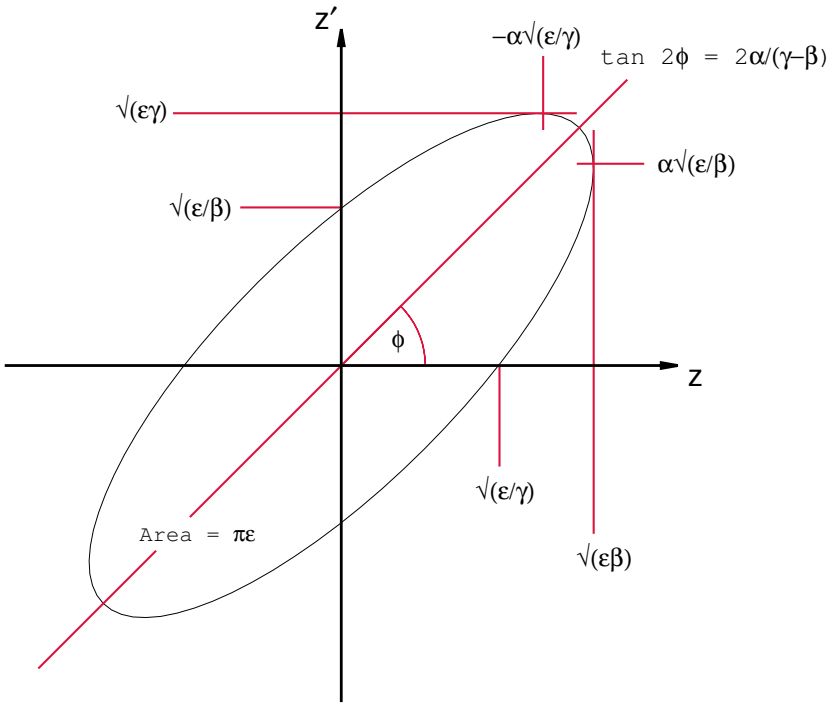

Figure 1.4: Phase space ellipse in the transverse z, z' plane. Where z represents either x or y.

The emittance defines the area of phase space contained by the ellipse. Liouville's theorem states that the phase space volume is conserved in a closed system. As protons emit little synchrotron radiation [20] up to the TeV scale the emittance may usually be regarded as a constant of the motion for a given energy (though at the multi-TeV scale radiation emission may become significant). Accelerating the beam invalidates Liouville's theorem, and the *physical emittance* (ϵ) will shrink with increasing energy. It is possible, however, to construct a *normalized emittance* (ϵ_γ), which is invariant with the beam energy. This is defined in Eq.(1.6), where β_{rel} and γ_{rel} are the relativistic beta and gamma functions.

$$\epsilon_\gamma = (\beta_{rel}\gamma_{rel})\epsilon \tag{1.6}$$

The emittance of a specific particle is termed the *single particle emittance*.[1] Different particles may have differing single particle emittances, and therefore will undergo betatron oscillations of differing amplitude. A *beam emittance* may also be defined: definitions vary, however typically it is defined as the emittance corresponding to an amplitude at $1\,\sigma$ of the (assumed) Gaussian charge distribution.

Dependence of the phase space trajectory on the $\alpha(s)$, $\beta(s)$, and $\gamma(s)$ functions can be removed by transformation to *Courant-Snyder coordinates* [21] (sometimes called the *normalized Courant-Snyder coordinates*), defined in Eq.(1.7),

$$\begin{pmatrix} \hat{z} \\ \hat{z}' \end{pmatrix} = \begin{pmatrix} \frac{1}{\sqrt{\beta_z(s)}} & \frac{\alpha_z(s)}{\sqrt{\beta_z(s)}} \\ 0 & \sqrt{\beta_z(s)} \end{pmatrix} \begin{pmatrix} z \\ z' \end{pmatrix} \qquad \text{where } z = x, y \tag{1.7}$$

where the new coordinates are denoted by $\hat{}$. In the Courant-Snyder coordinate system particles follow circular trajectories in phase space.[2]

So far all particles within the beam are assumed to have the designed momentum (p_0). In reality particles within the beam have a distribution in momentum. The momentum of a particle which differs from p_0 is typically defined in terms of a relative momentum deviation, δ, defined in Eq.(1.8).

$$\delta = \frac{p - p_0}{p_0} \tag{1.8}$$

Such offsets in momenta introduce *chromatic* errors into the beam dynamics. One of the most important of the chromatic aberrations in a particle accelerator is *dispersion*.

Magnetic rigidity relates the magnetic flux ($\mathbf{B}$) perpendicular to the motion of a charged particle, with the local radius of curvature and the particle momentum ($\mathbf{P}$). It is defined in Eq.(1.9) [22].

$$|\mathbf{B}\rho| = \frac{|\mathbf{P}|}{e} \tag{1.9}$$

[1] The term *single particle emittance* has been used throughout this thesis to denote the ϵ, as defined by Eq.(1.5), of a specific particle. This property is more technically denoted as the *Courant-Snyder invariant* of a particle.

[2] The terminology *Courant-Snyder* coordintes has been used in this thesis for consistency with [21], however it should be noted that these are the *Floquet* coordinates.

Particles of differing momenta have different local radii of curvature in the dipoles of an accelerator, and therefore follow differing orbits around the ring. The deviation of an off momentum particle orbit from that of the synchronous particle is defined by the *Dispersion function*, $D(s)$ [23]. In a region of non-zero dispersion the contribution to the orbit of a particle is described by Eq.(1.10).

$$\begin{aligned} \Delta x_{dispersion} &= D_x(s)\delta \\ \Delta y_{dispersion} &= D_y(s)\delta \end{aligned} \tag{1.10}$$

The orbit of a particle is therefore defined by Eq.(1.11).

$$z = z_{betatronic} + z_{dispersion} + z_{closed\ orbit|_{\delta=0}} \quad \text{where } z = x, y \tag{1.11}$$

1.2 Non-linear magnetic multipoles

In the linear approximation only dipolar and quadrupolar magnetic fields are considered. Non-linear magnetic fields, those of sextupolar or higher order, are also introduced in an accelerator both by design and through the presence of unavoidable imperfections in the lattice. In general the magnetic field of a multipole of order n (where $n = 1$ is a dipole, $n = 2$ is a quadrupole, $n = 3$ a sextupole, and so forth) is given by Eq.(1.12).

$$B_y(x, y, s) + iB_x(s, y, s) = [B_n(s) + iA_n(s)]\,(x + iy)^{n-1} \tag{1.12}$$

$B_n(s)$ and $A_n(s)$ are the respective *normal* and *skew* multipole coefficients, defined in Eq.(1.13), where a skew multipole is a normal multipole rotated by $\frac{\pi}{2n}$.

$$\begin{aligned} B_n(s) &= \frac{1}{(n-1)!}\frac{\partial^{n-1}B_y}{\partial x^{n-1}}\bigg|_{(0,0,s)} \\ A_n(s) &= \frac{1}{(n-1)!}\frac{\partial^{n-1}B_x}{\partial x^{n-1}}\bigg|_{(0,0,s)} \end{aligned} \tag{1.13}$$

The Hamiltonian in the linear approximation can be written according to Eq.(1.14), where $K(s)$ describes the variation of focusing strength around the ring.

$$\mathbf{H_0} = \frac{1}{2}p_x^2 + \frac{1}{2}p_y^2 + \frac{1}{2}K(s)x^2 - \frac{1}{2}K(s)y^2 \tag{1.14}$$

The contribution to the Hamiltonian of a multipole of order n is given by Eq.(1.15) [24].

$$\mathbf{H_n} = \frac{q}{p}\,\mathrm{Re}\left[\frac{1}{n}\left[B_n(s) + iA_n(s)\right](x+iy)^n\right] \tag{1.15}$$

The momentum kick received by a particle in the field of a certain magnetic multipole can then be obtained from Hamilton's equation

$$\frac{\mathrm{d}p_z}{\mathrm{d}s} = -\frac{\mathrm{d}\mathbf{H}}{\mathrm{d}z} \qquad \text{where } \; z = x, y \tag{1.16}$$

In the *thin lens approximation* magnetic elements are assumed to have zero length, the multipole coefficients in Eq.(1.15) are replaced by their integrated strength (over the true element length), and the multipoles are assumed to provide an instantaneous momentum kick to the beam. In this context Eq.(1.15) is sometimes referred to as a *thin kick* Hamiltonian.

The transverse coordinates (z,p_z where $z = x, y$) may be re-expressed in the action-angle coordinate system (ϕ_z,J_z where $z = x, y$), Eq.(1.17), used extensively in the study of oscillatory systems.

$$x = \sqrt{2J_x\beta_x}\cos\phi_x \qquad\qquad y = \sqrt{2J_y\beta_y}\cos\phi_y \tag{1.17}$$

In the action angle coordinate system, the conjugate momenta (the *action*, $J_{x,y}$) is an invariant of linear betatron motion and describes the betatron amplitude of a particle ($2J = \epsilon_{single\ particle}$). In the first order approximation the tune shift due to certain magnetic multipole is defined by Eq.(1.18),

$$\Delta Q_{x,y} = \frac{1}{2\pi}\frac{\mathrm{d}\left\langle\mathbf{H}\right\rangle}{\mathrm{d}J_{x,y}} \tag{1.18}$$

where $\langle\mathbf{H}\rangle$ indicates that the Hamiltonian has been averaged over the betatron phase vari-

ables. It should also be clear from the transformation to action angle coordinates that the perturbation to the Hamiltonian due to a non-linear magnetic multipole scales with the beta-function and the action. Denoting the Hamiltonian for an n^{th} order normal multipole as N_n, and the Hamiltonian for an n^{th} order skew multipole as S_n, this is seen in Eq.(1.19).

$$\begin{aligned} N_n &\propto \mathrm{Re}\left[(x+iy)^n\right] \\ &\propto \mathrm{Re}\left[\sum_{k=0}^{n}\binom{n}{k} i^k \beta_x^{\frac{n-k}{2}} \beta_y^{\frac{k}{2}} \left(\sqrt{2J_x}\cos\phi_x\right)^{n-k}\left(\sqrt{2J_y}\cos\phi_y\right)^{k}\right] \end{aligned} \tag{1.19}$$

$$\begin{aligned} S_n &\propto \mathrm{Im}\left[(x+iy)^n\right] \\ &\propto \mathrm{Im}\left[\sum_{k=0}^{n}\binom{n}{k} i^k \beta_x^{\frac{n-k}{2}} \beta_y^{\frac{k}{2}} \left(\sqrt{2J_x}\cos\phi_x\right)^{n-k}\left(\sqrt{2J_y}\cos\phi_y\right)^{k}\right] \end{aligned}$$

Non-linear magnetic multipoles introduced through the powering of non-linear magnets, or through magnetic errors, can substantially influence the beam dynamics. Geometric errors in an accelerator lattice however, can also play a significant role. Eq.(1.15) assumes that a particle is passing through the center of the generating element, however in general a lattice suffers from misalignment errors of its constituent elements, and the real closed orbit of the beam may be distorted away from the ideal. These effects result in the beam passing off axis through magnetic elements in the lattice. A transverse displacement of the beam from the magnetic axis of an element causes the beam to see, not only the primary field component, but also perturbations from all lower orders [25]. Thus a beam passing off axis through a sextupole will observe the sextupole, but also encounter quadrupole and dipole perturbations. This is known as *feed-down*. It can be illustrated by considering the (x,y) dependence of N_3 from Eq.(1.19) ($N_3 \propto \mathrm{Re}\left[(x+iy)^3\right] = (x^3 - 3xy^2)$), under the change of variables $x \rightarrow x + \Delta x$ (equivalent to introducing a misalignment of the relevant element). A Taylor expansion yields Eq.(1.20), which shows terms equivalent to quadrupole and dipole fields.

$$N_3(\Delta x \approx 0) \propto (x^3 - 3xy^2) + 3\Delta x(x^2 - y^2) + 3\Delta x^2(x) \tag{1.20}$$

$$\propto N_3 + 3\Delta x N_2 + +3\Delta x^2 N_1 \tag{1.21}$$

Rotational misalignment is also a significant concern. Normal and skew multipoles are related though rotation. Rotational misalignment of a purely normal or skew magnet therefore results in the beam seeing a mixture of normal and skew fields. Rotational misalignments of normal quadrupoles for example, can be an important source of skew quadrupole fields.

1.3 Formalism of non-linear beam dynamics

The dynamics of a circular accelerator may be defined in terms of transfer maps, which relate final to initial phase space coordinates [21, 24, 26]. Within the linear approximation the transfer map is a matrix, and in the case of the normalized Courant-Snyder coordinates, introduced in Section 1.1, a pure rotation matrix. For consideration of the non-linear beam dynamics it is usual to work in a frame where the linear dynamics is described by a pure rotation. The transfer map for an arbitrary segment of an accelerator, for example the *one turn map* ($\mathcal{M}$) which relates a particle's coordinates after a single turn to their initial values, is the product of the transfer maps for the constituent elements of the relevant sector [21],

$$\mathbf{x_f} = \mathcal{M}\mathbf{x_i} \qquad \text{with} \quad \mathcal{M} = \mathcal{M}_W\mathcal{M}_{W-1}\ \ldots\ \mathcal{M}_2\mathcal{M}_1 \tag{1.22}$$

where W represents a specific element in the lattice. The transfer map for a non-linear element is not described by a matrix, but rather by the exponential Lie operator, $e^{-:f:}$, defined,

$$\begin{aligned} e^{-:f:}g &= g + [f,g] + \frac{1}{2}[f,[f,g]] + \ldots \\ [f,g] &= \sum_i \frac{\partial f}{\partial q_i}\frac{\partial g}{\partial p_i} - \frac{\partial f}{\partial p_i}\frac{\partial g}{\partial q_i} \end{aligned} \tag{1.23}$$

where q_i and p_i are the canonical position and momentum coordinates, and $[f,g]$ is termed the *Poisson bracket* of f and g. The one turn map including non-linear sources therefore takes the form,

$$\mathcal{M} = e^{-:h_W:}e^{-:h_{W-1}:}\ \ldots\ e^{-:h_2:}e^{-:h_1:}R \tag{1.24}$$

where R represents a matrix describing the linear beam dynamics and h_w are the thin kick Hamiltonians of the non-linear elements. The product of exponential Lie operators can be expressed as another exponential Lie operator[3] [24, 26, 27], giving the one turn map,

$$\mathcal{M} = e^{-:h:} R \qquad \text{with} \quad h = \sum_{W=1}^{W} h_W + \sum_{W,M<W}^{W} [h_W, h_M] + \ldots \tag{1.25}$$

where from now on only terms to first order in h_W are retained. h may be expanded in terms of the solutions of the unperturbed motion, Eq.(1.17), according to Eq.(1.26) [24, 26, 27],

$$h = \sum_{jklm} h_{jklm} \left(2J_x\right)^{\frac{j+k}{2}} \left(2J_y\right)^{\frac{l+m}{2}} e^{i\left[(j-k)(\phi_x-\phi_{x_0})+(l-m)(\phi_y-\phi_{y_0})\right]} \tag{1.26}$$

where h_{jklm} are *Hamiltonian coefficients* containing contributions from all multipoles in the ring of order $n = j+k+l+m$. As an example, a multipole of order n gives rise to terms in the Hamiltonian $\propto x^{j+k}y^{l+m}$, where $n = j+k+l+m$, thus a skew quadrupole contributes to h_{1010}, h_{1001} and h_{0110}.

Non-linear sources in general create a system in which the phase space trajectory depends on both particle amplitude and betatron phase, and the linear invariant $J_{x,y}$ is no longer a constant of the motion. Transformation to normal form coordinates [21] is the non-linear generalization of transformation to Courant-Snyder coordinates in which linear betatron motion is described by a pure rotation. The principle is to perform a transformation, $e^{-:F:}$, from a system with amplitude and phase dependence to one in which the dynamics is described by only an amplitude dependent rotation [24, 26, 27]. This is illustrated in Fig. 1.5. Much of the detail regarding the non-linear dynamics is then contained in the generating function of the transformation, F, and a new non-linear invariant, $I_{x,y}$, can be introduced. Similar to h, F may be expanded in the normal form coordinates according to Eq.(1.27),

$$F = \sum_{jklm} f_{jklm} \left(2I_x\right)^{\frac{j+k}{2}} \left(2I_y\right)^{\frac{l+m}{2}} e^{i\left[(j-k)(\psi_x-\psi_{x_0})+(l-m)(\psi_y-\psi_{y_0})\right]} \tag{1.27}$$

[3]This is the *Campbell-Baker-Hausdorff* theorm.

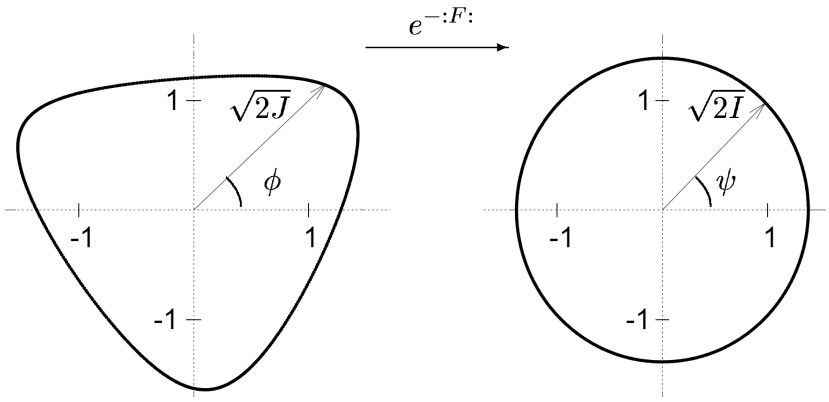

Figure 1.5: An illustration of transformation to normal form coordinates [24]. Normalized phase space portraits are shown for initial action-angle coordinates (left) and following transformation to normal form coordinates (right). The units of the axes are $0.5\sqrt{\text{mm}}$

where the coefficients f_{jklm} are related to h_{jklm} by Eq.(1.28) [24, 27].

$$f_{jklm} = \frac{h_{jklm}}{1 - e^{i2\pi[(j-k)Q_x + (l-m)Q_y]}} \tag{1.28}$$

From Eq.(1.28) it is seen that at certain values of the tunes the transformation required to shift the phase space to an amplitude dependent rotation diverges. Specifically this corresponds to cases where,

$$(j-k)Q_x + (l-m)Q_y = p \qquad \text{where } \; j,k,l,m,p \in \mathcal{Z} \tag{1.29}$$

A divergence of the transformation to normal form generally indicates an unclosed phase space trajectory due to a resonance in the beam motion. The condition in Eq.(1.29) corresponds to situations where particles lie on resonant frequencies, in most cases leading to their amplitudes growing unbounded (by the dynamics). f_{jklm} are therefore known as the *resonance driving terms*, or RDTs.

The resonance driving terms depend on local multipole strength and vary around the accelerator ring according to the distribution of contributing sources [27]. In particular the f_{jklm} show abrupt jumps at the location of relevant sources. As the normal form is by definition phase independent, it is possible to relate the turn-by-turn data at a given location on the

ring to the RDTs at that location, Eq.(1.32) [28]. N represents the turn number, $h_z^{\pm}$ and $\zeta_z^{\pm}$ are the original and normal form phase space coordinates. The second equality of Eq.(1.31) has been truncated to first order in the Poisson bracket.

$$\begin{aligned} h_z^{\pm} &= \sqrt{2J_z}e^{\mp i\left(\phi_z-\phi_{z_0}\right)} = z \pm ip_z \qquad \text{where } z = x, y \\ \zeta_z^{\pm} &= \sqrt{2I_z}e^{\mp i\left(\psi_z-\psi_{z_0}\right)} \end{aligned} \tag{1.30}$$

$$h_z^-(N) = e^{:F(N):}\zeta_z^-(N) \simeq \zeta_z^-(N) + \left[F(N), \zeta_z^-(N)\right] \tag{1.31}$$

$$\begin{aligned} h_x^-(N) = &\sqrt{2I_x}e^{i\left(2\pi Q_x N-\psi_{x_0}\right)} - \\ &2i\sum_{jklm} j f_{jklm}(2I_x)^{\frac{j+k-1}{2}}(2I_y)^{\frac{l+m}{2}} e^{i\left[(1-j+k)(2\pi Q_x N-\psi_{x_0})+(m-l)(2\pi Q_y N-\psi_{y_0})\right]} \end{aligned} \tag{1.32}$$

$$\begin{aligned} h_y^-(N) = &\sqrt{2I_y}e^{i\left(2\pi Q_y N-\psi_{y_0}\right)} - \\ &2i\sum_{jklm} l f_{jklm}(2I_x)^{\frac{j+k}{2}}(2I_y)^{\frac{l+m-1}{2}} e^{i\left[(k-j)(2\pi Q_x N-\psi_{x_0})+(1-l+m)(2\pi Q_y N-\psi_{y_0})\right]} \end{aligned}$$

Each term in these expansions corresponds with a certain mode in the beam motion, and contributes to a specific frequency in the spectrum of the motion [29]. The spectrum may be determined from an FFT of the turn-by-turn betatron oscillation data. The contribution of an RDT at a specific location on the ring to a given spectral line is described in Eq.(1.33) [29], where $P(a, b)$ represents the amplitude of the spectral line $aQ_x + bQ_y$ in plane P. Terms with $j = l = 0$ do not contribute to the motion in either plane.

$$\begin{aligned} H(1-j+k, m-l) &= 2j\left|f_{jklm}\right|(2I_x)^{\frac{j+k-1}{2}}(2I_y)^{\frac{l+m}{2}} \\ V(k-j, 1-l+m) &= 2l\left|f_{jklm}\right|(2I_x)^{\frac{j+k}{2}}(2I_y)^{\frac{l+m-1}{2}} \end{aligned} \tag{1.33}$$

In principle the $|f_{jklm}|$ may therefore be determined by a comparison of the amplitudes of various spectral lines [27]. As an example the $|f_{1001}| = \frac{H(0,1)}{2V(0,1)}$.

In practice there are several additional concerns which need to be taken into account. Firstly the decoherence of a kicked beam leads to a reduction in the amplitude of the spectral

lines observed in the turn-by-turn data, dependent on both the line in question and the detuning with amplitude [24]. Secondly, in order to reconstruct h_z^- from the turn-by-turn data both the position and momentum are required. If only position data is available then spectral analysis will mix lines $P(a, b)$ with $P(-a, -b)$. Consequently the contributions of different RDTs may not be distinct, for example without momentum data the f_{1001} and f_{1010} RDTs are not distinguishable. Finally situations may also arise where multiple RDTs contribute significantly to the same spectral line, which may make interpretation of the data more complicated.

To summarize:

- Multipoles of order n produce terms in the Hamiltonian $\propto x^{j+k}y^{l+m}$, where $j + k + l + m = n$.

- These terms in the Hamiltonian drive resonances $[(j - k), (l - m)]$ and give rise to resonance driving terms (RDTs) f_{jklm}.

- f_{jklm} contribute to specific frequencies in the spectrum of the beam motion: $H(1 - j + l, m - l)$ and $V(k - j, 1 - l + m)$.

- f_{jklm} varies around the ring dependent on the distribution of multipoles of order n, showing abrupt jumps at the location of the relevant sources.

- f_{jklm} are determined from the spectrum of the beam motion, which may be reconstructed from the turn-by-turn data in the BPMs, allowing the localization of the relevant multipole sources.

The formalism of RDTs has been used in this thesis when considering the linear betatron coupling in the LHC. This is referred to specifically in Section 1.4.6.

1.4 Phenomenology of non-linear beam dynamics

1.4.1 Chromaticity

Chromaticity is the variation of tune with the relative deviation from the ideal momentum (p_0). Under the influence of chromatic aberrations the tune may be described as a Taylor series about the unperturbed tune, Eq.(1.34).

$$Q_z\left(\frac{\Delta p}{p_0}\right) = Q_{z0} + Q'_z \times \left(\frac{\Delta p}{p_0}\right) + \\ + \frac{1}{2!}Q''_z \times \left(\frac{\Delta p}{p_0}\right)^2 + \frac{1}{3!}Q'''_z \times \left(\frac{\Delta p}{p_0}\right)^3 + ... \tag{1.34}$$

where

$$Q_z'^{...n} = \frac{\partial^n Q_z}{\partial \frac{\Delta p}{p_0}^n} \qquad z = x, y \tag{1.35}$$

Q' is the first order variation of the tune with the relative momentum deviation, and is normally referred to as *chromaticity*. Q'', Q''', and further higher order terms in the Taylor expansion are referred to as *non-linear chromaticity*. Chromaticity is in the first instance introduced into an accelerator via the momentum dependent focusing generated by quadrupoles (higher momentum particles are less strongly focused by quadrupolar fields), thus all alternating gradient machines have substantial *natural chromaticities* which are negative. Momentum dependent focusing can be illustrated by considering the transverse momentum kick from a thin normal horizontally focusing ($B_2 > 0$) quadrupole. From Eq.(1.15) and Eq.(1.16),

$$\Delta p_x = -\frac{\mathrm{d}}{\mathrm{d}x}\frac{1}{2}\frac{q}{p}B_2 L(x^2 - y^2) = -\frac{q}{p}B_2 L x \tag{1.36}$$

demonstrating that the magnitude of the horizontal momentum for a horizontally diverging particle (a particle with $p_x > 0$ and $x > 0$; or with $p_x < 0$ and $x < 0$) is reduced more for lower momentum particles upon passage through a focusing quadrupole. A detailed discussion relating the momentum kick to the change in divergent angle can be found in [30].

Non-linear magnetic fields in dispersive regions also generate chromatic perturbations, thus sextupoles are commonly used to correct the natural chromaticity. This can be illustrated by considering the tune shift, Eq.(1.18), from a thin normal sextupole, Eq.(1.15), with $x \rightarrow x + D_x\delta$. The chromaticity introduced by a normal sextupole is given by Eq.(1.37).

$$\begin{aligned}\Delta Q'_{x,y} &= \frac{1}{2\pi}\left\langle \frac{\mathrm{d}}{\mathrm{d}\delta \mathrm{d}J_{x,y}} \frac{1}{3}\frac{q}{p} B_3 L([x + D_x\delta]^3 - 3[x + D_x\delta]y^2) \right\rangle \\ &= \frac{\pm 1}{2\pi}\frac{q}{p} B_3 L D_x \beta_{x,y}\end{aligned} \tag{1.37}$$

Relevant sources for chromatic perturbations are summarized in Tab. 1.1.

Table 1.1: Sources of chromaticity [21]. In this notation K_2 represents a quadrupole. $(K_a)^b$ represents the b^{th} order contribution of multipole K_a.

Order	Source
Q_0	K_2
Q'	K_2, K_3
Q''	K_2, K_3, $(K_3)^2$, K_4
Q'''	K_2, K_3, $(K_3)^2$, K_4, $(K_3)^3$, K_3K_4, K_5

1.4.2 Detuning with amplitude

Amplitude detuning is the variation of tune with single particle emittance. This detuning may be described by a Taylor expansion about the unperturbed tune, Eq.(1.38).

$$\begin{aligned}Q_z(\epsilon_x, \epsilon_y) = \; & Q_{z0} + \frac{\partial Q_z}{\partial \epsilon_x}\epsilon_x + \frac{\partial Q_z}{\partial \epsilon_y}\epsilon_y + \\ & + \frac{1}{2!}\left(\frac{\partial^2 Q_z}{\partial \epsilon_x^2}\epsilon_x^2 + 2\frac{\partial^2 Q_z}{\partial \epsilon_x \partial \epsilon_y}\epsilon_x\epsilon_y + \frac{\partial^2 Q_z}{\partial \epsilon_y^2}\epsilon_y^2\right) + \ldots\end{aligned} \tag{1.38}$$

$\epsilon_{x,y}$ is the physical single particle emittance. The single particle physical emittance is related to the action ($J_{x,y}$) by Eq.(1.39).

$$2J_{x,y} = \epsilon_{x,y} \tag{1.39}$$

For practical purposes some authors prefer to relate the particle emittance to an amplitude in terms of the number of beam sigmas (σ) in the discussion of amplitude detuning. Assuming a Gaussian beam distribution this is given by Eq.(1.40).

$$N_\sigma = \sqrt{\frac{2J}{\epsilon_{Beam}}} \tag{1.40}$$

ϵ_{Beam} is the physical emittance of the beam, which may be determined from wire scanner (*BWS*) data [31]. The nominal physical emittance of the beam at $450\,\mathrm{GeV}$ is $0.0078\,\mu\mathrm{m}$, $\sigma_{nominal}$ is defined as the amplitude corresponding to this emittance.

Detuning with amplitude is generated by non-linear magnetic fields. As an example, the tune shift due to a thin normal octupole can be calculated from Eq.(1.18),

$$\begin{aligned}\Delta Q_x &= \frac{3}{8\pi}\frac{q}{p}B_4 L(\beta_x^2 J_x - 2\beta_x\beta_y J_y) \\ \Delta Q_y &= \frac{3}{8\pi}\frac{q}{p}B_4 L(\beta_y^2 J_y - 2\beta_y\beta_x J_x)\end{aligned} \tag{1.41}$$

which shows a linear dependence of $\Delta Q_{x,y}$ on the action, demonstrating that normal octupoles generate first order detuning with amplitude. Table 1.2 summarizes relevant sources for detuning with amplitude.

Table 1.2: Sources of detuning with amplitude [21]. In this notation K_2 represents a quadrupole.$(K_a)^b$ represents the b^{th} order contribution of multipole K_a.

Order	Source
Q_0	K_2
$\frac{\partial Q}{\partial \epsilon}$	$(K_3)^2$, K_4
$\frac{\partial^2 Q}{\partial \epsilon^2}$	$(K_3)^4$, $(K_3)^2K_4$, $(K_4)^2$, K_3K_5, K_6

1.4.3 Decoherence

On exciting a beam with a single kick betatron oscillations are induced, however amplitude detuning and chromaticity lead to a tune spread in the beam. As a result, oscillations of the composite particles following a single kick rapidly become out of phase, and the oscillation of the beam is said to decohere. Beam position monitors (BPMs) record the center of charge of the beam. Due to the decoherence of the betatron oscillations, the oscillation amplitude recorded by the BPM will decrease towards zero following a single kick, even though the oscillation amplitude of the individual particles is unchanged. Correction of non-linear sources in the accelerator removes sources of tune spread and reduces the decoherence of the beam, leading to a slower decay of the oscillation amplitude recorded by the BPMs. In the particular case of decoherence due to first order chromaticity, synchrotron motion leads to a periodic decoherence and recoherence of the beam motion. This occurs with a periodicity equal to that of the synchrotron motion, in the LHC this is $\sim 200\,\mathrm{turns}$.

Decoherence may also occur as a consequence of collective effects. The LHC beams utilized in the kicked-beam studies presented in this thesis consisted of a small number of low intensity bunches. Decoherence due to collective effects was therefore not relevant to the measurements presented in this thesis.

1.4.4 Resonances

It is normally desired to keep the accelerator tunes as far as possible from simple fractional values[4]. This is done in order to avoid the frequency of the betatron oscillations approaching resonant values. Resonances arise in the beam motion when perturbations (which may be linear or non-linear) act in synchronism with the oscillations of the beam in phase space, that is: the frequency of the betatron oscillations causes a particle to repeatedly encounter a perturbation such that the effect of subsequent encounters add coherently, which may lead to a rapid growth in the oscillation amplitude of the particle [36, 37, 38].

The general resonance condition is given by Eq.(1.42). The *order* (n) of a resonance is

[4]Exceptions to this rule are, for example, slow extraction using the third order resonance [32] or multiturn extraction and injection of the beam using non-linear resonances [33, 34, 35]. In principle the examination of beam losses on the crossing of resonances can also be used as a diagnostic for non-linear correction qualities.

$n = |a| + |b|$, where a and b are as defined in Eq.(1.42).

$$aQ_x + bQ_y = p \qquad \text{where} \quad a, b, p \in \mathcal{Z} \tag{1.42}$$

Eq.(1.42) defines a series of resonance lines in the (Q_x, Q_y) tune space, and is equivalent to Eq.(1.29). Figure 1.6 plots the resonance lines, initially for resonances of order $n = 5$ and lower (top), then for all resonances of $n \leq 10$ (bottom). The coordinate (Q_x, Q_y) at which an accelerator operates is known as the *working point*, and should be chosen to avoid (as far as possible) resonant values.

The resonant lines defined in Eq.(1.42) have a finite width in (Q_x, Q_y) tune space. The width of the resonance line is termed the *stopband* of a resonance. In most resonances particles which enter inside the stopband undergo a rapid growth in amplitude. Not all resonances, however, generate such instability in the beam motion. The difference linear coupling resonance $(Q_x - Q_y)$, for example, is inherently stable, and will be discussed further in Section 1.4.6.

The approach of the tune to a resonance results in characteristic distortions of the phase space trajectory [38]. The distortion features the same degree of symmetry as the order of the resonance. In the absence of any amplitude dependent detuning there is no region of stability in phase space when the beam lies on a resonant tune, however if detuning with amplitude is present then solutions to the Hamiltonian show stable fixed points at small amplitudes [38]. These fixed points define a central region of stability, around which *islands* of stable beam motion form, the number of islands equalling the order of the resonance. This is illustrated for the fourth order resonance in Fig. 1.7.

1.4.5 Dynamic aperture and the chaotic boundary

The dynamic aperture (DA) defines the boundary in phase space beyond which particle motion becomes unstable [40, 41]. Particles which pass beyond the DA grow rapidly in amplitude, and are lost from the accelerator. The Dynamic Aperture is therefore of key concern for the successful operation of an accelerator and provides an important benchmark for the LHC non-linear model.

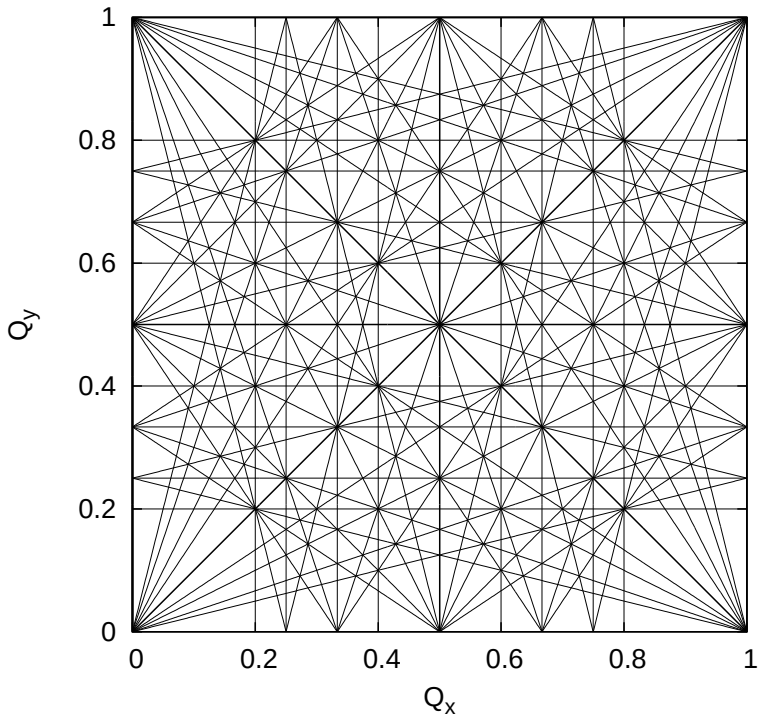

(a) $n \leq 5$

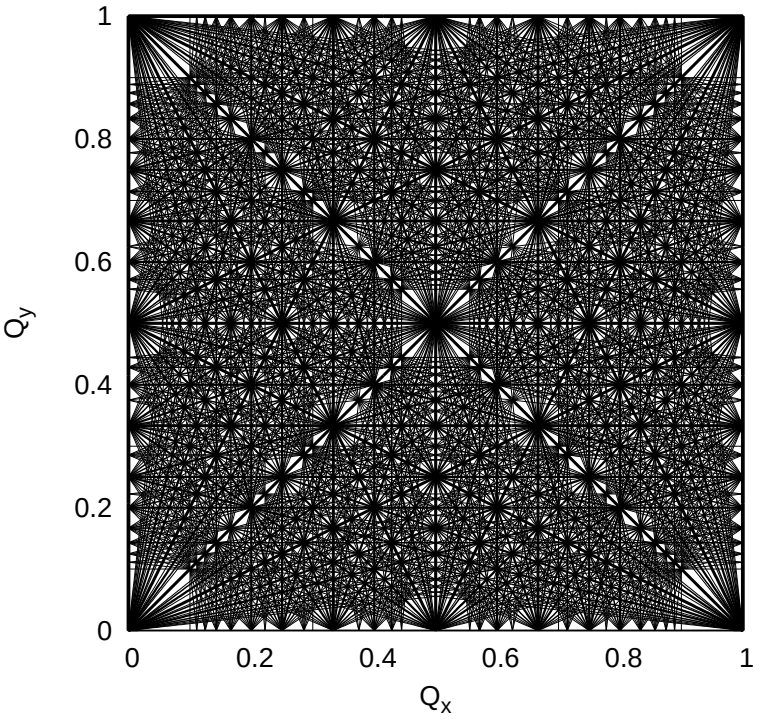

(b) $n \leq 10$

Figure 1.6: Resonance lines defined in (Q_x, Q_y) tune space by Eq.(1.42).

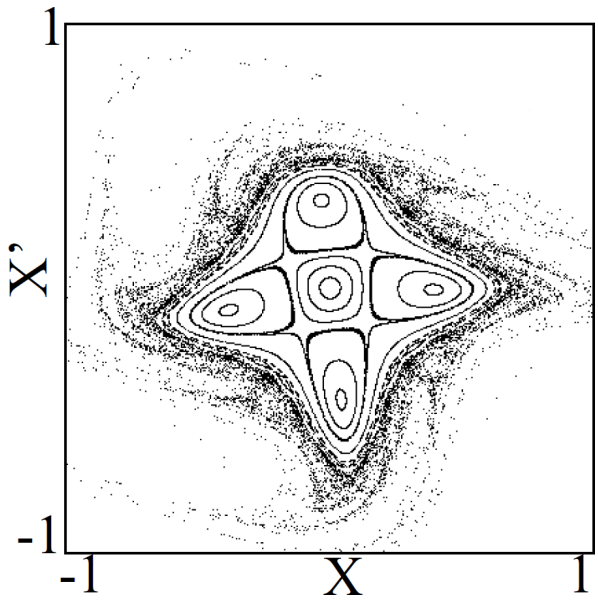

Figure 1.7: Simulated phase space trajectories in the vicinity of the fourth order resonance ($Q = 0.2453$) [39].

The dynamic aperture of a machine is closely related to the onset of chaotic motion. The long term dynamic aperture, sometimes denoted as D_∞, where the ∞ indicates the DA after an infinite number of turns, is generally associated with the boundary between regular and chaotic motion [41, 42]. Practically however, the property of interest is typically the phase space boundary inside of which particles will continue to circulate in the accelerator for a specific time. Consequently the dynamic aperture at is usually considered to be the amplitude beyond which particle motion becomes unstable, where stability it taken to refer to bounded motion over a certain number of turns in the machine. The boundary of stability is larger than the chaotic boundary at finite times, but will vary depending on the time period in question. The DA is therefore a function of time (or equivalently number of turns) with an asymptotic value representing the region of long term stability which is generally associated with the chaotic boundary. The DA is therefore normally quoted as a value associated with a number of turns. Such a definition of the dynamic aperture has been adhered to in this thesis, and unless explicitly stated the terms dynamic aperture or DA should be taken as referring to the stable boundary after a specific number of turns. The DA may be determined in simulation by examining the initial conditions of lost particles in a tracking study, using software such as SIXTRACK [43].

Chaotic motion is characterized by an exponential deviation in phase space of initially close particles [40, 41]. Formally this can be described by the *Lyapunov exponent* (λ), defined: $|\Delta(t)| \sim e^{\lambda t}|\Delta(t=0)|$, where Δ is the separation of two trajectories in phase space. A positive Lyapunov exponent is an indication of chaotic motion. Computationally efficient alternatives to calculation of the Lyapunov exponent as methods to detect the onset of chaos in a tracking simulation are the *distance* and *slope* methods [42]. The distance method is based upon examination of the final separation of two initially close particles. This may give an overestimate of the chaotic boundary, as weakly chaotic particles may not have time to separate substantially in order to be picked up [42]. The slope method is based upon examination of the evolution of the distance in phase space. The slope method may overestimate the boundary in the case of weakly chaotic particles, but is also capable of underestimating the chaotic boundary as a consequence of misidentifying large, but regular, oscillations near resonances [42]. Both methods are implemented in SIXTRACK.

It is also worth noting that, while not utilized in this thesis, the field of *Frequency Map Analysis* (FMA) can have significant applications to the examination of particle stability in accelerators [44, 45, 46].

1.4.6 Linear betatron coupling

In the LHC it is normally desired that the motion of the beam in the transverse (x,y) planes are independent. Such a situation is referred to as *uncoupled* motion, and the transverse phase space can be separated into two 2D ellipses in the (x, x') and (y, y') planes. Up to this point coupled motion, wherein the x and y phase spaces are not separable, has not been explicitly considered. Numerous aspects of the beam dynamics may act to couple the transverse motion. The main sources of linear transverse coupling are solenoidal and skew quadrupole fields, the latter being of most interest for studies of the LHC optics. While the transfer map for linearly coupled motion can take the form of a 4×4 transfer matrix, and it might therefore be considered an aspect of the linear dynamics, discussion of coupled beam dynamics includes some consideration of resonances and resonance driving terms, and has therefore been included within the non-linear phenomenology section of this chapter. Transverse betatron coupling can significantly impact the beam dynamics and is over-viewed

briefly in this section.

Parameterizations of linear coupling

The transverse linear dynamics may be described by a 4×4 transfer matrix:

$$\hat{\mathbf{M}} = \begin{pmatrix} \mathbf{P} & \mathbf{p} \\ \mathbf{q} & \mathbf{Q} \end{pmatrix} \tag{1.43}$$

where $\mathbf{P}$, $\mathbf{p}$, $\mathbf{q}$ and $\mathbf{Q}$ are 2×2 matrices. For uncoupled motion matrices $\mathbf{p}$ and $\mathbf{q}$ are 0.

In the *Edwards-Teng* parameterization, described in [47], the linear coupling may be characterized by a symplectic rotation of $\hat{\mathbf{M}}$ into its normal modes form $\bar{\mathbf{M}}$, in which the motion is decoupled:

$$\bar{\mathbf{M}} = \begin{pmatrix} \mathbf{X} & 0 \\ 0 & \mathbf{Y} \end{pmatrix} = \mathbf{R}\hat{\mathbf{M}}\mathbf{R}^{-1} \tag{1.44}$$

Edwards and Teng characterized the transformation $\mathbf{R}$ by the symplectic matrix:

$$\begin{pmatrix} \mathbf{I}\cos\theta & -\mathbf{K}^{-1}\sin\theta \\ \mathbf{K}\sin\theta & \mathbf{I}\cos\theta \end{pmatrix} \tag{1.45}$$

where $\mathbf{I}$ is the 2×2 unit matrix, and $\mathbf{K}$ is a 2×2 symplectic matrix ($\det(\mathbf{K}) = 1$).

The transfer matrix $\hat{\mathbf{M}}$ of the linear dynamics may therefore be described by the x and y twiss parameters of the uncoupled motion, together with the elements of matrix $\mathbf{K}$ and Teng's angle of rotation θ. In total, six of the twiss parameters, three elements of $\mathbf{K}$, and θ will completely characterize the motion.

The Edwards-Teng parameterization forms the basis of the MAD-X [48] handling of coupled motion. In MAD-X the relevant parameters are $\beta_{x,y}$,$\alpha_{x,y}$,$\mu_{x,y}$,$\gamma_{x,y}$ and r_{11},r_{12},r_{21},r_{22}, where the quantities $r_{11\ldots22}$ correspond to the elements of $\mathbf{K}$ multiplied by $\tan\theta$.

An alternative parameterization of linear coupling was developed by Mais and Ripken, described in [49].

When transverse coupling is non-negligible, particle trajectories are confined to toridal

paths in 4D x, x', y, y' phase space. Such a trajectory is described by four generating vectors and two phases:

$$\bar{z}(s) = \sqrt{\epsilon_I}\left[\bar{z_1}(s)\cos\phi_I - \bar{z_2}(s)\sin\phi_I\right] + \sqrt{\epsilon_{II}}\left[\bar{z_3}(s)\cos\phi_{II} - \bar{z_4}(s)\sin\phi_{II}\right] \tag{1.46}$$

where

$$\bar{z_i} = \begin{pmatrix} x_i \\ x_i' \\ y_i \\ y_i' \end{pmatrix} \qquad\qquad i = 1, 2, 3, 4 \tag{1.47}$$

As in the uncoupled case, two modes of oscillation exist (I, II), however in the Mais-Ripken parameterization these do not correspond to purely horizontal and vertical oscillation. Lattice functions are introduced by projecting the motion of modes I and II onto the transverse planes, and defining the elements of vectors $\bar{z_i}$ as the product of a position envelope function (β) with a position phase function (Φ), and an angle envelope function (γ) with an angle phase function ($\tilde{\Phi}$):

$$\begin{aligned}
\bar{z_1} &= \begin{pmatrix} x_1 \\ x_1' \\ y_1 \\ y_1' \end{pmatrix} = \begin{pmatrix} \sqrt{\beta_{xI}}\cos\Phi_{xI} \\ \sqrt{\gamma_{xI}}\cos\tilde{\Phi}_{xI} \\ \sqrt{\beta_{yI}}\cos\Phi_{yI} \\ \sqrt{\gamma_{yI}}\cos\tilde{\Phi}_{yI} \end{pmatrix} \qquad \bar{z_2} = \begin{pmatrix} x_2 \\ x_2' \\ y_2 \\ y_2' \end{pmatrix} = \begin{pmatrix} \sqrt{\beta_{xI}}\sin\Phi_{xI} \\ \sqrt{\gamma_{xI}}\sin\tilde{\Phi}_{xI} \\ \sqrt{\beta_{yI}}\sin\Phi_{yI} \\ \sqrt{\gamma_{yI}}\sin\tilde{\Phi}_{yI} \end{pmatrix} \\
\bar{z_3} &= \begin{pmatrix} x_3 \\ x_3' \\ y_3 \\ y_3' \end{pmatrix} = \begin{pmatrix} \sqrt{\beta_{xII}}\cos\Phi_{xII} \\ \sqrt{\gamma_{xII}}\cos\tilde{\Phi}_{xII} \\ \sqrt{\beta_{yII}}\cos\Phi_{yII} \\ \sqrt{\gamma_{yII}}\cos\tilde{\Phi}_{yII} \end{pmatrix} \qquad \bar{z_4} = \begin{pmatrix} x_2 \\ x_2' \\ y_2 \\ y_2' \end{pmatrix} = \begin{pmatrix} \sqrt{\beta_{xII}}\sin\Phi_{xII} \\ \sqrt{\gamma_{xII}}\sin\tilde{\Phi}_{xII} \\ \sqrt{\beta_{yII}}\sin\Phi_{yII} \\ \sqrt{\gamma_{yII}}\sin\tilde{\Phi}_{yII} \end{pmatrix}
\end{aligned} \tag{1.48}$$

$$\bar{z} = \begin{pmatrix} \sqrt{\epsilon_I\beta_{xI}}\cos(\Phi_{xI} + \phi_{xI}) + \sqrt{\epsilon_{II}\beta_{xII}}\cos(\Phi_{xII} + \phi_{xII}) \\ \sqrt{\epsilon_I\gamma_{xI}}\cos(\tilde{\Phi}_{xI} + \phi_{xI}) + \sqrt{\epsilon_{II}\gamma_{xII}}\cos(\tilde{\Phi}_{xII} + \phi_{xII}) \\ \sqrt{\epsilon_I\beta_{yI}}\cos(\Phi_{yI} + \phi_{yI}) + \sqrt{\epsilon_{II}\beta_{yII}}\cos(\Phi_{yII} + \phi_{yII}) \\ \sqrt{\epsilon_I\gamma_{yI}}\cos(\tilde{\Phi}_{yI} + \phi_{yI}) + \sqrt{\epsilon_{II}\gamma_{yII}}\cos(\tilde{\Phi}_{yII} + \phi_{yII}) \end{pmatrix} \tag{1.49}$$

Lagrange invariance requires that:

$$\bar{z}_{1,3}^{T}\mathbf{S}\bar{z}_{2,4} = \mathrm{CONST} \qquad \text{with } \mathbf{S} = \begin{pmatrix} 0 & 1 & 0 & 0 \\ -1 & 0 & 0 & 0 \\ 0 & 0 & 0 & 1 \\ 0 & 0 & -1 & 0 \end{pmatrix} \tag{1.50}$$

where $\mathbf{S}$ is the unit symplectic matrix. In order to characterize the volume of the tori by the quantities ϵ_I and ϵ_{II}, $\bar{z}$ is normalized such that:

$$\bar{z}_1^T\mathbf{S}\bar{z}_2 = 1 \qquad\qquad \bar{z}_3^T\mathbf{S}\bar{z}_4 = 1 \tag{1.51}$$

which yields[5]:

$$\beta_{xI}\Phi'_{xI} + \beta_{yI}\Phi'_{yI} = 1 \qquad\qquad \beta_{xII}\Phi'_{xII} + \beta_{yII}\Phi'_{yII} = 1 \tag{1.52}$$

The areas of the ellipses in mode I and II are then constants of the motion, however the projected areas in x, x' and y, y' are not conserved for coupled motion.

Analogously with the uncoupled case the position and angle envelope functions are related by:

$$\gamma_{zi} = \frac{(\beta_{zi}\Phi'_{zi})^2 + \alpha_{zi}^2}{\beta_{zi}} \qquad\qquad z = x, y \text{ and } i = I, II \tag{1.53}$$

The coupled dynamics is therefore described by four β functions, four γ functions (or equivalently four α functions) and two phase functions. Figure 1.8 illustrates how the Mais-Ripken lattice functions describe the projection of the 4D Taurus onto the x, x' or y, y' plane.

The Mais-Ripken parameterization is the basis of the Polymorphic Tracking Code's (PTC [50]) handling of coupled dynamics. The relevant PTC twiss parameters are β_{11},β_{12},β_{21},β_{22} corresponding to β_{xI},β_{xII},β_{yI},β_{yII}, and similarly for other twiss parameters.

In practice when measuring twiss parameters in the real accelerator, it is the horizontal and vertical functions which are observed. This corresponds with the Edwards-Teng twiss

[5]Considered here is the normalization under the influence of skew quadrupolar fields, solenoidal fields introduce additional complications [49].

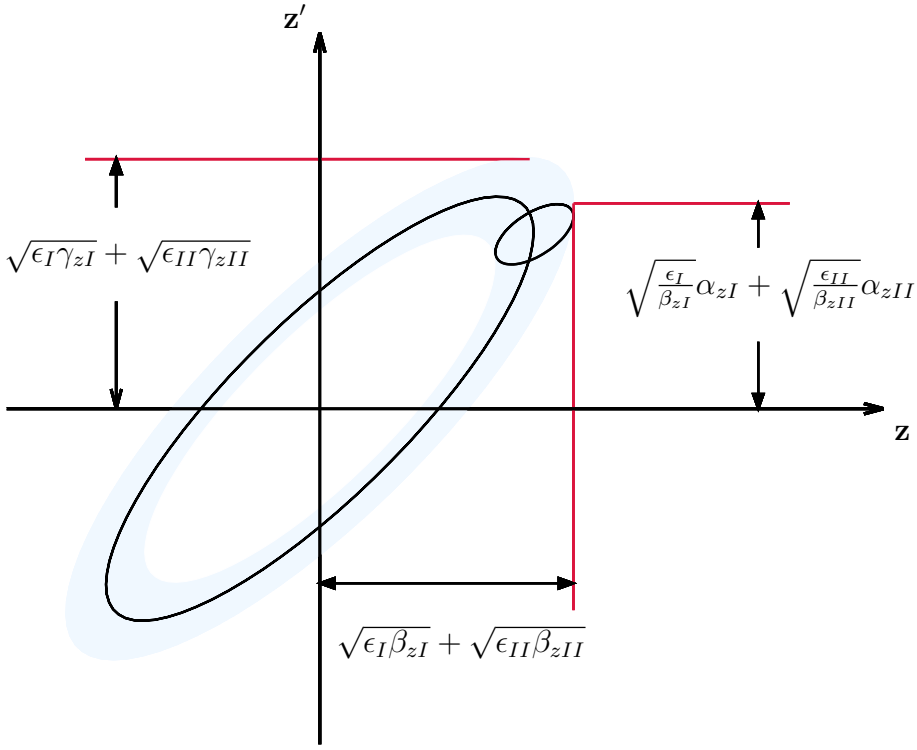

Figure 1.8: Projection of 4D taurus onto the z, z' plane (where $z = x, y$).

functions. If it is desired to compare PTC simulations of twiss parameters under the influence of non-negligible transverse coupling to measurements, it is therefore necessary to transform the PTC results into the Edwards-Teng parameterization, or vice-versa. Lebedev-Bogacz [51] and Alexahain et al. [52] have derived most of the necessary transformations.

Dynamics of coupled motion

Linear coupling is driven by skew quadrupole fields (these may be generated by dedicated skew quadrupoles in the lattice, and by magnetic and geometric errors in other elements) and solenoids. In the LHC the contribution of the skew quadrupole component dominates.

To first order linear coupling drives two resonances: $(Q_x + Q_y)$ and $(Q_x - Q_y)$. To higher order linear coupling may also give stationary terms in the Hamiltonian (a tune shift)

and drive the $2Q_x$ and $2Q_y$ resonances. The higher order effects are typically neglected. The dynamics of the beam are significantly affected by the approach to the sum $(Q_x + Q_y)$ and difference $(Q_x - Q_y)$ linear coupling resonances. This has been studied through Hamiltonian perturbation theory, this is the approach followed by Guignard [53] and Wiedeman [54], and also through the normal form / resonance driving term formalism [27]. The magnitude of the transverse coupling is characterized by coefficients C^- and C^+, corresponding to the difference and sum resonances respectively, which are simply proportional to the hamiltonian coefficients corresponding to these resonances ($2h_{1001}$ and $2h_{1010}$) [53].

As the tunes approach the difference resonance the amplitude is described by a relation in the form of Eq.(1.54) [54].

$$\epsilon_x + \epsilon_y = \text{CONST} \tag{1.54}$$

Consequently as the difference resonance is approached the beam motion may not become unstable (as neither emittance may grow unbounded). Rather there is a periodic exchange of emittance (equivalently energy) between the transverse planes. This leads to a characteristic 'beating' of betatron motion under the influence of difference coupling, which may be observed with kicked beams. Eq.(1.55) [53] and Fig. 1.9 show for a beam excited in a single plane how the the period (T) and amplitude ratio (G) associated with the beating of betatron oscillations due to linear coupling relate to the coupling parameters. The properties defined in Eq.(1.55) are indicated on Fig. 1.9.

$$\begin{aligned} \Delta &= \text{unperturbed tune split} \\ |C^-| &= \text{magnitude of the linear difference coupling} \end{aligned}$$

$$\begin{aligned} G &= \frac{A_{min}}{A_{max}} = \frac{|\Delta|}{\sqrt{\Delta^2 + |C^-|^2}} \\ T &= \frac{G}{|\Delta|\, f_{revolution}} \end{aligned} \tag{1.55}$$

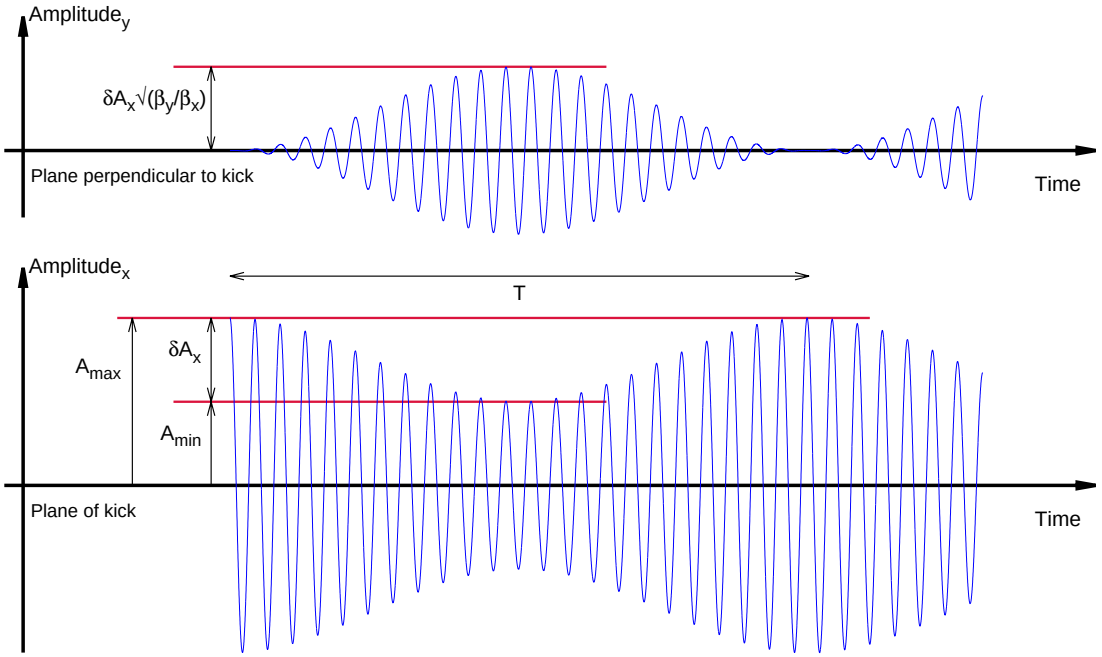

Figure 1.9: Illustration of the relation of linear difference coupling parameters to the beating of betatron oscillations of a beam which is kicked in a single plane. This ignores decoherence. In this plot the axes are labelled as x being the plane of the kick, and y the plane into which the kick is coupled, however this is simply for convenience and the axes may be reversed without consequence.

Close to the linear difference coupling resonance it is also found that while there are two modes of oscillation, they are perturbed from the uncoupled tunes of the accelerator as described by Eq.(1.56).

$$Q_1 = Q_x - \frac{\Delta}{2} + \frac{1}{2}\sqrt{\Delta^2 + |C^-|^2} \qquad (1.56)$$
$$Q_2 = Q_y + \frac{\Delta}{2} - \frac{1}{2}\sqrt{\Delta^2 + |C^-|^2}$$

Thus if the motion is uncoupled or far from the resonance ($\Delta \gg |C^-|$) the oscillation modes are well correlated with the unperturbed tunes, however as the resonance is approached ($\Delta \rightarrow 0$) the perturbed tunes are forced apart by the coupling, and there exists a minimum tune split which is equal to the magnitude of the C^- ($\delta Q_{min} = |Q_1 - Q_2| = |C^-|$). This is illustrated in Fig. 1.10.

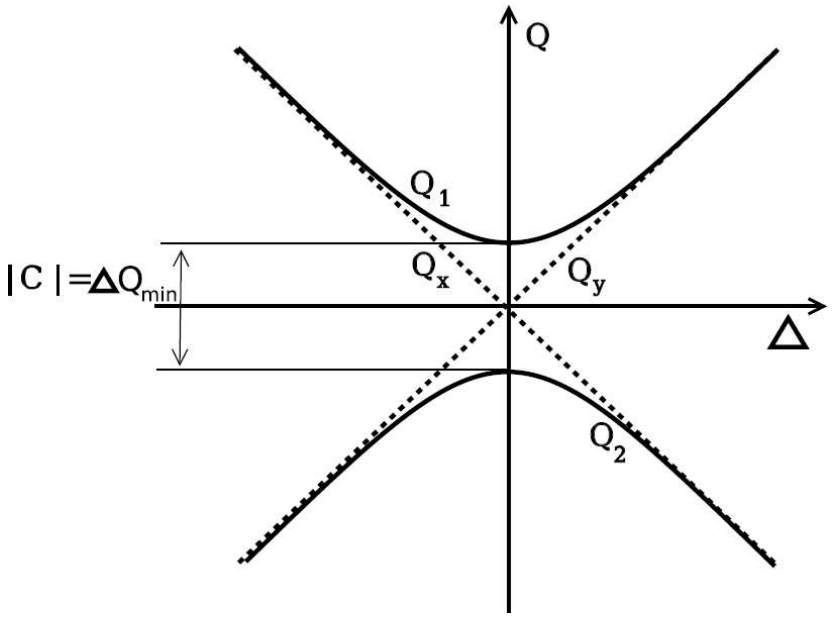

Figure 1.10: The dependence of the frequency of the oscillation modes on the tune split, under the influence of linear difference coupling [55].

The beating of betatron oscillations and the existence of a non-zero minimum tune approach are therefore the principle observable consequences of the linear difference coupling resonance.

In contrast with Eq.(1.54), as the tunes approach the sum resonance the amplitude is described by a relation in the form of Eq.(1.57).

$$\epsilon_x - \epsilon_y = \mathrm{CONST} \tag{1.57}$$

Unlike the relatively benign dynamics of difference coupling therefore, the sum resonance allows for unstable motion as only the difference in emittance is constrained. Resultantly the LHC working point ($Q_{x,y} = 0.28, 0.31$ for injection, and $Q_{x,y} = 0.31, 0.32$ for squeezed beams) is selected such that the linear coupling is dominated by the difference resonance.

Resonance Driving Terms for linear betatron coupling

Linear coupling in the LHC is dominated by the contribution of skew quadrupole fields, which generate terms $\propto xy$ in the Hamiltonian. As discussed in Section 1.3, this gives rise to the resonance driving terms f_{1001} and f_{0110} which correspond to the $Q_x - Q_y$ resonance, and the f_{1010} RDT which corresponds to the $Q_x + Q_y$ resonance. In the LHC the working point is selected so as to be close to the stable difference resonance as opposed to the unstable sum resonance, consequently the $|f_{1001}|$ in the LHC dominates relative to the $|f_{1010}|$.

The coupling RDTs can be measured in the LHC from spectral analysis of the betatron oscillations. Such oscillations may be induced with a kicker magnet or an AC-dipole [56] (which induces forced oscillations of the beam), however in the AC-dipole case the calculation of the RDTs must take into account the effect of the AC-dipole on the Hamiltonian [57]. Spectral analysis of injection oscillations has also been recently applied to measure the coupling RDTs in the LHC [7]. f_{1001} and f_{0110} describe the same dynamics, with f_{1001} corresponding to motion in the horizontal plane and f_{0110} corresponding to motion in the vertical plane. As standard therefore, when measuring the linear coupling in the LHC the average of f_{1001} and f_{0110} is considered, but is generally labelled as f_{1001}. This convention has been adhered to in this thesis.

f_{1001} is approximately related to the difference linear coupling coefficient $|C^-|$ by Eq.(1.58) [27], where $\overline{|f_{1001}|}$ is the mean amplitude of f_{1001} around the accelerator ring.

$$|C^-| \approx 4|(Q_x - Q_y)|\overline{|f_{1001}|} \tag{1.58}$$

Correction of the linear coupling RDTs is implemented in the LHC to enable both global and local correction of the linear coupling [55, 58].

1.5 Luminosity

The LHC accelerator is operated for the production of data which enables the study of High Energy Physics (HEP) interactions. Counter-rotating beams of hadrons are made to collide in four Interaction Points (IP), around which various HEP experimental apparatus are located.

The constituent particles which together comprise the hadrons within the beam may interact during these collisions via processes which are of interest to the HEP community.

Many of the interactions studied at the LHC HEP experiments are extremely rare, and, in order to differentiate signals of interest from background processes, a substantial volume of statistics is required. The rate for a specific interaction is given by,

$$R_p = L\sigma_p \tag{1.59}$$

where σ_p is the cross section for the interaction. L is the *Luminosity* of the accelerator, measured in units of *inverse barns per second* ($\mathrm{b}^{-1}\mathrm{s}^{-1}$) where $[\mathrm{b}] = [10^{-24}\,\mathrm{cm}^{-2}]$. Luminosity is the key figure of merit for collider operation. The general luminosity for colliding beams is defined as [59, 60],

$$L = (f_{rev} n_{coll})\, K N_1 N_2 \frac{1}{c} \int_{-\infty}^{+\infty} \int\int\int \rho_1\left(x, y, s, -s_0\right) \rho_2\left(x, y, s, s_0\right) \mathrm{d}x\, \mathrm{d}y\, \mathrm{d}s\, \mathrm{d}s_0 \tag{1.60}$$

where x, y are the transverse dimensions, s is the longitudinal dimension, and s_0 is a time-like variable ($s_0 = ct$) which defines the longitudinal separation of the bunches. $N_{1,2}$ are the numbers of particles per bunch in the two beams, $\rho_{1,2}$ define the particle density, f_{rev} is the revolution frequency, and n_{coll} is the number of colliding bunches per turn (in the LHC this differs from the total number of bunches, may vary between collision points, and will depend on the specific filling scheme). K is the kinematic factor:

$$K = \sqrt{\left(\bar{v}_1 - \bar{v}_2\right)^2 - \frac{\left(\bar{v}_1 \times \bar{v}_2\right)^2}{c^2}} \tag{1.61}$$

For typical operation in the LHC, with counter rotating relativistic beams of equal magnitude velocity, the kinematic factor is $\sim 2c$ [61].

An analytical expression for the Luminosity may be obtained by assuming the bunches

have uncorrelated Gaussian profiles in all planes, and equal bunch lengths [59, 60]:

$$L = \frac{N_1 N_2 \left(f_{ref} n_{coll}\right)}{2\pi\sqrt{\left(\sigma_{x,1}^2 + \sigma_{x,2}^2\right)}\sqrt{\left(\sigma_{y,1}^2 + \sigma_{y,2}^2\right)}} \tag{1.62}$$

where $\sigma_{z,b}$ is the size at the interaction point of beam b, in transverse plane z. This is related to the beam emittance and beta function at the Interaction Point by,

$$\sigma_{z,b} = \sqrt{\beta^*_{z,b}\epsilon_{z,b}} \qquad \text{where } z = x, y \text{ and } b = 1, 2 \tag{1.63}$$

where the dispersion function is assumed to be negligible at the interaction point. In practice an uncorrelated Gaussian beam profile may not accurately describe the charge distribution, however it is a useful approximation which illustrates the importance of a well corrected β function at the interaction points.

In addition to the assumption of Gaussian distributions of charge within the bunches, Eq.(1.62) also ignores a number of complications to the calculation of luminosity. To avoid parasitic collisions either side of the interaction point it is necessary to separate the beams by introducing a crossing angle into the LHC orbit at the Interaction Point. This reduces the luminosity. Additional complications can arise due to any transverse separation of the beams at the IP, and also due to small variations of the beta function along the length of the bunch at the IP, both of which will reduce the luminosity. Eq.(1.62) should be modified to:

$$L = \frac{N_1 N_2 \left(f_{ref} n_{coll}\right)}{2\pi\sqrt{\left(\sigma_{x,1}^2 + \sigma_{x,2}^2\right)}\sqrt{\left(\sigma_{y,1}^2 + \sigma_{y,2}^2\right)}} \times (reduction\, factors) \tag{1.64}$$

Details of the relevant factors may be found in [59, 60]. The value of the reduction factor will depend on the specific state of the collider at a given moment, however for the LHC a value of the order of ~ 0.8 is expected.

The luminosity described so far is the *instantaneous luminosity*, the luminosity of the collider at a given moment in time. Also of practical concern is the *integrated luminosity*

($[\mathrm{b}^{-1}]$) over a given period of time:

$$L_{int} = \int_0^T L(t)\delta t$$
$$Number\,of\,events = L_{int}\sigma_p \tag{1.65}$$

The integrated luminosity is determined, for example, by down-time throughout the run, and by the ratio of preparation time to time in collisions. During operation for luminosity production the instantaneous luminosity decays throughout the fill as particles are lost from the beams (*beam lifetime* [62]). Particle losses prior to bringing the beams into collision will also adversely affect the initial $N_{1,2}$ reducing the obtained L_{int}.

A well controlled linear optics is essential for effective luminosity production, both directly through the optics quality at a given moment, and more generally in the contribution to the smooth operation of the accelerator. Departures from the linear approximation, however, also play a substantial role in determining the performance of an accelerator. For example, correction of the non-linearities in a collider may provide additional space in the resonance diagram, allowing a larger beam-beam tune shift, and hence higher intensity beams, to be tolerated. Degradation of beam quality - for example emittance increase, beam loss, or the reduction of beam lifetime - due to non-linear beam dynamics will also reduce the delivered luminosity. An understanding of the non-linear dynamics can therefore be important for the effective operation of an accelerator such as the Large Hadron Collider.

Chapter 2

The LHC accelerator

The Large Hadron Collider is a hadron accelerator constructed in the former Large Electron Positron Collider tunnel at CERN. The work presented in this thesis was performed on the LHC during its first phase of operation between July 2010 and July 2013. In this section a brief overview of the LHC will be given.

2.1 The LHC lattice

The Large Hadron Collider (LHC) is a $26.66\,\mathrm{km}$ twin ring synchrotron collider operated by the CERN[1] laboratory. Two counter rotating hadron beams are circulated in the accelerator, and collide at four interaction points (IPs), to provide data for High Energy Physics (HEP) experimental apparatus: ATLAS [63, 64], LHCf [65, 66], Alice [67, 68], CMS [69, 70], TOTEM [71, 72], LHCb [73, 74], and MoEDAL [75]. The LHC is a key accelerator based instrument of study for a wide range of HEP phenomena.

The LHC consists of eight arcs (also called sectors), intersected by eight insertion regions (IRs). Naming conventions are defined such that the arc separating IR1 and IR2 is labelled Arc12, similarly for all other arcs. The octant of the LHC with IR1 at its center, and containing halves of Arc12 and Arc81, is labelled Octant 1, similarly for all other octants. *Beam 1* rotates clockwise around the LHC ring as viewed from above, *Beam 2* rotates counter-clockwise as viewed from above. The beams occupy separate apertures, except for those IRs where they are made to collide. The layout of the LHC is indicated in Figure 2.1.

The LHC machine is described in the *LHC design report* [76, 77, 78].

[1] *CERN*, the *European Organization for Nuclear Research*, is a High Energy Physics laboratory situated on the Franco-Swiss border just outside of Geneva. CERN takes its name from the acronym of the *Conseil Européen pour la Recherche Nucléaire*, the provisional council originally mandated to establish the institute.

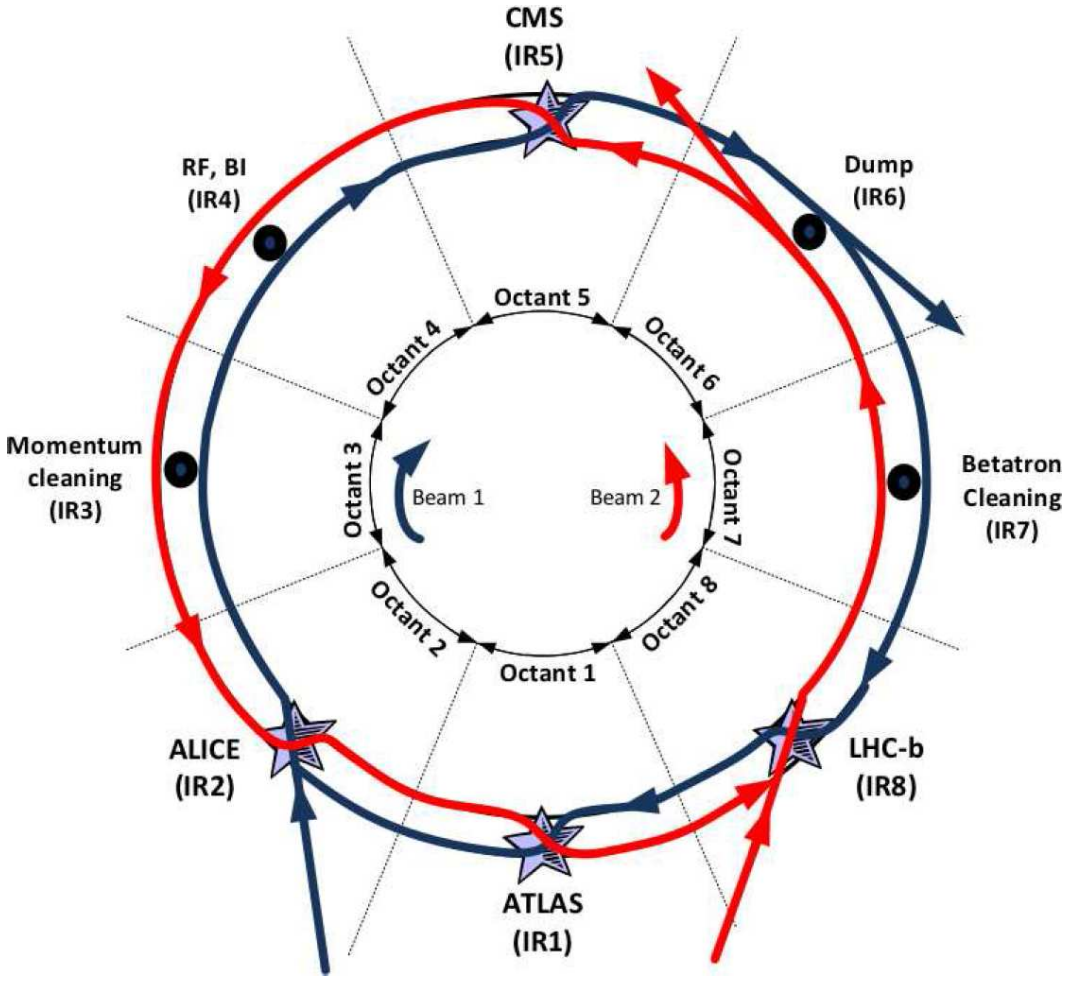

Figure 2.1: Schematic of the LHC layout [55].

2.1.1 The LHC arcs

Each LHC arc is constructed from 23 approximately regular cells of $106.9\,\mathrm{m}$. The layout of an LHC arc cell is shown in Fig. 2.2.

The cell utilizes an FBDB layout of alternating focusing and defocusing superconducting quadrupoles, inter-spaced with superconducting dipole magnets. These elements are commonly labelled MQF, MQD, and MB. Each cell contains two MQ (one focusing, one defocusing), inter-spaced by three MB (six MB per cell). The tunnel in which the LHC resides was originally constructed for an earlier electron-positron collider, the Large Electron

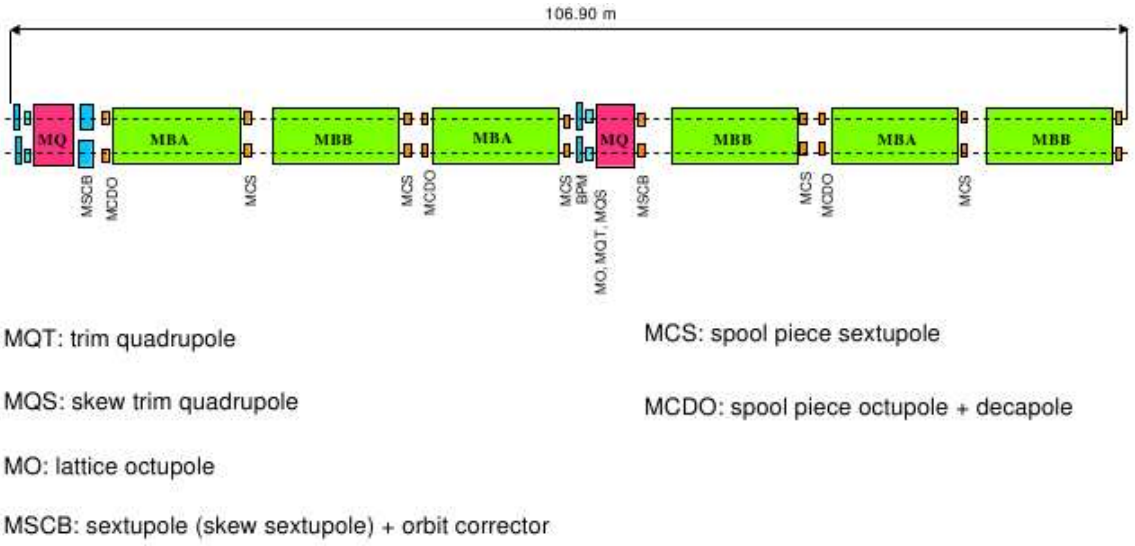

Figure 2.2: Schematic of an LHC arc cell [79].

Positron Collider (LEP), which has since been decommissioned. The transverse dimensions of the LEP tunnel are too small to house two independent rings, therefore the MB magnets in the LHC are of a dual bore design. Within each arc all MB are powered in series. The main quadrupoles are arranged in two families per arc: all MQF of the two apertures being powered in series, and all MQD of the two apertures being powered in series. A cross section of the LHC main dipole assembly is shown in Fig. 2.3 [80], together with a cross section of the MB magnet with field lines indicated [81]. A cross section of the LHC main quadrupole assembly is shown in Fig. 2.4 [82], together with a photo of an MQ magnet [83].

Inherent to the dual bore design and superconducting nature of the main arc magnets are significant higher order field errors [19]. Consequently superconducting *spool piece* magnets are installed throughout the arc for the local compensation of the magnetic errors in the main arc magnets [79]. Sextupolar correctors, known as the sextupolar spool pieces or MCS [84], are mounted on the ends of every main dipole. These elements are intended to correct the b_3 errors of the MB. A feature of the superconducting nature of magnets in the LHC is the decay of field components during the injection plateau followed by snap-back to their initial values at the beginning of the ramp [85]. In the LHC the decay and snap-back of b_3 errors in the main dipoles is a significant concern. The settings of the MCS therefore vary throughout injection in order to track changes in the b_3 content of the MB [84]. Octupole and decapole

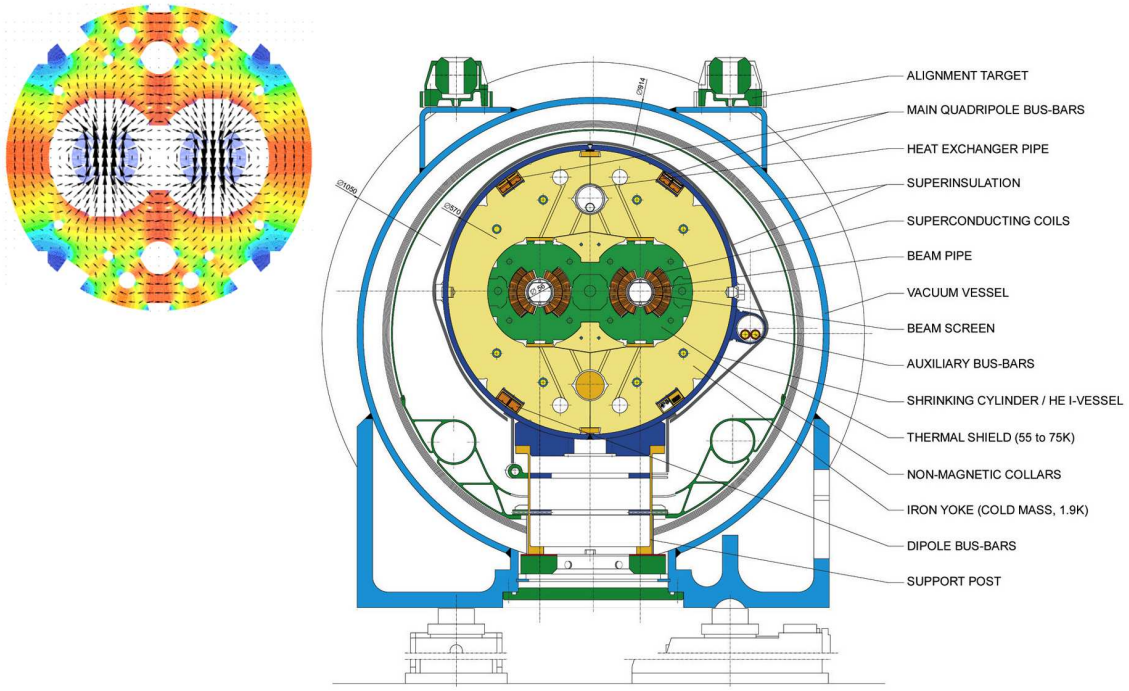

Figure 2.3: Cross section of the LHC main dipole assembly [80], alongside a cross section of the MB magnet with field lines indicated [81].

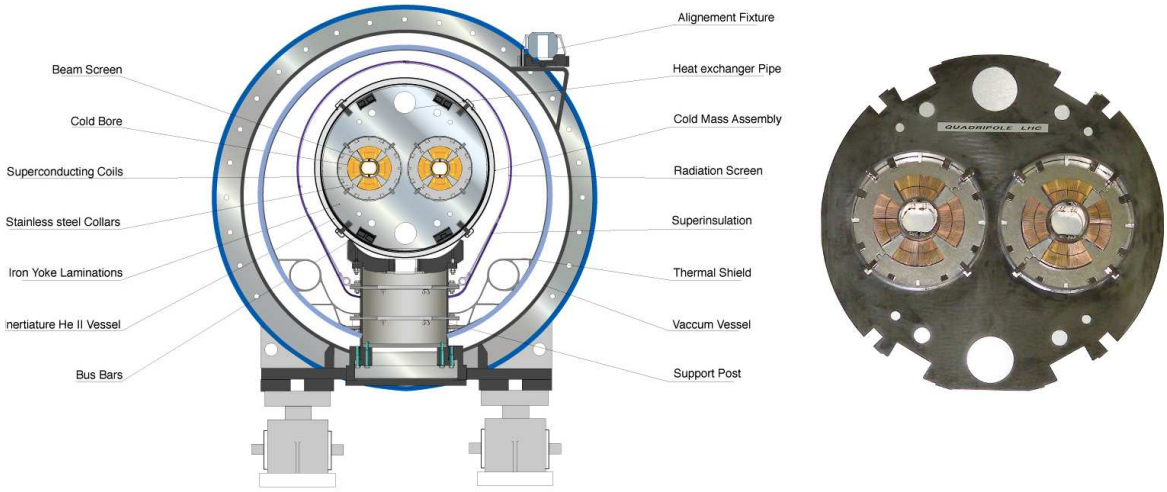

Figure 2.4: Cross section of the LHC main quadrupole assembly [82], together with a photo of an LHC MQ [83].

spool pieces [84] are also used in the LHC for the compensation of b_4 and b_5 errors in the main arc magnets. The octupole corrector magnets, MCO, are nested within the decapole corrector magnets, MCD, and together are referred to as the MCDO (or equivalently the MCOD). Due to the nested configuration only the MCD magnets are pre-cycled. MCDO are mounted on the ends of every second MB. Spool piece magnets in the LHC are single aperture, and are powered in series so as to define one family per Arc per beam.

In addition to the spool piece correctors, linear and non-linear *lattice correctors* are also present in the arcs, mounted on the main arc quadrupoles. All lattice correctors are powered independently between the two beams. Horizontal and vertical orbit correctors (MCBH and MCBV) are installed at each focusing and defocusing MQ respectively. Normal trim quadrupoles, MQT, are used primarily for correction of the tune in the LHC. Four MQT per arc are rotated by 45° to form skew quadrupoles, MQS, which are intended for correction of linear coupling. Normal and skew lattice sextupoles, MS and MSS, are also mounted on the MQ, and are intended for correction of the natural chromaticity and the chromatic coupling respectively. Of most significance for this thesis however, Landau octupoles, MO, are present to provide damping of coherent oscillations of the beam due to collective instabilities. The Landau octupoles are powered in series such that there are two families (focusing and defocusing) per arc per beam.

Figure 2.5 shows how the betatron phase (top), beta-function (center) and horizontal dispersion (bottom) vary through a single LHC arc cell. A schematic of the cell is also shown, which indicates the locations of the MB, MQ and beam position monitors (BPM).

2.1.2 The LHC insertion regions

The LHC features eight Insertion Regions, labelled IR1-IR8. The principal functions of the insertion regions are summarized in Table 2.1. Detailed descriptions of the layout of the IRs may be found in [79].

Of primary interest to this thesis are the experimental insertions, of which the LHC has four, located at IR1, IR2, IR5 and IR8. In the experimental IRs the beta-function is squeezed to small values in order to achieve a high luminosity. This is particularly true of IR1 and IR5,

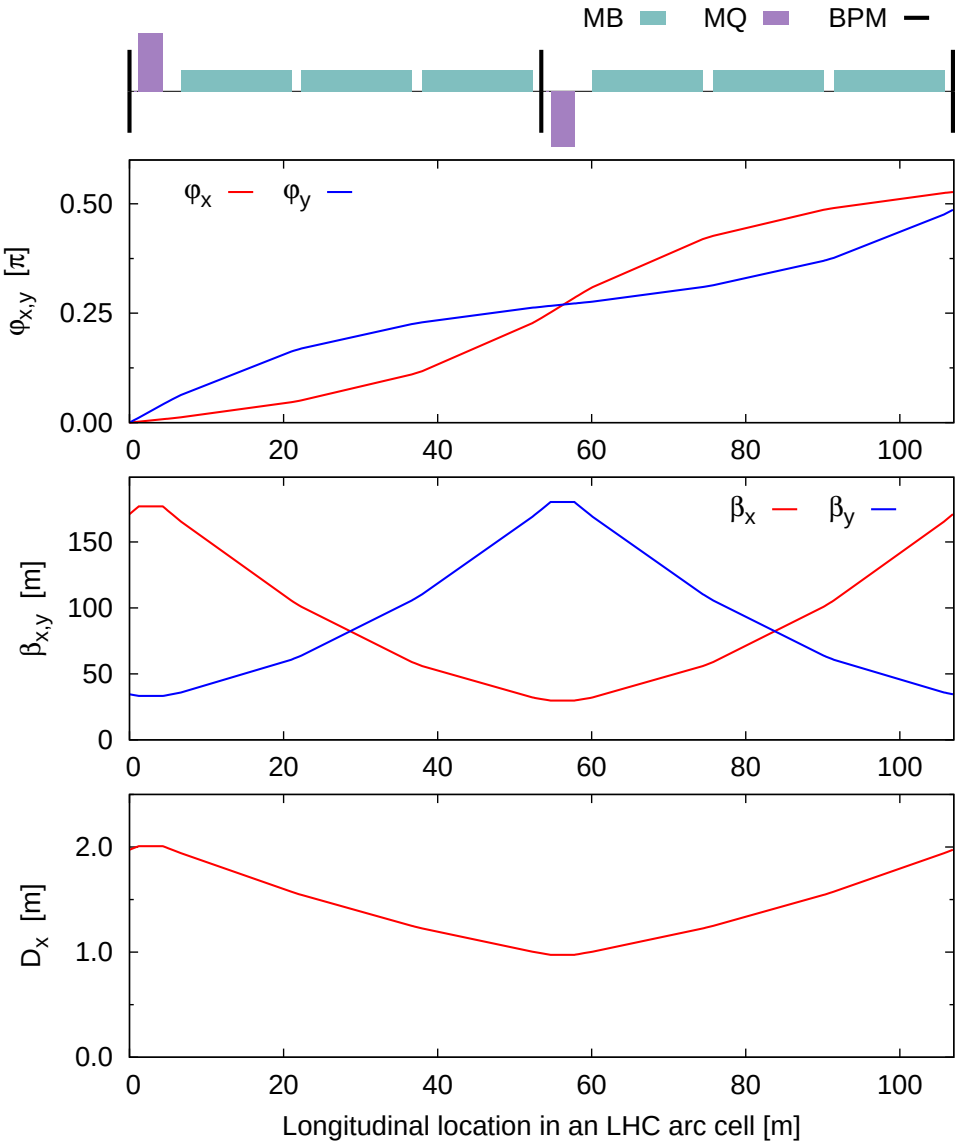

Figure 2.5: Betatron phase (top), beta-function (center) and horizontal dispersion (bottom) in a single LHC cell. A schematic of the cell is also shown which indicates the locations of the main dipoles (MB), main quadrupoles (MQ) and beam position monitors (BPM).

Table 2.1: LHC insertion regions.

IR1	ATLAS and LHCf experiments
IR2	Alice experiment and Beam 1 injection
IR3	Momentum cleaning
IR4	RF and LHC beam instrumentation
IR5	CMS and TOTEM experiments
IR6	Beam dump
IR7	Betatron cleaning
IR8	LHCb and MoEDAL experiments, and Beam 2 injection

as ATLAS and CMS operate with tightly squeezed beams as standard (with the exception of specific '*High* β' runs). IR2, Alice, typically operates without tightly squeezed beams for proton collisions, however during ion and proton-ion (Pb-Pb and p-Pb) collisions the β^* is reduced. During normal operation the β^* in Alice and LHCb is still squeezed, but only to the order of several meters ($3\,\mathrm{m}$ and $8\,\mathrm{m}$ respectively in 2012). This contrasts with a β^* in ATLAS and CMS of $0.6\,\mathrm{m}$ in 2012.

In order to achieve a small β^* at the interaction points, the beams are focused using a '*triplet*' arrangement of quadrupoles in the IRs. Such an arrangement necessarily has a substantial beta function in triplets and neighbouring elements. This is illustrated in Fig. 2.6, which plots the nominal beta function through IR1, for a β^* in the ATLAS Interaction Point (IP) of $0.6\,\mathrm{m}$. A schematic of the LHC lattice in this region is shown alongside. Labels *Q1, Q2* and *Q3* indicate the triplet quadrupoles, and *D1, D2* indicate the separation/recombination dipoles responsible for bringing the beams together in the common region from their separate apertures in the arcs. The *Q4, Q5, Q6* and *Q7* are matching quadrupoles.

Due to the large β either side of the Interaction Points, magnetic errors in the elements in the IRs can significantly influence the beam dynamics. To enable the correction of errors in the IRs, linear and non-linear corrector magnets are added in the insertions, distributed symmetrically about the IP. Of particular concern to this thesis, combined b_3 / b_6 correctors, and combined a_3 / b_4 / a_4 correctors are installed on the non-IP sides of the *Q3* triplet quadrupoles. A schematic of the corrector layout in the LHC experimental insertions is shown in Figure 2.7.

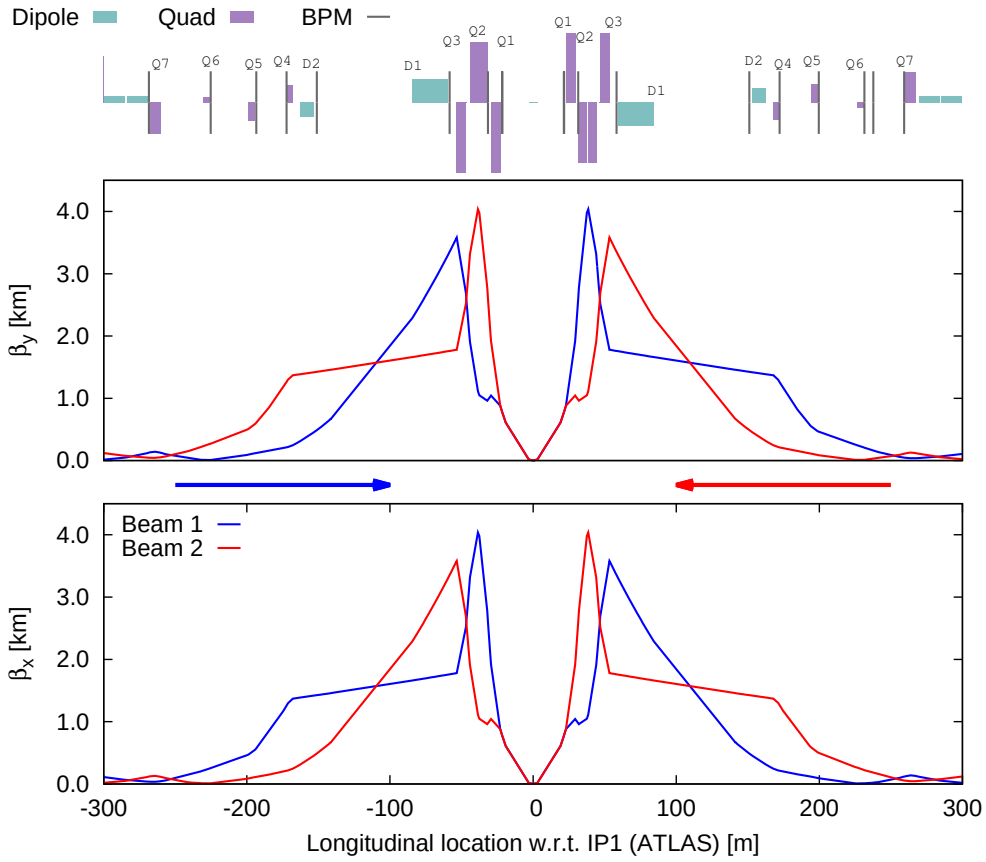

Figure 2.6: Beta function through IR1 (ATLAS), with $\beta^* = 0.6\,\mathrm{m}$. A schematic of the lattice in this IR is shown (top). Labels *Q1, Q2* and *Q3* indicate the triplet quadrupoles, and *D1, D2* indicate the separation/recombination dipoles responsible for bringing the beams together in the common region from their separate apertures in the arcs. The *Q4, Q5, Q6* and *Q7* are matching quadrupoles.

During luminosity production the LHC operates with many bunches, and parasitic crossing points exist on either side of the IPs. In order to prevent collisions at these locations, closed orbit bumps are introduced in a single plane of each experimental insertion to generate a crossing angle at the IP. An example of the simulated crossing angle in IP1 (for $\beta^* = 0.6\,\mathrm{m}$ at $4\,\mathrm{TeV}$) is shown in Figure 2.8.

Differing conventions exist to describe the LHC crossing angle. Throughout the studies described in this thesis the crossing angle is defined as the angle made by the beam with the longitudinal axis in its direction of travel. Thus, considering Figure 2.8, the crossing angles

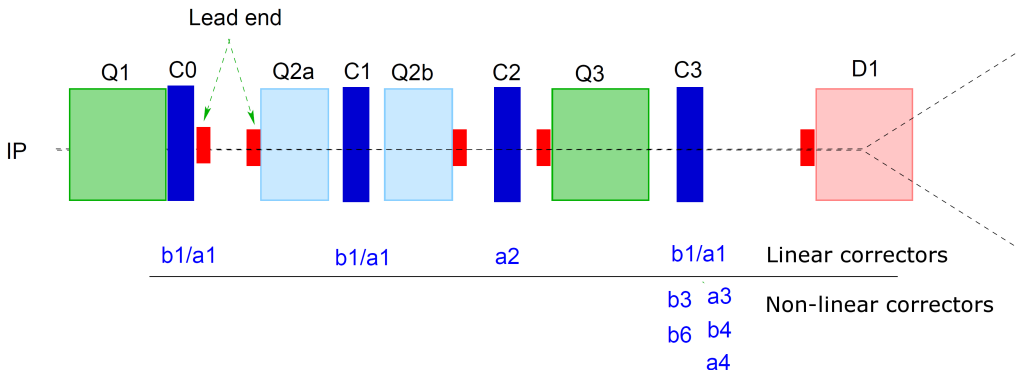

Figure 2.7: Corrector layout in the LHC experimental insertions [86].

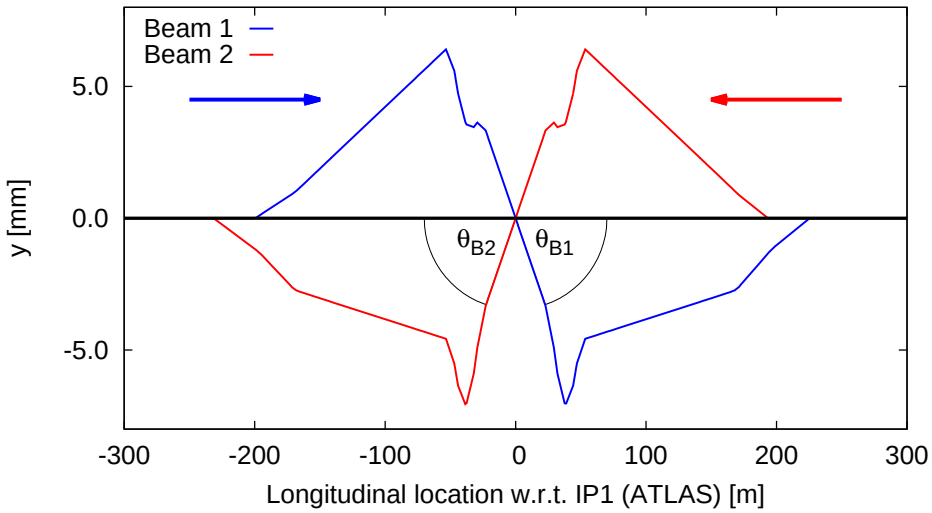

Figure 2.8: Simulated nominal crossing angle in IP1 for $\beta^* = 0.6\,\mathrm{m}$ at $4\,\mathrm{TeV}$.

of Beam 1 and Beam 2 are defined to be θ_{B1} and θ_{B2} respectively. Dedicated closed orbit bumps may also be applied to separate the beams at the IPs themselves. These *separation bumps* are applied, for example, during injection, ramp, and squeeze to prevent collisions at these stages in the LHC cycle.

2.1.3 Error estimates for the LHC lattice

During LHC construction, measurements were performed of individual magnet misalignments within the cryostats and the alignment of the cryostats within the LHC. The Windows Interface to Simulation Errors (WISE [87]) produces estimates of the geometric errors in the LHC lattice [88] from these measurements.

Estimates of the magnetic errors in the LHC are also produced by WISE, based on direct magnetic measurements and on the associated uncertainties. Low current measurements were performed at room temperature on all magnets at industry (*'warm measurements'*), and *'cold'* measurements (under operational conditions) were performed on a fraction of the magnets once delivered to CERN. For magnets without cold measurements a *'warm-to-cold'* correlation is introduced in the modelling of the field, however this has an associated uncertainty. Typical uncertainties included in the WISE modelling are the uncertainty on this warm-to-cold correlation, measurement errors, hysteresis, and power-supply accuracy. Sixty magnetic instances (known as *seeds*) of the LHC are defined by WISE in order to encompass the likely magnetic state of the accelerator. A description of the production of the magnetic error estimates may be found in [89].

The geometric and magnetic error estimates generated by WISE may be incorporated into LHC lattice models for beam dynamics simulation codes.

2.2 The operational cycle of the LHC

The operational cycle of the LHC begins with a pre-cycle of the majority of the magnets in the accelerator [90]. No beam is present in the machine at this stage. In general the pre-cycle requires that the current in the magnets is ramped up to a large value (in some cases it is then also driven to large negative values), then back to the required settings. The exact nature

of the pre-cycle depends on the type of magnet in question. The pre-cycle ensures that the LHC magnets lie on the correct hysteresis branch and, where necessary, have a reproducible behaviour of decay and snap-back, or a small residual magnetization.

Following the pre-cycle, beam is injected into the LHC from its injector chain at an energy of $450\,\mathrm{GeV}$ and $\beta^* \sim 11\,\mathrm{m}$. Depending on the purpose of the fill the number, intensity, and filling pattern of bunches may vary. For the beam dynamics studies presented in this thesis it was usual to operate with a small number of non-colliding bunches, typically between one and three, of low intensity, $\sim 10^{10}\,\mathrm{protons/bunch}$. During operation for luminosity production a significantly larger number of bunches, of the order of 10^3, with high intensity, $\geq 10^{11}\,\mathrm{protons/bunch}$, are used. This stage of the LHC's operational cycle is referred to as *Injection*.

Once beam is injected the energy of the LHC is increased to collision energy, in a stage referred to as the *Ramp*. During the period studied in this thesis the LHC operated with collision energies of $3.5\,\mathrm{TeV}$ and $4\,\mathrm{TeV}$. The current of the LHC magnets must track the energy changes during the ramp. Having completed the ramp the LHC enters a mode known as *Flattop* where the beams are at high energy but the β^* has not yet been squeezed in the experimental insertions. Typically a number of optics checks, for example tune measurement and correction, are performed at Flattop. The β^* is then reduced down to the value for collisions (the *Squeeze*). The beams may then be brought into collision. Stable operation with collisions is referred to as *Stable Beams*.

At the end of an LHC fill the beams are extracted from the accelerator (*Beam Dump*). In the case of a requested beam dump the current in the magnets is decreased to the pre-injection levels via a pre-cycling of the elements where necessary. In the case of an emergency dump an independent pre-cycle is required before returning to injection.

Figure 2.9 plots the β^* in IP1, and the current in the main dipoles and Landau octupoles, throughout an LHC fill. The operational mode is also shown. The currents and β^* should be taken as indications only: the details of the β^* and magnetic cycle varied throughout the period examined in this thesis. Some LHC modes have not been discussed in this section as they are not relevant to the studies presented in this thesis. A complete description of the LHC's various modes of operation may be found in [91].

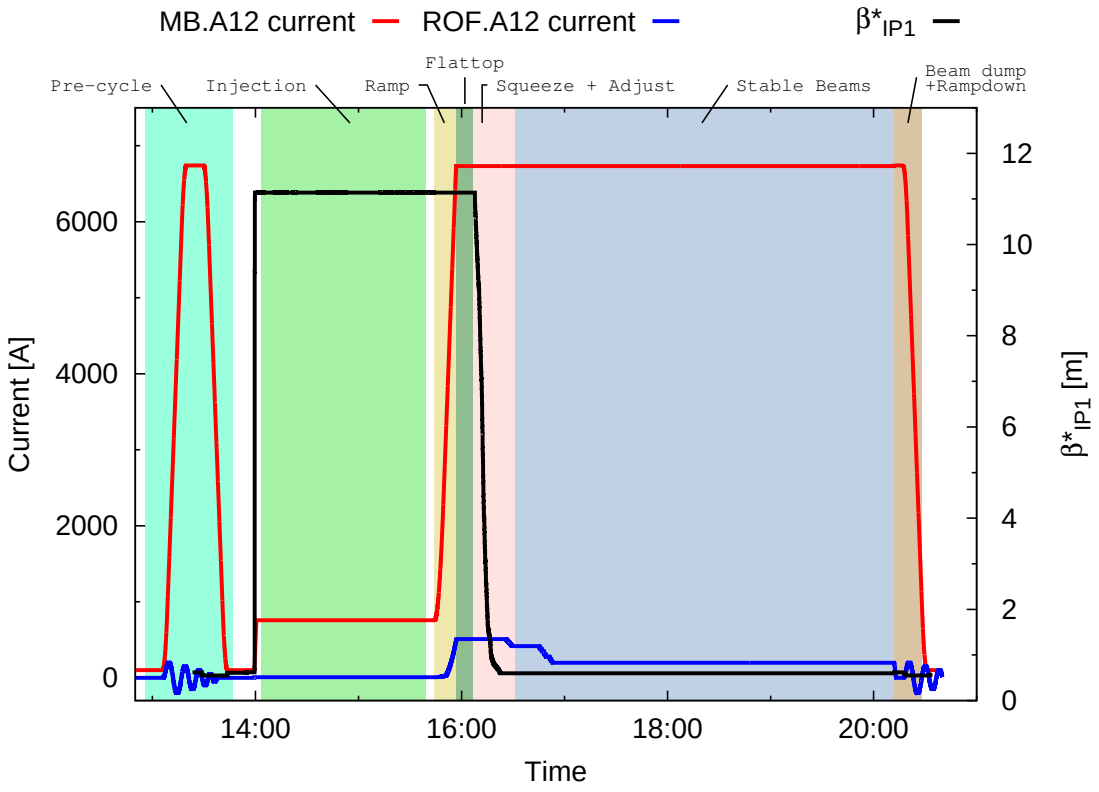

Figure 2.9: The operational cycle of the LHC, as characterized by the IP1 β^* and the current in the main dipoles and the Landau octupoles. Beam modes of particular relevance to this thesis are indicated.

2.3 Beam instrumentation in the LHC

Beam-based study of the LHC underpins the analysis of the LHC dynamics presented in this thesis. This section provides an overview of the beam instrumentation used to perform such measurements in the LHC.

2.3.1 Wirescanners for transverse profile measurement

Measurement of the transverse profile of low intensity bunches in the LHC can be performed with the use of dedicated linear wirescanners [92]. In the LHC design a $36\,\mu\mathrm{m}$ carbon wire is driven through the bunch in a single turn, generating a shower of secondary particles. The position of the wire is monitored using a high precision potentiometer, while the shower is

measured in a scintillator / photomultiplier detector. The intensity of the secondary shower is proportional to the charge density at the location of the wire, allowing a determination of the transverse profile of the bunch. Operational software for the LHC wirescanner provides a calculation of the emittance via a single Gaussian fit to the measured bunch profile. The value of the β-function used in the calculation may be either the nominal value at the wirescanner, or a value propagated from optics measurements in nearby BPMs [55].

Four wirescanners (*BWS*) are present in the LHC: two horizontal and two vertical, where the second pair of horizontal and vertical monitors are backups in case of malfunction. The BWS are installed in IR4 and IR5. Several further instruments are available for the study of beam profile in the LHC [76], however they are not relevant to the studies presented in this thesis.

2.3.2 Beam position monitors

Transverse center-of-charge beam position in the LHC can be monitored on a turn-by-turn (TbT) and bunch-by-bunch basis by around 500 dual-plane Beam Position Monitors (BPM) in each ring [76]. Two types of BPM are used in the LHC: stripline BPMs are utilized in the common apertures as they are capable of distinguishing between counter rotating bunches, while button BPMs are used throughout the rest of the LHC. Figure 2.10 shows schematics for the two BPM types.

Both types of monitor work on the principle that passage of a charged particle bunch induces a signal in the BPM electrodes [94]. The beam position is then given by the ratio between the difference and sum of the induced signal in opposite electrodes, multiplied by a scaling factor. LHC BPMs consist of two pairs of opposing electrodes, allowing determination of the beam position in both transverse planes.

The majority of the LHC BPMs ($\sim 360/\mathrm{beam}$) are located in the arcs, mounted by the main quadrupoles as seen in Fig. 2.1. All arc BPMs are of the button variety. The betatron phase advance between BPMs in the LHC arcs is $\sim 45^\circ$, this is roughly optimal for reconstruction of the linear optics, and allows phase space reconstruction from comparison of TbT data in BPMs separated by $\sim 90^\circ$. Stripline BPMs are only used in the insertion

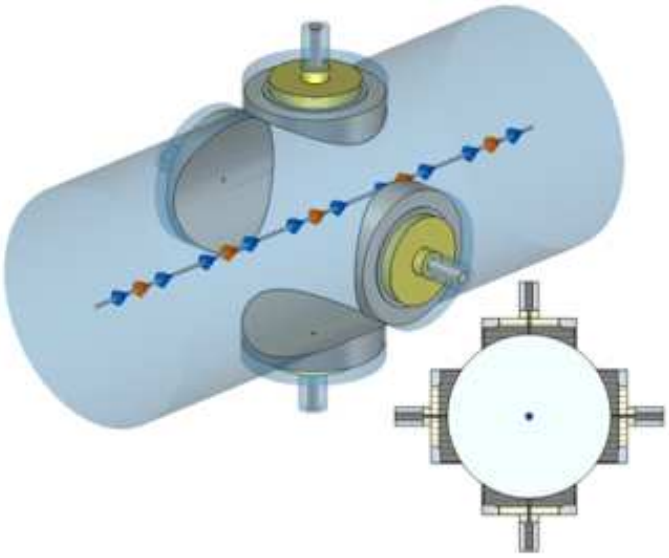

(a) Button BPM

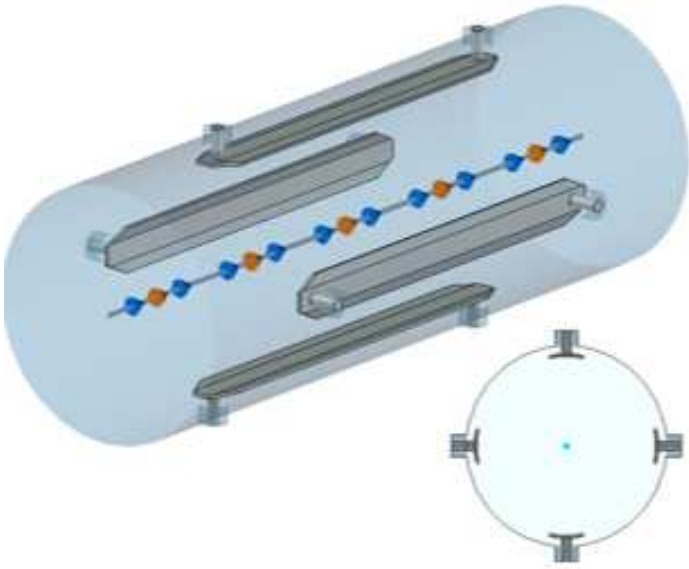

(b) Stripline BPM

Figure 2.10: Schematic illustration of the two types of Beam Position Monitor (BPM) used in the LHC [93].

regions at locations where the two beams occupy the same aperture. Enlarged button BPMs (relative to those in the arcs) are also used in the IRs. The location of BPMs in an insertion region is shown for IR1 in Fig. 2.6, where BPMs are indicated by vertical grey lines.

In the LHC corrections for geometric and electrical non-linearity of the BPM responses are performed automatically on turn-by-turn data prior to its delivery to users. Corrections for the non-linearity applied during the LHC's first operation run (*Run 1*: 2009-2013) are known to be imprecise at large amplitudes [93]. Significant issues also exist with the responses of the IR BPMs [93]. The correction of BPM non-linearity is reviewed in [93, 95].

2.3.3 BBQ system for tune and coupling measurement

Continuous, passive monitoring of tune and linear coupling in the LHC is provided by the *Base Band Tune* (BBQ) system [96, 97]. The BBQ measures the tune based on the principle of performing spectral analysis on the difference signal between opposing pickups of dedicated BPMs located in IR4 (this is equivalent to spectral analysis of the transverse position).

Incoming signals from the BPM pickups pass through a diode peak detector, isolating the low frequency (base band) betatron modulation of the beam position from the high frequency periodic revolution signal. For this reason the measurement technique used in the LHC BBQ is known as Direct Diode Detection [98]. Filtering of the signal may then be performed for the expected betatron frequency. Isolating the betatron oscillation with a peak detector prior to spectral analysis allows the BBQ to analyse very small (of the order of μm) oscillations of the beam. This enables monitoring of the betatron tune without the need for external excitation, allowing the BBQ to operate continuously during LHC operation.

In addition to measurement of the betatron tune, the BBQ also provides an estimate of $|C^-|$ from the relative amplitude of the spectral lines corresponding to linear coupling [96, 99]. As the BBQ measurement of linear coupling is based on betatron oscillation data collected at a single location no momentum information is available, and spectral analysis is unable to distinguish between lines corresponding to f_{1001} and f_{1010}. The BBQ therefore measures a mixture of $|C^+|$ and $|C^-|$. In practice difference linear coupling dominates in the LHC and $|C_{BBQ}| \approx |C^-|$.

While in general it is possible to measure tune and coupling with the BBQ in the absence of any external excitation, small transverse excitation can be performed by the LHC *Chirp* in order to improve the quality of the BBQ data [96].

2.3.4 Experimental kickers

Experimental kickers are present in the LHC to facilitate study of the beam dynamics. These elements apply transverse momentum kicks to the beam, shifting it to a larger phase space amplitude and inducing betatron oscillations which can be observed in the BPMs. Kicker dipole magnets for Beam 1 and Beam 2 in the horizontal and vertical planes (four magnets in total) are located in IR4. The kickers for each plane and each beam function independently. The kicker dipole coils are formed from a single turn of solid copper, this allows for a very fast response of the kicker but requires large currents to generate a significant deflection of the beam. The experimental kickers in the LHC can operate in three possible modes [100], referred to as the *Tune Kicker* (MKQ), *Aperture Kicker* (MKA), and the *AC-dipole*.

The tune and aperture kickers [100, 101] operate as traditional kicker magnets, ramping up and down within one turn in order to apply a single transverse kick then allow free betatron oscillations. The MKQ and MKA are principally distinguished by the achievable kick amplitude. The MKQ can generate kicks up to $\sim 2\,\sigma_{\mathrm{nominal}}$ at $450\,\mathrm{GeV}$, and is intended to induce betatron oscillations for the study of the linear beam dynamics. The MKA produces large amplitude kicks for study of the non-linear dynamics. Prior to 2012 the MKA was limited to provide kicks $\leq 6\,\sigma_{\mathrm{nominal}}$ at $450\,\mathrm{GeV}$. This was upgraded to $\leq 14\,\sigma_{\mathrm{nominal}}$ at $450\,\mathrm{GeV}$ for the 2012 run [102]. The possible excitation is considerably reduced at top energy compared to injection. Excitation with a single kick is a destructive measurement. In practice this generally limits the applicability of the MKQ and MKA to studies of the LHC at injection where it is possible to rapidly dump and re-inject fresh beam.

Rather than applying a single kick, as with the MKQ and MKA, in AC-dipole mode the dipole kicker magnets are powered sinusoidally, generating driven oscillations of the beam [56]. By exciting at frequencies at close to the natural tunes of the LHC ($Q_{x,y} \times f_{rev} \sim 3\,\mathrm{kHz}$) it is possible to generate forced oscillations of large amplitude with relatively little power, even at top energy. The AC-dipole excitation can be ramped up and down close to adi-

abatically [103], allowing beam dynamics measurements to be performed with only a small increase in emittance [104]. This allows multiple kicks to be applied to the same bunches, facilitating optics measurements at top energy. Furthermore the driven oscillations generated by the AC-dipole do not decohere, as is the case with a single kick. In the LHC measurement with the AC-dipole is typically based on $\sim 2000\,\mathrm{turns}$ of comparatively clean betatron oscillation data. The downside to optics measurement with the AC-dipole is that the driven oscillations introduce additional perturbations into the linear and non-linear beam dynamics which must be correctly accounted for in any analysis [57, 105]. Where possible therefore, beam dynamics measurement for the studies presented in this thesis were performed with the use of single kicks generated by the MKQ and MKA.

Excitation of the LHC beams to large amplitude can represent a considerable risk to the accelerator [76]. Consequently the experimental kickers in the LHC may only be used with a small number of low intensity bunches (of the order of $10^{10}\,\mathrm{protons/bunch}$). This is particularly true in the case of the MKA, which may only kick a single low intensity bunch. Following upgrade of the MKA for beam dynamics studies in 2012 the MKA was physically disarmed in the LHC tunnel for regular operation, and required dedicated interventions to enable and disable the MKA generator before and after beam dynamics measurements [102]. To aid machine protection, and during AC-dipole studies to prevent degradation of the beam quality, the amplitude of kicks applied during beam dynamics measurements are typically increased gradually to a sufficient magnitude while monitoring the beam losses. Beam loss is usually observed with dedicated *Beam Loss Monitors* (BLM): ionisation chambers located around the LHC ring outside the magnet cryostats, which detect secondary particles from showers created by losses from the LHC beams [76].

2.3.5 Beam current monitors

Measurement of individual bunch intensities in the LHC is provided by the *Fast Beam Current Transformers* (FBCT) [76]. FBCT measure the beam current by detecting the magnetic field of the bunch which generates a current in the secondary winding of a transformer placed around the beam.

Chapter 3

Modelling and correction of the linear optics

The studies presented in this chapter consider two main issues: whether the linear behaviour of the LHC is replicated in the best available models, and the beam-based correction of the linear optics.

A well understood and controlled linear optics is important for efficient operation of an accelerator. The understanding of the linear optics may assessed through comparison of simulation to measured data. Such a comparison was performed for the LHC in collaboration with M.C. Alabau-Pons, F. Schmidt and R. Tomás (CERN) [1, 2].

Linear optics may be controlled through beam-based measurement and correction. Correction of the linear optics in LHC experimental insertions is essential to achieving the best possible luminosity in the HEP experimental apparatus, and to prevent luminosity imbalance between the HEP experiments. Correction of linear optics errors around the LHC ring can also reduce the RMS closed orbit, improving a wide range of machine parameters and aiding in luminosity production. Furthermore the LHC has stringent safety tolerances on the linear optics in order to ensure machine protection. The machine must be corrected within these tolerances before it can run with operational intensity beam. The beam-based measurement and correction of the linear optics reported in this chapter represents an application of methodology pioneered by the CERN Optics Measurement and Correction (OMC) team during the first years of LHC commissioning [55, 106, 107]. The commissioning of the linear optics of the LHC is performed by the OMC team, of which the author was a member at the time of the studies presented. Results reported in this chapter reflect contributions from all the members of the team [4]. Measurements are performed collectively, typically two team members perform the excitations of the LHC beams while observing the losses and intensity to avoid unsafe beam loss, and a further two team members process the incoming kick data. Once initial measurements have been performed the team attempts to find local or global corrections for the optics errors. The author played a leading role in the measurements and corrections presented in this chapter.

Due to the influence of the linear optics functions on the non-linear phenomenology of a particle accelerator, a well understood and corrected linear optics is an important prerequisite to the study of non-linear beam dynamics. The results presented in this chapter lay a foundation for analysis of the non-linear dynamics of the LHC which will be presented in Chapters 4 to 6.

3.1 Introduction

The quality of the linear optics correction in the Large Hadron Collider contributes substantially to the machine performance. As described in Chapter 1.5, β^*, the beta-functions at the LHC Interaction Points (IP), determine the luminosity. It is important from the perspective of the HEP experiments that the real beta-functions are as close as possible to the intended values, and hence that the linear optics in the IRs is well controlled. As the orbit feedback routines in the LHC assume the nominal[1] LHC model, correction of the linear optics functions towards their nominal values also results in an improved RMS Closed Orbit around the LHC ring [4]. Consequently the quality of the linear optics correction not only influences luminosity production directly, but also impacts upon a wide range of machine parameters and operational aspects. Furthermore, in order to guarantee machine protection tight tolerances on linear optics errors are imposed on the Large Hadron Collider. The linear optics must be commissioned following any change to the LHC lattice in order to check whether the machine operates within these safety constraints. If the machine is found to operate out-with safe tolerances the linear optics must be corrected.

The linear optics quality is typically defined by the so-called *beta-beating* of the accelerator. The beta-beating is the relative deviation of the beta function from the designed value. It is defined by Eq.(3.1).

$$\frac{\Delta\beta_z(s)}{\beta_z(s)} = \frac{\beta_z(s)_{measured} - \beta_z(s)_{nominal}}{\beta_z(s)_{nominal}} \qquad \text{where } z = x, y \tag{3.1}$$

To ensure machine protection, the tolerance on the maximum beta-beat in the LHC is set at $\leq 15\%$ in the horizontal plane and $\leq 19\%$ in the vertical [108]. As found in 2009-2011, the LHC is out-with these tolerances if no optics corrections are applied [106, 107]. This makes beam-based measurement and correction of the linear optics an essential prerequisite to luminosity production.

In addition to the measurement and correction of the beta-beat, the *normalized horizontal dispersion beating*, defined in Eq.(3.2), may also be measured and corrected in the LHC.

[1] *nominal* refers to the ideal designed machine.

Normalized horizontal dispersion is considered rather than the horizontal dispersion beat, as it is a quantity independent of BPM calibration [109].

$$\Delta\frac{D_x(s)}{\sqrt{\beta_x(s)}} = \frac{D_x(s)_{measured}}{\sqrt{\beta_x(s)_{measured}}} - \frac{D_x(s)_{nominal}}{\sqrt{\beta_x(s)_{nominal}}} \tag{3.2}$$

Comparison can be made of beam-based measurements of the linear optics to simulations which incorporate the known sources of optics errors. These comparisons allow for an assessment of the understanding of the errors in the machine, and an analysis of the relative importance of the sources which may assist in directing future efforts.

As seen in Chapter 1, the linear optics functions impact upon the non-linear phenomenology of an accelerator. A well understood and corrected linear optics is therefore an important prerequisite to study of the non-linear dynamics. The studies of linear LHC optics presented in this chapter lay a foundation for study of the non-linear dynamics in the following chapters.

Section 3.2 begins by describing the methods used to measure and correct the linear optics. Section 3.3 then presents a comparison of predictions from the best available LHC models to measured data obtained during commissioning of the 2010 collision optics at $\beta^* = 3.5\,\mathrm{m}$ and an energy of $3.5\,\mathrm{TeV}$. Finally Section 3.4 presents results of the LHC optics commissioning at $4\,\mathrm{TeV}$, performed in 2012, where a record quality of the linear optics correction was achieved.

3.2 Measurement and correction of the linear optics

In this section the methods used to measure and correct the linear optics in the LHC are summarized. References are provided to more detailed descriptions.

3.2.1 Linear optics measurement

Linear optics measurements in the LHC are performed by analysing the betatron oscillations of excited beams. These excitations may be performed with the use of a kicker magnet, or

by using an AC-dipole to drive forced oscillations of the beam [56]. The AC dipole has the advantage that it is non-destructive if ramped adiabatically [103], however the forced oscillations introduce additional perturbations which must be compensated for in the analysis [57].

Tune and betatron phase are determined from spectral analysis of the betatron oscillations of the excited beams. The betatron oscillations are observed in the LHC BPMs [110], which record the turn-by-turn (TbT) center of charge of the beam. Prior to any spectral analysis however, the turn-by-turn BPM data is cleaned via a Singular Value Decomposition (SVD) [111].

The SVD of an $m \times n$ matrix $\mathbf{M}$ is given by Eq.(3.3).

$$\mathbf{M} = \mathbf{U}\mathbf{\Sigma}\mathbf{V}^{\dagger} = \sum_{i} u_i \sigma_i v_i^{\dagger} \tag{3.3}$$

$\mathbf{U}$ and $\mathbf{V}$ are $m \times m$ and $n \times n$ unitary matrices, the m and n columns of which are the left and right singular vectors of $\mathbf{M}$ respectively. $V^{\dagger}$ is the conjugate transpose of V. Matrix $\mathbf{\Sigma}$ is a $m \times n$ diagonal matrix of real positive elements σ_i, which are the singular values of $\mathbf{M}$. The magnitude of σ_i reflects the dominance of a given mode.

To clean LHC BPM data, the matrix $\mathbf{M}$ may be constructed of the turn-by-turn data of all BPMs (m) for a desired number of turns (n). This is decomposed into $\mathbf{U}$ and $\mathbf{V}$, describing the spatial and temporal modes respectively. Modes with small singular values tend to be the result of uncorrelated noise between the LHC BPMs. By truncating $\mathbf{\Sigma}$ to retain only large singular values (small values of σ_i are replaced with 0), it is possible to reconstruct a refined matrix $\tilde{\mathbf{M}}$ of the turn-by-turn BPM data with reduced noise. Following the SVD procedure, spectral analysis is performed on the cleaned BPM data. The tune and betatron phase at the LHC BPMs are determined by performing an interpolated FFT using a modified version of the SUSSIX software [44, 112, 113] designed for the frequency analysis of betatron oscillation data.

Once the betatron phase is determined the beta function at the BPMs may be calculated using the *Three BPM Method* [114]. Eq.(3.4) defines the beta-function at three BPMs in terms of the phase advances and the elements of the transfer matrices between the BPMs.

Figure 3.2.1 presents the quantities used in the calculation schematically.

$$\begin{aligned}\beta_1 &= \frac{\cot\Delta\phi_{12} - \cot\Delta\phi_{13}}{\frac{m_{11}}{m_{12}} - \frac{o_{11}}{o_{12}}}\\ \beta_2 &= \frac{\cot\Delta\phi_{12} + \cot\Delta\phi_{23}}{\frac{m_{22}}{m_{12}} + \frac{n_{11}}{n_{12}}}\\ \beta_3 &= \frac{\cot\Delta\phi_{23} - \cot\Delta\phi_{13}}{\frac{n_{22}}{n_{12}} - \frac{o_{22}}{o_{12}}}\end{aligned} \tag{3.4}$$

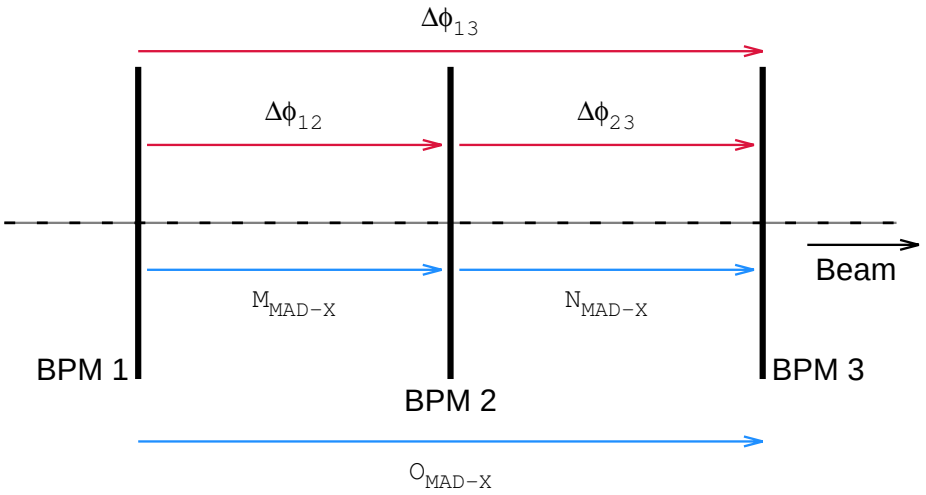

Figure 3.1: A schematic illustration of the 3-BPM method used to measure the beta-function in the LHC BPMs. $\Delta\phi$ are the phase advances between the BPMs determined from spectral analysis of the turn-by-turn betatron oscillation data in the BPMs. $\mathbf{M}_{MAD-X}$, $\mathbf{N}_{MAD-X}$ and $\mathbf{O}_{MAD-X}$ represent the transfer matrices between the BPMs with elements m_{ij}, n_{ij} and o_{ij}. To enable the measurement the transfer matrices are taken from the nominal model. These quantities may be used in conjunction with Eq.(3.4) to determine the β function at the BPMs.

The phase advances between the BPMs are determined from the spectral analysis previously described. The elements of the transfer matrix are assumed to be those of the nominal model. The uncertainty in the beta function is determined by the uncertainty in the phase measurement and the phase advance between the BPMs [114]. In particular phase advances of $0°$, $90°$ or $180°$ lead to a divergence in the uncertainty on the calculations in Eq.(3.4).

Consequently in the insertion regions, where the phase advance between the BPMs is small, or in situations where some of the BPMs malfunction, the uncertainty on the measured beta-beat may become large. For this reason, and because of the reliance on the nominal model in Eq.(3.4), corrections are normally calculated for the directly observed betatron phase rather than the beta-beat.

To measure the dispersion at the LHC BPMs the mean orbit is calculated from the turn-by-turn betatron oscillation data. Performing such a measurement at several RF frequencies allows the dispersion to be calculated using Eq.(3.5), where Δz is the shift in the mean horizontal or vertical orbit, and $\Delta p/p_0$ is the relative shift in momentum due to the RF trim.

$$D_z = \frac{\Delta z}{\frac{\Delta p}{p_0}} \qquad \text{where } z = x, y \tag{3.5}$$

As previously mentioned, the normalized dispersion ($D/\sqrt{\beta}$) is the preferred quantity for study, as it is independent of BPM calibration [109].

3.2.2 Linear optics correction

Two methods are utilized in the LHC for the correction of the linear optics. The *segment-by-segment* method [55, 107] corrects errors locally, and is focused towards the identification and compensation of strong, highly localized errors. In contrast the response matrix approach [115] corrects the linear optics globally, and is better suited to the compensation of widely distributed sources.

The segment-by-segment method was developed in order to provide a method to identify and locally correct optics errors in the LHC [55]. A section of the ring is treated as a beam line. The measured optics parameters at the start of the section are taken as initial conditions at entry into the beam line, and are propagated through using the nominal model in MAD-X [116]. The propagated optics parameters may be compared with the observations. Any deviation of the real machine from the nominal model shows up as a difference between the propagated optics functions and the observations after the point in the beam line where the error is located. The error can then be reconstructed by applying magnet trims in the

model which reproduce the observed discrepancy. Applying the reconstructed trims to the machine in reverse compensates the optics errors. The segment-by-segment technique has been developed for a wide range of linear optics parameters. For correction of the beta-beating in the LHC it is implemented by correcting the discrepancies in the betatron phase. This has the same impact as correcting the beta-beat directly [115]. This method was applied to great effect in the first years of LHC operation [55, 106, 107].

Following correction of strong local errors with the segment-by-segment technique, remaining errors may be corrected globally. A response matrix ($\mathbf{R}$) of the linear optics functions to the trims of the quadrupole circuits[2] is constructed using the nominal MAD-X model, Eq.(3.6) [55].

$$\left(\Delta\vec{\phi}_x, \Delta\vec{\phi}_y, \frac{\Delta\vec{\beta}_x}{\beta_x}, \frac{\Delta\vec{\beta}_y}{\beta_y}, \Delta\frac{\vec{D}_x}{\sqrt{\beta_x}}, \Delta Q_x, \Delta Q_y\right) = \mathbf{R}\Delta\vec{k} \tag{3.6}$$

The correction is then determined by Eq.(3.7), where $\mathbf{R}^+$ is the pseudoinverse of $\mathbf{R}$ determined by SVD, and ω are weightings applied to the optics functions.

$$\Delta\bar{k} = -\mathbf{R}^+\left(\omega_1\Delta\vec{\phi}_x, \omega_2\Delta\vec{\phi}_y, \omega_3\frac{\Delta\vec{\beta}_x}{\beta_x}, \omega_4\frac{\Delta\vec{\beta}_y}{\beta_y}, \omega_5\Delta\frac{\vec{D}_x}{\sqrt{\beta_x}}, \omega_6\Delta Q_x, \omega_6\Delta Q_y\right) \tag{3.7}$$

Cuts are applied on the minimum Δk to avoid making insignificant trims. If the Δk obtained from global correction are too large segment-by-segment correction may first need to be implemented to remove some of the stronger sources.

3.3 Comparison of simulated linear optics to measurement

Significant linear optics errors are present in the LHC insertion regions which generate a substantial beta-beat in the *virgin*[3] machine. These were first identified in 2009-2010 [106, 107]. These errors are well understood [117], and may be corrected effectively with the segment-by-segment technique [106, 107]. Of primary interest therefore was whether the residual beta-beating in the LHC, after local correction of the linear optics errors in the

[2] *circuit* refers to a set of magnets powered in series.
[3] *virgin machine*: an optics of the machine with all beam-based corrections removed.

insertion regions, is compatible with the current knowledge of the lattice errors. To assess the understanding of the linear optics after local corrections have been performed, measurements of the residual beta-beating in the LHC were compared to the predictions of LHC models including all known sources [1, 2].

To examine the beta-beating in the LHC a model was constructed in MAD-X [48]. As described in Section 2.1.3, the Window Interface to Simulation Errors [87] generates estimates of geometric and magnetic errors in the LHC lattice from measurements performed during construction. The measured alignment errors were applied to the lattice. Magnetic errors (normal and skew) of order $n = 2$ (quadrupole) up to $n = 15$ were then applied to the main dipoles and quadrupoles in the LHC arcs, and the correction circuits in the arcs were set to their nominal values. The closed orbit was matched to the zero orbit, the coupling was matched to $|C^-| \approx 0$, and tunes and chromaticities were matched to their nominal values. As the model was to be compared to the measured beta-beating following local corrections (but before global corrections had been applied) no errors were applied in the interaction regions. The twiss functions in the model were determined using the PTC module [50] in MAD-X to allow the inclusion of higher-order errors in thick lattice elements. Consequently it was necessary to transform the Mais-Ripken beta-functions output by PTC_TWISS into the Edwards-Teng parameterization for comparison with the measured data (see Section 1.4.6 for a brief discussion of the Mais-Ripken and Edwards-Teng parameterizations of linearly coupled motion).

The predictions of the model were compared to measurements of the beta-beat obtained during commissioning of the 2010 collision optics ($\beta^* = 3.5\,\mathrm{m}$ at $3.5\,\mathrm{TeV}$) [1, 2]. Figure 3.2 plots the simulated and measured beta-beat. Data for the simulated beta-beat are the mean and $\mathrm{standard\ deviation}$ of the values obtained for the sixty WISE seeds.

At top energy, where local corrections have been performed, the agreement between the simulated beta-beat and the measurements is good. While some discrepancies are visible, notably in the horizontal plane of Beam 2, they are clearly associated with steps in the beta-beat located at the IRs (and in particular at IR8). These discrepancies may therefore be confidently identified with slight imperfections in the local corrections utilized in 2010. Between the uncompensated errors in IRs the global scale of the beta-beat obtained from simulation is

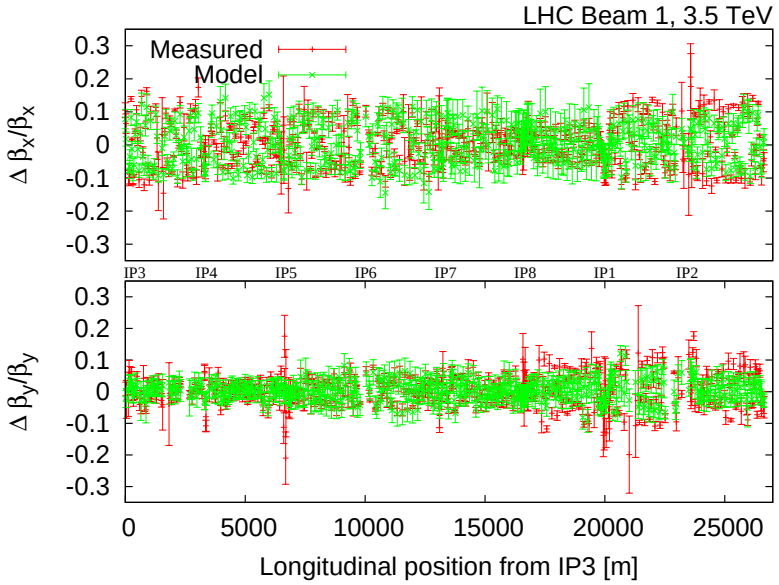

(a) Beam 1

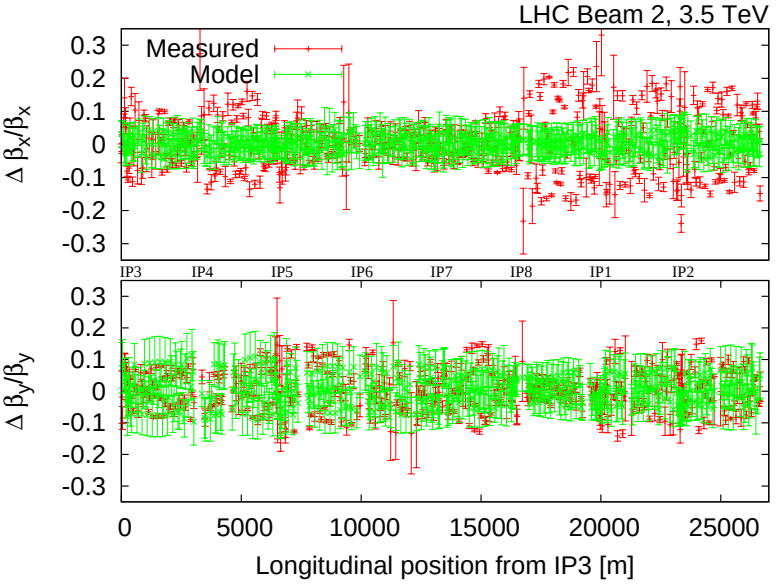

(b) Beam 2

Figure 3.2: Comparison of the modelled and measured beta-beating in the LHC at $3.5\,\mathrm{TeV}$, $\beta^* = 3.5\,\mathrm{m}$, following local correction of errors in the Insertion Regions. Measurements were performed on the 4$^{\text{th}}$ September 2010 by R. Tomás *et al.* Figure adapted from [2]

compatible with the measurement. The precise shape of the beta-beating around the ring is not perfectly reproduced, however simulation and observation agree within the uncertainty defined by the measurement error and the variation between the WISE seeds (of the order of $\sigma(\frac{\Delta\beta}{\beta}) = \pm 0.05$, dependent on location, plane, and beam [1, 2]). This represents, therefore, a respectable validation of the LHC model in the arcs within the linear regime. The simulated beta-beat was also studied at injection [1, 2]. In this case no local corrections were applied in the IRs and a comparison of the measured and modelled beta-beat is less meaningful due to discrepancies introduced by the insertion errors, however a beta-beating of the correct order of magnitude was obtained [1, 2].

The importance to the beta-beat of the various sources included in the model was assessed [1, 2] by introducing the errors in a step-wise fashion, together with any corresponding corrections. The simulated beta-beat in the complete model was of the order of $10\,\%$, depending on the specific beam, plane, and location. Approximately half of this was generated by the quadrupolar errors in the arc dipoles. The quadrupolar errors in the arc quadrupoles also generated a comparable beta-beat. While the effect of the specific WISE seed was negligible for the errors in the dipoles, in the arc quadrupoles there is a non-negligible uncertainty in the warm-to-cold correlation[4] of the magnetic error measurements. The peak and global scale of the beta-beat are minimally affected by this, however the specific shape of the beta-beat around the ring does vary dependent on the seed. The uncertainty in the warm-to-cold correlation of the b_2 errors in the arc quadrupoles represents, therefore, a limit on the understanding of the linear optics. Higher order errors made only a small contribution to the beta-beating: up to a peak of $\sim 1\,\%$, but considerably lower at most locations. The effect of the geometric errors was small but non-negligible, increasing the beta-beat by between $1\,\%$ and $3\,\%$. The role of the closed orbit was assessed by performing matchings to either the zero orbit, or to a target produced from measured orbit data. The difference in the beta-beatings for the two orbits was of the order of $1\,\%$.

Significant errors exist in the LHC insertions which lead to substantial beta-beatings, however these errors are well understood and corrected via the beam-based commissioning of the linear optics. At $\beta^* = 3.5\,\mathrm{m}$, $3.5\,\mathrm{TeV}$ the scale of the residual beta-beating in the LHC, after correction of local errors in the IRs, agrees well with expectations from simulations

[4]The warm-to-cold correlation was introduced in Chapter 2.1.3.

which include the known lattice misalignments and the magnetic errors in the arcs [1, 2]. The residual beta-beat is dominated by the quadrupolar errors in the main arc dipoles and quadrupoles, with small contributions from feed-down [1, 2]. As the arc optics are not significantly affected by changes of β^* the conclusions of this section may be extrapolated to other LHC optics. These results provide a good verification of the LHC model in the linear regime.

3.4 Commissioning of linear LHC optics for proton operation at $\beta^* = 0.6\,\mathrm{m}$, $4\,\mathrm{TeV}$

During the first years of LHC operation at $3.5\,\mathrm{TeV}$ (circa 2009-2011) the methodology described in Section 3.2 was implemented in the LHC with great success. In particular the beta-beat was corrected to the level of $\sim 10\%$ for operational states of the machine [55, 106, 107]. As β^* was reduced over this period however, a growing luminosity imbalance was observed between the ATLAS and CMS experiments. Due to concern that the imbalance could grow to an intolerable level upon further reduction of the β^* to $0.6\,\mathrm{m}$ in 2012, special attention was given to linear optics commissioning for the $\beta^* = 0.6\,\mathrm{m}$, $4\,\mathrm{TeV}$ proton-proton run. This was primarily characterized by an increase in the time available for linear optics commissioning compared to previous occasions.

During $\beta^* = 0.6\,\mathrm{m}$, $4\,\mathrm{TeV}$ commissioning for proton-proton operation the methods described in Section 3.2 were applied to the LHC, however with more time available for the linear optics commissioning than in preceding years a number of differences in strategy were possible. In 2012 measurements were performed on the virgin LHC over its entire magnetic cycle. This contrasted with previous methodology, wherein corrections were applied incrementally at every change in optics. Larger amplitude betatron oscillations were excited compared with previous commissioning studies, which assisted in the reduction of measurement uncertainties. Finally, local corrections in the insertions were found by examining measurements throughout the betatron squeeze, and global corrections were performed on the betatron phase and dispersion simultaneously. The results of these measurements and corrections are presented in this section.

3.4.1 Injection ($450\,\mathrm{GeV}$)

The first optics studied was at injection. The peak beta-beating before correction was observed to be in the $30-40\,\%$ range, with a normalized horizontal dispersion beat up to $0.4\,\mathrm{m}^{-\frac{1}{2}}$. Independent global corrections were found for Beam 1 and Beam 2.[5] Simulations of the correction predicted that simultaneous correction on the phase advance and normalized horizontal dispersion gave the best quality correction. It was corrections found by this method which were implemented. Figures A.1a and A.1b in Appendix A.1 show the Beam 1 and Beam 2 correction trims applied to the machine.

Figures 3.3 and 3.4 show the Beam 1 and Beam 2 beta-beating and normalized horizontal dispersion before and after correction. In both beams the beta-beat has been considerably reduced (to $< 10\,\%$) and the horizontal normalized dispersion beat improved (down to $\sim 0.01\,\mathrm{m}^{\frac{1}{2}}$). In Beam 1 the vertical dispersion was unaffected, while in Beam 2 it was marginally worse after application of the optics corrections. The slight worsening of the Beam 2 $D_y(s)$ is not relevant to LHC operation. The correction was highly effective.

3.4.2 Top Energy ($4\,\mathrm{TeV}$)

Following measurement and correction of the linear optics at injection, studies were performed at the new top energy of $4\,\mathrm{TeV}$. Measurements on the virgin machine were performed throughout the betatron squeeze. As the β^* was reduced the beta-beating was seen to increase dramatically, showing clear jumps in the beta-beat at the experimental IRs. This was the result of errors in the IRs having a more significant impact as the beta-function was increased in the elements surrounding the IP. Figure 3.5 shows the beta-beating at several points in the squeeze. As dispersion measurements require studies on and off the reference momentum, and hence additional beam time, dispersion was only measured at the end of the betatron squeeze. Given the $\sim 100\%$ beta-beat observed at $\beta^* = 0.6\,\mathrm{m}$ corrections to the optics were vital.

[5] MQM and MQT type magnets were used for the correction. These elements are on separate circuits for the two beams, which allowed independent correction of Beam 1 and Beam 2

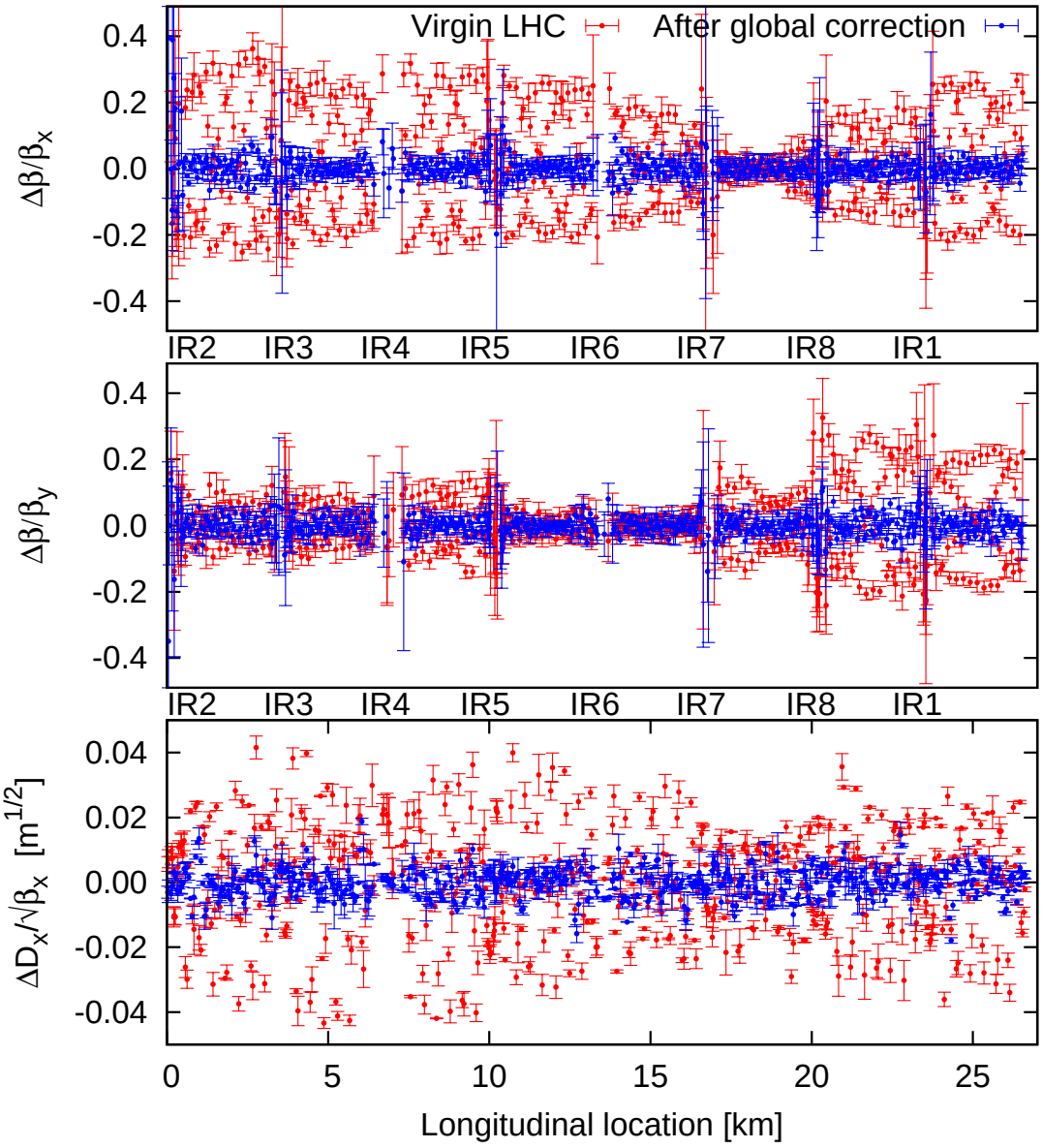

Figure 3.3: Beta-beat and normalized horizontal dispersion beat in LHC Beam 1 at injection, before and after global correction of the linear optics.

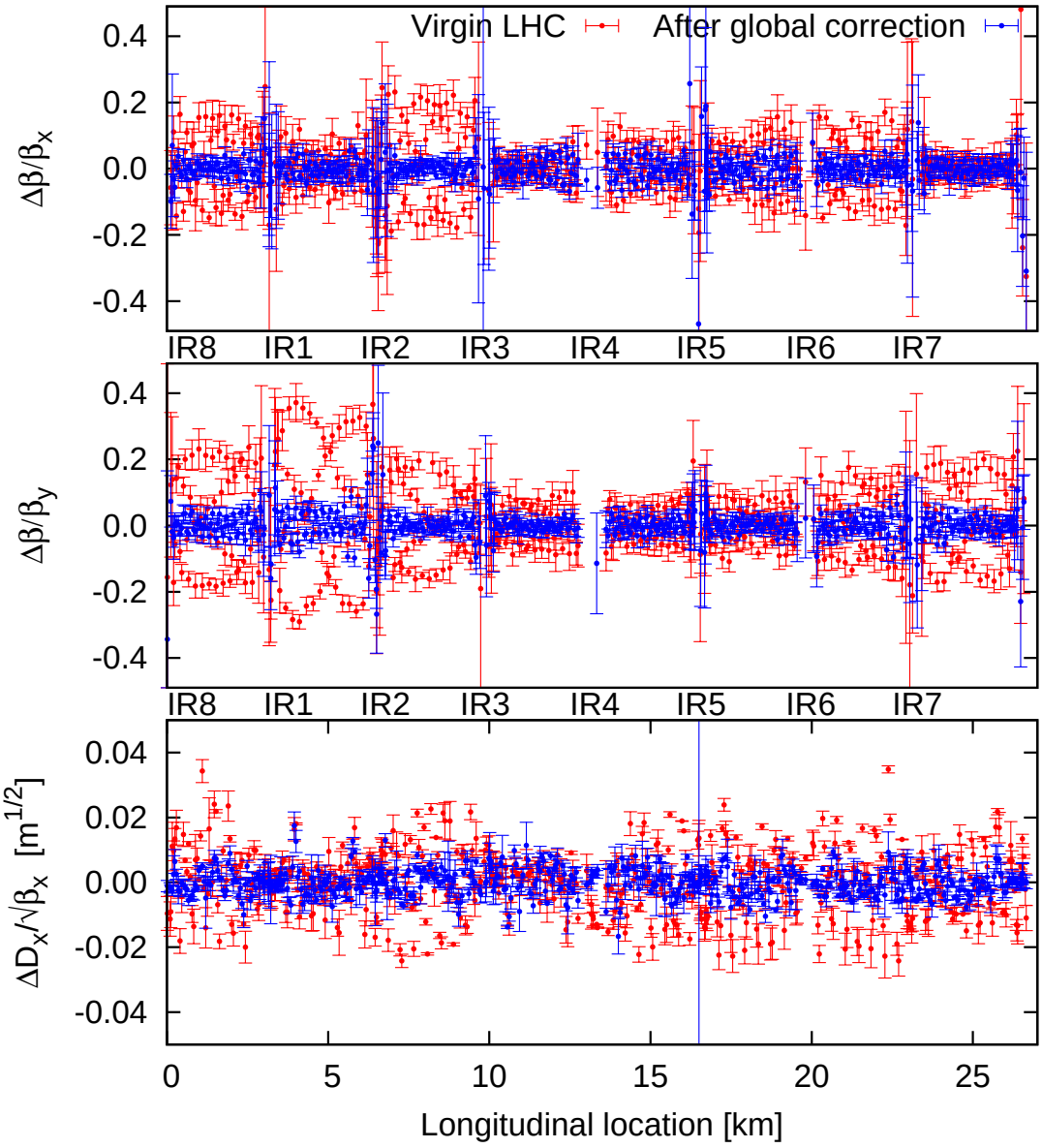

Figure 3.4: Beta-beat and normalized horizontal dispersion beat in LHC Beam 2 at injection, before and after global correction of the linear optics.

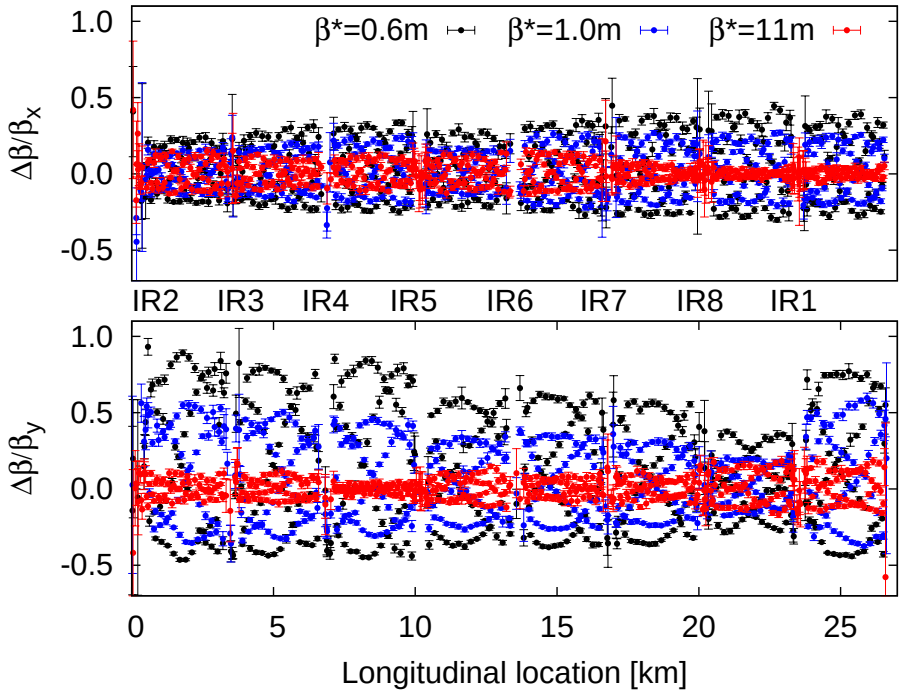

(a) Beam 1

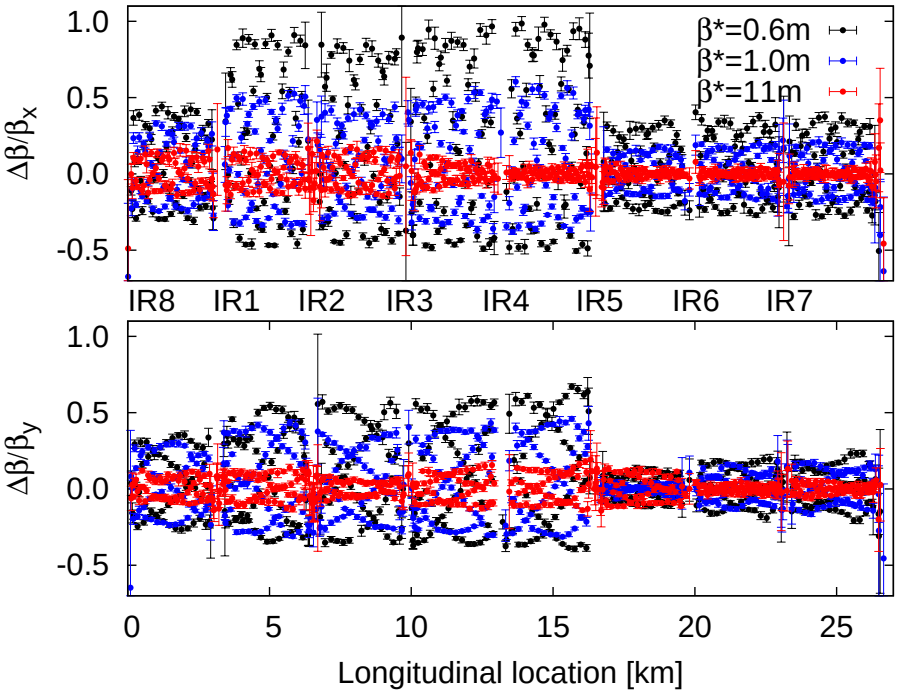

(b) Beam 2

Figure 3.5: Beta-beating in the virgin LHC at several stages of the $4\,\mathrm{TeV}$ betatron squeeze for proton-proton operation. $\beta^* = 11\,\mathrm{m}$ corresponds to the optics at Flattop.

Local corrections

Significant optics errors were identified in IR1, IR5, IR6 and IR8. Errors in the IRs are best corrected locally with the use of the Segment-by-segment technique described in Section 3.2. In contrast with previous optics commissioning, the strategy adopted was to find trims which would simultaneously correct multiple optics throughout the betatron squeeze (as the triplet magnets are common to both beams it was also necessary, as with previous years, that these trims simultaneously correct both beams). Unique solutions to the error distribution through the IR do not necessarily exist, and such a method assists in removing some of the possible degeneracy in sources of the phase errors in the IR [4]. The simultaneous correction of multiple optics is illustrated in Fig. 3.6, which shows for three optics and both beams the measured deviations of the betatron phase from the nominal model, together with the reconstructed phase errors on applying the inverse correction trims in the nominal model.

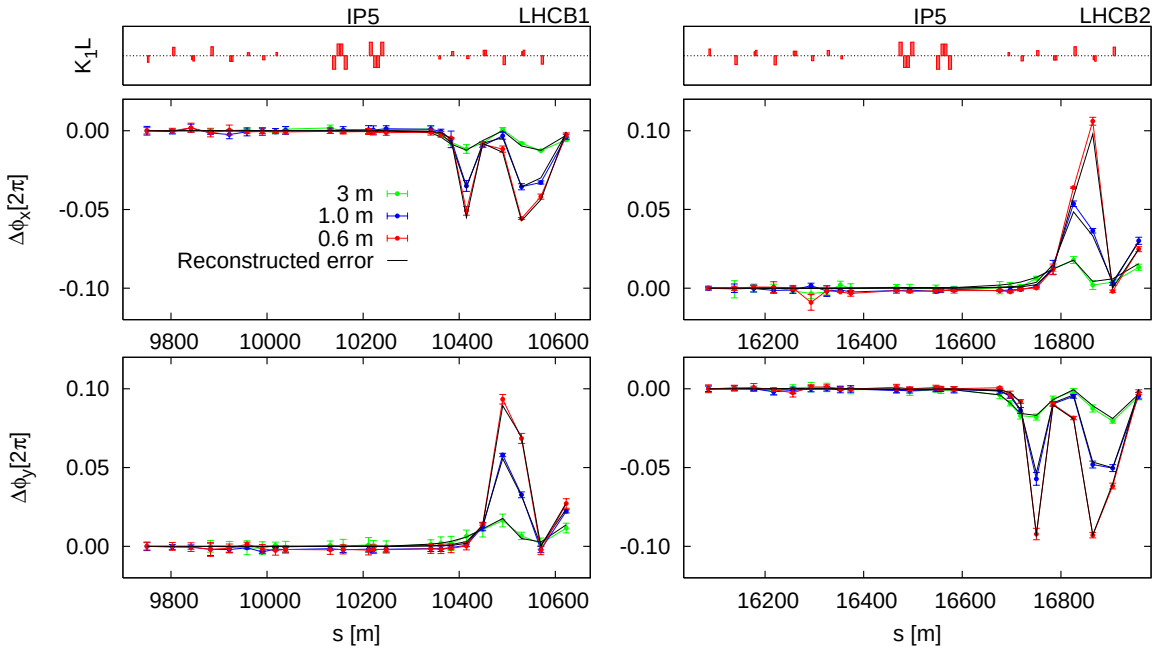

Figure 3.6: Simultaneous local correction of multiple optics in IR5. This plot has been adapted from that shown in [4].

The measured deviations of the betatron phase from the nominal model at $\beta^* = 0.6\,\mathrm{m}$ through IR1, IR5, IR6 and IR8 are shown in Fig. A.2 to A.5 in Appendix A.2. Reconstructed

phase errors corresponding to the local corrections applied to these IRs are also shown. The local corrections are summarized in Table A.1 in Appendix A.2.

The local corrections were implemented in the LHC as constant trims from Flattop to $\beta^* = 0.6\,\mathrm{m}$, and led to a significant reduction in the beta-beating and normalized horizontal dispersion beat. Figures 3.7 and 3.8 plot the beta-beating and normalized horizontal dispersion beat at $\beta^* = 0.6\,\mathrm{m}$, before and after the application of the local corrections in IR1, IR5, IR6 and IR8.

Global corrections

The local corrections alone brought the linear optics within the tolerances defined for safe operation, however as small a beta-beat as possible was desired in order to optimize the operation of the machine. Errors in the LHC arcs and residuals from the segment-by-segment technique may be corrected using the global method. As in the case of injection, global optics corrections were calculated for the measured betatron phase and normalized horizontal dispersion after local correction. The applied trims are plotted in Fig. A.6 in Appendix A.3, and the resulting improvement in the beta-beating and normalized horizontal dispersion beat are shown in Fig. 3.9 and 3.10 for LHC Beam 1 and Beam 2 respectively.

Record beta-beat

Following local and global corrections, a peak beta-beat was achieved in the LHC of $(7 \pm 4)\,\%$. This is a record for hadron colliders, and equals the record for lepton colliders, held by CESR [118]. Notably the CESR performance has been matched in spite of the LHC's larger circumference and greater number of insertions. The RMS beta-beat achieved was $\sim 2\,\%$, approaching a scale normally only seen in light sources. These results represent an unprecedented quality of the LHC linear optics correction. Table 3.1 presents the peak and RMS beta-beat and normalized horizontal dispersion beat in the LHC following each stage of correction.

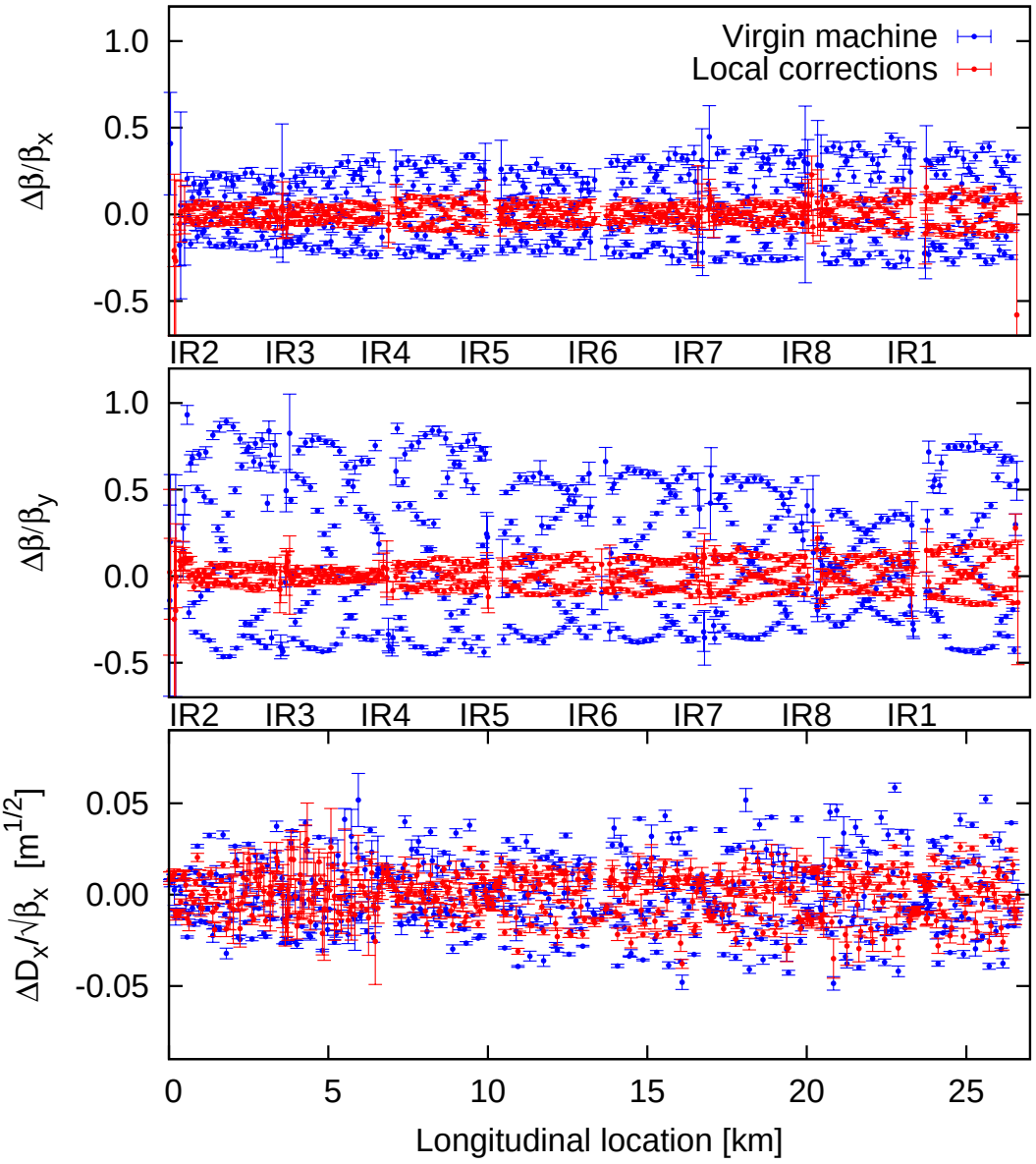

Figure 3.7: Beta-beat and normalized horizontal dispersion beat in LHC Beam 1 at $\beta^* = 0.6\,\mathrm{m}$, before and after local optics correction in IR1, IR5, IR6 and IR8.

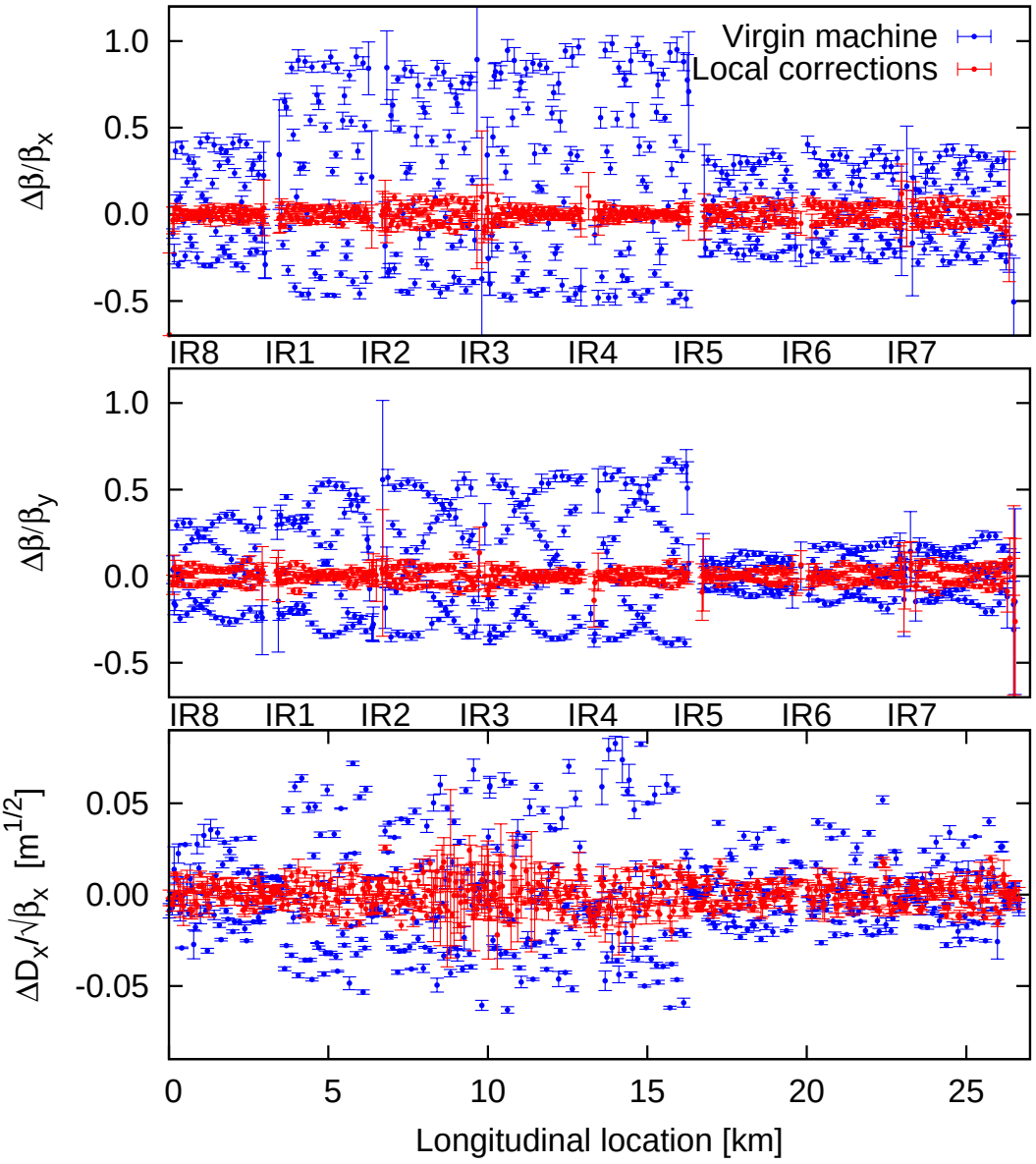

Figure 3.8: Beta-beat and normalized horizontal dispersion beat in LHC Beam 2 at $\beta^* = 0.6\,\mathrm{m}$, before and after local optics correction in IR1, IR5, IR6 and IR8.

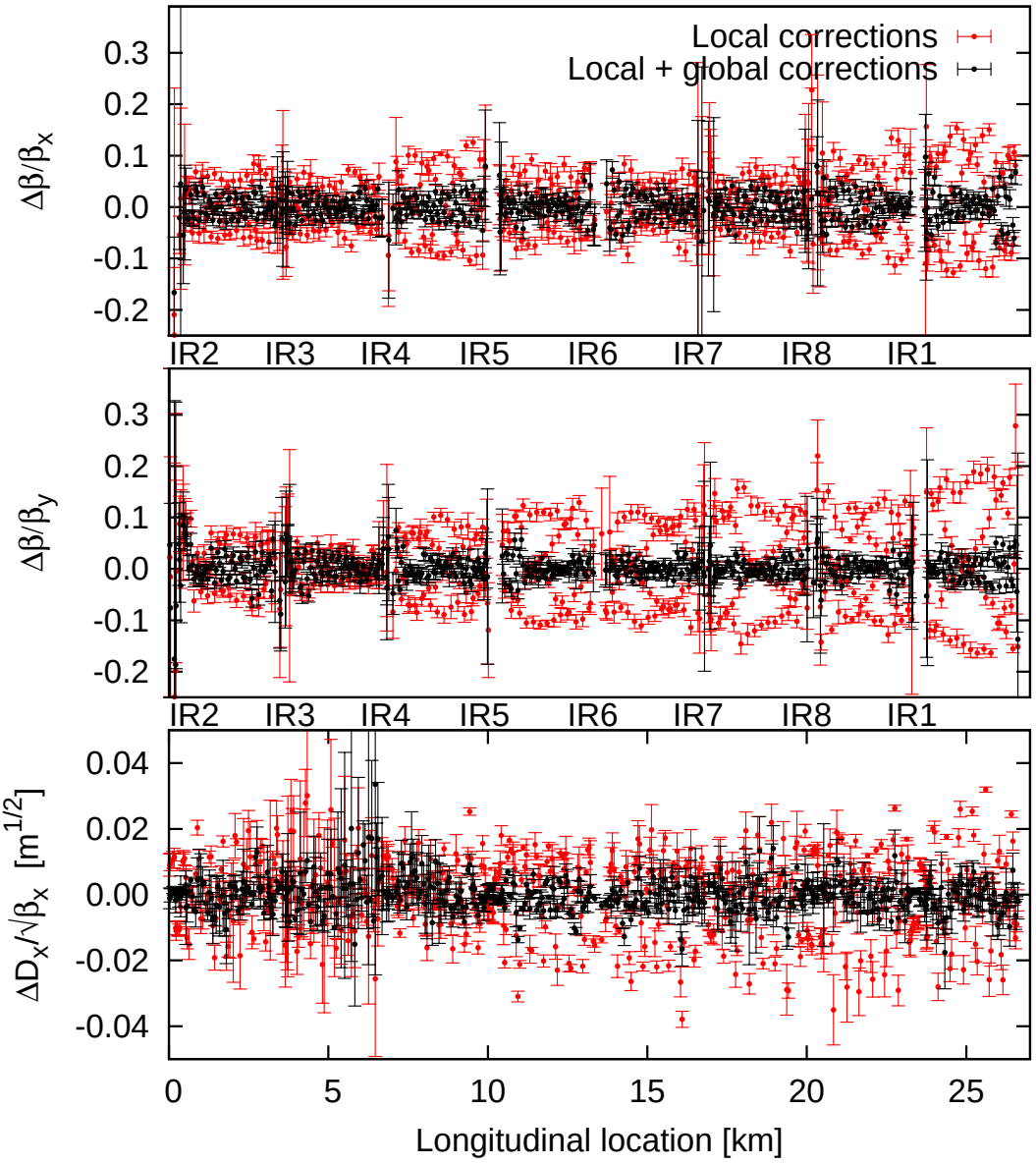

Figure 3.9: Beta-beat and normalized horizontal dispersion beat in LHC Beam 1 at $\beta^* = 0.6\,\mathrm{m}$, before and after global correction.

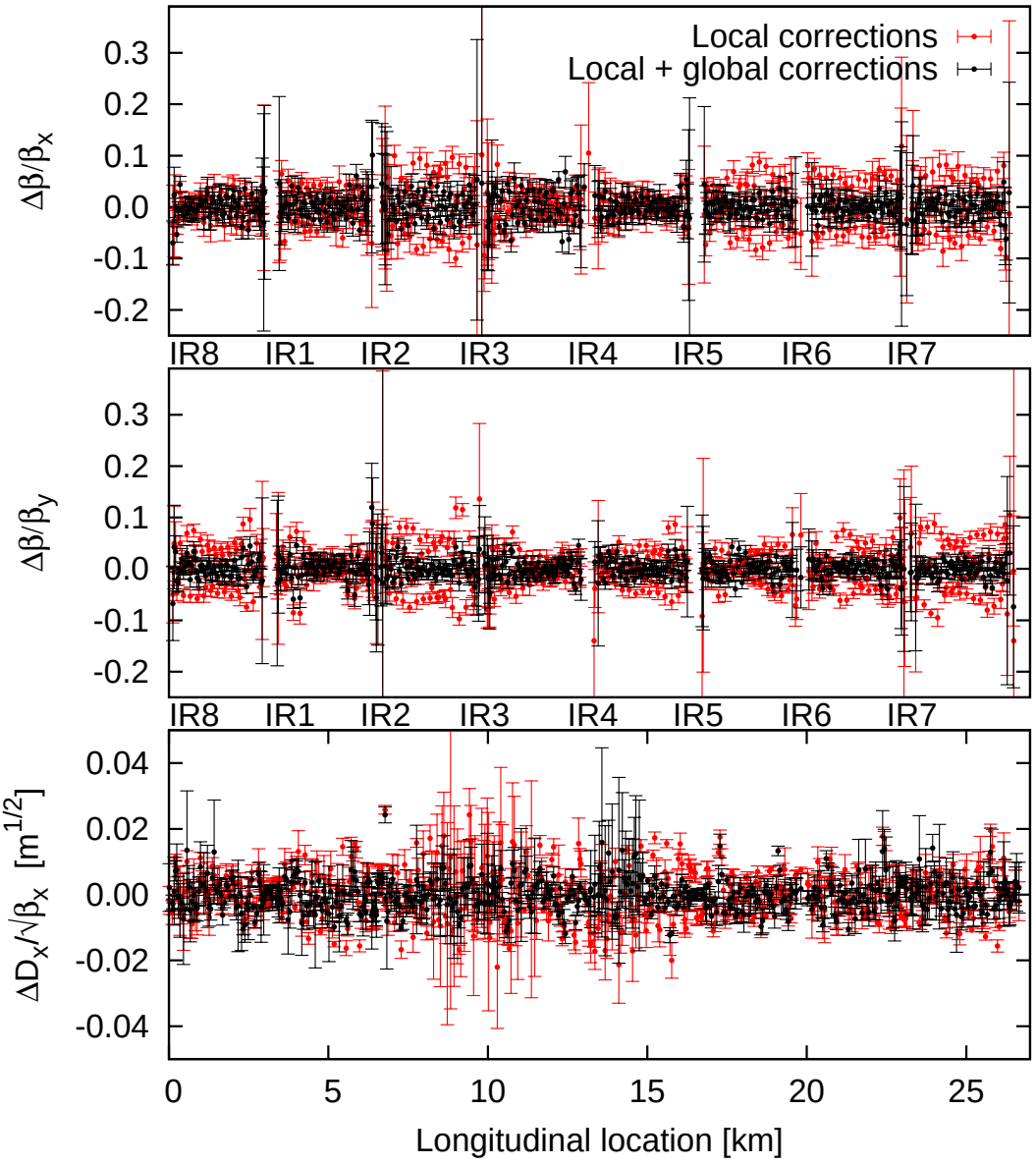

Figure 3.10: Beta-beat and normalized horizontal dispersion beat in LHC Beam 2 at $\beta^* = 0.6\,\mathrm{m}$, before and after global correction.

Table 3.1: RMS and peak beta-beat and normalized horizontal dispersion beat at $\beta^* = 0.6\,\mathrm{m}$ in the virgin LHC, and following local and global corrections. Adapted from [4].

(a) Beam 1

	$\frac{\Delta\beta_x}{\beta_x}$ [%]		$\frac{\Delta\beta_y}{\beta_y}$ [%]		$\frac{\Delta D_x}{\sqrt{\beta_x}}$ $[10^{-2}\sqrt{\mathrm{m}}]$	
	RMS	peak	RMS	peak	RMS	peak
Before corr.	20	44±2	34	93±5	1.8	5.8±0.2
Local corr.	6.2	15±2	7.9	19±2	1.2	3.2±0.1
Global corr.	2.2	7±4	1.8	6±2	0.3	1.5±0.7

(b) Beam 2

	$\frac{\Delta\beta_x}{\beta_x}$ [%]		$\frac{\Delta\beta_y}{\beta_y}$ [%]		$\frac{\Delta D_x}{\sqrt{\beta_x}}$ $[10^{-2}\sqrt{\mathrm{m}}]$	
	RMS	peak	RMS	peak	RMS	peak
Before corr.	33	99±5	23	67±2	2.1	9.2±0.4
Local corr.	4.1	10±2	3.9	12±2	0.7	2.6±0.2
Global corr.	1.8	6±2	1.5	7±3	0.4	2.4±0.2

3.5 Conclusions

The linear optics of the LHC, as characterized by the beta-beating and normalized horizontal dispersion beat, is well understood and controlled. Presented in this chapter was a comparison of the simulated LHC beta-beat at $\beta^* = 3.5\,\mathrm{m}$, $3.5\,\mathrm{TeV}$ to measurements performed after local correction of the linear optics, and results of the $\beta^* = 0.6\,\mathrm{m}$, $4\,\mathrm{TeV}$ linear optics commissioning for proton operation.

At $\beta^* = 3.5\,\mathrm{m}$, $3.5\,\mathrm{TeV}$ it was found that following local corrections of the errors in the LHC insertions, the scale of the remaining beta-beat agreed well with simulations incorporating the known errors in the arcs. It was determined from simulation that the beta-beat (after compensation of the errors in the insertions) was dominated by the quadrupolar errors in the arc dipoles and quadrupoles. The uncertainty in the warm-to-cold correlation of the b_2 errors in the arc quadrupoles was non-negligible and defined the limit on the understanding of the observed beta-beat. While this uncertainty affected the local shape of the beat-beat around the ring, the variation was within the measurement and simulation uncertainties. The

peak and global scale of the beta-beat was in general unaffected, and agreed well with the observations, providing a good validation of the LHC model in the linear regime. As the arc optics are not significantly affected by changes in the β^* this conclusion may be extrapolated to other LHC optics.

Significant optics errors exist in the LHC insertions. As demonstrated during commissioning of the $\beta^* = 0.6\,\mathrm{m}$, $4\,\mathrm{TeV}$ optics for proton operation however, these errors can be identified and corrected locally within the IRs. During the $\beta^* = 0.6\,\mathrm{m}$, $4\,\mathrm{TeV}$ commissioning local corrections alone reduced the peak LHC beta-beat from $\sim 100\,\%$ to within operational tolerances. Following local corrections in the insertions, global corrections were applied to compensate for errors in the arcs and any residuals from the local correction. Upon implementing these corrections a peak beta-beat of $(7 \pm 4)\,\%$ was achieved in the LHC (with a considerably lower beta-beat around most of the ring). This is a record for hadron colliders which also matches the record for lepton colliders held by CESR.

The good understanding of the linear optics and the superb quality of the linear optics corrections which are typified by these results represent a solid foundation in the study of the LHC dynamics. Efforts continue during the LHC's first long shutdown towards the improvement of linear optics correction quality, however further advancements in LHC optimization may also now be sought through an improved understanding of the non-linear dynamics.

Chapter 4

Measurement and correction of non-linear observables in the LHC at injection

The non-linear dynamics of a circular accelerator such as the Large Hadron Collider can significantly impact upon its performance. As the LHC progresses to more challenging regimes of operation it is to be expected that the non-linear single particle dynamics in the transverse planes will play an increasing role in limiting the performance of the accelerator. As such it is important that the non-linear sources are well understood and controlled. Beam-based studies of non-linear observables such as the higher order chromaticity, detuning with amplitude, and dynamic aperture provide the means to quantify the non-linear dynamics of an accelerator.

Degradation of beam quality due to the non-linear dynamics at injection ($450\,\mathrm{GeV}$) will adversely affect luminosity production throughout an entire LHC fill. The non-linear dynamics also play a significant role in the growth or damping of instabilities at injection. Detailed studies of the non-linear dynamics in the Large Hadron Collider at injection were performed in two experimental sessions during the LHC's first operational run. Initial studies, performed in 2011, focused primarily on the non-linear chromaticity. Discrepancies with the LHC models were identified, and partially explained. Corrections for the non-linear dynamics were obtained through the minimization of second and third order chromaticities. During the second non-linear dynamics experiment, performed in 2012, studies focused on the measurement of non-linear observables using kicked beams. Measurement of first and second order amplitude detuning were performed, together with a determination of the dynamic aperture. First observations of non-linear coupling in the LHC optics were made. Simultaneous correction of the non-linear chromaticity, detuning with amplitude, and dynamic aperture was demonstrated. It was shown that at nominal injection optics, with Landau octupoles powered, the LHC model agreed well with the observed dynamics.

4.1 Introduction

Since commissioning of the LHC began in 2009 great progress has been achieved in the measurement, correction and modelling of the linear optics [1, 2, 4, 106, 107]. It has also been demonstrated that the chromatic beta-beating and the chromatic coupling are well understood [4, 119]. In order to optimize the future performance of the machine as it moves into more challenging operational regimes however, further understanding of non-linearities in the LHC will be essential.

Non-linearities in the machine contribute to the Dynamic Aperture (DA), lead to the development of resonances in the motion, and may drive particles towards such resonant frequencies. These effects are detrimental to beam lifetime and luminosity production. On the other hand the introduction of well understood and controlled non-linearity can be important for the damping of dangerous instabilities in beam motion. To effectively control and correct the non-linearity in operation it is necessary therefore, to quantify the machine non-linearity through beam-based measurements of properties determined by higher order fields. Such studies allow for verification or invalidation of the magnetic model, and may also be significant for the study of upgrade scenarios.

Beam based studies of non-linearities in the LHC were first performed at injection ($450\,\mathrm{GeV}$) in 2011 [5, 6, 120], focused primarily on the study of non-linear chromaticities with depowered Landau octupoles (MO). Further studies were performed on Beam 2 in 2012, with a focus on measurements utilizing kicked beams at the nominal magnetic configuration for injection. This included Landau octupoles powered at their operational settings[1].

In this chapter results of analysis of the non-linear beam dynamics at injection are presented. Section 4.2 summarises the methods used to measure non-linear beam properties in the LHC. Section 4.3 presents the results of studies of the non-linear dynamics of the LHC at injection with depowered Landau octupoles. Measurements and correction of the second and third order chromaticities are presented, followed by a comparison of the measurements to simulation and a discussion of possible sources of discrepancy. Section 4.4 presents studies of the non-linear dynamics performed in the LHC at nominal injection optics, including

[1] *Operational settings* in this context refers to the settings present in the machine during operation for luminosity production in June 2012. During the second half of 2012 the MO polarity in operation was reversed.

Landau octupoles at their nominal settings. Measurements of non-linear chromaticity are presented. A revised model of the LHC at injection, building on experience from the non-linear chromaticity analyses, is introduced. Results of studies of the non-linear dynamics at nominal injection optics, from the perspective of kicked beam experiments, are then presented, together with a comparison to simulation. Section 4.5 discusses the application of the LHC model to machine configurations at injection which have not been studied directly.

4.2 Measurement of non-linear observables

4.2.1 Non-linear chromaticity

Chromaticity is the variation of tune with the relative deviation from the ideal momentum (p_0). As described in Chapter 1.4.1, under the influence of chromatic aberrations the tune may be described as a Taylor series about the unperturbed tune, Eq.(4.1).

$$\begin{aligned} Q_z\left(\frac{\Delta p}{p_0}\right) = Q_{z0} + Q'_z\left(\frac{\Delta p}{p_0}\right) + \\ + \frac{1}{2!}Q''_z\left(\frac{\Delta p}{p_0}\right)^2 + \frac{1}{3!}Q'''_z\left(\frac{\Delta p}{p_0}\right)^3 + ... \end{aligned} \tag{4.1}$$

where

$$Q_z^n = \frac{\partial^n Q_z}{\partial \frac{\Delta p}{p_0}^n} \qquad z = x, y \tag{4.2}$$

The non-linear chromaticity are the terms Q'' and higher in Eq.(4.1).

The coefficients in Eq.(4.1) may be measured directly by observing the tune shift while varying the momentum of the Beam, higher orders in general requiring a larger momentum excursion. A change in momentum of the beam is generated via a change in the frequency of the RF-cavities. The relative momentum offset is related to the frequency shift by Eq.(4.3) [121], where α_C is the momentum compaction factor.

$$\frac{\Delta p}{p} = -\frac{1}{\alpha_C - \gamma_{rel}^{-2}}\frac{\Delta f_{RF}}{f_{RF}} \approx -\frac{1}{\alpha_C}\frac{\Delta f_{RF}}{f_{RF}} \tag{4.3}$$

The variation of the momentum compaction factor with momentum in the LHC is negligible and the non-linear chromaticity is in general calculated assuming a constant momentum compaction factor. The LHC tunes may be monitored throughout a scan of the relative momentum offset using the BBQ system [97].

The second order chromaticity (Q'') and third order chromaticity (Q''') may be corrected using octupole and decapole magnets respectively, as these elements have an impact linear in their strength and will not affect the lower orders except through feed-down (Tab. 1.1).

4.2.2 Amplitude detuning

Amplitude detuning is the variation of tune with single particle emittance, and was introduced in Chapter 1.4.2. This detuning may be described by a Taylor expansion about the unperturbed tune, Eq.(4.4),

$$\begin{aligned} Q_z(\epsilon_x, \epsilon_y) = \; & Q_{z0} + \frac{\partial Q_z}{\partial \epsilon_x}\epsilon_x + \frac{\partial Q_z}{\partial \epsilon_y}\epsilon_y + \\ & + \frac{1}{2!}\left(\frac{\partial^2 Q_z}{\partial \epsilon_x^2}\epsilon_x^2 + 2\frac{\partial^2 Q_z}{\partial \epsilon_x \partial \epsilon_y}\epsilon_x\epsilon_y + \frac{\partial^2 Q_z}{\partial \epsilon_y^2}\epsilon_y^2\right) + ... \end{aligned} \tag{4.4}$$

where $\epsilon_{x,y}$ is the physical single particle emittance.

The detuning with amplitude can be measured by exciting the beam to large amplitudes using a kicker magnet. The LHC Aperture Kicker (MKA) [100, 101, 122] used in these studies is capable of providing single kicks of up to $14\,\sigma_{\mathrm{nominal}}$. On applying such a kick betatron oscillations of the beam are excited. Spectral analysis of the turn-by-turn (TbT) data in the Beam Position Monitors (BPM) then yields the tune. In these studies spectral analysis was performed using the *'SUSSIX'* code for frequency analysis of non-linear betatron motion [112]. Performing such an analysis for a range of kick strengths allows for a measurement of the variation of tune with betatron oscillation amplitude. The mean and standard deviation obtained by performing this analysis for all BPMs (there are ~ 500 dual plane BPMs per Beam in the LHC) are taken as the value and uncertainty on the tune.

The action of the kick may be determined from the TbT BPM data using Eq.(4.5)

$$2J_{x,y} = \frac{\sum_{BPMs} \frac{\left(\frac{1}{2}Peak-to-Peak\right)^2}{\beta_{x,y}}}{N} \tag{4.5}$$

where $Peak - to - Peak$ is the peak-to-peak amplitude of the turn-by-turn oscillation data in the relevant plane of the BPM and N is the number of BPMs. The procedure of averaging over the available BPMs automatically cancels the effect of first order focusing errors around the ring. The effect of the measured beta-beat on the action determined with Eq.(4.5) has been examined for the studies presented in this Chapter, and found to be negligible [123]. This reflects the high quality of the linear optics correction in the LHC.

Eq.(4.5) makes the implicit assumption of an elliptical phase space trajectory: it is valid in the linear regime where the phase space has not been distorted by higher order resonances. The application of Eq.(4.5) to the real LHC is therefore an approximation, the validity of which will depend on the degree to which the phase space is distorted. If detuning with amplitude drives the tunes towards resonant frequencies such distortions could impact upon the determination of the detuning. The validity of Eq.(4.5) under the conditions relevant to the studies presented in this Chapter is discussed briefly towards the end of Section 4.4.4. This method of determining the action of the kicks also assumes that any emittance exchange due to coupling is negligible.

In the LHC corrections for various geometric and electrical non-linearities are automatically performed on the turn-by-turn BPM data at its point of delivery to users, however there are known to be small imperfections in the compensation of the BPM non-linearity at very large amplitudes. The correction of the BPM non-linearity is reviewed in [93, 95]. As described in Chapter 3.2.1, prior to analysis of the turn-by-turn BPM data Singular Value Decomposition (SVD) cleaning is performed on a matrix constructed from the TbT data of all available BPMs [111]. This assists in the removal of uncorrelated noise.

Ideally, detuning terms in Eq.(4.4) are reconstructed by kicking at a range of amplitudes along several angles in the $(2J_x, 2J_y)$ plane. A fit may then be performed to the surface defined by these measurements. In practice such a procedure requires a significant amount of dedicated beam time in the LHC. Consequently measurements may be performed only in

the horizontal and vertical planes. Under such conditions, when the excitation of a single plane dominates, the 2D Taylor expansion of Eq.(4.4) may be approximated to 1D Taylor series, Eq.(4.6).

$$\begin{aligned} &Q_x(\epsilon_x, 0) \\ &Q_x(0, \epsilon_y) \\ &Q_y(\epsilon_x, 0) \\ &Q_y(0, \epsilon_y) \end{aligned} \tag{4.6}$$

Typically it is required to perform a small excitation in the opposite plane from the dominant kick. This ensures the amplitude of the spectral line corresponding to the tune of the unkicked plane is sufficiently above the noise level to allow for a reliable determination of both tunes. So long as any variation in the excitation amplitude of this additional kick is small with respect to the amplitude range being examined, determination of the detuning is unaffected (though the effect may show up as changes in the Q_{z0} of fits to the measured data). Keeping all kicks in the sub-dominant plane at constant amplitude throughout the study should help ensure this condition is satisfied, however any substantial coupling of the kicks into the opposite plane will introduce complications if a 1D analysis is attempted.

Diagonal terms in the 2D Taylor expansions for Q_x and Q_y cannot be measured directly if only horizontal or vertical kicks are performed. Some of these missing terms may be determined from the well known identities relating the diagonal terms of Q_x to the on axis terms of Q_y and vice-versa. Eq.(4.7) is the well known equivalence of first order amplitude detuning cross terms. Eq.(4.8) are the equivalent identities for the second order detuning, which relate the diagonal detuning of $Q_{x,y}$ to the on axis detuning of $Q_{y,x}$.

$$\frac{\partial Q_x}{\partial \epsilon_y} = \frac{\partial Q_y}{\partial \epsilon_x} \tag{4.7}$$

$$\frac{\partial^2 Q_x}{\partial \epsilon_x \partial \epsilon_y} = \frac{\partial^2 Q_y}{\partial \epsilon_x^2} \qquad \frac{\partial^2 Q_y}{\partial \epsilon_x \partial \epsilon_y} = \frac{\partial^2 Q_x}{\partial \epsilon_y^2} \tag{4.8}$$

If the data is available such identities relating the detunings of Q_x and Q_y can provide a qualitative test of the measurement quality and the fits to the data. Identities (4.7) relating the first order detuning cross terms allow for such a test with both 1D and 2D methods. While poor agreement of these terms in the detuning expansion may be indicative of a poor quality fit or bad data, a good agreement does not necessarily imply the reverse.

Recent theoretical advances, verified experimentally in the LHC, now allow for the study of amplitude detuning using an AC dipole kicker magnet [105]. As opposed to measurements with a single kick this has the advantage of being non-destructive, however the analysis is substantially complicated with respect to the single kick method and data quality may be lower. At injection energy in the LHC the single kick method is most suitable, and was utilized for the studies presented in this Chapter.

4.2.3 Dynamic aperture

A possible method to observe the dynamic aperture is to measure beam loss following large amplitude kicks. The principle behind such a measurement is illustrated in Fig. 4.1. A kick shifts the beam to large amplitude in z' (the angle amplitude in the plane of the kick, z denotes the position amplitude in the plane of the kick), resulting in particles passing beyond the dynamic aperture and being lost. The distance of the excited beam from the dynamic aperture may then be determined from the measured beam losses following the kick, while the kick amplitude itself is determined from the turn-by-turn BPM data.

The fractional beam loss is given by the integral of the charge distribution, normalized to its total charge, over the region of phase space outwith the DA. It is assumed that the charge distribution is small with respect to the dynamic aperture, such that the integral may be taken between the limits $N = \pm\infty$ (where N represents the amplitude in z, in units of $[\sigma_{beam}]$). Assuming a circularly symmetric single Gaussian charge distribution the integral is then reduced to Eq.(4.9), where N' represents the amplitude in z', in units of $[\sigma_{beam}]$.

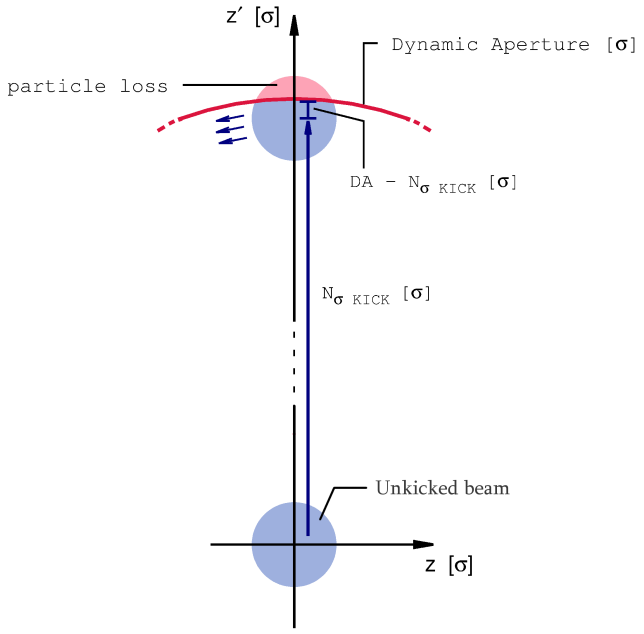

Figure 4.1: Illustration of the method used to measure the dynamic aperture. The value of $(DA - N_{\sigma KICK})$ is determined from the beam loss over many turns.

Equation (4.9) can be expressed in terms of the error function, and rearranged to give an expression for the DA in terms of the measured beam loss and kick amplitude, Eq.(4.10). A more detailed derivation of these relations is provided in Appendix B.4.

$$\frac{\Delta I}{I} = \frac{1}{\sqrt{2\pi}} \int_{DA-N_{\sigma KICK}}^{+\infty} e^{-\frac{1}{2}N'^2} \, \mathrm{d}N' \tag{4.9}$$

$$\frac{DA - N_{\sigma KICK}}{\sqrt{2}} = \mathbf{erf}^{-1}\left[1 - 2\frac{\Delta I}{I}\right] \tag{4.10}$$

In the LHC the beams are round ($\epsilon_x = \epsilon_y$) to a close approximation and the beam size is small compared to the possible DA of the nominal machine, however there is known to be an overpopulation of the transverse tails with respect to a single Gaussian charge distribution for the bunch types used for DA measurement in the LHC [124]. To limit the impact of any overpopulation of the tails on the estimate of the DA, the beam should be kicked as close to the aperture as allowed by beam losses. Alternatively the analysis of the beam losses may be

extended to a more realistic charge distribution, this is described in Appendix B.4.

Losses at the dynamic and physical apertures may in general be distinguished by a consideration of the timescale over which the losses take place. Losses on a physical aperture usually occur on a timescale of a few turns, while losses upon the dynamic aperture are generally slower and occur over many turns. It is in principal possible to study the losses on a turn by turn basis using the sum signal of the BPMs, however this data was in practice unavailable. Losses during the measurements presented in this Chapter were studied using the LHC Beam Current Monitors, BCT. The BCT data used have a resolution of $0.5\,\mathrm{Hz}$, approximately $550\,\mathrm{turns}$. While this is insufficient to allow for a completely conclusive determination of whether losses occurred on the physical aperture, it may provide a strong indication. To definitively verify that losses are occurring at the dynamic aperture however, it is desirable to perform a second measurement with non-linearities reduced as far as possible, while the physical aperture is unchanged. The removal of non-linear sources may be expected to increase the DA. If a corresponding increase in the loss aperture is seen in the measurement then the dynamic aperture is the source of the observed losses.

4.3 Measurements of non-linear observables at injection, with Landau octupoles set to zero

First studies of the non-linear dynamics in the LHC were performed at injection optics in 2011. Substantial second and third order chromaticities were observed during an initial study with Landau octupoles set to zero, which led to a first correction of the higher order chromaticity shortly after. Corrections for non-linear chromaticity presented in this section will also be relevant to an analysis of kicked beam observables presented later in the chapter.

4.3.1 First measurement of the non-linear chromaticity

As a first step in the study of the non-linear dynamics of the LHC, measurements of the higher order chromaticity were performed at injection optics, with Landau octupoles set to zero. Measurements were performed by varying the relative momentum offset, $\delta = \frac{p-p_0}{p_0}$, within the range $\pm 2 \times 10^{-3}$. The RF frequency trim was varied in regular steps, pausing for

$\sim 10\,\mathrm{s}$ following each trim. Two scans were performed, one over the range $\delta = \pm 1 \times 10^{-3}$, another over the full $\pm 2 \times 10^{-3}$ range. The non-linear chromaticities were determined from fits of third order polynomials to tune data logged by the LHC BBQ. Measurements at $\delta = 0$ were compared at the start, middle, and end of the RF scan in order to verify that the unperturbed tunes remained steady throughout the measurement. Data in the horizontal plane of Beam 2 for the $\delta = \pm 1 \times 10^{-3}$ scan was rejected due to a drift of the unperturbed tune.

Figure 4.2 presents the results of non-linear chromaticity measurements with depowered Landau octupoles for Beam 1 (top) and Beam 2 (bottom). Results of the $\pm 1 \times 10^{-3}$ scan are displayed in blue, and results of the $\pm 2 \times 10^{-3}$ scan in red. Table 4.1 summarizes the second and third order chromaticities determined from third order polynomial fits to the measured data.

Table 4.1: Results of second and third order chromaticity measurements on the LHC at injection with Landau octupoles set to zero.

	$Q''_x\ [10^3]$	$Q''_y\ [10^3]$	$Q'''_x\ [10^6]$	$Q'''_y\ [10^6]$
$\delta = \pm 1 \times 10^{-3}$				
Beam 1	-1.8 ± 0.08	1.0 ± 0.1	-3.7 ± 0.5	0.3 ± 0.5
Beam 2	$-$	0.82 ± 0.09	$-$	0.5 ± 0.5
$\delta = \pm 2 \times 10^{-3}$				
Beam 1	-1.8 ± 0.03	0.86 ± 0.02	-2.2 ± 0.1	0.73 ± 0.07
Beam 2	-1.7 ± 0.05	0.82 ± 0.02	-1.1 ± 0.2	0.90 ± 0.06

Similar results were obtained for both LHC beams, with the exception of Q'''_x, for which the Beam 2 value was approximately half that observed for Beam 1. The Q'' is in general very consistent between the $\pm 1 \times 10^{-3}$ and $\pm 2 \times 10^{-3}$ scans, however the Q''' value shows significant variations, indicating the larger range in δ is important for an accurate determination of the third order chromaticity. This is relevant for future measurements of the higher order chromaticity, as accessing larger trims of the RF frequency requires the masking of specific elements of the machine protection architecture, which would automatically the dump the beams.

With depowered Landau octupoles the second order chromaticity of the LHC was expected to be small. The measured Q'' and Q''' however was substantial, and as will be

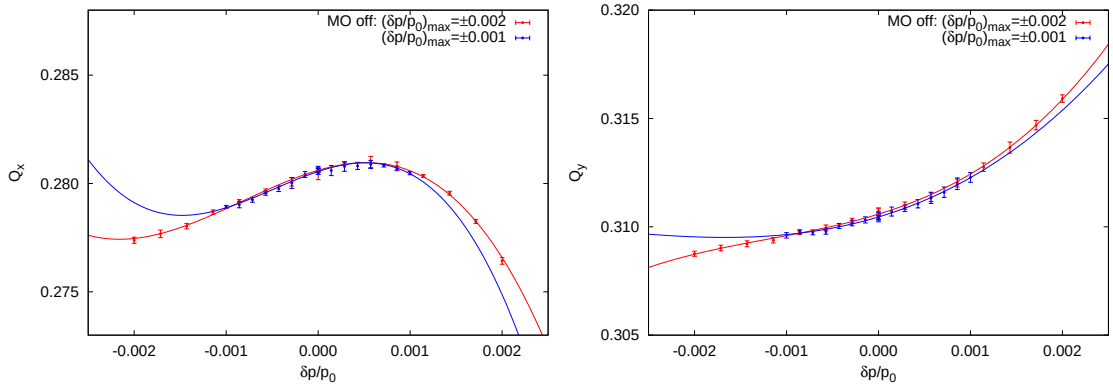

(a) Beam 1

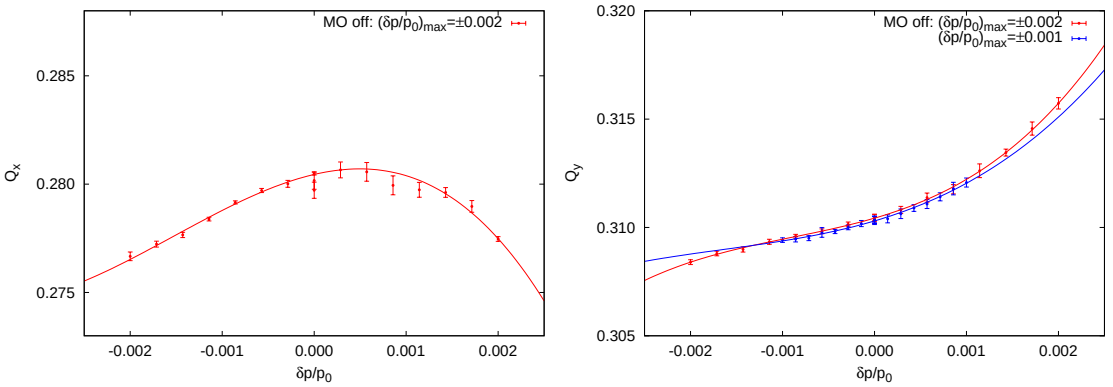

(b) Beam 2

Figure 4.2: Measurement of non-linear chromaticity in the LHC at injection optics with depowered Landau octupoles. Measurements were performed over two momentum ranges, $\pm 1 \times 10^{-3}$ (blue) and $\pm 2 \times 10^{-3}$ (red).

discussed in Section 4.3.3 significantly in excess of expectations from the known magnetic and alignment errors.

4.3.2 Correction of the non-linear chromaticity

Observation of substantial non-linear chromaticity at injection, with Landau octupoles set to zero, prompted a first attempt at correction of the second and third order terms shortly after the initial measurement. The non-linear chromaticity correction study was performed on LHC Beam 2, in parallel with a separate non-linear dynamics study performed on Beam 1 [5]. The LHC was pre-cycled, Landau octupoles were powered off, and the octupolar spool pieces (MCO) were driven from their nominal settings to their zero field settings (± 3 A, dependent on the Arc). Two families of LHC Beam 2 MCO, those in Arc 78 and Arc 81, were malfunctioning and remained depowered throughout the study.

Correction of the Q'' was performed by applying a global trim to the operational families of MCO. Similarly, correction of the Q''' was performed by applying a global trim to all families of decapole spool pieces (MCD), which were initially at their nominal settings. Independent knobs[2] for Q'' and Q''' were determined prior to the experiment based on simulation of MCO and MCD trims in MAD-X [48] and PTC [50]. Following an initial measurement of the non-linear chromaticity, settings of these knobs were adjusted to compensate the observed second and third order chromaticities. Details of the knob definitions and corrector circuit powering are provided in Appendix B.1. Figure 4.3 and Tab. 4.2 show results of the Q'' and Q''' correction. Application of the corrections caused a substantial reduction in both the second and third order chromaticities of both beams in both planes.

Table 4.2: Second and third order chromaticity of LHC Beam 2 before and after correction with MCO and MCD respectively.

	$\mathbf{Q''_x}[10^3]$	$\mathbf{Q''_y}[10^3]$	$\mathbf{Q'''_x}[10^6]$	$\mathbf{Q'''_y}[10^6]$
Before correction	-2.14 ± 0.02	0.74 ± 0.03	-1.90 ± 0.06	0.80 ± 0.09
After correction	-0.72 ± 0.02	-0.19 ± 0.02	-0.37 ± 0.05	-0.15 ± 0.04

[2] *knob*: in the context of LHC operations a knob is a collection of magnet trims which may be applied to the machine in order to produce a desired shift in the beam properties.

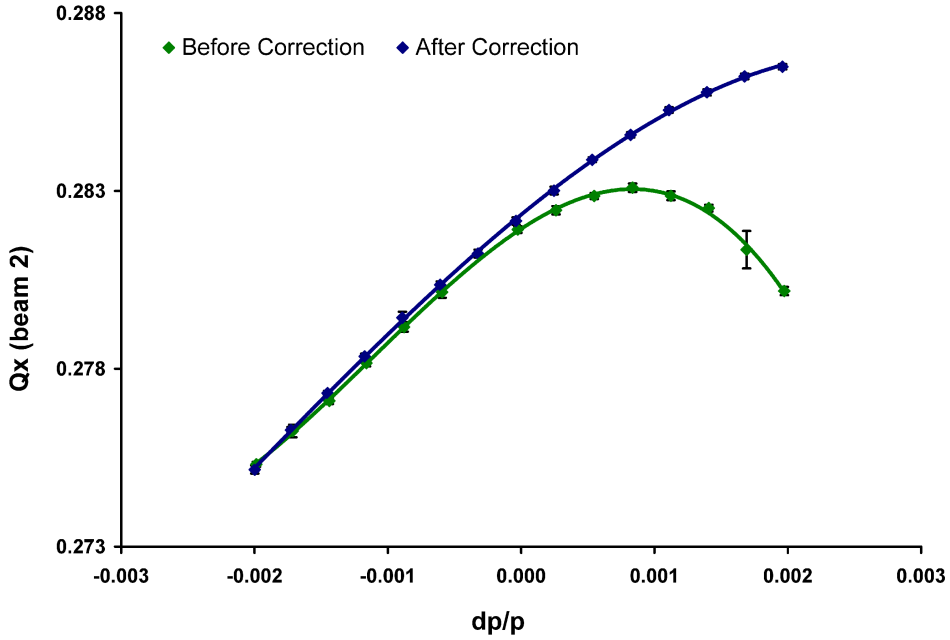

(a) Horizontal chromaticity

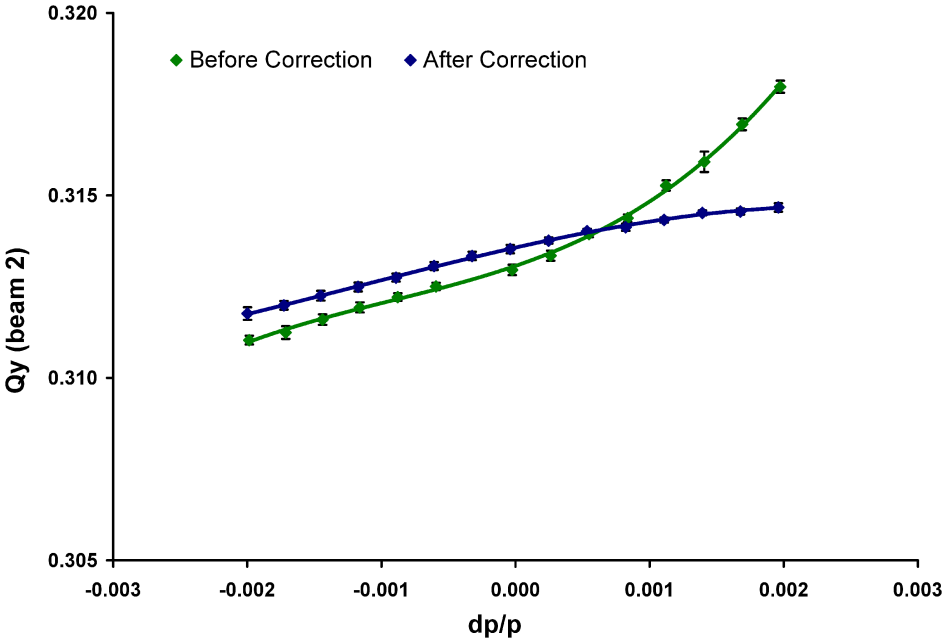

(b) Vertical chromaticity

Figure 4.3: Measurement of LHC non-linear chromaticities, before and after correction with octupolar and decapolar correctors.

Before and after correction of the non-linear chromaticity the CERN Optics Measurement and Correction (OMC) team applied a series of kicks with the LHC aperture kicker. The beams were excited in either the horizontal or vertical plane with single kicks. The kick amplitude was limited to $< 6\,\sigma_{\mathrm{nominal}}$ by the maximum strength of the aperture kicker (at the time), and by beam loss on a collimator (due to a malfunction which prevented its withdrawal). It was possible however to measure first order detuning with amplitude and examine decoherence of the kicks. These observations of first order detuning and decoherence have previously been reported in [55, 120].

Upon correction of the non-linear chromaticity the first order detuning with amplitude was observed to decrease. Large reductions were seen in the detuning terms $\frac{\partial Q_x}{\partial \epsilon_x}$ and $\frac{\partial Q_x}{\partial \epsilon_y}$. The first order detunings of Q_y both elicited a change of sign, with $\frac{\partial Q_y}{\partial \epsilon_x}$ showing a small reduction in magnitude and $|\frac{\partial Q_y}{\partial \epsilon_y}|$ remaining constant within the measurement uncertainty. This is illustrated in Fig. 4.4 and Tab. 4.3. It was also observed that on application of the non-linear chromaticity correction the decoherence of the betatron oscillations was significantly reduced, this is illustrated in Fig. 4.5.

Table 4.3: Measurement of first order amplitude detuning in the LHC in 2011 at injection optics with Landau octupoles powered to zero. Measurements were performed before and after correction of the non-linear chromaticity. Adapted from [120].

	$\frac{\partial Q_x}{\partial \epsilon_x}$ $[10^3\,m^{-1}]$	$\frac{\partial Q_y}{\partial \epsilon_x}$ $[10^3\,m^{-1}]$	$\frac{\partial Q_x}{\partial \epsilon_y}$ $[10^3\,m^{-1}]$	$\frac{\partial Q_y}{\partial \epsilon_y}$ $[10^3\,m^{-1}]$
Before correction	-12.2 ± 0.2	8.4 ± 0.5	9.4 ± 1.3	-2.5 ± 1.5
After correction	-2.9 ± 0.6	-2.7 ± 1.7	0.6 ± 0.5	2.4 ± 0.8

The observed reduction in the decoherence of kicked beams and of detuning with amplitude, upon correction of non-linear chromaticity, reflects the fact that the corrector magnets used for the compensation are mounted directly on every second main dipole in the LHC arcs, and the main dipoles are the dominant sources of the relevant non-linearities at injection when the Landau octupoles are unpowered. This local nature of the correction allows for the simultaneous correction of non-linear chromaticity together with amplitude detuning and decoherence. It should also be noted that the reduction of decoherence due to the non-linear chromaticity correction had practical benefits for the OMC studies, as it allowed spectral analysis of the betatron motion to be performed on an increased number of turns

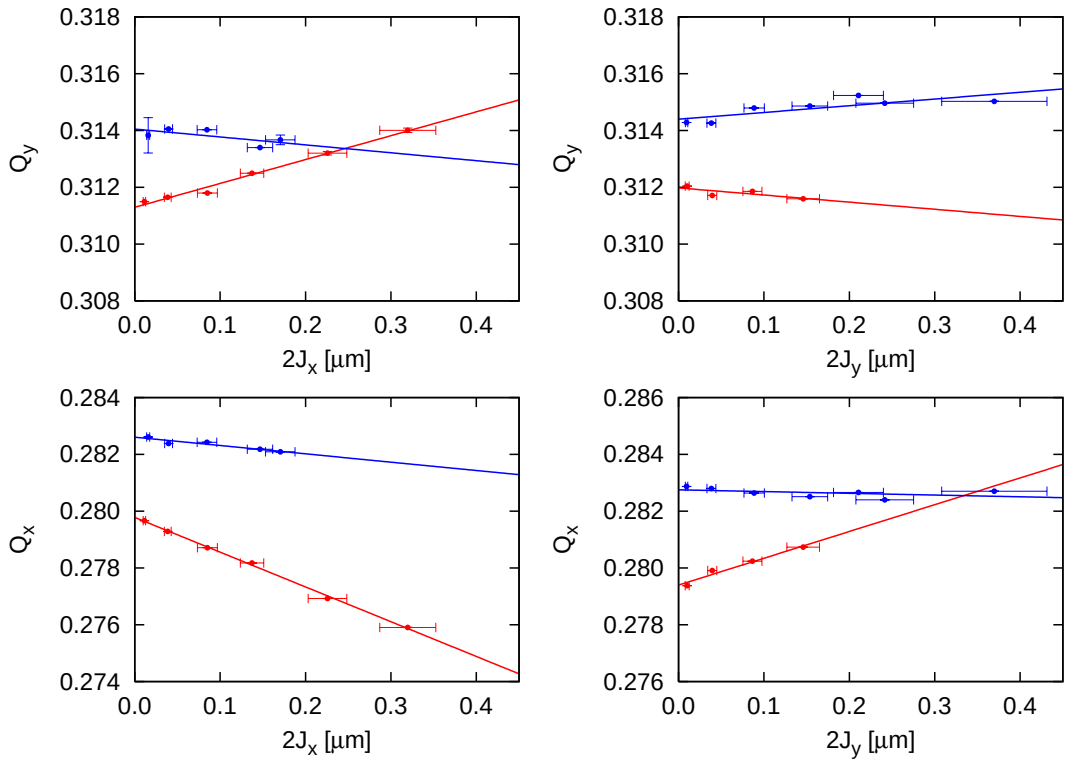

Figure 4.4: Measurement of first order amplitude detuning in the LHC in 2011, at injection optics with Landau octupoles powered to zero. Measurements are shown before (blue) and after (red) correction of the Q'' and Q'''. Adapted from [120].

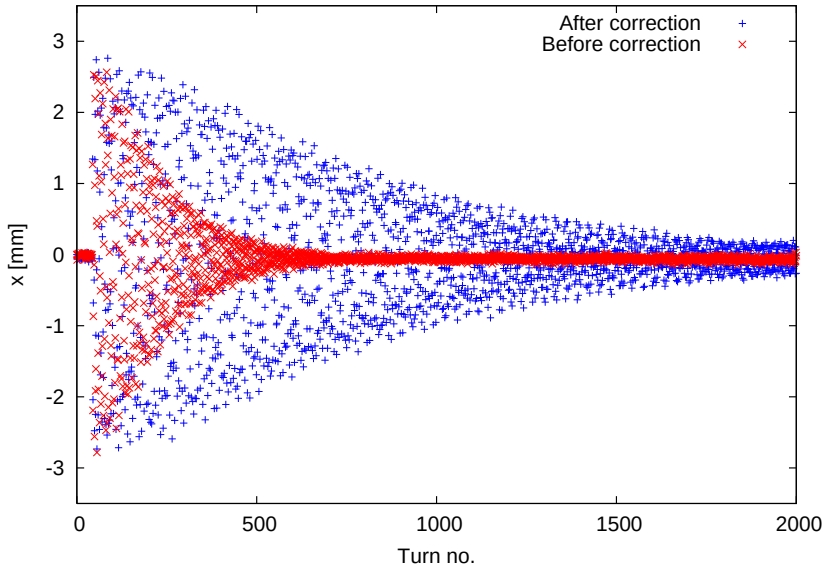

Figure 4.5: Turn-by-turn BPM data, recorded following $4.8\,\sigma_{\mathrm{nominal}}$ kicks in the horizontal plane, before (red) and after (blue) correction of the non-linear chromaticity. The decoherence was substantially reduced by the applied corrections. Adapted from [120].

which improved the quality of the optics measurements [120]. The corrections of non-linear chromaticity presented in this section were not included in regular LHC operation, but will be of relevance to the analysis of non-linear observables with kicked beams presented in Section 4.4.

First corrections of the non-linear dynamics in the LHC at injection (with depowered Landau octupoles) were highly successful. The second and third order chromaticities were significantly reduced, with corresponding reductions observed in both the first order amplitude detuning and the decoherence of kicked beams. This represents an important demonstration of the ability to effectively control the non-linear dynamics of the LHC.

4.3.3 Comparison to simulation

The Q'' and Q''' measured at injection, with Landau octupoles set to zero, were substantial. To assess the understanding of the relevant sources, the measurements outlined in the previous sections were compared to simulation. Simulations were performed using the MAD-X model introduced in Chapter 3.3, which had previously proved successful in reproducing the

magnitude of the beat-beating in the LHC following local correction of the errors in the IRs. These simulations incorporated estimates of geometric and magnetic errors (based on measurements performed during LHC construction) from the Windows Interface to Simulation Errors[3] (WISE) [87, 89, 88], which represented the best available knowledge of the errors in the LHC lattice. Tunes and first order chromaticities were matched in the MAD-X model to their values during the non-linear chromaticity measurements. Closed orbit and linear coupling were matched towards zero. Malfunctioning MCO families in LHC Beam 2 were set to zero in the model. The non-linear chromaticity in the model was determined using the PTC_NORMAL module in MAD-X [116, 50].

The Q'' determined from these simulations were significantly smaller than observed in the machine. For injection optics with depowered Landau octupoles, Q'' of approximately -100 ± 100 and 200 ± 100 (where the uncertainty is associated with variation between the WISE seeds) were predicted in the horizontal and vertical planes respectively. This represented roughly an order of magnitude discrepancy with the observed Q''_x. Predicted values for the Q''' also showed a considerable discrepancy with respect to the Q'''_y measured in both beams, and with the Q'''_x in Beam 1. The measurement of Q'''_x for Beam 2 is ambiguous due to inconsistencies between the value obtained during the initial non-linear chromaticity studies and the value obtained prior to the non-linear chromaticity correction. The discrepancies of the model with respect to the observations are summarized in Tab. 4.4; Q'''_x of Beam 2 is not considered, due to the aforementioned inconsistencies.

Comparable discrepancies were also observed in the simulated first order amplitude detuning (determined with PTC_NORMAL). It was observed in the model that trims of the MCO chosen to reproduce the measured Q'' also reproduced observed values of the detuning with amplitude.

While the absolute values of the non-linear chromaticity are not well reproduced by the known magnetic and geometric errors, the shifts in Q'' and Q''' upon applying trims of the MCO and MCD to correct the non-linear chromaticity agree very well between simulation and observation. This is illustrated in Tab. 4.5, which compares the modelled and measured $\Delta Q''$ and $\Delta Q'''$ upon applying the non-linear chromaticity correction.

[3]WISE, the Windows Interface to Simulation Errors, was introduced in Chapter 2.1.3.

Table 4.4: Discrepancies of the simulated Q'' and Q''' in the LHC at injection (with Landau octupoles depowered) with respect to observations at injection optics. The Q'''_x of Beam 2 has not been considered due to inconsistencies between the initial measurements and measurements performed immediately prior to the non-linear chromaticity correction.

	$\Delta Q''_x$ $[10^3]$	$\Delta Q''_y$ $[10^3]$	$\Delta Q'''_x$ $[10^6]$	$\Delta Q'''_y$ $[10^6]$
Beam 1				
$measured - modelled$	-1.7 ± 0.1	0.7 ± 0.1	-1.2 ± 0.1	0.6 ± 0.1
$\frac{measured-modelled}{measured}$	$\sim 94\%$	$\sim 70\%$	$\sim 55\%$	$\sim 86\%$
Beam 2				
$measured - modelled$	-1.7 ± 0.1	0.6 ± 0.1	–	0.8 ± 0.1
$\frac{measured-modelled}{measured}$	$\sim 94\%$	$\sim 73\%$	–	$\sim 89\%$

Table 4.5: Measured and simulated shifts in the second and third order chromaticities, due to trims applied to the MCO and MCD during non-linear chromaticity correction.

Horizontal	$\mathbf{\Delta Q''}$ $[10^3]$	$\mathbf{\Delta Q'''}$ $[10^6]$
Measured	1.4 ± 0.03	1.5 ± 0.08
Modelled	1.3	1.6

Vertical	$\mathbf{\Delta Q''}$ $[10^3]$	$\mathbf{\Delta Q'''}$ $[10^6]$
Measured	-0.93 ± 0.04	-0.97 ± 0.1
Modelled	-0.90	-0.91

The poor agreement of Q''' may be a contributed to by discrepancies in the Q'' sources, therefore the first consideration for the model is investigation of the the second order chromaticity discrepancy. There are a number of potential explanations for the Q'' observations. Chromatic coupling driven by a_3 errors in the dipoles have the potential to generate a significant Q'' in the LHC [125]. Measurements of the linear coupling resonance driving terms as a function of the relative momentum offset demonstrated, however, that the simulated chromatic coupling is in excellent agreement with that present in the machine [119]. Consequently chromatic coupling may be excluded as a significant source of the observed Q'' discrepancy.

Another possible explanation for the Q'' discrepancy could be feed down resulting from a systematic misalignment of the MCD with respect to the main arc dipoles (which are the dominant source of b_5 errors at injection). Using the aforementioned shifts in Q'' upon simultaneous correction of the second and third order chromaticity (Tab. 4.5), it is possible to place constraints on the allowed systematic misalignment of the MCD. Assuming that the discrepancy between the modelled and measured $\Delta Q''$ in Tab. 4.5 is entirely the result of a

systematic misalignment of the MCD, the allowed magnitude is $\Delta x = -0.055 \pm 0.04\,\mathrm{mm}$. Applying this misalignment in the model it was determined that a systematic misalignment of the MCD with respect to the main dipoles could generate up to $Q''_x = -200 \pm 150$ and $Q''_y = 150 \pm 110$. Systematic misalignment of the MCD is not therefore the dominant source of the discrepancy between the model and measurements, although it does potentially remain as a small but non-negligible contribution to the second order chromaticity at injection optics with depowered Landau octupoles.

The hysteresis of the octupolar spool pieces represents another potential source of the discrepancy. The MCO in the LHC are nested within the MCD [84]. In such an arrangement only one of the magnets may be pre-cycled, in this case the MCD [90], in addition to which the MCO are weakly powered at injection. Consequently the field of the MCO at injection may be highly dependent on the magnetic history. Following the observations of substantially higher Q'' than predicted from the known magnetic and geometric errors, the FiDeL[4] group at CERN calculated the MCO fields following a nominal LHC pre-cycle, including the effects of hysteresis. The estimates of the actual field are shown in Tab. 4.6 and differ substantially from the previously implemented values [126]. It should be noted however, that the estimate becomes imprecise at small fields, such as those present in the machine at injection.

The discrepancies in the MCO fields due to hysteresis were applied in the MAD-X model. The resulting changes in chromaticity are shown in Tab. 4.7. The previously discussed effect of a $0.055 \pm 0.04\,\mathrm{mm}$ systematic misalignment of the MCD with respect to the main arc dipoles (which gives the closest agreement to the observed $\Delta Q''$ on correction of the non-linear chromaticity with the MCO and MCD) is also shown.

The MCO hysteresis, as characterized by Tab.4.6, explains approximately $30\,\%$ of the observed Q'' discrepancy in the horizontal plane, and $57\,\%$ in the vertical. It represents an important contribution to the non-linear dynamics at injection and should be incorporated into the model. MCO hysteresis together with a systematic alignment of the MCD could explain the majority of the Q'' discrepancy in the vertical plane, however there remains a

[4] *FiDeL*: the *Field Description of the LHC*. The FiDeL group at CERN is responsible for matters concerning prediction of the magnetic state of the LHC.

Table 4.6: Effect of hysteresis on the MCO field following a nominal pre-cycle of the accelerator. Calculation was performed by the FiDeL group at CERN [126], for nominal injection settings. It is known that these calculations become imprecise at low MCO fields [126].

(a) Beam 1

Family	Expected field [Tm]	Actual field [Tm]	Discrepancy [%]
Arc 12	0.000069	−0.000005	−108
Arc 23	−0.000160	−0.000234	46
Arc 34	−0.000134	−0.000208	55
Arc 45	−0.000120	−0.000194	62
Arc 56	0.000063	−0.000012	−119
Arc 67	0.000088	0.000014	−84
Arc 78	0.000018	−0.000056	−417
Arc 81	−0.000139	−0.000214	53

(b) Beam 2

Family	Expected field [Tm]	Actual field [Tm]	Discrepancy [%]
Arc 12	−0.000104	−0.000178	72
Arc 23	0.000098	0.000024	−76
Arc 34	0.000097	0.000023	−76
Arc 45	0.000085	0.000011	−87
Arc 56	−0.000100	−0.000174	75
Arc 67	−0.000136	−0.000211	54
Arc 78	0	(depends on previous cycling)	unknown
Arc 81	0	(depends on previous cycling)	unknown

Table 4.7: Simulated impact of the MCO field discrepancies due to hysteresis on the non-linear chromaticity. The effect of adding a $0.055 \pm 0.04\,\mathrm{mm}$ systematic misalignment of the MCD with respect to the main arc dipoles is also shown.

	$\Delta Q''_x$ $[10^3]$	$\Delta Q''_y$ $[10^3]$	$\Delta Q'''_x$ $[10^6]$	$\Delta Q'''_y$ $[10^6]$
measurement$-$model	-1.7 ± 0.1	0.6 ± 0.1	-1.0 ± 0.1	0.70 ± 0.1
(model + MCO hysteresis)$-$model	-0.5	0.34	$+0.006$	-0.003
(model + MCD alignment)$-$model	-0.2 ± 0.15	0.15 ± 0.11	0	0

sizable discrepancy in the horizontal plane, $\Delta Q''_x \sim 1000$, which is presently unaccounted for.

There may be other sources relevant to the Q'' discrepancy, for example the local quality of b_3 correction in the main dipoles, however no data is available to assess such contributions. The Q''' discrepancy remains unexplained, however until the Q'' observations are adequately understood the focus remains the lower order.

Studies of non-linear chromaticity performed at injection, with Landau octupoles set to zero, identified substantial discrepancies in the non-linear modelling of the LHC. The MCO hysteresis was identified as a prominent source of the discrepancy, whereas systematic misalignments of the MCD were constrained by the data such that they could only make a small contribution to the Q''. A substantial discrepancy remains in the second order chromaticity in the horizontal plane. First corrections of the non-linear dynamics were performed successfully via beam based correction of the second and third order chromaticities, with corresponding reductions observed in the first order detuning with amplitude and the decoherence of kicked beams.

4.4 Measurements of non-linear observables at nominal injection optics

The nominal injection optics of the LHC include powering of the Landau octupoles. The Landau octupoles introduce substantial amplitude detuning and second order chromaticity. Study of the LHC at injection with depowered Landau octupoles is useful for identifying discrepancies in the behaviour of the weaker sources, for example the MCO hysteresis dis-

cussed in the preceding section, however it is the nominal optics, including the nominal settings of the MO, which are of interest operationally.

Measurements of the non-linear chromaticity at nominal injection optics were performed in 2011. This was followed in 2012 by detailed examinations of non-linear observables using kicked beams. In particular upgrades to the LHC aperture kickers and favourable collimation settings allowed examination of a large amplitude range. This facilitated the measurement of amplitude detuning terms higher than first order, a first observation of the dynamic aperture of the LHC, and observations of the non-linear coupling.

4.4.1 Measurement of non-linear chromaticity at nominal injection optics

Measurements of the non-linear chromaticity at injection optics in 2011 were performed during the same experimental period as the initial measurements with depowered Landau octupoles discussed in Section 4.3.1. The same procedure was utilized for measurements at the nominal optics as for studies with MO depowered. The relative momentum offset was scanned in several steps over two ranges, $\delta = \pm 1 \times 10^{-3}$ and $\delta = \pm 2 \times 10^{-3}$, and the second and third order chromaticity were determined from polynomial fits to tune data logged by the LHC BBQ. Table 4.8 and Fig. 4.6 show results of non-linear chromaticity measurements at nominal injection optics.

Table 4.8: Results of second and third order chromaticity measurements of the LHC at nominal injection optics.

	$Q''_x\ [10^3]$	$Q''_y\ [10^3]$	$Q'''_x\ [10^6]$	$Q'''_y\ [10^6]$
$\delta = \pm 1 \times 10^{-3}$				
Beam 1	-5.9 ± 0.1	2.8 ± 0.1	-4.5 ± 0.6	0.2 ± 0.6
Beam 2	-5.8 ± 0.1	2.5 ± 0.1	-3.6 ± 0.7	0.8 ± 0.6
$\delta = \pm 2 \times 10^{-3}$				
Beam 1	-6.1 ± 0.2	2.6 ± 0.1	-1.9 ± 0.7	1.1 ± 0.2
Beam 2	-6.1 ± 0.4	2.1 ± 0.06	-2.7 ± 0.7	1.1 ± 0.2

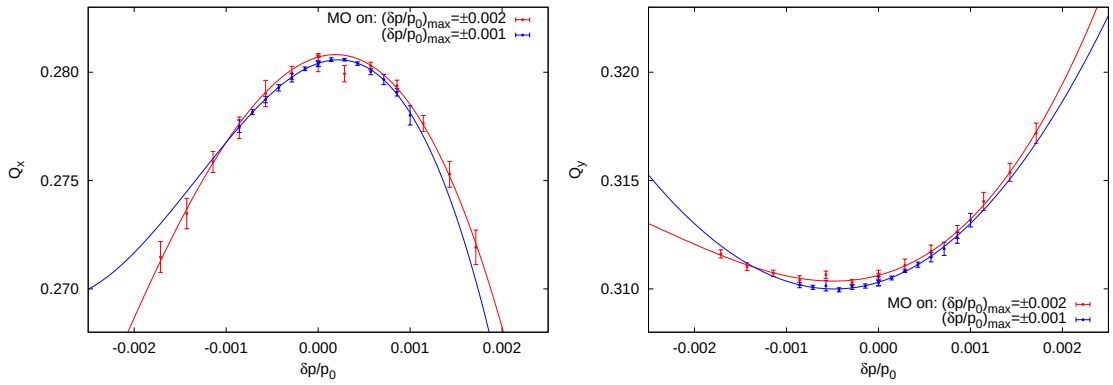

(a) Beam 1

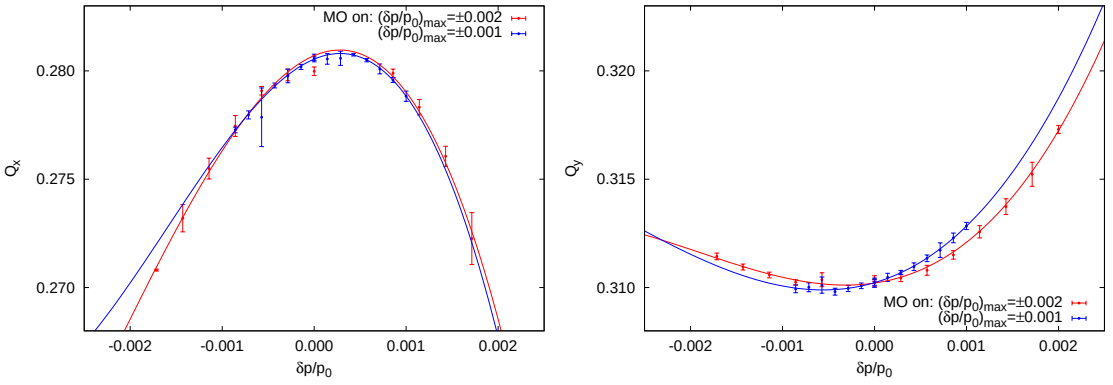

(b) Beam 2

Figure 4.6: Measurement of non-linear chromaticity in the LHC at nominal injection optics. Measurements were performed over momentum ranges: $\pm 1 \times 10^{-3}$ (blue) and $\pm 2 \times 10^{-3}$ (red).

Compared to measurements with Landau octupoles powered off, Q'' was substantially increased. The measured change in Q'' upon inclusion of the MO agreed well with simulation, indicating the MO circuits functioned as expected. The large Q'' introduced by the Landau octupoles defines the momentum offset of the LHC beams at which the Q' becomes negative, which may influence the growth of instabilities in the beam motion. At the nominal on-momentum first order chromaticity ($\delta = 0$, $Q' = 2$), and for the MO settings considered in 2011, this occurs at $\delta > 3 \times 10^{-4}$ in the horizontal plane and $\delta < -8 \times 10^{-4}$ in the vertical plane. These tolerances are dependent upon the on-momentum first order chromaticity, for example if the on-momentum Q'_x was to drop to $Q'_x \sim 0.5$ the momentum offset at which the horizontal chromaticity became negative would decrease to $\delta \sim 1 \times 10^{-4}$, which may then become comparable with the RMS momentum deviations of the LHC bunches [76].

4.4.2 Experimental procedure for study of the non-linear dynamics with kicked beams

Initial studies of the non-linear dynamics of the LHC at injection were performed in 2011, and focused on measurements of the non-linear chromaticity. In 2012 detailed measurements were performed of the non-linear observables in the LHC at injection, using kicked beams, which allowed measurement of detuning with amplitude, dynamic aperture, and a first observation of non-linear coupling. This section describes the experimental procedure applied during 2012 studies of the non-linear dynamics using kicked beams.

Measurements of the non-linear observables such as detuning with amplitude and dynamic aperture require large amplitude excitation of the beam. The LHC aperture kicker, capable in 2012 of providing kicks up to $\sim 14\,\sigma_{\mathrm{nominal}}$ (where $\sigma_{\mathrm{nominal}}$ is defined as corresponding to a normalized emittance of $3.75\,\mu\mathrm{m}$) was used to provide the excitation for these studies. Single probe bunches were used for the measurement which had intensities ($\sim 1 \times 10^{10}\,\mathrm{protons}$) below the damage threshold of the LHC. The collimators in the LHC were retracted from their operational settings in order to allow measurements out to large amplitudes. The horizontal and vertical primary collimators were left at $11.6\,\sigma_{\mathrm{nominal}}$ in order to shield the LHC triplets, all other collimators were retracted beyond this aperture.

An initial series of measurements were performed on LHC Beam 2 at nominal injection

optics, with kicks applied in either the horizontal or vertical planes. Multiple kicks were performed, with amplitude increasing incrementally up to the limit defined by beam losses. A distinct experiment [127] was performed on LHC Beam 1 in parallel with these studies, as such all results presented in the following sections pertain to measurement of LHC Beam 2.

Following a successful series of measurements at nominal injection settings, the Landau octupoles were powered to zero, and the MCO were driven to their zero field settings. The corrections for the second and third order chromaticities found during the 2011 non-linear measurement program were then applied. A second series of kicks were then performed on this *'corrected'* machine in the horizontal, vertical, and diagonal planes. As in the case of the nominal measurement series, the kick amplitudes were increased incrementally out to the maximum defined by beam losses.

Unperturbed tunes, first order chromaticities, and linear coupling were very stable throughout the measurement. The value Q' was ~ 2 (the nominal value for the LHC) in both planes throughout the experimental period. The tunes also remained close to their nominal values (0.28 and 0.31 in the horizontal and vertical planes respectively). The only substantial change was observed in Q_y following a beam-protection dump during measurements of the corrected machine. After recovery, the vertical tune was corrected to a value 0.0027 smaller than had previously been present in the machine. A correction has been applied to the detuning data to compensate for this shift. Emittance measurements of the unkicked beams were performed regularly throughout the experiment, this too was found to be extremely stable. Details of the settings of the relevant corrector circuits, and of the kicks applied during the measurement are provided in Appendix B.2 and B.3 respectively.

4.4.3 An updated model of the LHC at injection

Studies of the non-linear chromaticity performed on the LHC at injection in 2011 provided valuable information in regard to the non-linear dynamics. To quantify the understanding of the non-linear dynamics in analysis of the non-linear dynamics using kicked beams, it was desired to incorporate the experience of the earlier studies into an updated model of the LHC at injection, which could then be compared to results of the kicked-beam measurements. The details of this model are described in this section.

Estimates of the geometric errors in the LHC lattice [88] generated by the Windows Interface to Simulation Errors [87] from measurements performed during LHC construction were applied to the model lattice in MAD-X. Magnetic errors of order (b_3,a_3) up to (b_{15},a_{15}), also generated by WISE from magnetic measurements, were assigned to the main dipoles and quadrupoles in the LHC arcs and in the IRs. Given the excellent quality of the linear optics correction in 2012 [4], described in Chapter 3.4, it was assumed that the b_2 errors had been well corrected during commissioning and were not included in the model. Incorporating a $\sim 10\%$ beta-beating in the model had a negligible impact on the amplitude detuning and dynamic aperture at nominal injection settings, validating the application of this assumption.

The Landau octupoles and non-linear correctors in the LHC were set in the model to the settings present in the machine during the measurement (with the exception of the normal sextupole correctors in the arcs, the sextupolar spool pieces or MCS, which will be discussed shortly). Notably this included three families of arc octupole correctors (MCO), out of a total of eight, which were malfunctioning throughout 2012 and had zero field. It should be noted that in 2012, compared to 2011, an additional family of the MCO (Arc 12) were malfunctioning, therefore non-linear dynamics studies performed in the two years cannot be directly compared. Adjustments were then applied to the settings of the MCO to reproduce a best estimate of their substantial hysteresis effects, which studies of the non-linear chromaticity, presented in the preceding sections, determined were an important contribution to the Q'' [6, 126].

The settings of the sextupolar spool pieces present in the machine were not applied directly to the model. Corrections for dynamic b_3 are included in the machine settings of the MCS, but the dynamic components are not included in the WISE errors applied to the model. The compensation of the dynamic b_3 was therefore assumed to be perfect, and corrections for the static b_3 defined in the WISE seeds applied to the MCS in the model. A systematic misalignment of the MCD, corresponding to the limit determined in Section 4.3.3, was included in the updated model. The contribution to the detuning from the additional MCD alignment (of the order $1 \times 10^3\,\mathrm{m}^{-1}$) was small at nominal injection settings.

Tunes and chromaticities were matched to the measured values. The closed orbit was matched towards a zero reference orbit, but retained a realistic RMS in the arcs. Crossing and

separation bumps through the LHC insertions, which were present during the experiment, were reproduced in the model.

It was observed in simulations of detuning with amplitude in at top energy in the LHC that the linear coupling could significantly influence the non-linear phenomenology of the machine [105]. The quality of the linear coupling model is therefore a concern for study of the non-linear dynamics, which had not been addressed in previous studies of the non-linear dynamics. Linear coupling is characterized by the magnitude of the f_{1001} resonance driving term (RDT), which drives the $(Q_x - Q_y)$ resonance, and varies around the LHC ring. The global quantity $|C^-|$ is related to the mean amplitude of the RDT around the accelerator ring ($\overline{|f_{1001}|}$) by Eq.(4.11), [27].

$$|C^-| = 4|(Q_x - Q_y)|\,\overline{|f_{1001}|} \tag{4.11}$$

The value of f_{1001} in the LHC BPMs was determined from spectral analysis of turn-by-turn data obtained following small amplitude ($\sim 2\,\sigma$) kicks, performed in the course of the study of non-linear kicked-beam observables. A small kick was used for the determination of f_{1001} in order to avoid any amplitude dependent contribution. The mean amplitude of f_{1001} was extremely stable throughout the kicked-beam measurements described in the following sections, however there were significant local variations of $|f_{1001}|$ around the ring. The local fluctuations in the amplitude of the RDT corresponded to an equivalent range of $0.002 \leq |C^-| \leq 0.004$ (it should be emphasised that the range in $|C^-|$ quoted is an equivalent to the f_{1001} fluctuation, intended to give a sense of the scale of the local variation of the RDT, rather than an actual change of $|C^-|$ which is a global quantity).

The best procedure would be to reproduce the linear coupling in the model by locally matching to the measured f_{1001} around the ring. This is not currently implemented for the LHC model and applying the measured a_2 errors does not guarantee the correct local f_{1001}. In the MAD-X model therefore, a_2 errors were not included, which gave a relatively flat $|f_{1001}|$ around the ring. The linear coupling was then matched using the LHC global coupling knobs [128] in order to produce a given phase and amplitude of f_{1001} in the center of Arc12. In order to assess the uncertainty in the non-linear observables due to the linear coupling

~ 2000 random realisations of the LHC were then defined. The $|f_{1001}|$ was defined on an even distribution within the band defined by the observed local fluctuations of the RDT. The phase of f_{1001} at the matching location was varied randomly with a uniform distribution. The sixty seeds defined by the WISE magnetic model were also varied randomly with a uniform distribution. Evidently this is a somewhat artificial construct, in reality the $|f_{1001}|$ and its phase vary around the ring according to the distribution of a_2 sources, however the purpose is to assess the uncertainty arising in the non-linear observables due to the variation of f_{1001} around the ring, not to directly reproduce this effect in the model.

The non-linear observables measured with kicked beams, as described in Section 4.2, were simulated in this model by tracking particles initially displaced from the closed orbit. Both the Polymorphic Tracking Code (PTC [50]) module within MAD-X, and SIXTRACK [43], were used for such simulations. The PTC Normal module in MAD-X also provided a convenient way to determine the detuning with amplitude and the non-linear chromaticity. A thin lattice model of the LHC was utilized for these studies, as opposed to the thick lattice used considered in Chapter 3 and Section 4.3.3. This was necessary to allow simulation of the dynamic aperture with SIXTRACK, and to allow matching of the coupling to be performed in MAD-X (the relevant procedures in PTC being too time consuming). Differences between the thin and thick lattice predictions for the non-linear chromaticity were negligible for the optics considered in the preceding Section.

For the model of the nominal injection optics no matching of the non-linear parameters is performed. The model therefore represents the current understanding of the non-linear sources. All comparisons between measured and simulated non-linear observables at nominal injection optics presented in the following sections utilize this model.

Non-linear parameters of the model, in particular the non-linear chromaticity and detuning with amplitude, may be matched to produce a so-called ‘effective model’, which reproduces observed properties of the machine. As will be described in Section 4.4.4, this has been performed for the state of the machine in the latter half of the kicked-beam experiment, where departures from the nominal magnetic cycles of the octupolar correctors in the arcs made estimates of the hysteresis errors in these elements impractical. Such matchings were performed in MAD-X using macros which call the PTC normal module.

4.4.4 Experimental results from non-linear dynamics measurements with kicked beams, and comparison to simulation

Decoherence

As described in Section 4.4.2, following amplitude detuning and DA measurements at nominal injection settings Landau octupoles were powered to zero and Q'' and Q''' corrections, found in 2011, were applied. A check of the effectiveness of the 2011 non-linear chromaticity corrections was required before proceeding with the remainder of the study, however, due to a parallel experiment running on Beam 1, direct verification of the correction via measurement of Q with $\frac{\Delta p}{p_0}$ was not possible. To perform a brief check of the correction quality therefore, small $(2\sigma_x, 2\sigma_y)$ kicks were performed at nominal injection settings, following the depowering of the MO to zero and the zeroing of MCO field, and after inclusion of the 2011 non-linear chromaticity corrections. The decoherence of the three kicks were compared. This is shown in Fig. 4.7.

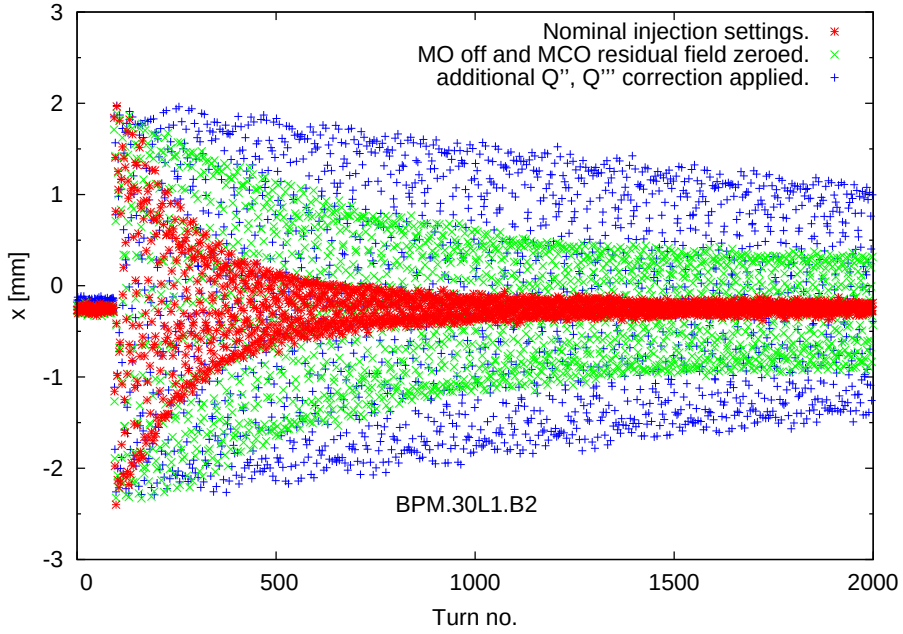

Figure 4.7: Decoherence of $(2\sigma_x, 2\sigma_y)$ kicks at injection. The decoherence of kicks at the three different optics studied are shown: nominal injection settings settings (red), with Landau octupoles powered to zero and the MCO residual field zeroed (green), and the 'corrected' optics with Q'' and Q''' corrections applied on top of the preceding state (blue).

The decoherence of the kicked beam was substantially reduced by the depowering of the MO to zero together with the zeroing of MCO residual fields, and again on the application of the 2011 non-linear chromaticity corrections. This qualitatively indicated the 2011 corrections were still valid, and the experiment proceeded using this new configuration. It is also interesting to observe that upon correction of the octupolar and decapolar non-linearities (blue data) a periodic beating of the decoherence pattern is revealed, corresponding to the decoherence due to first order chromaticity together with the synchrotron motion.

Amplitude detuning

As described in Section 4.4.2 amplitude detuning measurements were performed at nominal injection settings, and at the corrected optics. During the nominal measurement only horizontal or vertical kicks were applied (together with small excitations in the opposite plane to ensure successful tune measurements), however coupling of the kicks into the opposite plane did occur. Attempting to fit the 2D Taylor expansion up to second order, Eq.(4.4), fails in this case due to a lack of data in the diagonal plane. As described in Section 4.2.2 the quality of the fit can be checked qualitatively by comparing detuning terms in the expansion of Q_x and Q_y which are by definition identical. These values differed significantly in the 2D fit, implying the detunings calculated by this method were unphysical. This is not unexpected. The second order diagonal term does not influence pure horizontal or vertical detuning, and was only weakly constrained by the data due to the coupling of large kicks into the opposite plane. Under such conditions its inclusion in the regression model is inappropriate and can be expected to reduce the fit quality. A regression without the diagonal term, equivalent to the 1D analysis of Eq.(4.6), is more suitable to the available data.

Making the approximation to 1D Taylor expansions, Eq.(4.6), requires that some data is excluded from the fit due to a substantial coupling of the highest amplitude vertical kick into the horizontal plane (this coupling is discussed in more detail in the following section). The calculated detunings are given in Tab. 4.9a. First order cross terms of the Q_x and Q_y fits, Eq.(4.7), agree well.

Table 4.9: Results of fits to measured amplitude detuning.

(a) Nominal injection settings. 1D polynomial fits

Anharmonicity	[unit]	Fit	± Fit error
Q_x (from J_x fit)	$[tune\ units]$	0.2821	20×10^{-5}
Q_y (from J_x fit)		0.3124	10×10^{-5}
Q_x (from J_y fit)		0.28035	9×10^{-5}
Q_y (from J_y fit)		0.31409	1×10^{-5}
$\frac{\partial Q_x}{\partial \epsilon_x}$	$[10^3\mathrm{m}^{-1}]$	-29	7
$\frac{\partial Q_y}{\partial \epsilon_x}$		19	3
$\frac{\partial Q_x}{\partial \epsilon_y}$		24	4
$\frac{\partial Q_y}{\partial \epsilon_y}$		-32.8	0.4
$\frac{\partial^2 Q_x}{\partial \epsilon_x^2}$	$[10^9\mathrm{m}^{-2}]$	-60	30
$\frac{\partial^2 Q_y}{\partial \epsilon_x^2}$		34	10
$\frac{\partial^2 Q_x}{\partial \epsilon_y^2}$		11	34
$\frac{\partial^2 Q_y}{\partial \epsilon_y^2}$		-13	3
–			
–			

(b) MO off, and Q'', Q''' corrections applied. Fits to 2D Taylor expansions.

Anharmonicity	[unit]	Fit	± Fit error
Q_x	$[tune\ units]$	0.28061	6×10^{-5}
Q_y		0.31151	2×10^{-5}
–			
–			
$\frac{\partial Q_x}{\partial \epsilon_x}$	$[10^3\mathrm{m}^{-1}]$	0.8	1
$\frac{\partial Q_y}{\partial \epsilon_x}$		-1.4	0.4
$\frac{\partial Q_x}{\partial \epsilon_y}$		-2.0	0.7
$\frac{\partial Q_y}{\partial \epsilon_y}$		2.8	1
$\frac{\partial^2 Q_x}{\partial \epsilon_x^2}$	$[10^9\mathrm{m}^{-2}]$	-18	5
$\frac{\partial^2 Q_y}{\partial \epsilon_x^2}$		6	1
$\frac{\partial^2 Q_x}{\partial \epsilon_y^2}$		11	3
$\frac{\partial^2 Q_y}{\partial \epsilon_y^2}$		-20	3
$\frac{\partial^2 Q_x}{\partial \epsilon_x \partial \epsilon_y}$		7.6	3
$\frac{\partial^2 Q_y}{\partial \epsilon_x \partial \epsilon_y}$		8	3

When measuring the detuning with amplitude of the corrected configuration the beam was kicked horizontally, vertically, and diagonally. In this case fitting to the 2D Taylor expansion, Eq.(4.4), is feasible. Tab. 4.9b presents the results of the fits to measured data for this configuration. The measured detunings are consistent with Eq.(4.7) and Eq.(4.8).

Fig. 4.8 plots $Q_{x,y}(\epsilon_x, const)$ and $Q_{x,y}(const, \epsilon_y)$ as determined from the fits described above. Results from the nominal injection setting measurement are shown in red, and results from the corrected configuration measurement are shown in blue. Uncertainties on the fit are indicated in grey. The measured tunes for the horizontal and vertical kicks are also shown, plotted against the measured $\epsilon = 2J$ of the kick in the dominant plane. The highest amplitude vertical kick during the nominal measurement is plotted in black, this is to indicate it was excluded from the fit due to a significant coupling into the opposite plane.

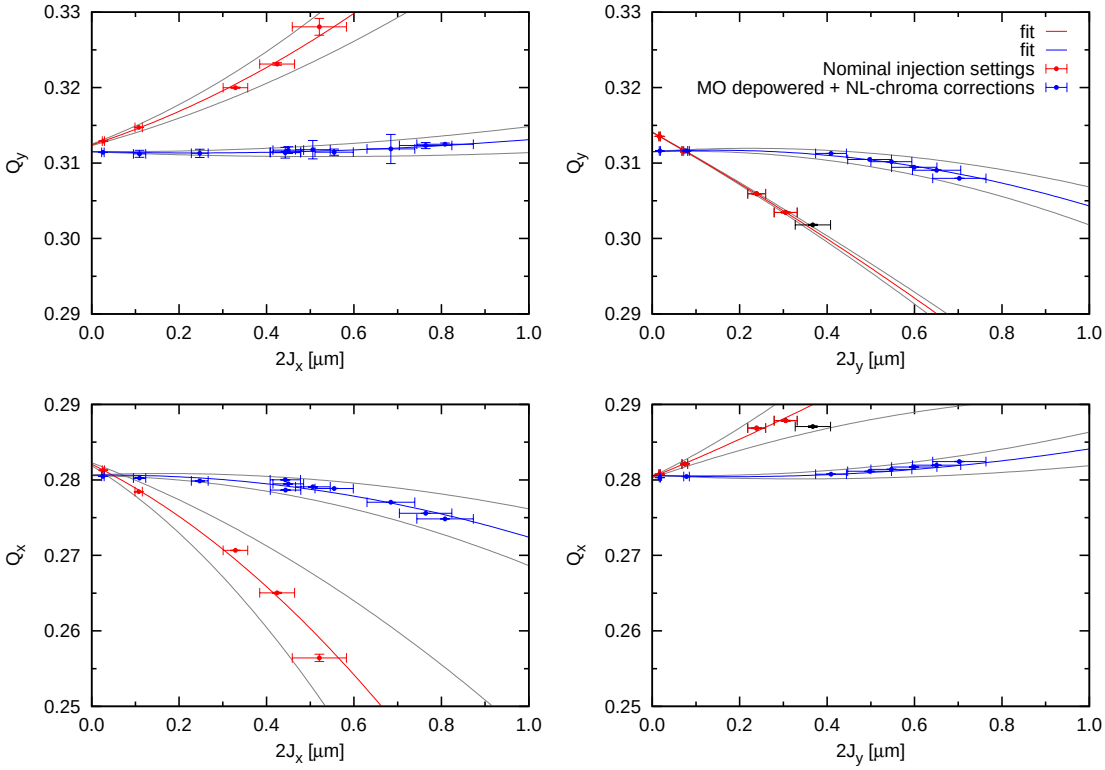

Figure 4.8: Detuning with amplitude of the LHC at nominal injection settings (red), and with Landau octupoles set to zero and additional corrections for Q'' and Q''' applied (blue). The tune is plotted against the horizontal and vertical single particle emittance of the kicks. Points shown in black represent kicks where there was substantial coupling of the kick into the opposite plane.

The amplitude detuning in the nominal case is substantial. Considering the tune shift with ϵ_x (Fig. 4.8, left), by a kick amplitude of $\sim 8.3\,\sigma_{x\,nominal}$ Q_x and Q_y are driven towards the fourth and third order resonances respectively. This is well illustrated by Fig. 4.9 which plots the turn-by-turn position and phase-space at an LHC arc BPM following the $(8.3\,\sigma_x,\ 0.6\,\sigma_y)$ kick. The three and four island structures corresponding to these resonances are evident. Regarding the approach of the tune to these resonances, it is insufficient to consider only the first order amplitude detuning. Higher order detuning terms are large, and are observed to impact significantly the detuning over the amplitude range studied, including within the $5.7\,\sigma_{\mathrm{nominal}}$ aperture defined in operation by the collimators.

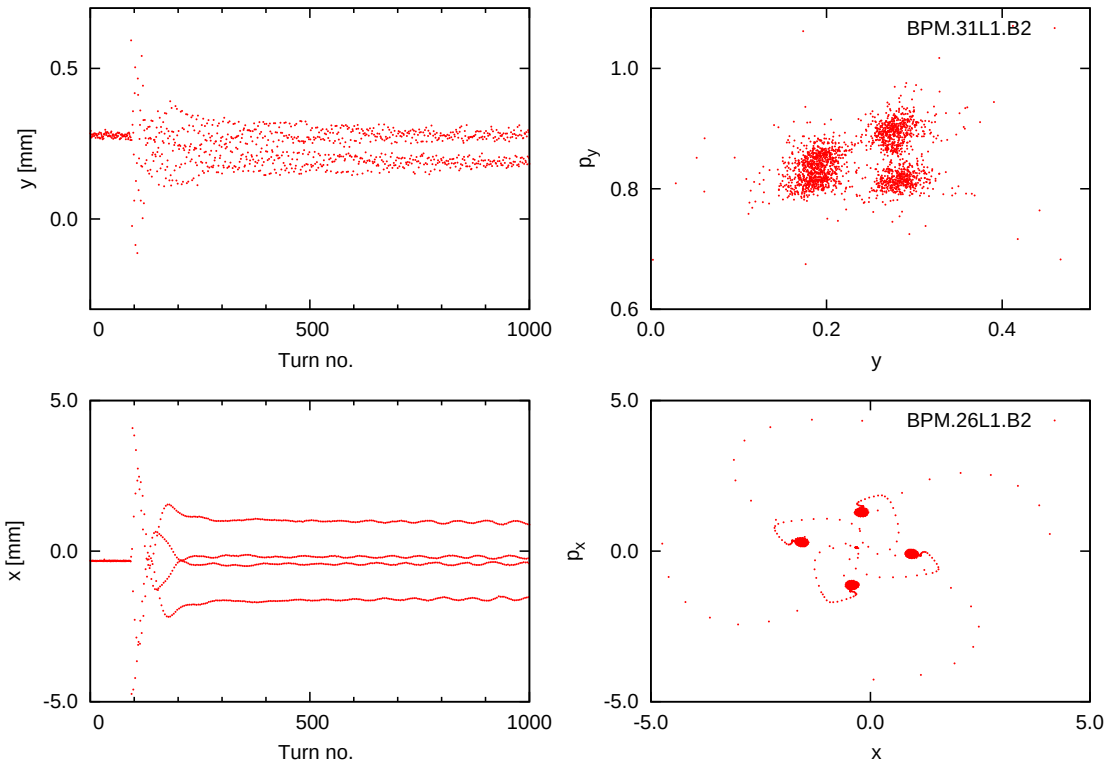

Figure 4.9: Turn-by-turn (TbT) and phase space data for a $(8.3\sigma_x, 0.6\sigma_y)$ kick with nominal LHC injection settings in the vertical plane at BPM.31L1.B2 (top), and the horizontal plane at BPM.26L1.B2 (bottom).

Regarding the tune shift with ϵ_y in the nominal case (Fig. 4.8, right, red data), the first order detuning is again substantial, but drives the tunes together. Second order detunings with ϵ_y are not so substantial as with ϵ_x, however, as will be discussed in the following section, amplitude dependent coupling plays an important role at large amplitudes in the vertical plane.

Following the depowering of the Landau octupoles to zero, and the application of corrections for the non-linear chromaticities, detuning with amplitude was significantly smaller. Magnitudes of the first order terms were reduced by factors between 10 and 30, and second order detunings with ϵ_x were reduced by factors 3 and 5. Second order detuning of Q_x with ϵ_y ($\partial^2 Q_x/\partial\epsilon_y^2$) was unaffected by the depowering of the Landau octupoles and subsequent non-linear chromaticity correction, but had been small initially. Second order detuning of Q_y with ϵ_y ($\partial^2 Q_y/\partial\epsilon_y^2$) increased by $\sim 50\%$, but had a post-correction magnitude comparable

with that of $\partial^2 Q_x/\partial\epsilon_x^2$, which had been reduced considerably. Losses upon kicking the beam were reduced and it was possible to perform kicks out to higher amplitudes than at nominal optics. No important resonances were approached within the available aperture.

Figure 4.10 displays histograms of the simulated first order detunings in the 2000 realisations of the LHC considered. The mean and standard deviations of the distribution are indicated. The $|f_{1001}|$ and the phase at the matching point substantially influenced the uncertainty in the detuning with amplitude. Uncertainties in the magnetic model accounted for $< 30\,\%$ of the quoted uncertainty. In light of the significant impact the f_{1001} resonance driving term has on the detuning, it may be important in future non-linear studies to investigate the feasibility of matching locally to a measured f_{1001}.

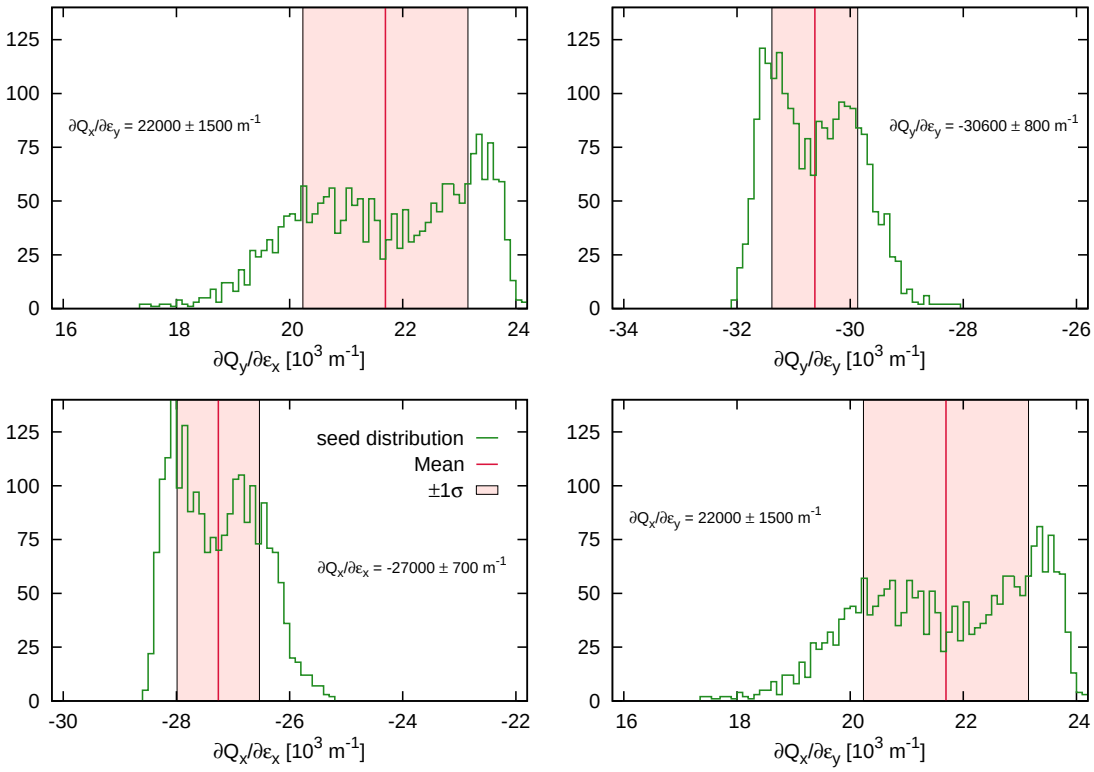

Figure 4.10: Histogram showing the distribution of first order detuning with amplitude of ~ 2000 random instances of the LHC, with $|f_{1001}|$ defined on an even distribution within the band defined by measurements of local fluctuations of the RDT around the LHC ring, and a uniform distribution in the phase of f_{1001} at the matching location. The WISE seeds were also varied randomly on a uniform distribution.

Table 4.10 compares the modelled and measured amplitude detunings. A good agreement is observed between the modelled and measured first order amplitude detuning, which may be expected given that the first order detuning at nominal injection settings is dominated by the Landau octupoles. None the less this is an important verification of the non-linear LHC model at nominal injection optics.

Table 4.10: Comparison of modelled and measured detuning with amplitude at nominal injection settings.

Detuning	[unit]	Measured	± error	Model	± error
$\frac{\partial Q_x}{\partial \epsilon_x}$	$[10^3 \mathrm{m}^{-1}]$	-29	7	-27.0	0.7
$\frac{\partial Q_y}{\partial \epsilon_x}$		19	3	22	1.5
$\frac{\partial Q_x}{\partial \epsilon_y}$		24	4	22	1.5
$\frac{\partial Q_y}{\partial \epsilon_y}$		-32.8	0.4	-30.6	0.8
$\frac{\partial^2 Q_x}{\partial \epsilon_x^2}$	$[10^9 \mathrm{m}^{-2}]$	-60	30	-14	3
$\frac{\partial^2 Q_y}{\partial \epsilon_x^2}$		34	10	17	8
$\frac{\partial^2 Q_x}{\partial \epsilon_y^2}$		11	34	-10	9
$\frac{\partial^2 Q_y}{\partial \epsilon_y^2}$		-13	3	-3	4

In contrast to the first order terms there are more substantial differences in the second order detunings. While the modelled values show a qualitatively similar behaviour to the observations, there are still considerable discrepancies with respect to the measurements. Over the amplitude range examined the discrepancies between the model and the measurement have a relevant effect, and in particular result in Q_y reaching the third order resonance at a horizontal amplitude $0.7 \pm 0.6\,\sigma_{\mathrm{nominal}}$ larger than was measured (as calculated from the mean and standard deviation values of the first and second order detuning). Likewise there is a similar effect in the approach of Q_x to the fourth order resonance. This may indicate that second order perturbations of the octupoles in the LHC are being underestimated in present models.

An attempt was not made to model the corrected configuration of the LHC only from knowledge of the machine state. Deviations from the standard hysteresis cycle of the MCO

meant their field was uncertain, and there are still unidentified sources of detuning and Q'' which could have become significant when the Landau octupoles were less strongly powered (studies of the influence of linear coupling on amplitude detuning and non-linear chromaticity with depowered MO indicated it could not explain the missing $\Delta Q''$). The corrected optics was instead simulated in MAD-X by reproducing, on-top of the nominal model, the trims applied to the MO, MCO, and MCD; and then matching settings of the octupolar elements to reproduce the measured amplitude detuning. This model was used to simulate the dynamic aperture of the corrected machine configuration, as will be described in Section 4.4.4.

As discussed in Section 4.2.2, the use of Eq.(4.5) to determine the action of applied kicks is an approximation if the phase space trajectory is distorted away from an ellipse. At the corrected configuration the small detuning with amplitude resulted in the tunes not approaching any important resonances within the amplitude range examined, and the phase space was not significantly distorted away from an ellipse. This was further verified by observing an excellent agreement of the detuning with amplitude in the matched model of the corrected configuration as determined from ptc_normal (which correctly handles non-linear distortion of phase space) and from tracking simulations using Eq.(4.5). The use of Eq.(4.5) was therefore deemed justified for study of the corrected configuration.

Having determined that Eq.(4.5) was valid for the corrected configuration, the validity to the nominal LHC optics was assessed by comparing the action of the applied MKA kicks, determined using Eq.(4.5), measured at both the nominal and corrected configurations. The MKA is known to have good magnetic reproducibilty, discrepancies between the action measured at the two configurations would therefore indicate that Eq.(4.5) is no longer reliable. In the horizontal plane a discrepancy was observed for the two highest amplitude kicks at the nominal optics, corresponding to the approach of the horizontal and vertical tunes to the fourth and third order resonances, however the discrepancy was well within the uncertainty on the measured action. In the vertical plane no significant discrepancy was observed, with the exception of the highest amplitude kick at nominal optics. This discrepancy was within the measurement uncertainty, and as has been previously discussed this kick had already been excluded from the determination of the detuning with amplitude due to the significant coupling of the vertical kick into the horizontal plane. The use of Eq.(4.5) for the studies of the nominal LHC optics described in this Chapter was therefore deemed justified.

The results presented here represent a partial, but important, verification of the non-linear model in respect of the amplitude detuning. The consistency between model and measurement is good for the first order terms, while the higher order contributions show a qualitatively similar behaviour. Amplitude ranges relevant to operation are smaller than those considered in the non-linear study presented here (collimators in operation define an aperture of $\sim 5.7\,\sigma_{\mathrm{nominal}}$).

Non-linear coupling

The linear coupling measured by the LHC BBQ [97, 99] during these studies was stable at $|C^{\pm}| \approx 0.002$ throughout the experiment ($C^{\pm}$ indicates the BBQ measures a mixture of C^{+} and C^{-}, which in the LHC is dominated by the C^{-}). This value is consistent, via Eq.(4.11), with the $|f_{1001}|$ at BPMs close to the BBQ position on the LHC ring. In parallel with the non-linear dynamics experiment, the regular injections of LHC Beam 2 required during these studies were used to demonstrate the measurement of linear coupling (as determined from f_{1001}) using injection oscillations [7]. The linear coupling RDT measurements, which were obtained by this method for every injection during the experiment, were consistent with the BBQ and kicked beam values, and showed the f_{1001} to be very stable. Linear coupling was therefore small (in the range 0.002 to 0.004) and stable throughout these measurements.

Difference linear coupling (C^{-}, driven by the f_{1001} resonance driving term) defines a closest approach of the normal mode tunes, Eq.(4.12).

$$|\delta Q_{min}| = |C^{-}| \tag{4.12}$$

On applying vertical kicks to the beam at nominal injection optics, the detuning with amplitude forced the horizontal and vertical tunes together. Figure 4.11 plots the measured (green) and the modelled (blue) tune split, $|Q_x - Q_y|$, against the action of applied vertical kicks. The modelled tune split was examined by tracking kicked particles in the non-linear model described in Section 4.4.3. The linear coupling in the model was matched to $\delta Q_{min} = 0.006$, to avoid any underestimation of the role played by linear coupling. In both modelled and measured cases the separation of the tunes appear to approach a minimum, however the

observed value, $\delta Q_{min} \sim 0.015$ $(\mathrm{Model} : \sim 0.02)$, is significantly larger than possible due to linear coupling.

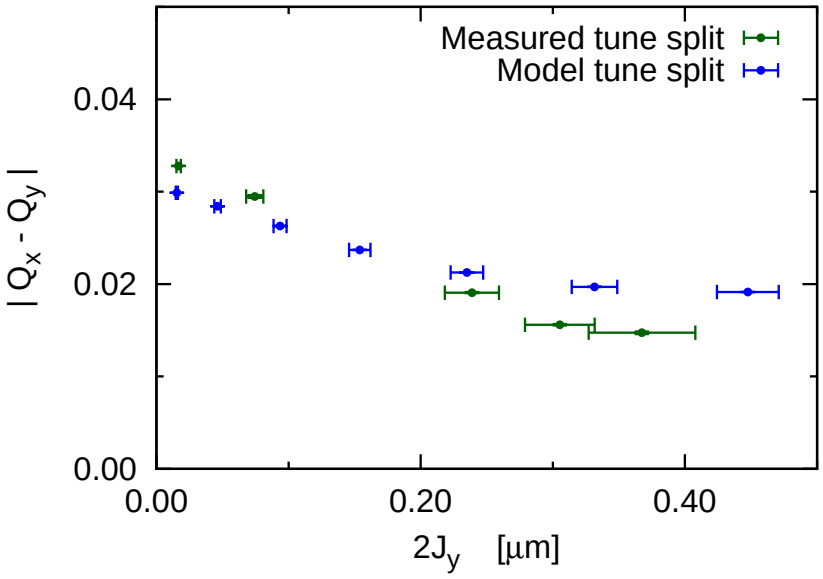

Figure 4.11: Modelled and measured variation in the tune-split with vertical kick amplitude at nominal injection optics.

Coupling between the transverse planes results in periodic emittance transfer, and hence the familiar beating of the betatron oscillations. Assuming any external excitation is kept constant in one plane, coupling may be identified by a growth of ϵ_{max} in the unkicked (or minimally kicked) plane with increasing excitation in the dominant plane. When the transverse planes are fully coupled, $\Delta = 0 \rightarrow |Q_x - Q_y| = \delta Q_{min} = |C^-|$ (where Δ is the unperturbed tune split and $|Q_x - Q_y|$ is the separation of the normal mode tunes which are measured in the machine), the emittances are completely shared and $\epsilon_{max\,x} = \epsilon_{max\,y}$. This does not violate conservation of phase space volume as the peak ϵ of one plane corresponds with the minimum ϵ of the other.

Eq.(4.5) calculates ϵ_{max}, which in the absence of coupling defines the action of the kick. Figures 4.12a and 4.12b plot ϵ_{max}, calculated using Eq.(4.5), in the (ϵ_x, ϵ_y) plane for the horizontal and vertical kicks applied during the amplitude detuning measurements. Figure 4.12a plots the results for measurements at nominal injection optics, Fig. 4.12b plots the results for measurements at the corrected optics with MO depowered to zero, and Q'' and Q''' correc-

tions applied.

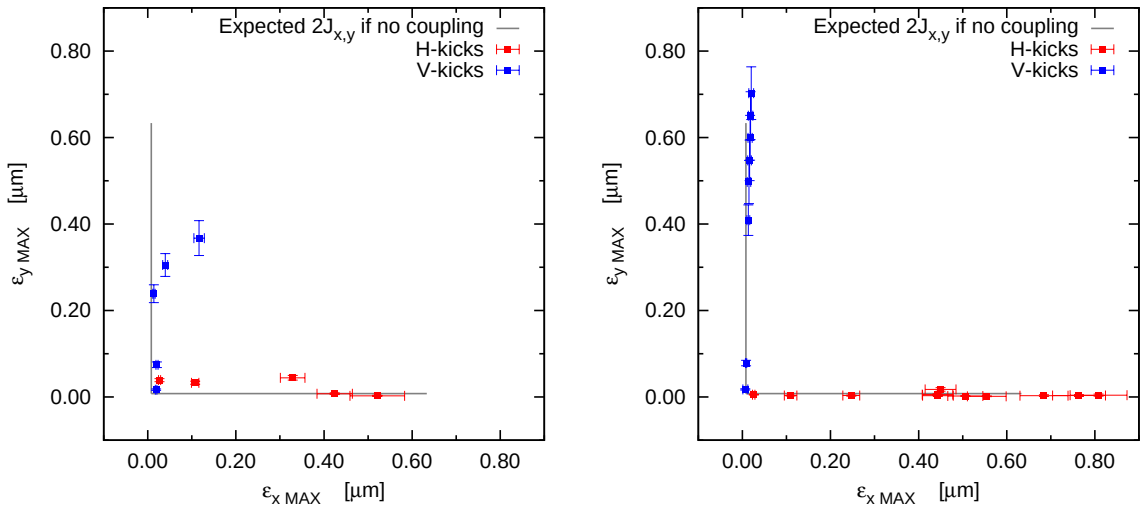

(a) Nominal injection optics.

(b) MO depowered to zero, and Q'' and Q''' corrections applied.

Figure 4.12: ϵ_{max} calculated using Eq.(4.5) for the horizontal and vertical kicks applied during amplitude detuning measurements.

Considering the vertical kicks applied at nominal injection optics, Fig. 4.12a, as vertical kick amplitude is increased there is substantial growth of $\epsilon_{x,max}$. At the largest amplitudes examined $\epsilon_{x,max}$ becomes comparable with the action of the vertical kick. This is a strong indication that the transverse planes are significantly coupled, which should not be the case when the tune split is so much greater than the linear $|C^-|$. Equivalent behaviour is not observed at the corrected optics. This rules out any systematic effect of the MKA as the source of this growth.

A similar behaviour to that observed in Fig. 4.12a is also seen in simulation. This is shown in Fig. 4.13 which compares the measured ϵ_{max} (green) with the modelled ϵ_{max} of tracked particles (red, blue). Examining the simulated tracking data it was seen that the growth of ϵ_{max} in the unkicked plane was the result of beating of the betatron oscillations between the transverse planes, and was therefore driven by transverse coupling.

Due to the rapid decoherence of large amplitude kicks at nominal injection optics, any clear beating of the measured betatron oscillations is obscured for the kicks of interest. Con-

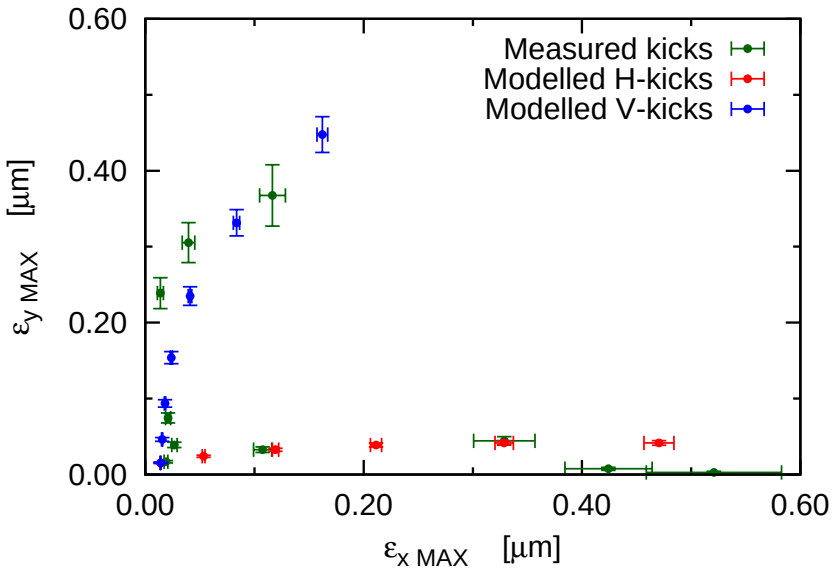

Figure 4.13: Comparison of the modelled and measured ϵ_{MAX} of kicks in the horizontal or vertical planes at nominal injection optics.

sidering Fig. 4.14 however, which displays an example of the turn-by-turn data obtained at a BPM following a large amplitude vertical kick, some important qualitative features are observable. The amplitude of the small horizontal kick is well understood, measurements at the corrected optics showing an excellent agreement with theoretical predictions at small amplitudes [7]. The amplitude of the horizontal and vertical kicks are indicated in Fig. 4.14. Following the application of the kicks the betatron oscillation amplitude in the horizontal plane shows a rounded growth then decay up to a value considerably in excess of the initial horizontal excitation. Such an observation is characteristic of emittance exchange due to coupling.

The earlier described growth of $\epsilon_{x,max}$ with vertical kick amplitude is a convincing signal of coupled motion. The qualitative features of Fig. 4.14 are additional indications. That the δQ_{min} in the model corresponds with the transverse planes becoming coupled is clear from the growth of $\epsilon_{x,max}$ with vertical kick amplitude and an associated beating of the betatron oscillations of tracked particles. This can also be demonstrated in simulation by showing that a δQ_{min} is not approached if the initial tune split is increased. This is shown in Fig. 4.15.

As has been described in this section, the linear coupling was independently measured

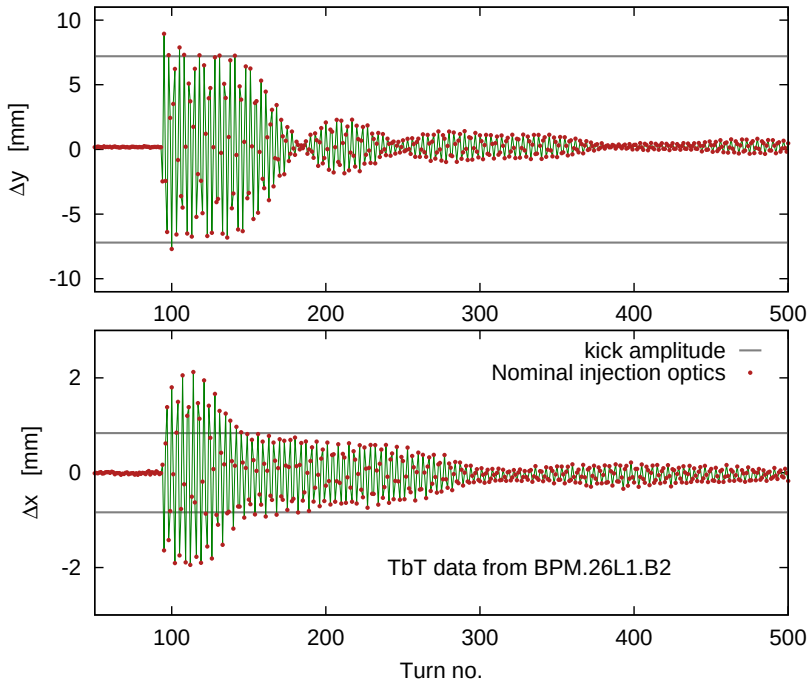

Figure 4.14: Measured TbT data from a large amplitude vertical kick at nominal injection optics.

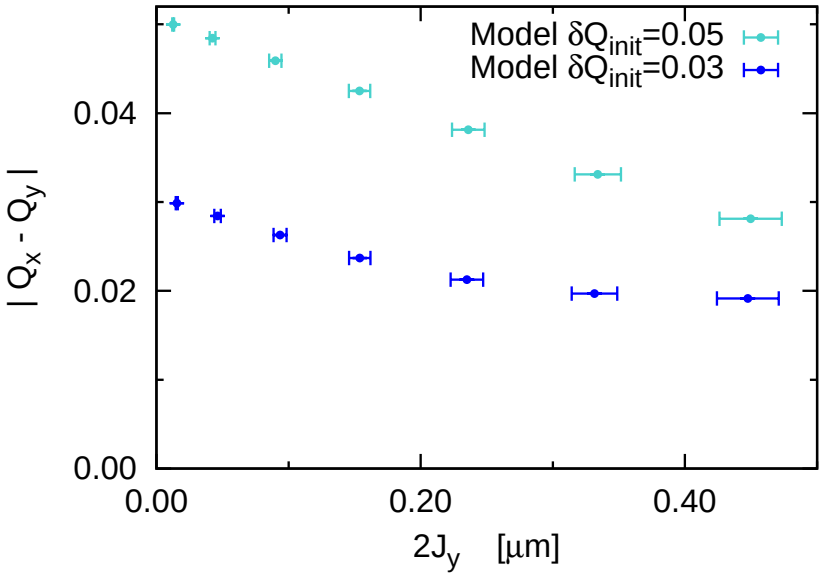

Figure 4.15: Variation of the simulated tune split ($|Q_y - Q_x|$) with the action of vertical kicks at nominal injection optics. This is shown for the nominal tune split with unkicked beams, and for an increased initial separation of the tunes.

by the LHC BBQ and by spectral analysis of low amplitude betatron oscillation data. The two measurements were consistent, and the linear $|C^-|$ was determined to be in the range 0.002 to 0.005. On kicking the beam to large vertical amplitudes, a $\delta Q_{min} = 0.015$ was approached. This δQ_{min} is significantly in excess of the linear $|C^-|$. An observed increase of the peak emittance in the horizontal plane with vertical kick amplitude, together with the qualitative features of the raw turn-by-turn data, indicate this was a δQ_{min} driven by coupling. It is concluded therefore, that an amplitude dependent (non-linear) coupling between the transverse planes of the LHC, giving rise to an amplitude dependence of the δQ_{min}, has been observed.

Similar non-linear coupling effects are reproduced in the LHC model, namely the approach to a δQ_{min} (comparable with measurement) which is significantly in excess of the known linear $|C^-|$. Growth of the peak emittance in the unkicked plane was consistent with measurements, and the beating of the betatron oscillations of tracked particles clearly identified coupling as the source of this growth. It was shown that on increasing the initial tune separation no saturation of the tune split was observed over the same amplitude range.

In light of these observations a new avenue has been opened through which the LHC dynamics may be studied. The respectable agreement between the simulated and measured non-linear coupling now allows for the use of the non-linear LHC model in the determination of the dominant sources, and further studies are underway with the aim of studying the reported effect in more detail. In the mean time however, the studies presented here represent a further validation of the understanding of the LHC non-linearities.

Dynamic aperture

As described in Section 4.2.3 it is possible to determine the distance of the beam from an aperture by examining the beam losses. If the beam is excited with a kick it is possible to obtain the amplitude of excitation using Eq.(1.40) and Eq.(4.5). Together such measurements allow a determination of the aperture. Figure 4.16 plots the surviving beam intensity $30\,\mathrm{s}$ after the application of a kick with the LHC MKA, as a function of the kick amplitude in units of $\sigma_{\mathrm{nominal}}$.

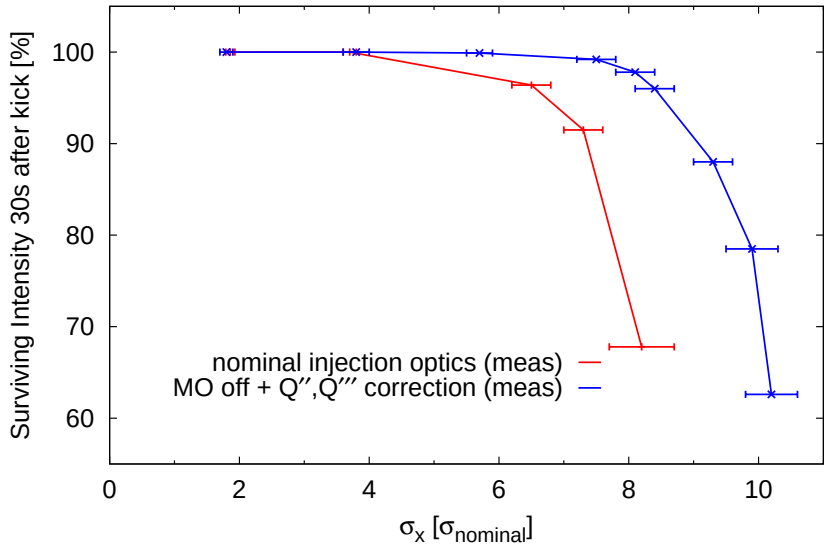

(a) Horizontal kicks

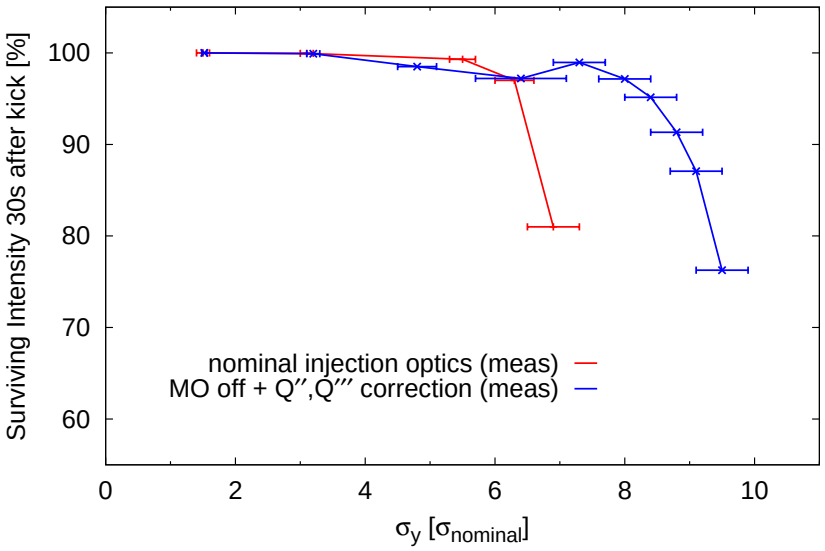

(b) Vertical kicks

Figure 4.16: Surviving beam intensity versus kick amplitude in nominal sigma, $30\,\mathrm{s}$ ($\sim 3 \times 10^5\,\mathrm{turns}$) after the kick was applied.

It is clear from the increasing losses with increasing kick amplitude that in all cases considered the beam is being driven towards an aperture. Following correction of octupolar and decapolar non-linearities (blue data in Fig. 4.16) the aperture was substantially increased. Consequently the aperture observed before correction at nominal injection optics (red data in Fig. 4.16) may confidently be identified with the dynamic aperture, and not the physical aperture defined by the collimators.

At the largest amplitudes considered by the DA measurement, imperfect correction of the BPM non-linearity, as implemented in the LHC during 2012, caused a slight underestimate of the kick amplitude [95]. An improved correction method for BPM non-linearity in the LHC has been developed for operation of the in 2015 [95]. To determine the dynamic aperture therefore, the BPM non-linearity corrections applied online at the time of the measurement were inverted in the $peak - to - peak$ data used to determine the kick amplitude (closed orbit was also taken into account), and the improved corrections applied. This increased the calculated kick amplitudes by $\sim 0.3\,\sigma_{\mathrm{nominal}}$ for the highest amplitude horizontal and vertical kicks, and by $0.5\,\sigma_{\mathrm{nominal}}$ for the highest amplitude diagonal kick.

The distance between the bunch center and the aperture was estimated in two ways. In the approximation of a Gaussian charge distribution, Eq.(4.10) was applied to the beam losses following those kicks which showed losses $\geq 20\,\%$. In most cases this was only the highest amplitude kick, however where more than one kick was used the results were very consistent (within $0.1\,\sigma_{\mathrm{nominal}}$). The beam loss due to a double Gaussian charge distribution, as measured by scraping the beams with collimators at injection in 2012 [124], was then compared with the measured loss curves of Fig. 4.16. The predicted loss curve fit well to the observations, both at nominal injection settings and after correction of non-linear sources, and agreed well with the single Gaussian method (within $0.1\,\sigma_{\mathrm{nominal}}$).

The amplitudes of the apertures corresponding to these measurements are given in Tab. 4.11. The aperture was observed to increase following correction of octupolar and decapolar non-linearities. The values before correction therefore, represent a measurement of the dynamic aperture of the LHC. The values after correction of octupolar and decapolar non-linearities are harder to interpret. In the horizontal and vertical planes the aperture after correction increased to within $\sim\ 1.1\,\sigma_{\mathrm{nominal}}$ of the applied collimator aperture

($11.6\,\sigma_{\mathrm{nominal}}$). Furthermore the collimator aperture is itself subject to uncertainties in relation to both the beta-beat and distortion of the closed orbit from the reference used to center the collimators about the beam. Losses on the collimators may therefore have contributed to the measured aperture in the horizontal and vertical planes.

Table 4.11: LHC aperture determined from beam loss and turn-by-turn betatron oscillation data.

Angle	measurement $\pm$ error	
$\arctan\left(N_{\sigma y}/N_{\sigma x}\right)$	nominal optics	corrected optics
4°	$8.8 \pm 0.7\,\sigma_{\mathrm{nominal}}$	$10.8 \pm 0.6\,\sigma_{\mathrm{nominal}}$
40°	–	$11.1 \pm 0.6\,\sigma_{\mathrm{nominal}}$
80°	$8.8 \pm 0.6\,\sigma_{\mathrm{nominal}}$	$10.5 \pm 0.6\,\sigma_{\mathrm{nominal}}$

Figure 4.17 plots the intensity of the LHC beams recorded by the beam current monitor (BCT) following the largest amplitude kicks in the horizontal, vertical, and diagonal planes at the corrected optics configuration. As described in Section 4.2.3 losses against a physical aperture usually occur over a few turns. While the $\sim 550\,\mathrm{turn}$ resolution of the BCT does not allow for an absolutely conclusive determination of the source of the observed losses as the physical aperture, the abrupt drop in intensity observed for the horizontal and vertical kicks, followed by relatively flat losses is a very strong indication that for these kicks losses occurred on a physical limitation. In contrast the losses observed for the highest amplitude diagonal kick are characteristic of loss on the dynamic aperture.

The dynamic aperture in the model of nominal injection settings described in Section 4.4.4 has been determined using SIXTRACK [43] for $3.3 \times 10^5\,\mathrm{turns}$. The simulation examined 50 angles in the (σ_x, σ_y) plane, tracking sets of 30 particles distributed in $2\,\sigma$ steps. Matching of the coupling was performed as described in Section 4.4.4. Simulations with $|C^-| = 0.002$ and $|C^-| = 0.004$ were considered, corresponding to the uncertainty arising from local variations of $|f_{1001}|$. Four phases ($0.0\,\pi$, $0.5\,\pi$, $1.0\,\pi$ and $1.5\,\pi$) of f_{1001} at the matching point were considered for each amplitude examined. The WISE seeds of magnetic errors are included automatically by SIXTRACK. A comparison of the SIXTRACK simulation to the measured dynamic aperture is shown in Fig. 4.18. The phase and amplitude of f_{1001} is seen to have a notable impact upon the simulated dynamic aperture.

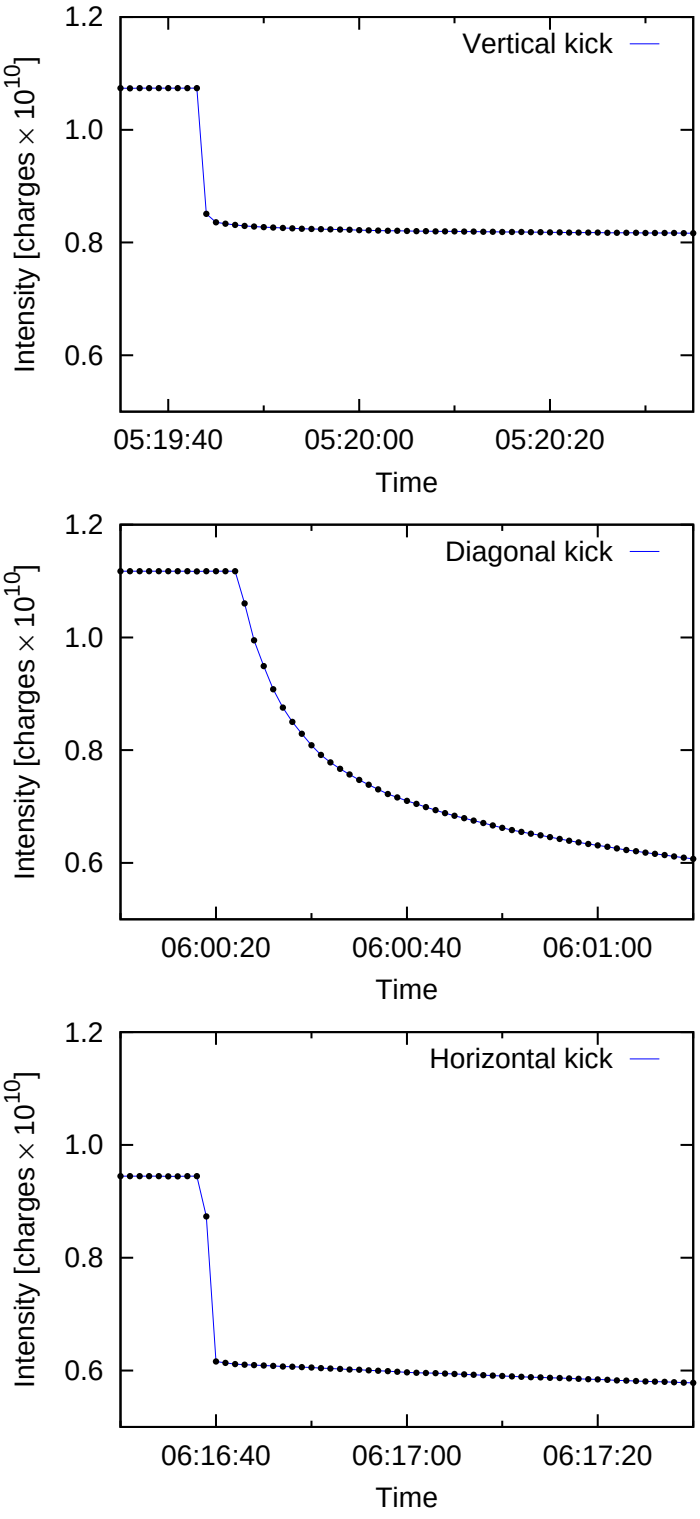

Figure 4.17: Beam intensity recorded by the LHC Beam Current Monitors following the highest amplitude kicks in the horizontal, vertical, and diagonal planes at the corrected optics configuration.

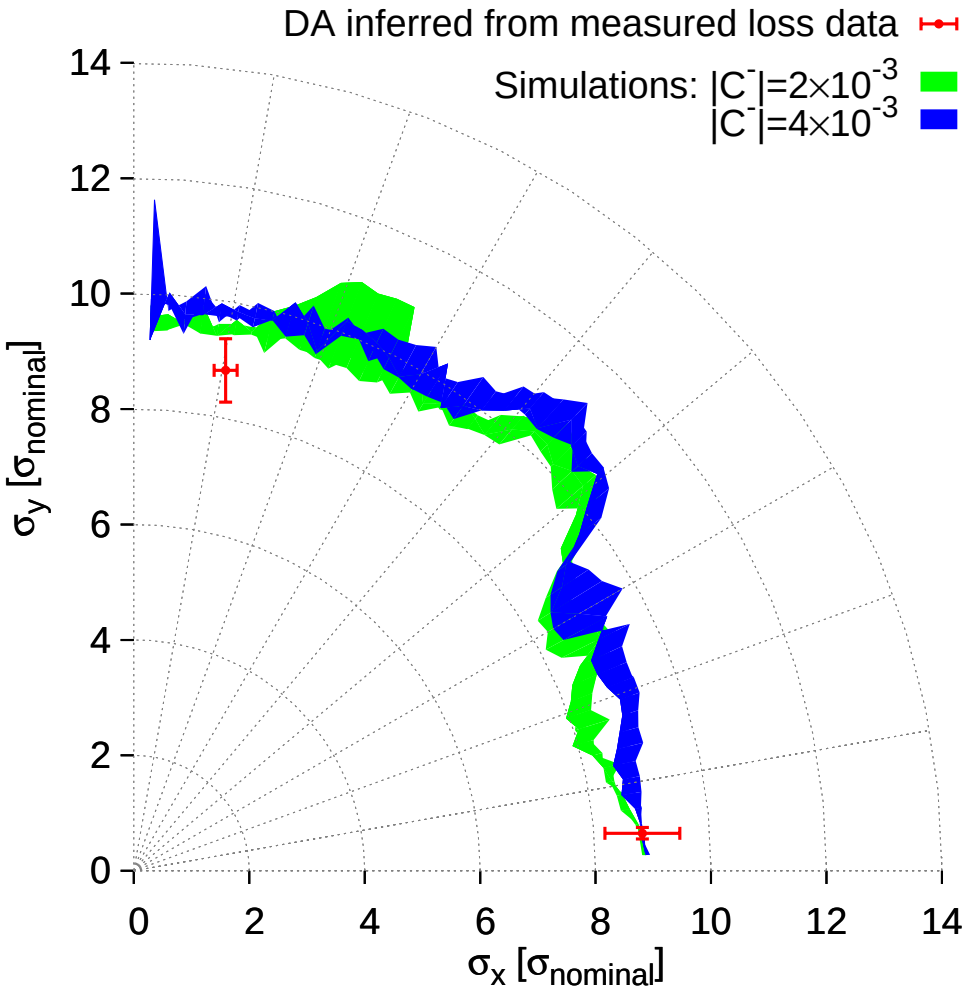

Figure 4.18: Comparison of the modelled and measured dynamic aperture at nominal injection optics in the LHC. Simulations with $|C^-| = 0.002$ and $|C^-| = 0.004$ have been considered in order to characterize the uncertainty in the DA arising from the reproduction of $|f_{1001}|$ in the model. Similarly, four phases ($0.0\,\pi$, $0.5\,\pi$, $1.0\,\pi$ and $1.5\,\pi$) of f_{1001} at the matching point were considered for each amplitude examined. The area shown for the simulated amplitudes corresponds to the maximum and minimum DA defined by the four phases.

The agreement between model and measurement is good. The measured DA in both planes agrees well inside the factor of two margin of safety ($DA_{designed}/DA_{desired} = 2$) which was specified during the LHC design phase. It is clear that to some degree the modelling of linear coupling is limiting the simulation of the non-linear dynamics, up to the level of $\sim 1.5\,\sigma_{\mathrm{nominal}}$ at certain angles. An improved method of local matching to the real f_{1001} in the machine may assist in this regard.

As described in Section 4.4.4, a MAD-X model of the corrected optics was created by matching to the measured first order detuning. Following the matching of the first order terms, the second order detuning showed a similar qualitative behaviour to the observations, but showed a $\sim 50\,\%$ deficit compared to the measured values. Dynamic aperture studies were performed on this model using SIXTRACK, the results are shown in Fig. 4.19. In Fig. 4.19 the settings of the collimators in the horizontal and vertical planes are indicated by solid orange lines. The aperture defined by the collimators in units of $\sigma_{\mathrm{nominal}}$ can be influenced by beta-beating at their location. An estimate of $\pm 0.3\,\sigma_{\mathrm{nominal}}$ is obtained for the uncertainty collimator aperture, assuming a maximum beta-beat of $5\,\%$. This is indicated in Fig. 4.19 by a patterned orange area about the collimator setting. Any distortion of the closed orbit from the reference used to center the collimators will also reduce the aperture. It has not been possible to quantify this effect, and no attempt is made to account for it in Fig. 4.19, however some departure from the reference should be expected due to the low intensity of the beams used for the DA measurement.

The simulated DA of the effective model showed an increase relative to that of the nominal machine, reflecting the observed increase in the real machine. The influence of the linear coupling on the dynamic aperture also appeared to be reduced upon reduction of the non-linearities. At $\sim 11\,\sigma$, the simulated dynamic aperture agrees well with the measured value for the diagonal kicks. In the horizontal plane it is difficult do draw meaningful conclusions: the measured aperture, simulated DA, and collimator aperture (which it should be noted does not include reduction due to closed orbit distortion away from the reference orbit) are all approximately consistent. In the vertical plane detailed conclusions regarding the validity of the matched model cannot be drawn beyond the fact that the vertical dynamic aperture is outside the aperture of the collimators, as appeared to be the case in the real machine.

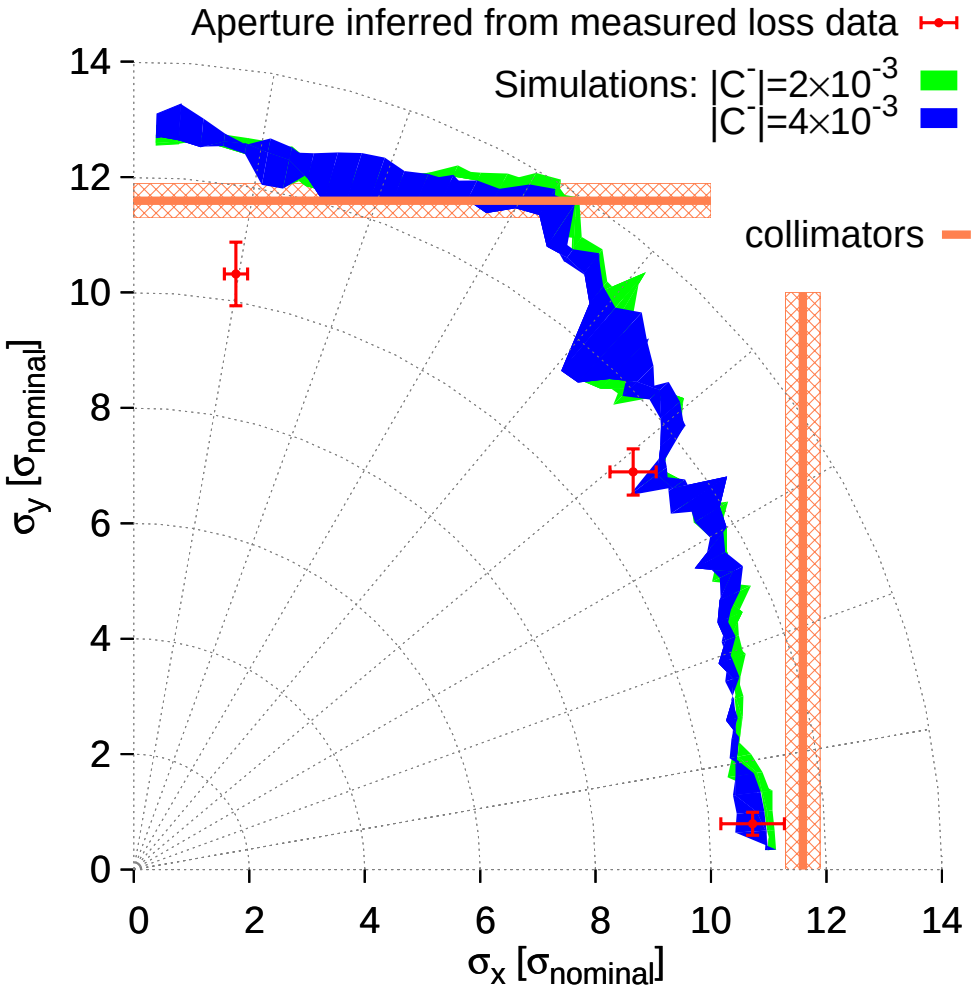

Figure 4.19: Comparison of the modelled and measured dynamic aperture, following depowering of the MO and the application of corrections for Q'' and Q'''. Simulations with $|C^-| = 0.002$ and $|C^-| = 0.004$ have been considered in order to characterize the uncertainty in the DA arising from the reproduction of $|f_{1001}|$ in the model. Similarly, four phases ($0.0\,\pi$, $0.5\,\pi$, $1.0\,\pi$ and $1.5\,\pi$) of f_{1001} at the matching point were considered for each amplitude examined. The area shown for the simulated amplitudes corresponds to the maximum and minimum DA defined by the four phases. Collimator settings are indicated by orange lines, where the patterned orange area indicates the uncertainty in collimator aperture defined by an assumed maximum beta-beat of $5\,\%$.

4.5 Application of the non-linear model to new injection optics

Observations and simulation agree well for the nominal injection settings present in the LHC during the first half of 2012. In light of this the LHC non-linear model may be extrapolated to new regimes which have not been studied directly.

During the latter half of 2012 the Landau octupole polarity in the LHC was reversed ($K_4 = +3\,\mathrm{m}^{-4}$) with respect to the settings studied in preceding sections ($K_4 = -3\,\mathrm{m}^{-4}$). Figure 4.20 plots the detuning due to first and second order terms for the original and reversed polarities. Predictions for the reversed polarity were obtained by applying the shifts in first and second order terms obtained from simulation to the values measured at the original polarity. Evidently the effects of coupling and higher order detuning are ignored in these predictions: they are intended to provide an indication of the effect MO polarity has on the first and second order detuning, rather than detailed predictions of the machine behaviour.

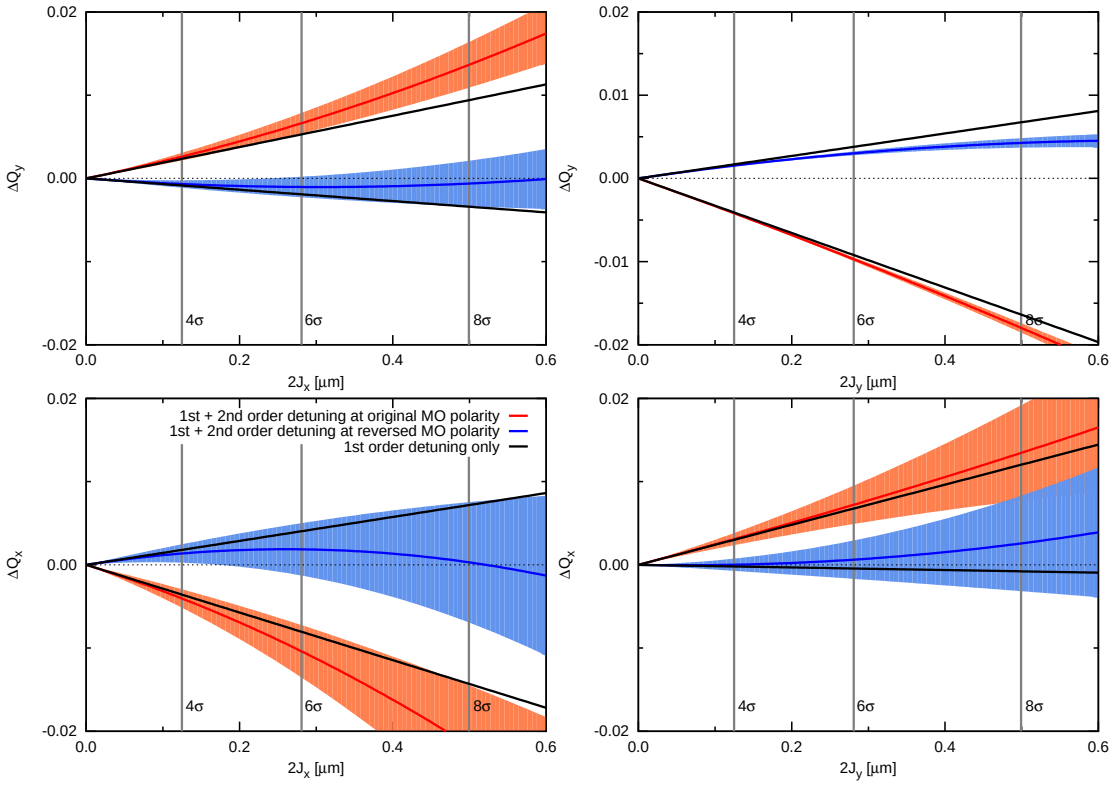

Figure 4.20: Effect of Landau octupole polarity on first and second order detuning with amplitude at injection.

At the original MO polarity present in the LHC, the detuning generated by the Landau octupoles acted in the same direction as the substantial detuning of the machine in the absence of the MOs. Perhaps more significantly the first and second order detunings also acted in the same direction. After reversal of the Landau octupole polarity the first order detuning generated by the MO acted in opposition to that of the bare machine. The first order detuning was also partially compensated by the second order terms. As a consequence the detuning with amplitude predicted for the Landau octupole polarity utilized in the latter half of 2012 operation is considerably reduced compared to that measured for the original settings.

When the LHC restarts following its first Long Shutdown (2013-2014), it is desired to shift from luminosity production with $50\,\mathrm{ns}$ bunch spacing to $25\,\mathrm{ns}$. The reduced bunch spacing may lead to the development of collective instabilities in the beam motion, and it may be necessary to increase the powering of the MO to provide additional damping. For tests of the $25\,\mathrm{ns}$ configuration, performed during the first operational run, the MO powering was increased by a factor of four, to $K_4 = 12\,\mathrm{m}^{-4}$. This is considerably in excess of previously envisioned powering scenarios for the Landau octupoles. Figure 4.21 plots the (first and second order only) amplitude detuning obtained from PTC_NORMAL for simulations with Landau octupoles set to the polarity of late 2012, but with four times higher strength.

The detuning is substantial, with both first and second order terms being increased considerably. In particular the third order resonance could be reached by $\sim 5\,\sigma_{y\,(\mathrm{nominal})}$, inside the operational aperture defined by the collimators. It may be necessary to consider whether having the third order resonance within the collimator aperture could present machine safety concerns. Also relevant is the dynamic aperture of such an optics. The DA determined for $3.3 \times 10^5\,\mathrm{turns}$ ($\sim 30\,\mathrm{s}$) in SIXTRACK is plotted in Fig. 4.22. A coupling range of $0.5 \times 10^{-3} \leq |C^-| \leq 6 \times 10^{-3}$ was considered, representing a realistic range of possible values at injection.

The modelled DA is considerably reduced from that obtained for simulations of the early 2012 optics. At $3.3 \times 10^5\,\mathrm{turns}$ the predicted dynamic aperture at injection is comparable with the operational aperture ($\sim 5.8\,\sigma_{\mathrm{nominal}}$) of the collimators for most angles. Also of concern is that the chaotic boundary identified by SIXTRACK was particularly small: generally between $1\,\sigma_{\mathrm{nominal}}$ and $4\,\sigma_{\mathrm{nominal}}$ dependent on angle, coupling, and seed. In some cases

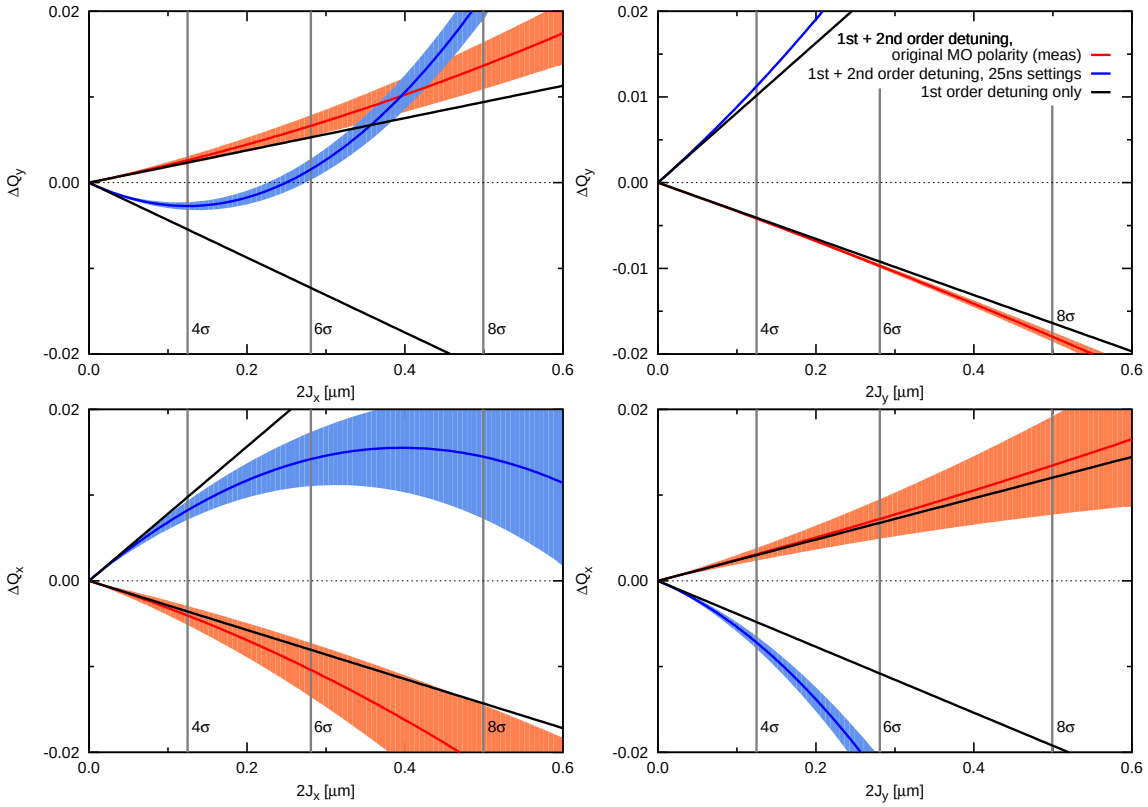

Figure 4.21: Simulated detuning with amplitude (first and second order) for the Landau octupole settings proposed for $25\,\mathrm{ns}$ operation of the LHC.

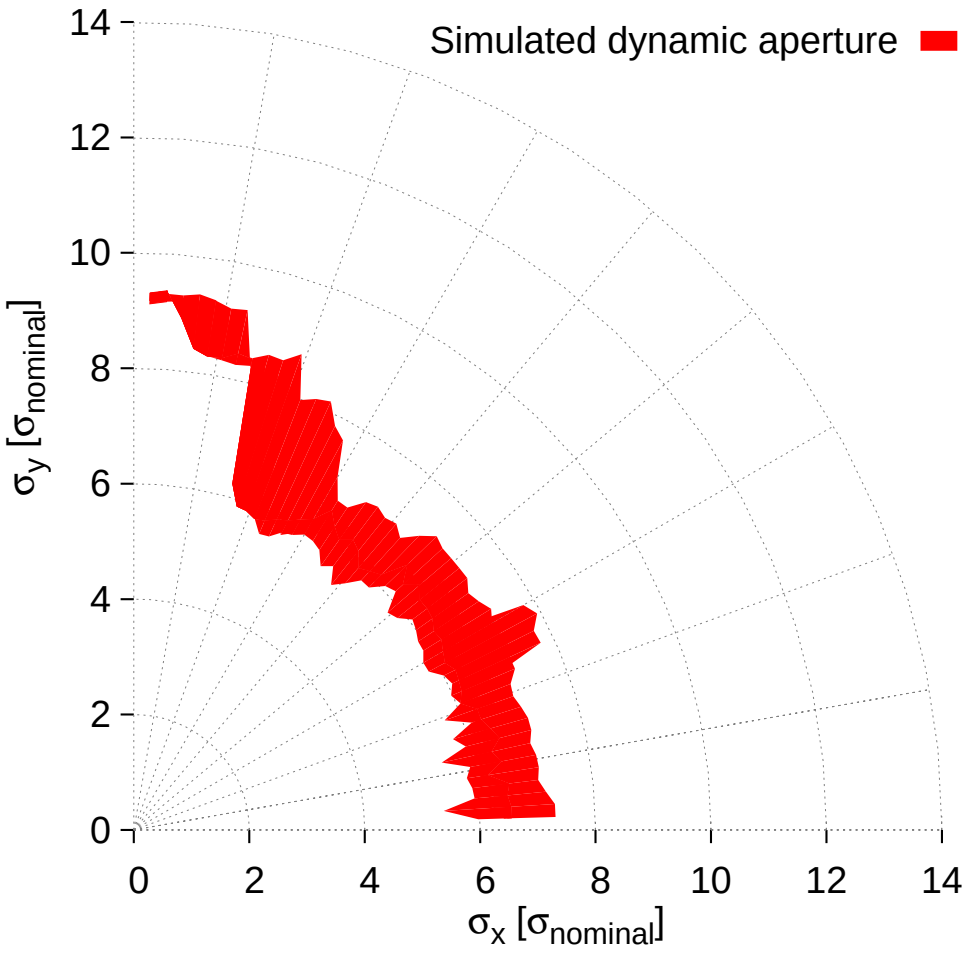

Figure 4.22: Simulated dynamic aperture after 3.3×10^5 turns (~ 30 s) for the Landau octupole powering applied during tests of operation with 25 ns bunch spacing ($K_4 = 12\,\mathrm{m}^{-4}$). A coupling range of $0.5 \times 10^{-3} \leq |C^-| \leq 6 \times 10^{-3}$ was considered.

however, SIXTRACK identified the smallest amplitude tracked particles (corresponding to $\sim 0.1\,\sigma_{\mathrm{nominal}}$) as following chaotic orbits. Over long periods of time it is possible that the dynamic aperture will decrease towards the chaotic boundary [41, 42]. Given the results of these simulations this could indicate the potential for beam loss if the DA becomes comparable with the beam size, and may warrant further study.

4.6 Conclusions

Measurements of several non-linear observables have been performed in the LHC at injection. The results have been compared to simulation allowing for an assessment of the understanding of the non-linear transverse dynamics of the machine.

Initial investigations were made of the non-linear dynamics through study of higher order chromaticity. Measurements revealed large second and third order chromaticities at injection optics with depowered Landau octupoles. Substantial discrepancies were seen in the simulated non-linear chromaticity with respect to these observations. It was determined that hysteresis of the octupolar spool piece magnets was a significant contribution to this discrepancy. Constraints were placed on any systematic misalignment of the decapolar spool pieces with respect to the main arc dipoles. A notable discrepancy remained in the Q''_x of the LHC model compared to the measured values. Beam-based correction of second and third order chromaticity was demonstrated, and was observed to reduce first order detuning with amplitude and the decoherence of kicked beams. Measurement of non-linear chromaticity with Landau octupoles powered to their nominal settings indicated the MO behaved as expected.

Detailed measurements of the non-linear observables were performed using kicked beams at nominal injection optics in 2012. It was found that first order amplitude detuning was large, but agreed well with the modelled values. Second order amplitude detuning was also measured in the LHC for the first time. While the simulated second order detunings showed a qualitatively similar behaviour to the measurements, there were significant deficits. At the highest amplitudes examined this resulted in a delayed approach of the model to the third and fourth order resonances. These discrepancies are smaller, but still relevant, within the aperture defined by the collimators in operation. Further studies will be required to improve the understanding of these higher order effects. Following measurements at nominal injection

optics, Landau octupoles were depowered and corrections for the non-linear chromaticities (found in 2011) were applied. Significant reductions in the amplitude detuning were observed, which led to improved decoherence of kicked beams. It should be highlighted that the validity a year later of non-linear dynamics corrections found in 2011 is a significant demonstration of the stability of the non-linear dynamics in the LHC.

During measurements of the detuning with vertical amplitude performed at nominal injection optics, a substantial coupling of the large amplitude vertical kicks into the horizontal plane was observed. This corresponded with the tune split approaching a δQ_{min} which was considerably in excess of the linear $|C^-|$. It has been concluded that an amplitude dependent non-linear coupling was observed. The approach to the δQ_{min} and the coupling of vertical kicks into the horizontal plane are reproduced in the model, representing a further verification of the understanding of the non-linear dynamics in the LHC. The non-linear coupling in the LHC optics is now an area of growing interest. As a consequence of the observations presented in this Chapter, further theoretical and simulation studies are being performed in order to better understand the effect, and identify the dominant sources in the LHC.

The dynamic aperture at nominal injection optics was measured. Agreement with the model was good in both planes, particularly in the horizontal. The measured and simulated dynamic aperture agreed well within the safety margin specified in the LHC design phase. It was shown that through a minimization of readily observed non-linear parameters it is possible to increase the dynamic aperture in the LHC.

These observations validate many aspects of the LHC non-linear model at nominal injection optics, in particular: the first order detuning, the non-linear coupling, and the dynamic aperture. Some areas have been highlighted as requiring further study however, notably the higher order terms in the amplitude detuning, and the requirement for a better linear coupling model. Observation of the non-linear coupling, and its reproduction in the model, have opened the door to more detailed studies of this phenomenon. The ability to control the non-linear transverse dynamics has been well established by the manipulations performed during this experiment. Most notably the demonstration of dynamic aperture correction in the LHC is an important step forwards. These are promising results for the future exploitation of the LHC.

Chapter 5

The tune, linear coupling and first order chromaticity dependence of the LHC on Landau octupole powering

During regular operation of the LHC the Landau octupoles are strongly powered and play a significant role in the damping of instabilities in the beam motion. It is important therefore that the dynamics introduced by the Landau octupoles are well understood. During the 2012 LHC run however, several observations were made at top energy, $4\,\mathrm{TeV}$, which demonstrated a dependence of the tune, linear coupling and first order chromaticity upon Landau octupole powering. The observed shifts in these properties upon changes in Landau octupole powering were larger than might reasonably have been expected, and were not reproduced in the best LHC models.

Understanding the dependence of first order chromaticity was of particular importance, as it can significantly influence the growth of instabilities in the beam motion. The ability to reproduce and predict these features of the beam dynamics in simulation was an important goal in improving the accuracy of the LHC model, and in expanding its applicability. In this chapter the observations of the relationship between Q, Q', $|C^-|$ and the Landau octupole powering are analysed, leading to an understanding of the effect.

5.1 Introduction

Over the course of the 2012 LHC run observations were made at top energy ($4\,\mathrm{TeV}$) of significant shifts in the tune ($Q_{x,y}$), linear coupling ($|C^-|$), and first order chromaticity ($Q'_{x,y}$), which appeared to be correlated to changes in the Landau octupole (MO) powering.

Understanding the source of these apparent dependencies on MO powering is important for anticipating shifts in the fundamental beam properties, for correction of the effect, and for the identification of artifacts in the measurements. The incorporation of these features of the dynamics into the LHC model is significant both for its accuracy and its applicability.

The influence of the Landau octupoles on first order chromaticity is of particular importance. The Landau octupoles in the LHC are intended for the damping of instabilities in the beam motion through the introduction of amplitude dependent detuning, however first order chromaticity also plays a significant role in the suppression of the head-tail instability. If the powering of the Landau octupoles, intended for the damping of instability, causes the first order chromaticity to become either negative, or large and positive, then the beam may become unstable. An analysis of the first order chromaticity dependence on Landau octupole powering was therefore an important complement to study of the amplitude detuning. In contrast the tune dependence is too small to be of serious concern for operation. Together with the first order chromaticity shifts and the peculiar observations of the coupling however, they represent an unanticipated behaviour of the LHC which warranted further investigation.

This chapter is concerned with understanding the influence of Landau octupole powering on the tune, linear coupling and first order chromaticity. Section 5.2 begins by presenting observations of shifts to these properties which were correlated with changes in the Landau octupole powering. Section 5.3 then discusses analysis of the available data together with the effort to reproduce the effect in the LHC model, finally arriving at an understanding of the influence of the Landau octupoles on these beam properties. Section 5.4 details a simple analytical description of the chromaticity variation which may be useful in circumstances where simulation is impractical.

Throughout this chapter the use of *'chromaticity'* may be taken as referring to the first order chromaticity, Q'. Similarly *'coupling'* refers to the linear coupling.

5.2 Observations of tune, linear coupling, and first order chromaticity variations with Landau octupole powering

The analysis described in this Chapter is based on observations made during four beam dynamics experiments which are described briefly in sections 5.2.1 to 5.2.4. The measured shifts to tune, chromaticity, and coupling, which were correlated with changes in Landau octupole powering, are summarized in section 5.2.5.

Measurements of tune, chromaticity, and coupling were performed using the LHC BBQ system. During all measurements the focusing (MOF) and defocusing (MOD) Landau octupoles in all arcs were trimmed simultaneously. In order to consistently characterize the Landau octupole powering, the current in the Arc12 MOD ($I_{MOD:a12}$) has been used throughout this chapter. With the exception of observations presented in Section 5.2.3 the data presented was not the result of dedicated measurements, but was obtained parasitically.

5.2.1 Initial observation of tune and linear coupling dependence on Landau octupole powering

Variations of the tune and linear coupling with Landau octupole powering were first observed parasitically during measurements of the LHC aperture. Upon depowering the MO from $I_{MOD:a12} = 450\,\mathrm{A}$ to $50\,\mathrm{A}$ shifts to the coupling (Fig. 5.1) and tune (Fig. 5.2) were noticed in data obtained from the LHC BBQ.

A clear decrease in the coupling measured by the BBQ was observed for both beams. The change in $|C^-|$ was significant ($> 2 \times 10^{-3}$) on the scale relevant to typical LHC operation, and well outside the amplitude of noise on the measurement. The change in $|C^-|$ was clearly associated with the depowering of the Landau octupoles, and demonstrated plateaus coinciding with breaks in the ramping of the MO current. This was indicative of an influence of the Landau octupole powering on the LHC linear coupling (as measured by the BBQ system) which could potentially be relevant for operation.

The raw tune signal was extremely noisy, but improved as the MO powering was decreased. Small positive tune shifts were seen in both planes for both beams, with the shift becoming more apparent in the final MO trim (from $I_{MOD:a12} \sim 200\,\mathrm{A}$ to $50\,\mathrm{A}$) as the noise

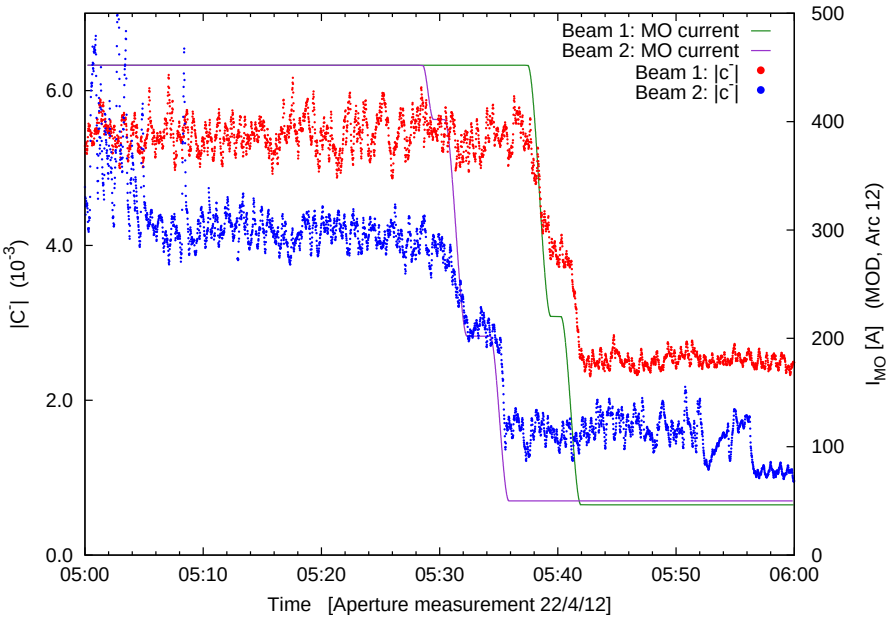

Figure 5.1: Coupling logged by the BBQ system while depowering the Landau octupoles during measurement of the LHC aperture. Landau octupole powering is also displayed.

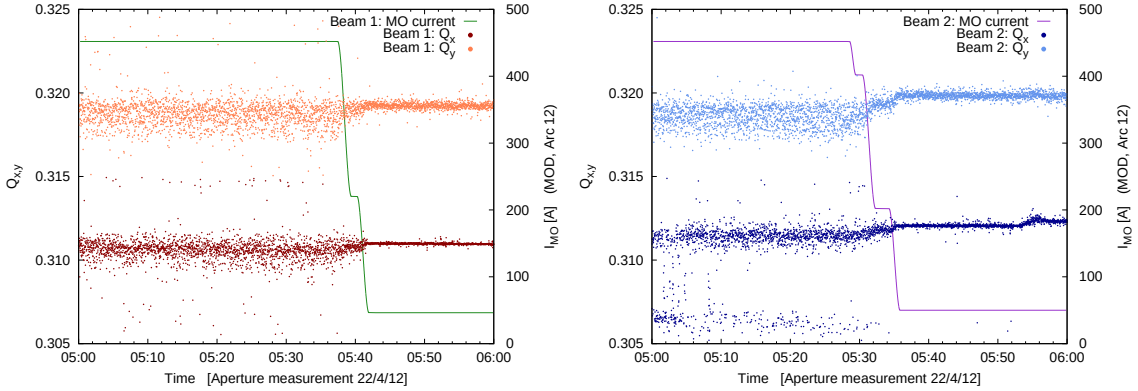

(a) Beam 1 **(b)** Beam 2

Figure 5.2: Tunes logged by the BBQ system while depowering the Landau octupoles during measurement of the LHC aperture. Landau octupole powering is also displayed.

decreased. It should also be highlighted that in the horizontal plane of Beam 2 (Fig. 5.2b, dark blue data) the BBQ regularly misidentified the tune with a peak at around 0.306 in the horizontal spectrum while the octupoles were powered, the source of which is unknown.

Towards the end of the aperture measurement the Landau octupoles were re-powered to their nominal currents and corresponding shifts in the coupling and tunes from the BBQ were observed. The changes in coupling and tune were approximately equivalent to those observed upon the depowering of the MO, and are shown in Fig. 5.3 and Fig. 5.4 respectively. It should be noted that on re-powering of the MO, the Beam 2 Q_x was again misidentified with the spectral line at 0.306.

The tune and coupling shifts corresponding to these two changes of MO powering have been combined and are presented in Tab. 5.1 in Section 5.2.5

5.2.2 Confirmation of BBQ observations from commissioning data, and analysis of linear coupling RDTs

Following the initial observations of a tune and coupling dependence on MO powering, old optics commissioning data [129] was re-analysed in an attempt to verify the results.

Optics measurements of the LHC are usually performed by exciting coherent betatron oscillations using the LHC AC-dipoles. By performing spectral analysis on the betatron oscillations during the AC-dipole flattop it is possible to determine resonance driving terms (RDTs) of the motion [57]. The RDT corresponding to linear $|C^-|$ is f_{1001}, and was introduced in Section 1.4.6. The coupling coefficient and RDT are approximately related by Eq.(5.1) [27], where $\overline{|f_{1001}|}$ is the mean amplitude of f_{1001} around the LHC ring.

$$|C^-| \approx 4|(Q_x - Q_y)|\overline{|f_{1001}|} \tag{5.1}$$

Initial observations (presented in the preceding section) of a shift in linear coupling dependent on Landau octupole powering were based on changes in the $|C^-|$ recorded by the LHC BBQ. The f_{1001} is a more robust quantity for study than $|C^-|$ as determined by the BBQ (which only describes the coupling at a single location - IP4 - and must utilize only

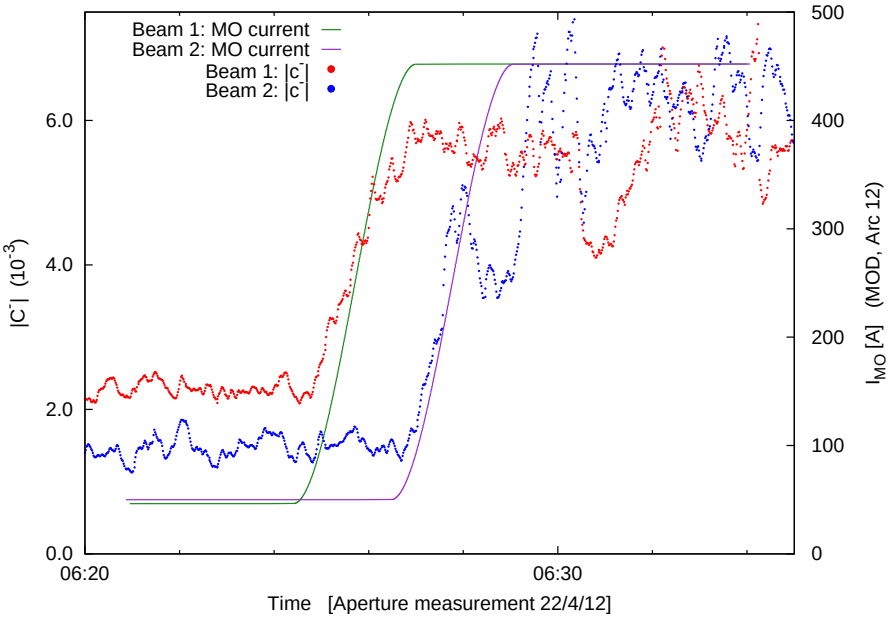

Figure 5.3: Coupling logged by the BBQ system while re-powering the Landau octupoles during measurement of the LHC aperture. Landau octupole powering is also displayed.

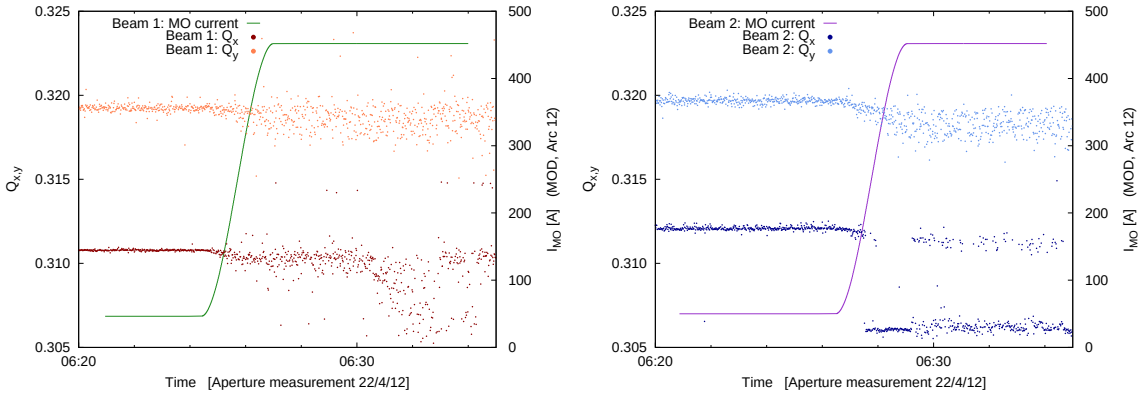

(a) Beam 1 **(b)** Beam 2

Figure 5.4: Tunes logged by the BBQ system while re-powering the Landau octupoles during measurement of the LHC aperture. Landau octupole powering is also displayed.

the real part of the turn-by-turn signal, as opposed to the complex signal used to find f_{1001}). Conversely, the necessity of using the AC-dipole to excite large amplitude betatron oscillations limits the applicability of such an analysis to dedicated studies. Typically during optics measurement and correction (OMC) studies with the AC-dipole the Landau octupoles are powered at zero or low current.

During a single session of the $\beta^* = 0.6\,\mathrm{m}$ commissioning however, optics measurements with the AC-dipole were performed with MO at nominal settings (at the time $I_{MOD:a12} = 250\,\mathrm{A}$), prior to their depowering for the main series of optics studies. This enabled a measurement of how the $|f_{1001}|$ varied with the MO powering, and a comparison to measurements of the coupling made using the LHC BBQ system.

Figures 5.5 and 5.6 show the coupling and tune data logged by the BBQ while the Landau octupoles were trimmed to zero. As in Section 5.2.1 the tune data of both planes in both beams demonstrated a small positive shift, coinciding with the depowering of the Landau octupoles. Regarding the coupling measured by the BBQ, the Beam 2 measurement is so noisy prior to the MO being depowered that it is difficult to make any definitive statement regarding a change in $|C^-|$. In Beam 1 however, there is again a correlation observed between the Landau octupole depowering and a reduction in $|C^-|$ as measured by the BBQ. The reduction was significantly smaller than seen in Fig. 5.1 and Fig. 5.3, going from $\sim 1 \times 10^{-3}$ to $\sim 0.5 \times 10^{-3}$, but still visible (it should be noted that the change in MO powering was also much smaller than that considered in the previous section). These observations would appear to validate the observation of coupling and tune shifts presented in the previous section, and imply the shifts directly relate to the MO powering rather than any coincidental shift during in the initial observation.

An analysis of the coupling RDTs however, raises some puzzling issues. Figures 5.7 and 5.8 show the $|f_{1001}|$ and $|f_{1010}|$ obtained from spectral analysis of turn-by-turn (TbT) BPM data for AC dipole kicks performed before (blue) and after (red) the depowering of the MO. Plots on the left of Fig. 5.7 and Fig. 5.8 show the coupling RDTs measured around the LHC ring, while plots on the right are histograms of the values measured in the BPMs. It is apparent from the histograms for Beam 1 (Fig. 5.7 right) that there has been no significant change to the linear coupling RDTs. A change to the linear coupling of the magnitude seen

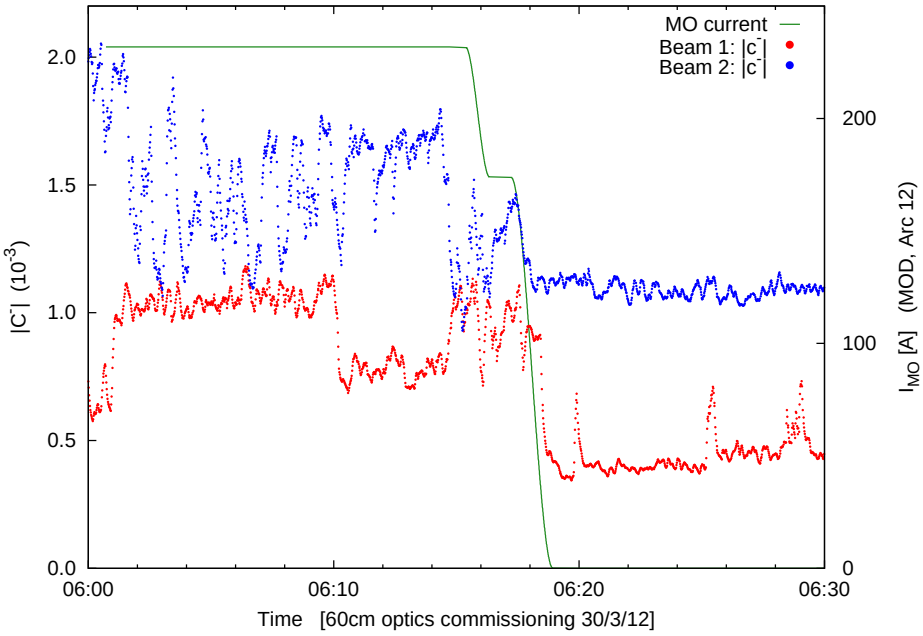

Figure 5.5: Coupling logged by the LHC BBQ system during $0.6\,\mathrm{m}$ optics commissioning studies. Landau octupole powering is also displayed.

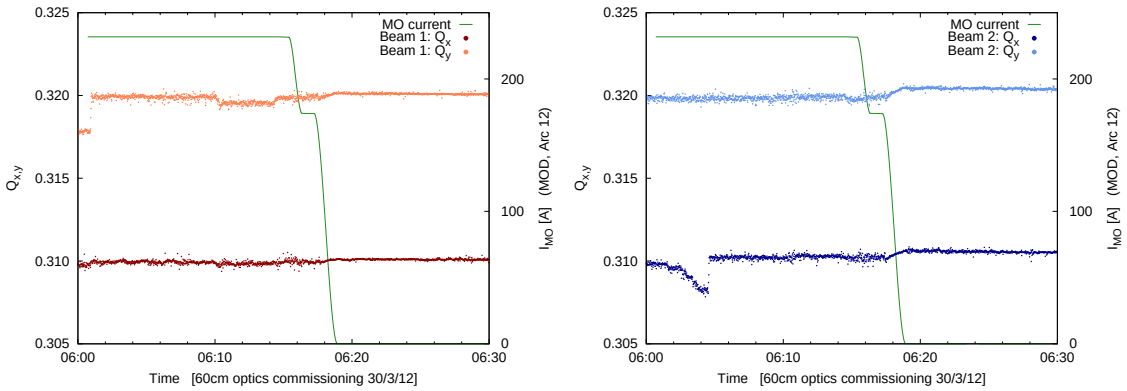

(a) Beam 1 **(b)** Beam 2

Figure 5.6: Tunes logged by the LHC BBQ system during $0.6\,\mathrm{m}$ optics commissioning studies. Landau octupole powering is displayed.

in the BBQ data ($> 2 \times 10^{-4}$) should be clearly visible as a shift in the RDTs, this is not observed in the Beam 1 data. In the analysis of Beam 2 we do see a small reduction in the $|f_{1001}|$, though this includes a non-negligible contribution from the change in the tune split. Given the poor quality of the Beam 2 BBQ data, a definite statement cannot be made regarding the agreement of Beam 2 resonance driving term and BBQ measurements of the linear coupling. RDT and BBQ measurements for the coupling in Beam 1 however, are in contradiction.

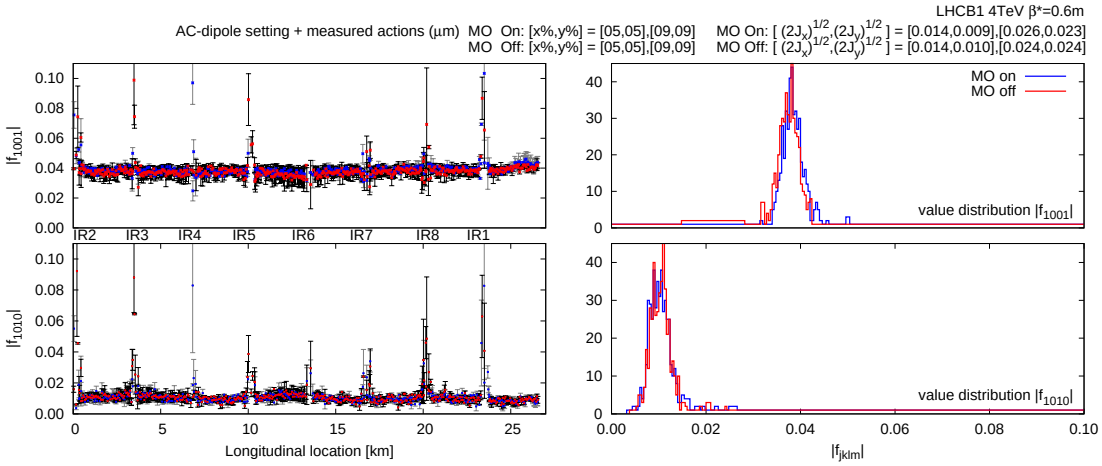

Figure 5.7: Comparison of Beam 1 $|f_{1001}|$ and $|f_{1010}|$ before/after MOs depowered during $0.6\,\mathrm{m}$ optics commissioning studies.

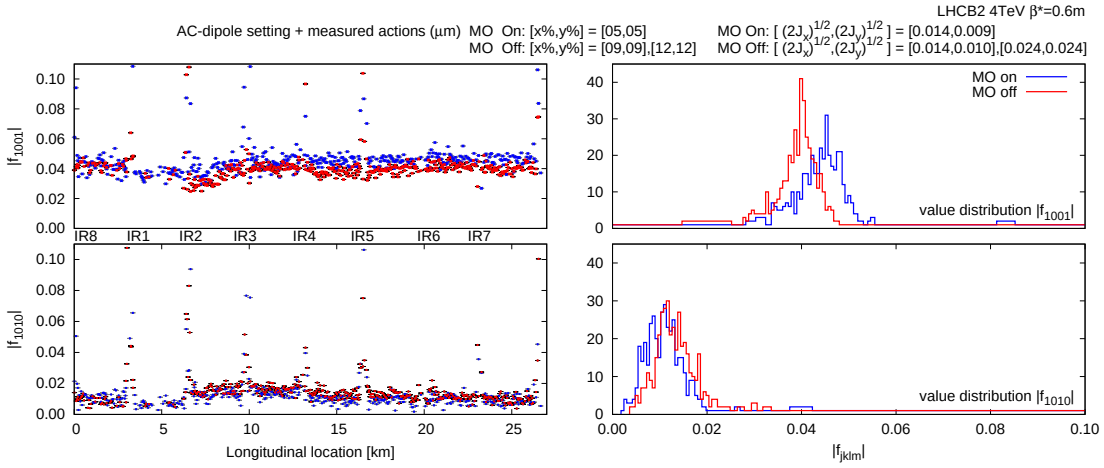

Figure 5.8: Comparison of Beam 2 $|f_{1001}|$ and $|f_{1010}|$ before/after MOs depowered during $0.6\,\mathrm{m}$ optics commissioning studies.

5.2.3 Measurement of first order chromaticity with Landau octupole powering

The observations of tune and coupling variations with Landau octupole powering presented in the preceding sections were obtained parasitically. While data regarding the tune and $|C^-|$ may be obtained in this way, observations of the chromaticity generally require dedicated studies. Such dedicated measurements of the variation of Q' with Landau octupole powering were performed during studies of the instability threshold for octupole powering [130, 131]. Both beams were studied at Flattop. Data was also obtained for Beam 1 at $\beta^* = 0.6\,\mathrm{m}$. During the Flattop measurement both beams became very briefly unstable, most noticeably in the vertical plane, when the Landau octupoles were trimmed from $I_{MOD:a12} \sim 80\,[\mathrm{A}]$ to zero, but recovered when the Landau octupoles were re-powered.

A substantial first order chromaticity change, of the order of six units in the horizontal plane and two units in the vertical, was observed upon depowering the MO from $I_{MOD:a12} = 450\,\mathrm{A}$ to $0\,\mathrm{A}$. This is shown at Flattop for Beam 1 and Beam 2 in Fig. 5.9 and Fig. 5.10 respectively, and for Beam 1 at $\beta^* = 0.6\,\mathrm{m}$ in Fig. 5.11. The shifts in Q' were clearly associated with trims of the MO, and substantial enough to be of significant concern for LHC operation.

Coupling shifts correlated to the change in MO powering were once more observed in the BBQ data. These are shown in Fig. 5.12 (Flattop) and Fig. 5.13 ($\beta^* = 0.6\,\mathrm{m}$). The coupling shifts were several times larger than the noise on the BBQ measurement. Tune data (Fig. 5.14 and 5.15) recorded by the BBQ also showed small positive shifts in both planes of both beams, consistent with previous observations.

5.2.4 Measurements of tune and linear coupling with reversed Landau octupole polarity

The data presented in the preceding sections was all obtained for the same polarity of the Landau octupoles. The low quality of the coupling measurements obtained during $0.6\,\mathrm{m}$ commissioning, and presented in Section 5.2.2, also made a comparison of the BBQ and RDT measurements difficult. In this section observations with reversed Landau octupole

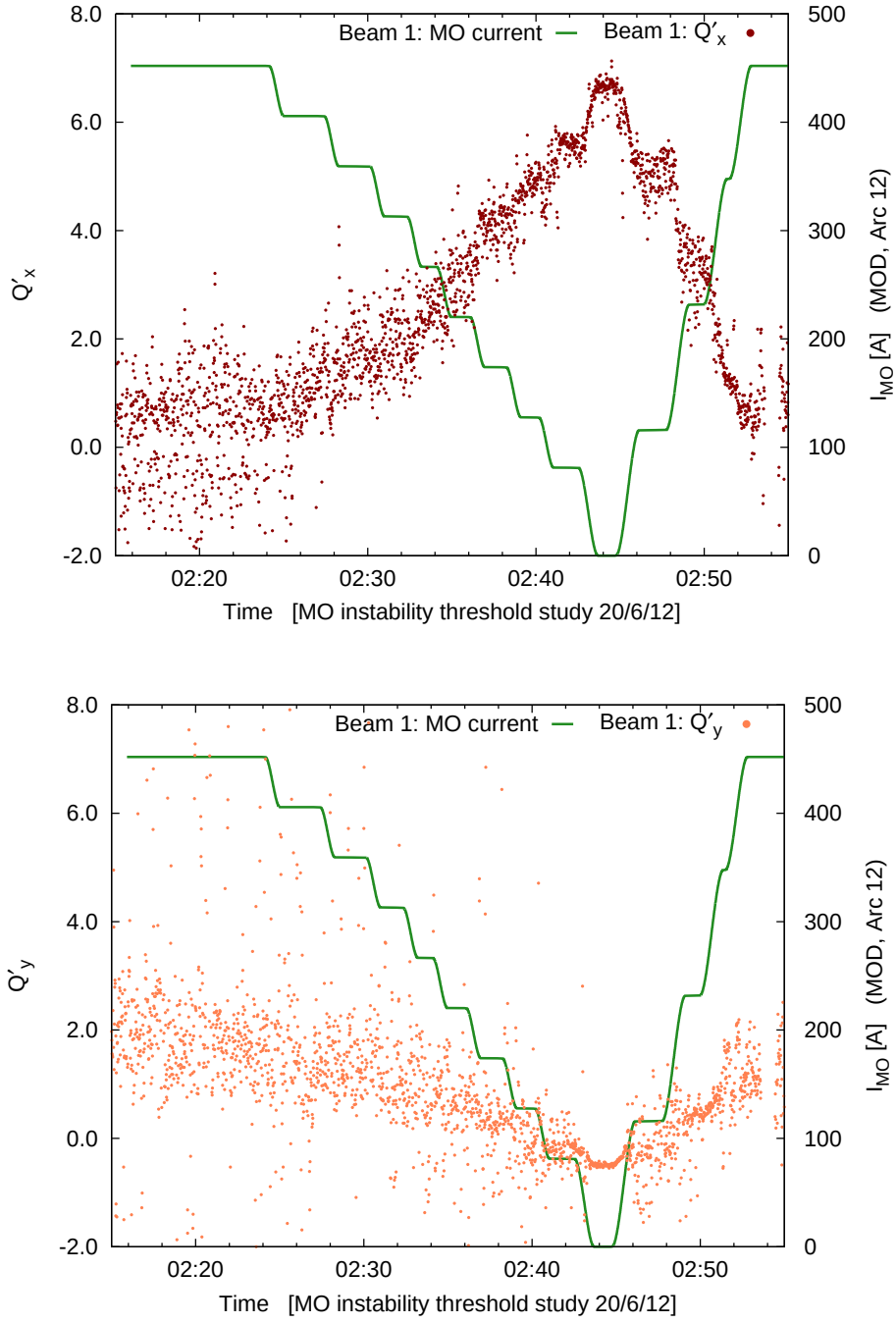

Figure 5.9: Chromaticities logged by the LHC BBQ system for Beam 1 at Flattop during studies of the octupole threshold for instability. Landau octupole powering is also displayed.

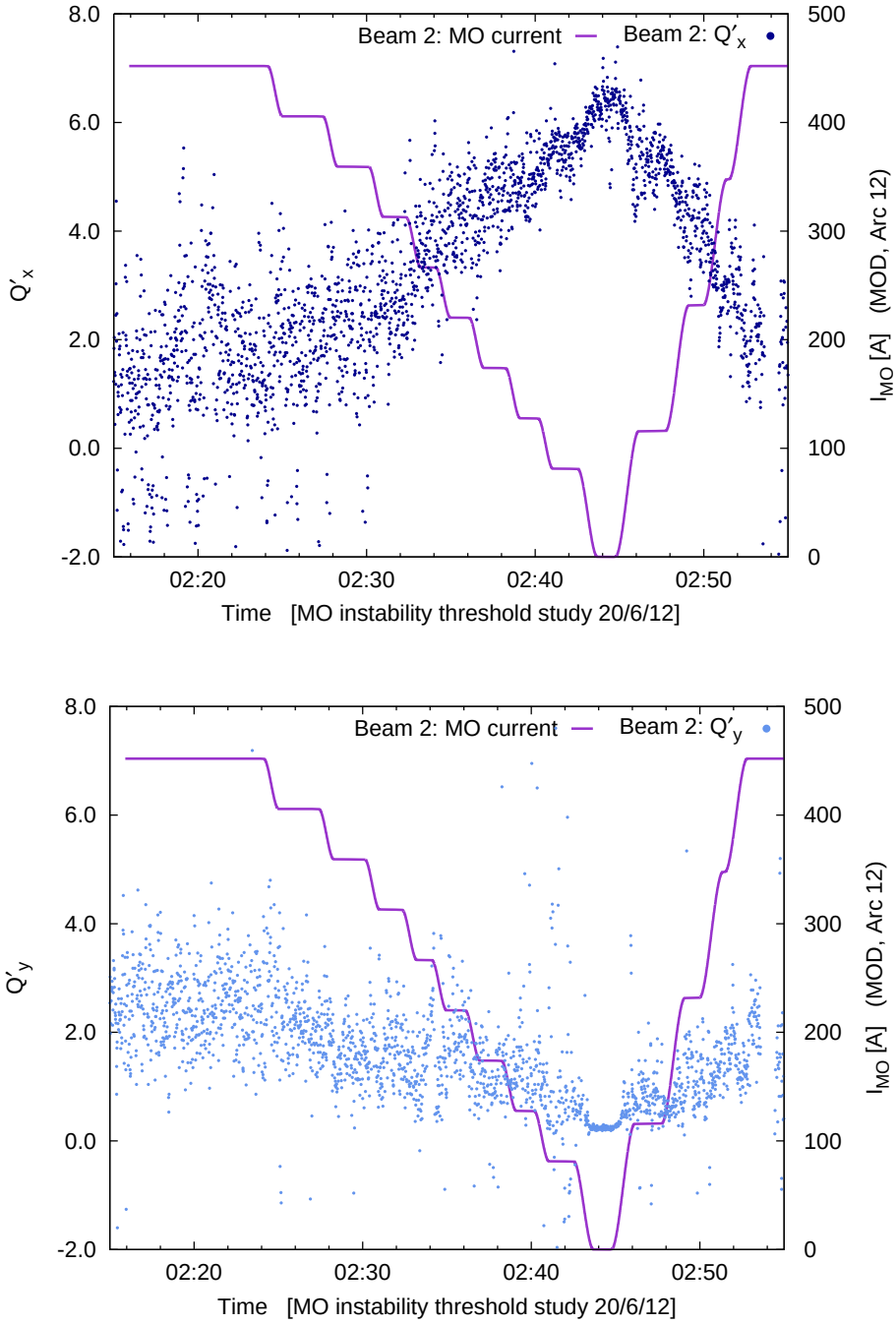

Figure 5.10: Chromaticities logged by the LHC BBQ system for Beam 2 at Flattop during studies of the octupole threshold for instability. Landau octupole powering is also displayed.

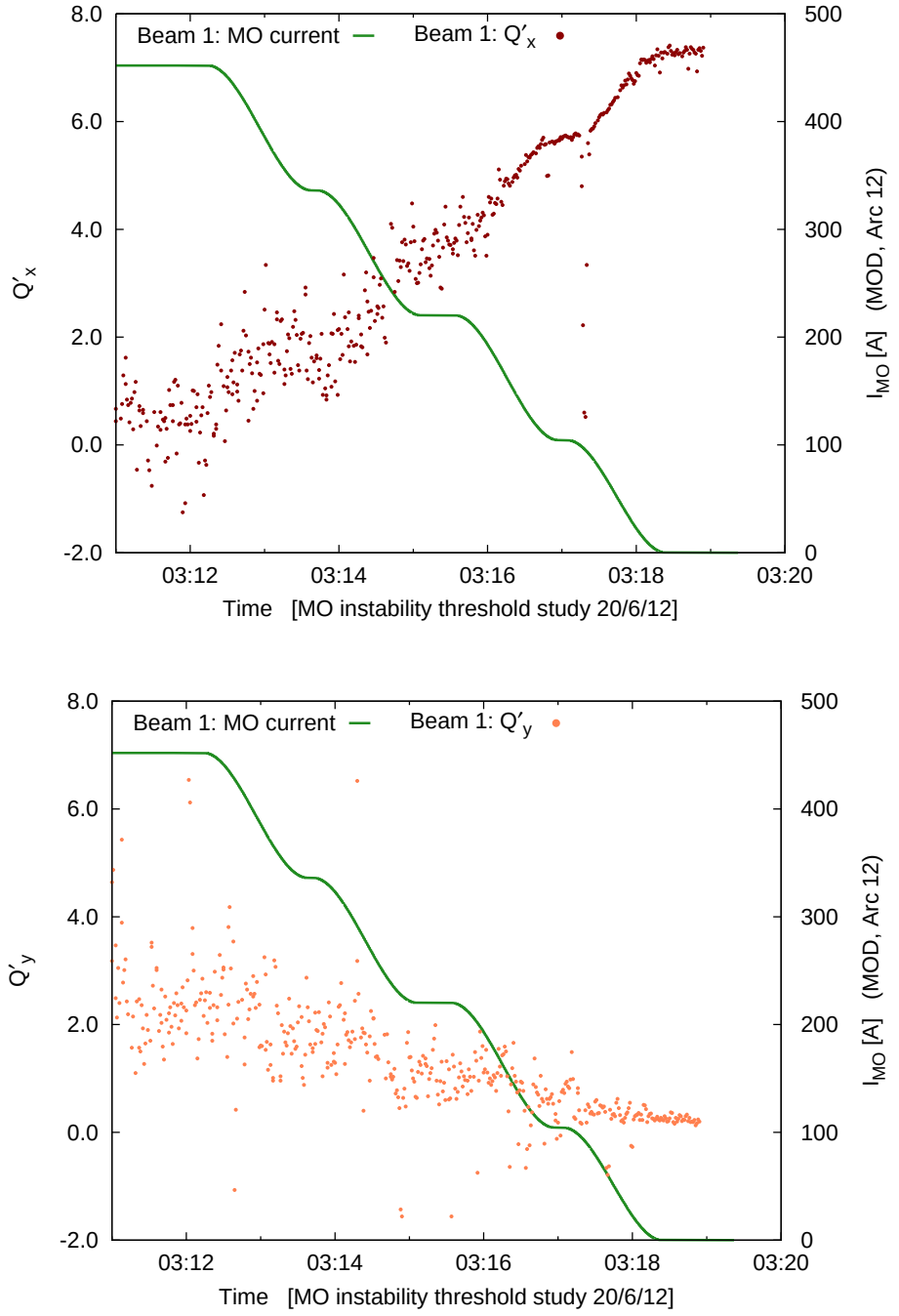

Figure 5.11: Chromaticity of Beam 1 logged by the LHC BBQ system at $\beta^* = 0.6\,\mathrm{m}$ during studies of the octupole threshold for instability. Landau octupole powering is also displayed.

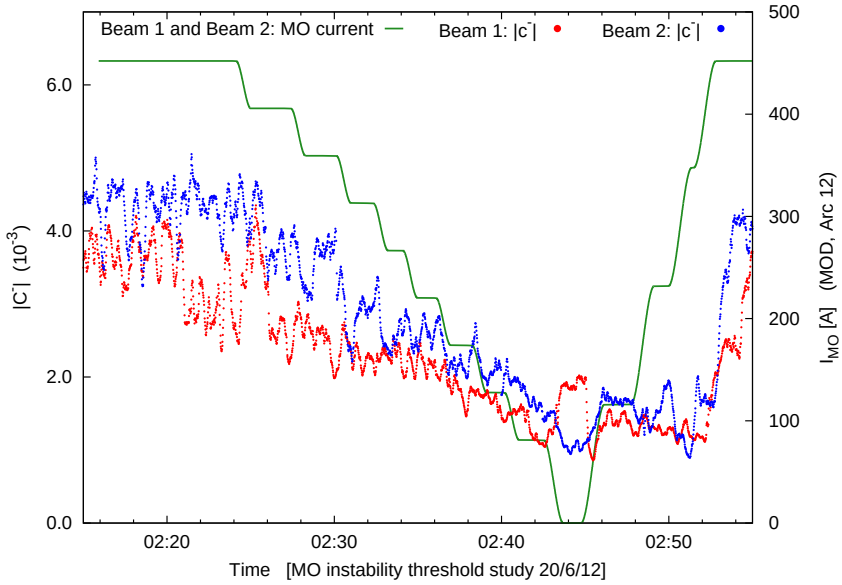

Figure 5.12: Coupling logged by the LHC BBQ system at Flattop during studies of the octupole threshold for instability. Landau octupole powering is also displayed.

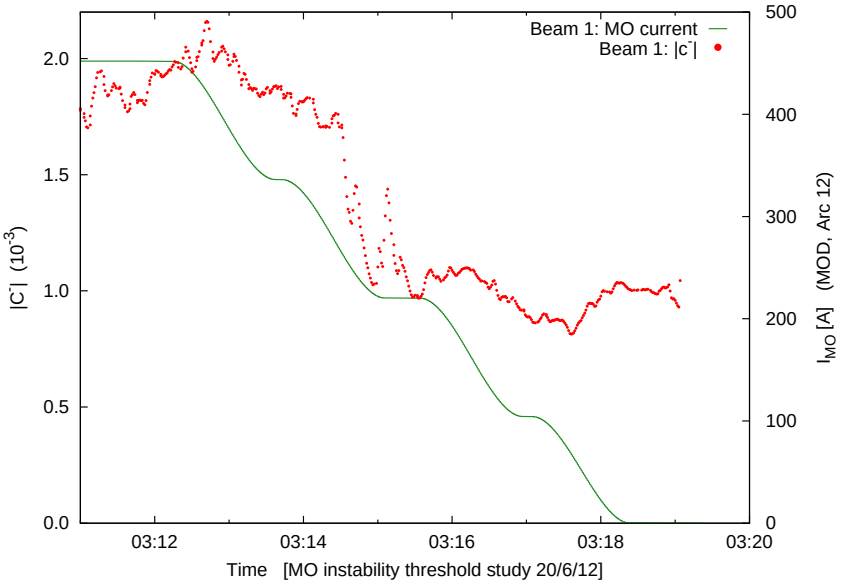

Figure 5.13: Coupling logged by the LHC BBQ system at $\beta^* = 0.6\,\mathrm{m}$ during studies of the octupole threshold for instability. Landau octupole powering is also displayed.

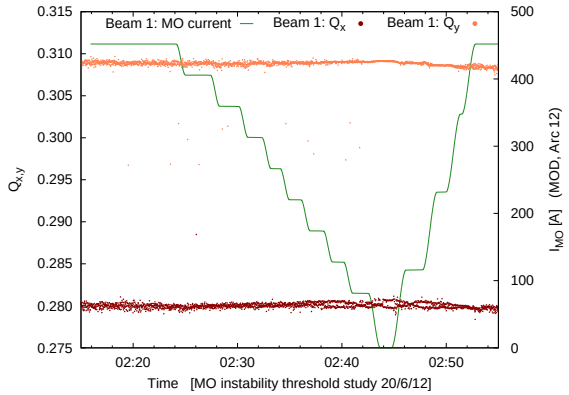

(a) Beam 1

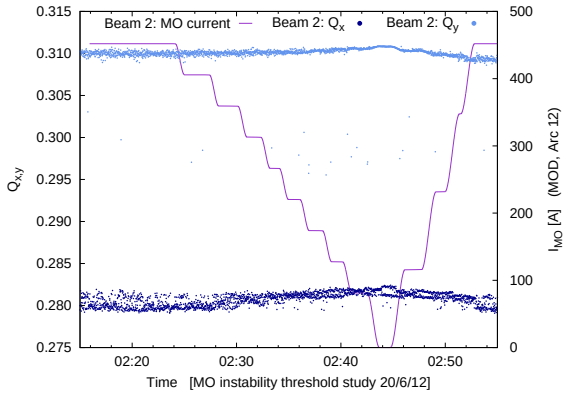

(b) Beam 2

Figure 5.14: Tunes logged by the LHC BBQ system at Flattop during studies of the octupole threshold for instability. Landau octupole powering is also displayed.

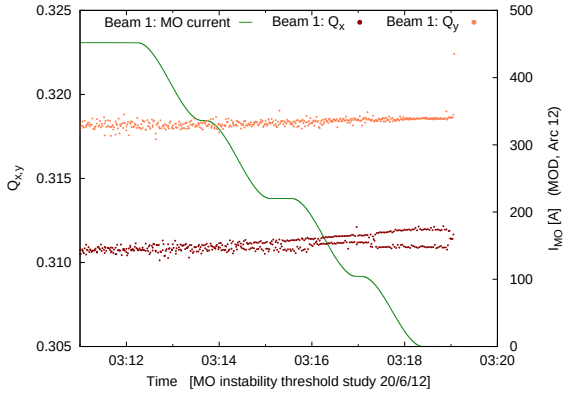

Figure 5.15: Tunes logged by the LHC BBQ system at $\beta^* = 0.6\,\mathrm{m}$ during studies of the octupole threshold for instability. Landau octupole powering is also displayed.

polarity are reported, including high quality measurements of both the coupling determined by the BBQ and the linear coupling RDTs.

During linear optics studies of new MQY[1] settings [117], optics measurements with the AC-dipole were performed with and without Landau octupoles powered, allowing a comparison of the coupling measured by the BBQ to the $|f_{1001}|$. These measurements were performed at Flattop on a virgin optics (beta-beating corrections removed), with new MQY calibrations under investigation applied. At this stage in the LHC operation the polarity of the Landau octupoles had been reversed with respect to the measurements considered in sections 5.2.1, 5.2.2 and 5.2.3. The magnitude of the current in the MO had also been increased to $I_{MOD:a12} = -500\,\mathrm{A}$. Before performing AC-dipole measurements with the MO off, corrections to the tunes were applied for the drifts which occurred on depowering the MO. Changes to the $|f_{1001}|$ resulting from variation of the tune split are therefore negligible.

Figures 5.16 and 5.17 plot the tune and coupling recorded by the BBQ. Considering the Beam 1 tune data a coherent tune shift in both planes is once more observed, with the opposite sign to previous measurements (recall the polarities of the MO were reversed with respect to the previous measurements). In Beam 2 the vertical tune is consistent with the Beam 1 measurement. In the horizontal plane however the tune (as identified by the BBQ) jumps to a new spectral line as the MO powering approaches zero, and prior to this no trend in the observed line is apparent. Conclusions with respect to the Beam 2 Q_x are therefore not possible. Regarding the coupling, as with the measurements presented in the preceding sections a clear shift in the $|C^-|$ recorded by the BBQ is observed on depowering the MO towards $0\,\mathrm{A}$. Significantly however, in spite of the reversal of MO polarity the $|C^-|$ recorded by the BBQ is still observed to decrease. Upon reversal of the MO polarity it would be expected for most sources that the sign of $\Delta|C^-|$ would have changed.

Measurements of $|f_{1001}|$ and $|f_{1010}|$ are plotted in Fig. 5.18 and 5.19. The measurement of $|f_{1001}|$ and $|f_{1010}|$ before and after MO depowering on Beam 1 is of excellent quality, and no shift compatible with the BBQ measurement is observed. On Beam 2 the measurement is of slightly lower quality, but is still in contradiction with the BBQ. While shifts in the $|C^-|$ measured by the BBQ are consistently observed upon changes in Landau octupole

[1]MQY are large bore matching quadrupoles in the LHC insertion regions (IRs).

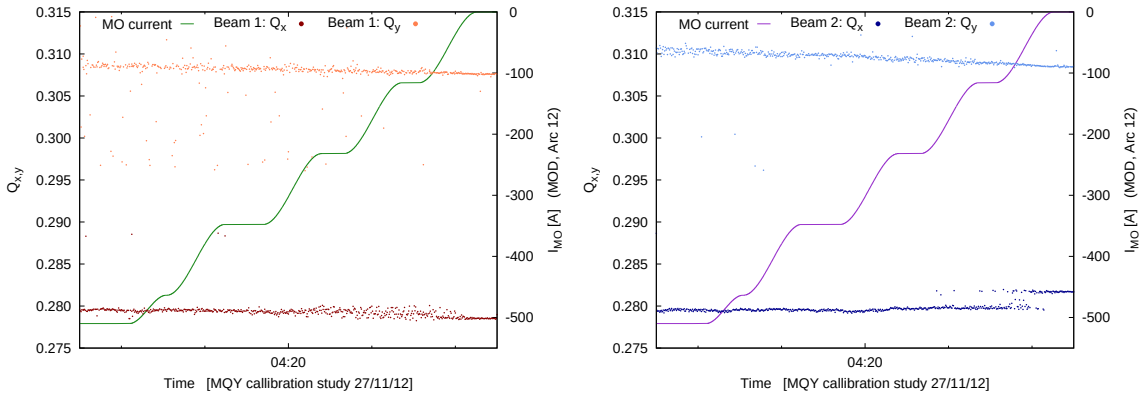

(a) Beam 1 **(b)** Beam 2

Figure 5.16: Tunes logged by the LHC BBQ system at Flattop during MQY calibration studies. Landau octupole powering is also displayed.

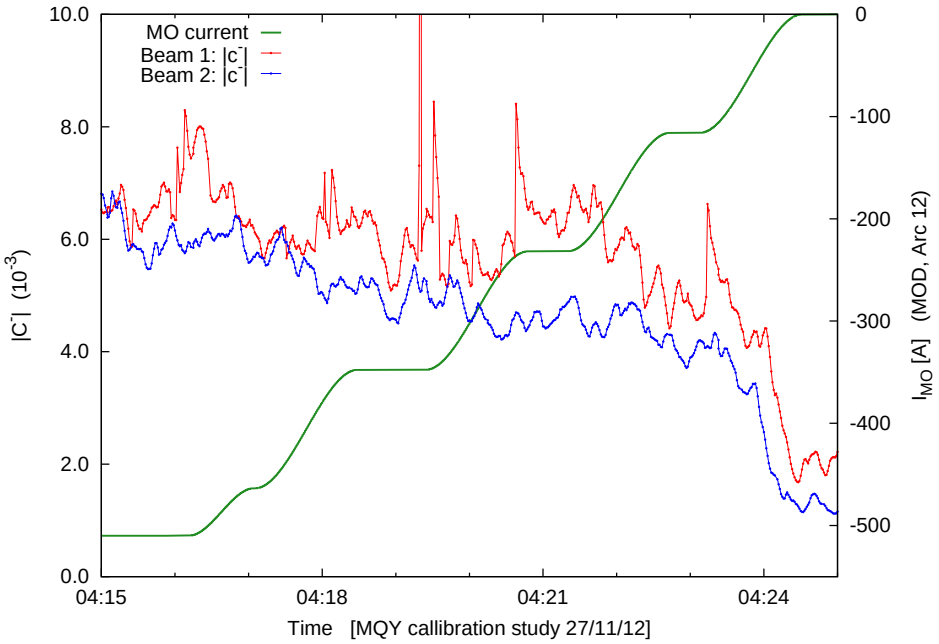

Figure 5.17: Couplings logged by the LHC BBQ system at Flattop during MQY calibration studies. Landau octupole powering is also displayed.

powering, it seems that where data is available these shift are also consistently contradicted by measurements of the linear coupling resonance driving terms.

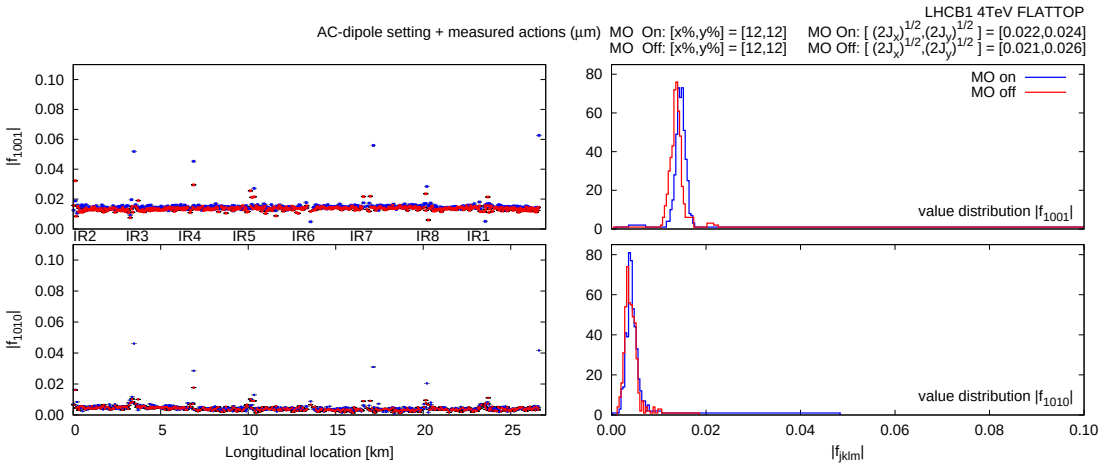

Figure 5.18: Comparison of Beam 1 $|f_{1001}|$ and $|f_{1010}|$ before/after MOs depowered during MQY calibration studies.

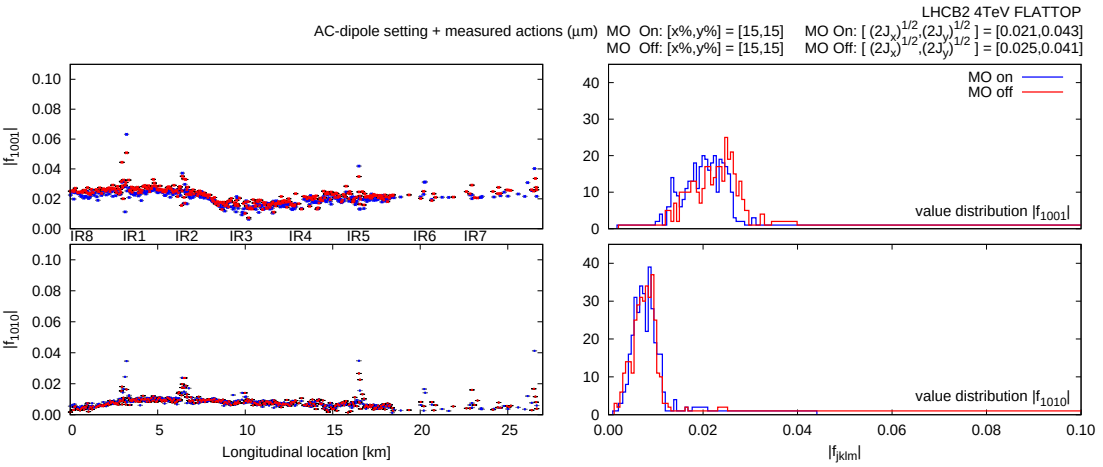

Figure 5.19: Comparison of Beam 2 $|f_{1001}|$ and $|f_{1010}|$ before/after MOs depowered during MQY calibration studies.

5.2.5 Measurements summary

Simple cleaning was performed on the measured BBQ data. A histogram of the BBQ data was considered, and cuts on the accepted values applied. This removed much of the outlying noise. An illustration of the cleaning procedure is shown in Fig. 5.20. In the case shown manual cleaning also removed data corresponding to a spectral line the BBQ repeatedly misidentified with the tune. Similar cleaning was performed on data with and without the Landau octupoles powered, and the mean of the retained data used to calculate the shifts to tune, coupling and chromaticity. Standard deviations of the distributions were added in quadrature to give the error on the shift.

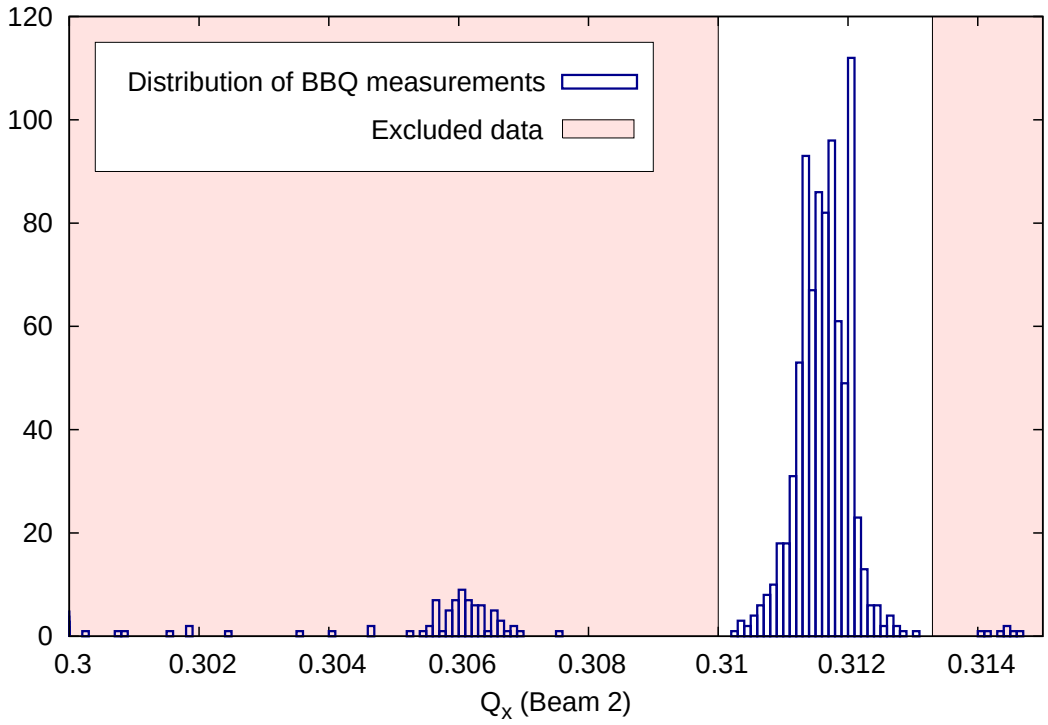

Figure 5.20: An example of cleaning BBQ data. A histogram of the BBQ data is plotted. Cuts (shown in pink) are applied to the tune data in order to exclude some of the obvious noise or misidentified peaks in the spectra.

Table 5.1 summarizes the observations described in the preceding sections. The tune, chromaticity, and coupling shifts have been calculated from LHC BBQ data.

Table 5.1: Summary of tune, chromaticity and coupling shifts. A $\Delta|C^-|$ equivalent to the change in $|f_{1001}|$ at the closest available BPM to the BBQ has been calculated using equation (5.1), and is quoted in the table in order to characterize the f_{1001} measurements.

		Section 5.2.2	Section 5.2.1	Section 5.2.3	Section 5.2.3	Section 5.2.4
		250→0[A]	450↔50[A]	450→0[A]	450→ 0[A]	-500→ 0[A]
	$\Delta = off - on$	$\beta^* = 0.6\,\mathrm{m}$	$\beta^* = 0.6\,\mathrm{m}$	$\beta^* = 0.6\,\mathrm{m}$	Flattop	Flattop
Beam 1	ΔQ_x ($\times 10^{-4}$)	2±1	5±2	7±4	5±4	−10±1
	ΔQ_y ($\times 10^{-4}$)	3±1	5±2	4±1	8±1	−10±3
	$\Delta Q'_x$	-	-	6.6±0.3	6.3±0.8	-
	$\Delta Q'_y$	-	-	−2.1±0.6	−2.3±0.4	-
	$\Delta\|C^-\|_{\text{from BBQ}}$ ($\times 10^{-3}$)	−0.6±0.1	−3.2±0.2	−0.9±0.1	−2.5±0.5	−4.5±0.3
	$\Delta\|C^-\|_{\text{from } f_{1001}}$ ($\times 10^{-3}$)	−0.02	-	-	-	−0.2
Beam 2	ΔQ_x ($\times 10^{-4}$)	4±1	6±3	-	20±6	-
	ΔQ_y ($\times 10^{-4}$)	7±1	13±6	-	8±2	−19±4
	$\Delta Q'_x$	-	-	-	4.7±0.7	-
	$\Delta Q'_y$	-	-	-	−2.2±0.6	-
	$\Delta\|C^-\|_{\text{from BBQ}}$ ($\times 10^{-3}$)	−0.4±0.3	−3.5±0.8	-	−3.5±0.2	−4.7±0.4
	$\Delta\|C^-\|_{\text{from } f_{1001}}$ ($\times 10^{-3}$)	−0.1	-	-	-	+0.2

In general the Beam 1 data (including the f_{1001} measurement) is of a higher quality than Beam 2, however tune, chromaticity and (BBQ) coupling shifts are apparent for both beams. The tune shifts of both the horizontal and vertical planes are consistently driven in the same direction, though their magnitude is small. The coupling as measured by the LHC BBQ was observed to decrease on the depowering of the Landau octupoles. This decrease is observed for both polarities of the MO, and has been shown to be inconsistent with measurements of the coupling RDTs.

The observed chromaticity variation with Landau octupole powering is substantial and of concern for the operation of the LHC. The remainder of this Chapter endevours to explain the tune, chromaticity, and coupling dependence on MO powering.

5.3 Understanding the tune, linear coupling and first order chromaticity dependence on Landau octupole powering

The LHC has two families of Landau octupole (focusing: MOF, and defocusing: MOD) per arc per beam. As designed both beams had 84 MOF and 84 MOD. Following the incident in September 2009 two $\mathrm{MOD}_{\mathrm{Beam\ 1}}$ and two $\mathrm{MOF}_{\mathrm{Beam\ 2}}$ in Sector 3-4 were lost[2]. An explanation of the observed dependencies of the tune, chromaticity, and (BBQ) coupling on the powering of these elements is desired.

One likely cause of a variation in the fundamental beam parameters with octupole powering is feed-down from misalignments and closed orbit. Another is the field quality of the Landau octupoles. In this section the role of these effects are assessed with reference to the observations. In this analysis a perfect reliability of the current-field transfer function of the Landau octupoles is assumed. During 2012 the transfer function was well verified at lower currents (up to $\sim 80\,\mathrm{A}$), however no data is available at the higher currents applied in these studies.

5.3.1 Matching systematic misalignments of MOF and MOD to observations

As an initial step towards understanding the dependencies of the relevant parameters on Landau octupole powering, an attempt was made to match systematic transverse and rotational misalignments of the MOF and MOD to reproduce the observed ΔQ, and $\Delta Q'$. It was also attempted to reproduce the $\Delta|C^-|$ observations made by the LHC BBQ. Matching was performed in MAD-X, the results of the matching procedure are summarized in Tab. 5.2.

Initially only the chromaticity shifts in the horizontal and vertical plane were constrained. Being dominated by horizontal misalignment, only the $\delta_{x:\ MOF,MOD}$ were varied in this case. Systematic misalignments of $|0.36|\,\mathrm{mm}$ in the MOF and $|0.1|\,\mathrm{mm}$ in the MOD were found to be necessary to reproduce the observations. While purely horizontal misalignment succeeded in reproducing the chromaticity shifts, it failed to reproduce the observed behaviour of the tune. To satisfy constraints on chromaticity and tune shifts together, it was necessary to

[2]When considering simulation in MAD-X therefore, we use the 2012:*'as-built'* sequence [132].

Table 5.2: Results for Beam 1 of attempts to match systematic misalignments of the MOF and MOD to measured ΔQ, $\Delta Q'$ and (BBQ) $\Delta|C^-|$ on depowering the Landau octupoles. Similar results were obtained for Beam 2. Attempts to match the coupling shift either failed or obtained unrealistic misalignments.

Matching:		Q' only	Q+Q'	Q+Q'+Coupling
Vary:		δ_x MOF & MOD	$\delta_{x,y}$ MOF & MOD	$\delta_{x,y,\psi}$ MOF & MOD
Systematic alignment	$MOF : \delta_x[\mathrm{mm}]$	-0.36	-0.36	FAILED
	$MOF : \delta_y[\mathrm{mm}]$	0	-0.008	FAILED
	$MOF : \delta_\psi[\mu\mathrm{rad}]$	0	0	FAILED
	$MOD : \delta_x[\mathrm{mm}]$	-0.1	-0.1	FAILED
	$MOD : \delta_y[\mathrm{mm}]$	0	0.39	FAILED
	$MOD : \delta_\psi[\mu\mathrm{rad}]$	0	0	FAILED

introduce sizable vertical misalignment (comparable in magnitude to the horizontal).

The systematic misalignments required to reproduce the tune and chromaticity shifts are large but not unrealistic, implying that Landau octupole feed-down does have the capacity to explain the observations. These results also set a scale of comparison for the measured Landau octupole misalignments and the measured orbit in the following sections.

Attempts were made to match systematic horizontal, vertical, and rotational misalignments of the MOF and MOD with constrained shifts to tune, chromaticity, and coupling. In all cases considered the matching either failed or produced unreasonable results. The failure to find a reasonable solution for the coupling shifts may suggest a source other than feed-down is responsible for the observations of $\Delta|C^-|$ made with the BBQ, or that they are the result of an artifact in the measurement.

5.3.2 Known misalignments of the Landau octupoles

Estimates of geometric errors in the LHC lattice are generated by the Windows Interface to Simulation Errors (WISE [87]) from measurements of the alignment errors [88]. WISE was introduced in Chapter 2.1.3. Table 5.3 shows the mean misalignments of the MOF and MOD for each Beam, determined from the WISE estimates. Comparing with Tab. 5.2 it is apparent from the experience of attempting to match systematic misalignments to the

measured $\Delta Q'$ that the systematic horizontal misalignments are substantially smaller than required to explain all of the chromaticity shift.

Table 5.3: Mean measured misalignments of the MOF and MOD

		$\bar{\delta_x}$[mm]	$\bar{\delta_y}$[mm]	$\bar{\delta_\psi}$[μrad]
B1	MOF	-0.0633	-0.146	-7.97
	MOD	-0.0588	-0.185	-0.476
B2	MOF	-0.0514	-0.231	-0.476
	MOD	-0.0663	-0.208	-7.98

A simple MAD-X model of the LHC was constructed which reproduced the conditions of the measurement at Flattop during the dedicated chromaticity measurements (Section 5.2.3). The misalignments of the individual Landau octupoles obtained from WISE were applied to the MO in MAD, then with the MO at their nominal settings the tune, chromaticity and coupling were matched to their values immediately preceding the measurement. All crossing and separation bumps in the IRs are removed from the MAD-X model in order to minimise the closed orbit in the simulation. This ensured that only the effect of the applied misalignments was seen. The shifts to Q, Q' and $|C^-|$ on depowering the MO to zero in the model are presented in Tab. 5.4.

Table 5.4: Q, Q' and $|C^-|$ shifts on depowering the MO ($I_{MOD:a12} = 450 \rightarrow 0\,[\mathrm{A}]$) in the MAD-X model (at Flattop) with measured misalignments applied to the MO. The shifts observed during dedicated chromaticity measurements (Section 5.2.3) are quoted for comparison.

	Beam 1		Beam 2	
	model	measured	model	measured
ΔQ_x ($\times 10^{-4}$)	-6	5 ± 4	-9	20 ± 6
ΔQ_y ($\times 10^{-4}$)	7	8 ± 1	16	8 ± 2
$\Delta Q'_x$	0.96	6.3 ± 0.8	1.36	4.7 ± 0.7
$\Delta Q'_y$	-0.53	-2.3 ± 0.4	-1.12	-2.2 ± 0.6
$\Delta\|C^-\|$ ($\times 10^{-3}$)	0.40	-3.5 ± 0.5	0.58	-3.5 ± 0.2

The sign of the $\Delta Q'$ is correct. As expected the magnitude is smaller than observed, however it represents a non-negligible contribution to the chromaticity dependence (between

$15\,\%$ and $50\,\%$ of observations dependent on plane and beam). The tune and (BBQ) coupling shifts were not reproduced.

5.3.3 Systematic closed orbit at the Landau octupoles

In addition to misalignment of the Landau octupoles another potential source of feed-down is the closed orbit of the beams. During the dedicated chromaticity study (Section 5.2.3) the orbit at the LHC BPMs was logged by the LHC steering software *YASP* [133]. All Landau octupoles in the LHC are located next to a BPM ($|s_{MO} - s_{BPM}| = 0.751\,\mathrm{m}$), this may be seen in Chapter 2, Fig. 2.2. The closed orbit in the MO may be approximated to that of the neighbouring BPM.

Figure 5.21 shows an example of the orbit logged by YASP for the horizontal plane of Beam 1, during the dedicated chromaticity study. Functioning BPMs logged by YASP are plotted in green. Malfunctioning BPMs are plotted in red.

The lower plot in Fig. 5.21 shows the orbit logged for all BPMs around the ring. The orbit was not substantially dispersive: the relative momentum offset corresponding to this orbit was $\frac{\delta p}{p} = 0.057 \times 10^{-3}$. Considering the upper plot of Fig. 5.21 however, which only displays the orbit at BPMs neighbouring an MO, there is a substantial systematic orbit at these BPMs. Indeed at two locations (BPM.29R7.B1 and BPM.33R7.B1) the logged orbit is in excess of $2\,\mathrm{mm}$ (this issue will be returned to in Section 5.3.5).

To assess the systematic closed orbit at the Landau octupoles during the dedicated chromaticity measurements (given the assumption the orbit excursion does not change substantially in the $0.751\,\mathrm{m}$ between the MO and corresponding BPM), the orbit was averaged over all functioning BPMs next to an MOF or MOD at each time interval recorded by YASP. The mean horizontal and vertical orbits at the MOF and MOD are plotted against time in Fig. 5.22 (Beam 1) and Fig. 5.23 (Beam 2). The β^* and measured MO current are also shown. Note that Beam 2 was dumped before measurements at $\beta^* = 0.6\,\mathrm{m}$ could be performed.

A substantial systematic closed orbit is observed in the horizontal plane for the MOF.

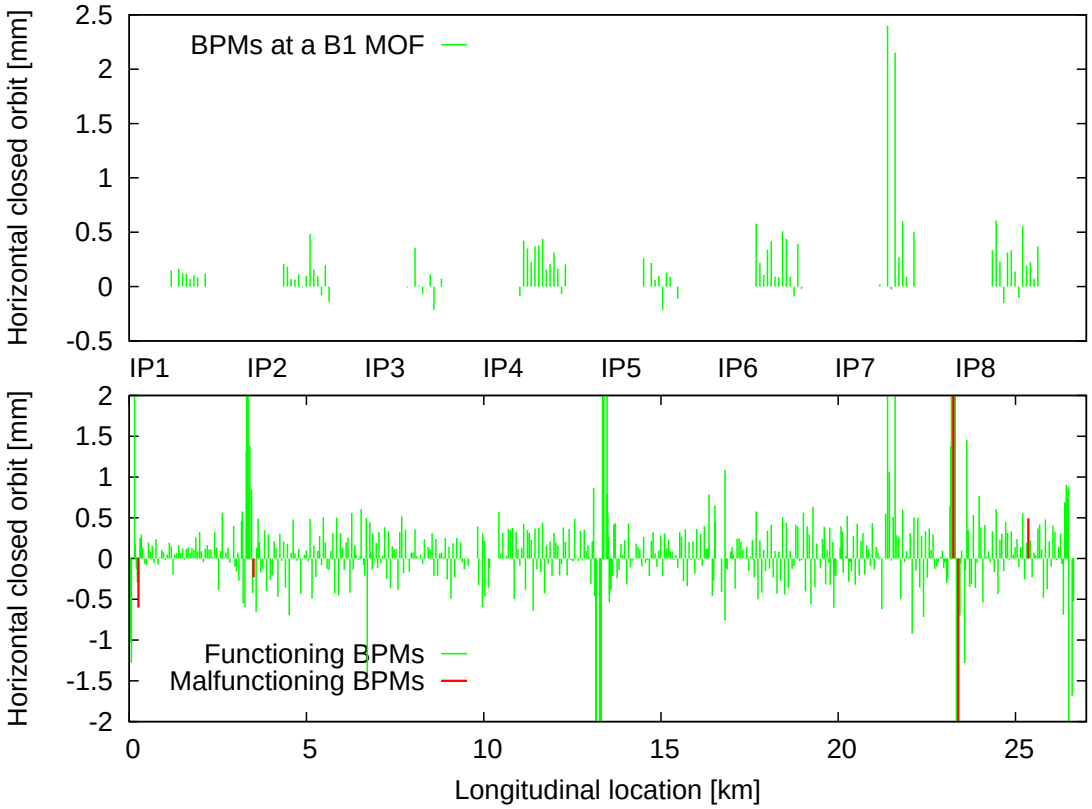

Figure 5.21: Beam 1 horizontal orbit as logged by YASP during the dedicated chromaticity study. Functioning BPMs are shown in green, malfunctioning in red. The lower plot shows the measured orbit at all BPMs. The upper plot shows the orbit measured at BPMs immediately preceding the Beam 1 MOF.

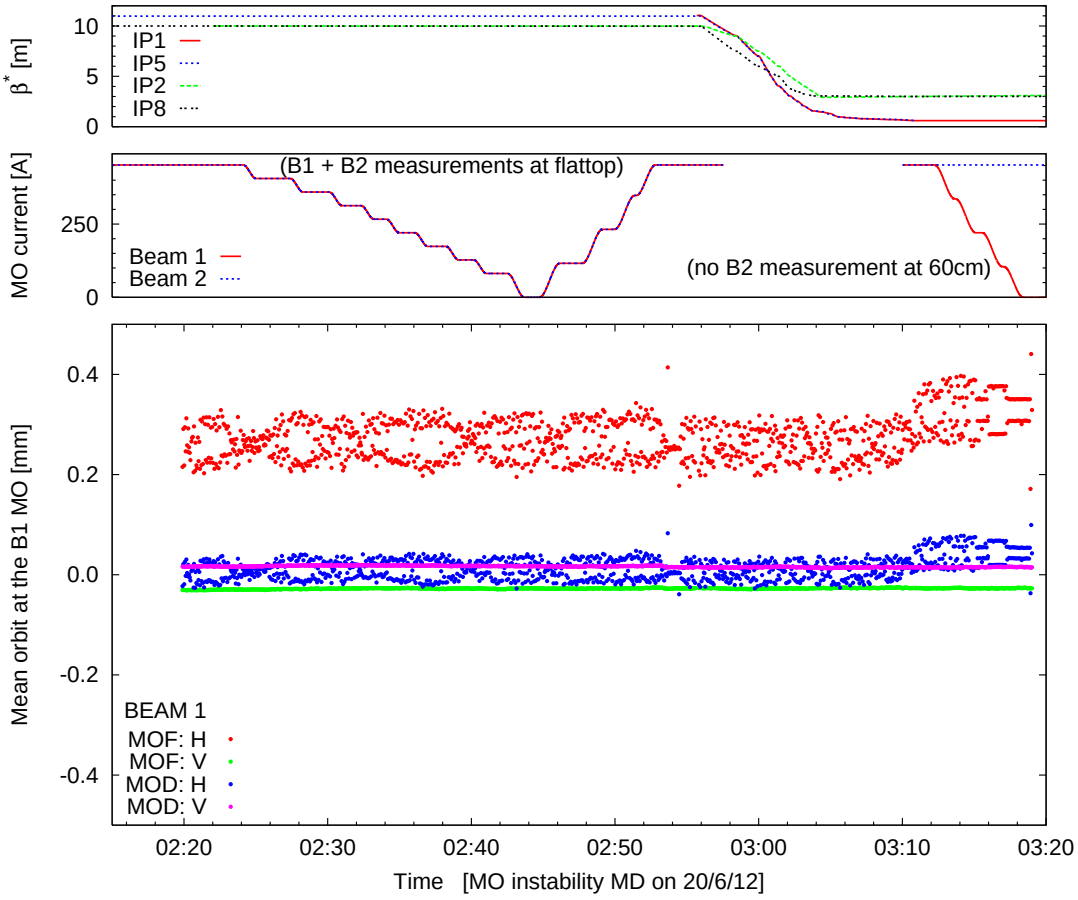

Figure 5.22: YASP orbit data for Beam 1, averaged over functioning BPMs located next to an MOF or MOD, during the dedicated chromaticity measurements (Section 5.2.3).

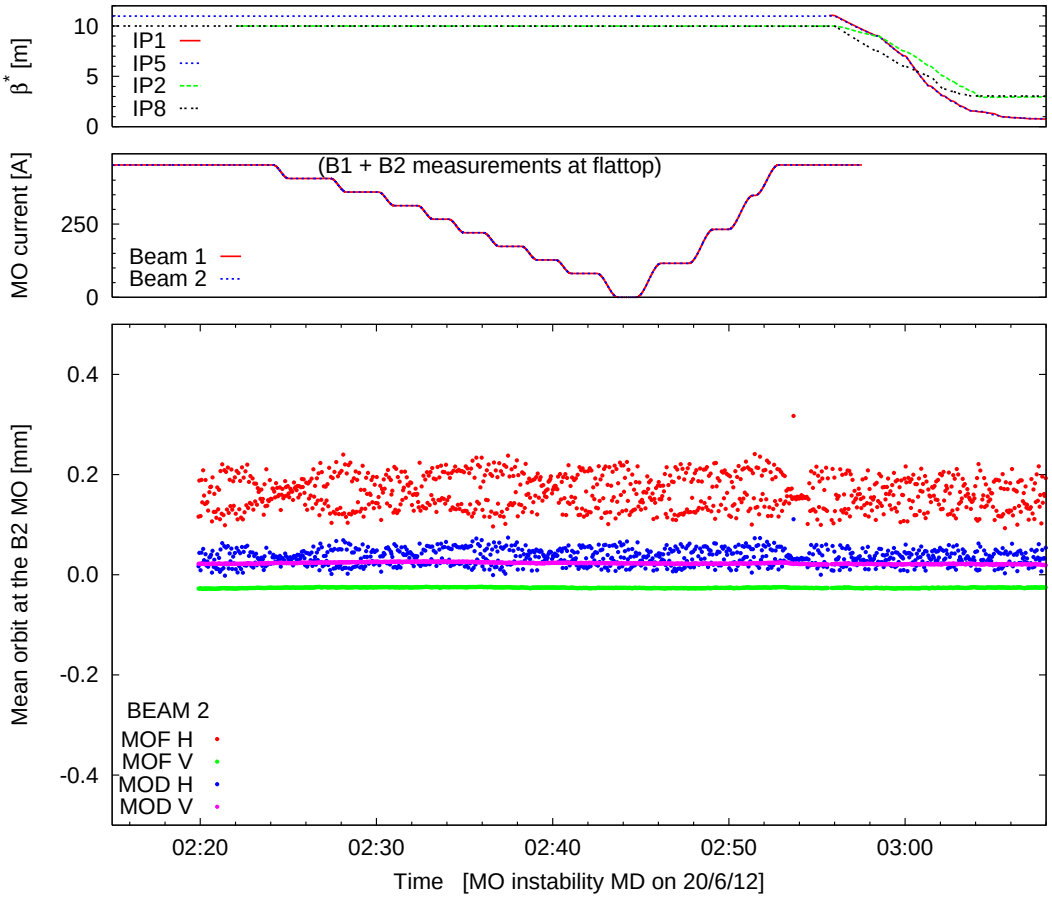

Figure 5.23: YASP orbit data for Beam 2, averaged over functioning BPMs located next to an MOF or MOD, during the dedicated chromaticity measurements (Section 5.2.3).

Significantly this misalignment is comparable in magnitude to that expected from experience of matching systematic misalignments to the observations. The systematic orbit of Beam 1 increased between the Flattop and post-squeeze measurements, which can explain the slightly larger chromaticity shifts seen following the squeeze.

The orbit logged by YASP does not take into account any misalignment of the BPMs, however alignment data was available for the BPMs with respect to the main quadrupoles (MQ). Combining these measurements with the MQ misalignments from WISE, a correction can be applied to the orbit data to account for this effect. Fig. 5.24 shows the effect of including this correction into the previous analysis of the mean horizontal and vertical closed orbit at the Beam 1 MOF. The effect in the horizontal plane is a small reduction, however the vertical plane shows a significant increase in the mean orbit, which may be relevant for the tune dependence. This effect has been quantified for the MOF and MOD of both beams and is summarized in the following section.

The MQ and MO alignment obtained from WISE, and the BPM alignment data, are implicitly trusted in this analysis. One potential complication may arise in the form of any systematic difference between the mechanical and magnetic axes in the LHC. This is not accounted for in this analysis, however the uncertainty in the model due to this effect is expected to be small when compared with the uncertainty in the systematic orbit and the vertical offset of the BPMs with respect to the MO obtained by this method.

5.3.4 Summary of the mean alignments and closed orbit, and their impact on the model

As discussed in the preceding sections, the MO misalignment together with both horizontal and vertical closed orbits appear to be relevant sources of MO feed-down. Table 5.5 presents the systematic misalignments and the closed orbit at the MOF and MOD of both beams.

Considering Tab. 5.5, the mean horizontal alignment of the beam with respect to the MO axis is comparable with that found when attempting to match systematic misalignments in Section 5.3.1. In the vertical plane the mean displacements are of the opposite sign to those seen when matching, and there is a large mean displacement at the MOF which again

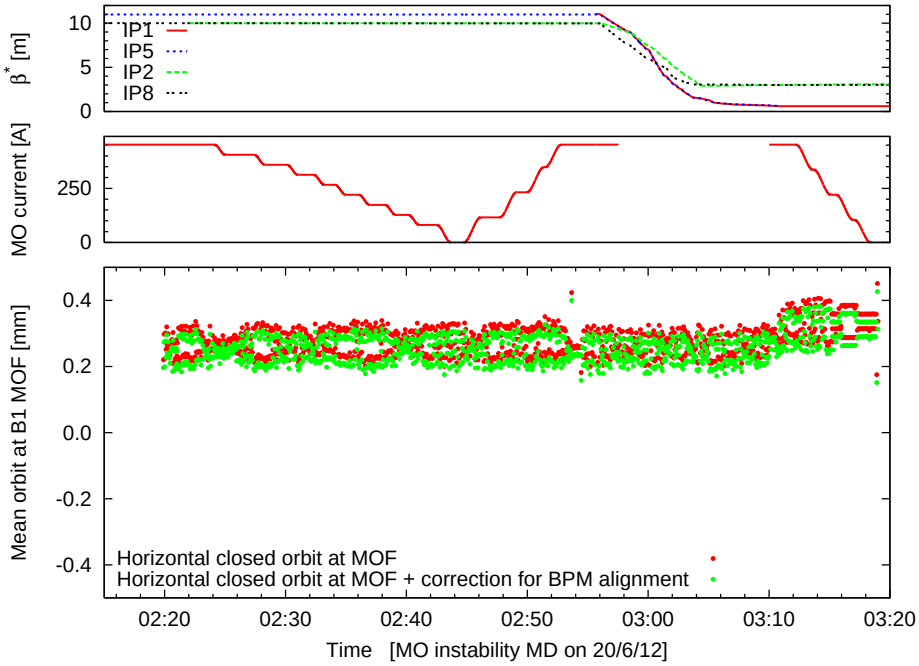

(a) Horizontal orbit

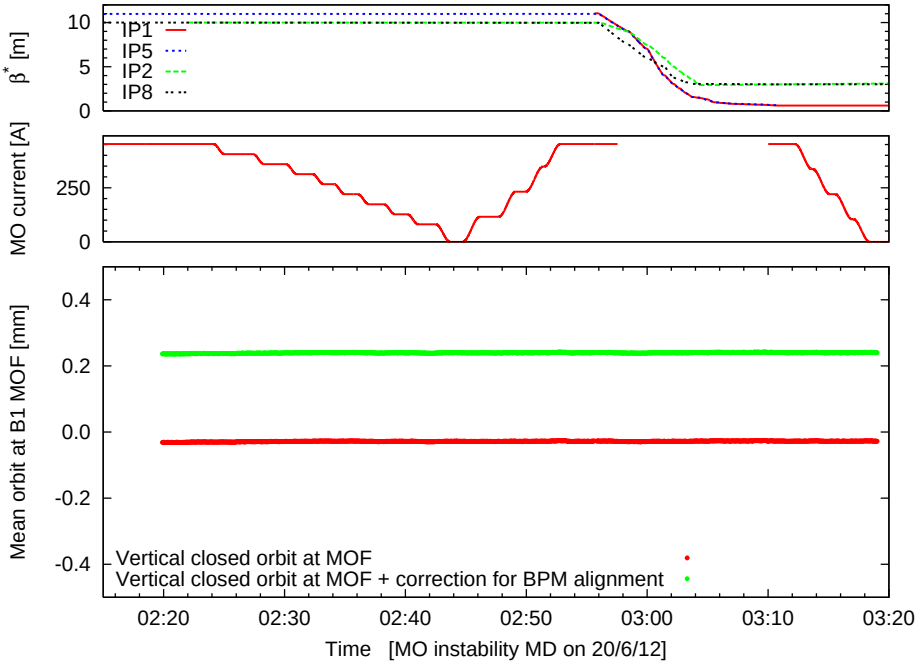

(b) Vertical orbit

Figure 5.24: YASP data, averaged over functioning BPMs located next to Beam 1 MOF during the dedicated chromaticity measurements (Section 5.2.3). Corrections for the BPM alignment are incorporated. Horizontal and vertical orbits are shown in the top and bottom plots respectively.

Table 5.5: Summary of systematic misalignments and closed orbit of the MOF and MOD of LHC Beam 1 and 2 during the dedicated chromaticity measurements (Section 5.2.3). The tilt error on the BPMs were negligible and have not been included in this table. The errors are the standard deviations on the mean orbit at functioning BPMs when averaged between 02:29 and 03:00. The total mean misalignment is quoted without error as the error on the MO misalignments was not available.

			MO	MQ	BPM wrt MQ	BPM	YASP orbit	YASP orbit & BPM align'	MO & YASP orbit & BPM align'
Beam 1	MOF	$\bar{\delta_x}$[mm]	-0.06	-0.07	0.04	-0.024	0.27±0.04	0.25±0.04	0.31
		$\bar{\delta_y}$[mm]	-0.15	-0.13	0.39	0.26	-0.029±0.001	0.239±0.001	0.389
		$\bar{\delta_\psi}$[μrad]	-7.97	-7.97	-	-	-	-	-
	MOD	$\bar{\delta_x}$[mm]	-0.06	-0.07	0.07	0.002	0.01±0.02	0.01±0.02	0.07
		$\bar{\delta_y}$[mm]	-0.19	-0.23	0.42	0.18	0.016±0.001	0.189±0.001	0.379
		$\bar{\delta_\psi}$[μrad]	-4.88	-4.88	-	-	-	-	-
Beam 2	MOF	$\bar{\delta_x}$[mm]	-0.05	-0.07	0.07	-0.027	0.17±0.03	0.17±0.03	0.22
		$\bar{\delta_y}$[mm]	-0.24	-0.22	0.46	0.25	-0.032±0.001	0.214±0.001	0.454
		$\bar{\delta_\psi}$[μrad]	-4.88	-4.88	-	-	-	-	-
	MOD	$\bar{\delta_x}$[mm]	-0.07	-0.07	0.03	-0.034	0.04±0.02	0.00±0.02	0.07
		$\bar{\delta_y}$[mm]	-0.21	-0.14	0.43	0.29	0.024±0.002	0.308±0.002	0.518
		$\bar{\delta_\psi}$[μrad]	-7.98	-7.98	-	-	-	-	-

disagrees with the matching results.

In Fig. 5.22, Fig. 5.23 and Tab. 5.5 there are non-negligible standard deviations (of between $0.02\,\mathrm{mm}$ and $0.04\,\mathrm{mm}$) in the horizontal closed orbit at the MO. This is the result of RF frequency trims, used to measure the chromaticity, affecting the orbit via the dispersion. As the RF trims are symmetric (corresponding to $\frac{\Delta p}{p_0} \sim \pm 1 \times 10^{-4}$) it is appropriate to consider the mean systematic orbit, calculated from the average of the systematic orbit in the MO logged by YASP throughout the dedicated chromaticity measurement. The standard deviation on the mean systematic orbit shown in Tab. 5.5 will not therefore define any meaningful uncertainty on the chromaticity shifts due to the closed orbit.

To simulate the effect of the closed orbit at the MO, systematic misalignments were added to these elements in the MAD-X model of Section 5.3.2. The resulting shifts to Q, Q' and $|C^-|$ on depowering the MO in this model are presented in Tab. 5.6.

The majority of the measured discrepancy in the chromaticity shift can be explained by

Table 5.6: Q, Q' and $|C^-|$ shifts on depowering the Landau octupoles in a MAD-X simulation at Flattop ($I_{MOD:a12} = 450 \rightarrow 0\,[\mathrm{A}]$), with measured MO misalignments applied, and additional systematic misalignments of the MOF and MOD incorporated to model the effect of the systematic closed orbit.

		MO alignment	MO alignment + orbit from YASP	MO alignment + orbit from YASP + BPM alignments	Measured 20/6/12 FLATTOP
B1	$\Delta Q_x(\times 10^{-4})$	-6	-2	-9	5±4
	$\Delta Q_y(\times 10^{-4})$	7	7	12	8±1
	$\Delta Q'_x$	0.96	5.7	5.3	6.3±0.8
	$\Delta Q'_y$	-0.53	-1.5	-1.5	-2.3±0.4
	$\Delta\|C^-\|(\times 10^{-3})$	0.40	0.7	0.6	-2.5±0.5
B2	$\Delta Q_x(\times 10^{-4})$	-9	-6	-15	20±6
	$\Delta Q_y(\times 10^{-4})$	16	15	27	8±2
	$\Delta Q'_x$	1.36	4.3	4.1	4.7±0.7
	$\Delta Q'_y$	-1.12	-2.0	-1.6	-2.2±0.6
	$\Delta\|C^-\|(\times 10^{-3})$	0.58	0.9	0.8	-3.5±0.2

feed-down from the systematic orbit in the MO. The observed tune shift is not explained by the systematic orbit, the model failing to show a coherent shift in both planes. The $\Delta|C^-|$ observed by the BBQ is also not explained by feed-down from the misalignments and systematic orbit.

A shift in the closed orbit due to the change in Landau octupole powering would result in shifts to the feed-down from all elements in the ring, not only the MO. The RMS orbit as recorded by all BPMs however, was not observed to vary with the MO powering. Examining the effect of the MO on the closed orbit in the MAD-X model, including misalignments, orbit, and MO field errors (which will be discussed in Section 5.3.6) there was a negligible change in the RMS orbit around the ring. It is not possible to be absolutely certain that there were no small variations in the feed-down of other elements, but given that no shifts to the RMS closed orbit are seen in the data or found in simulation, any such contributions are expected to be insignificant when compared with the feed-down from the Landau octupoles.

5.3.5 Local feed-down due to closed orbit

So far only the systematic displacement of the beam from the Landau octupole axis arising from the closed orbit has been considered. Figures 5.25 and 5.26 show the orbit logged by YASP (incorporating the correction for BPM misalignment) at a specific instant during the dedicated chromaticity measurements (Section 5.2.3) for each BPM neighbouring an MO.

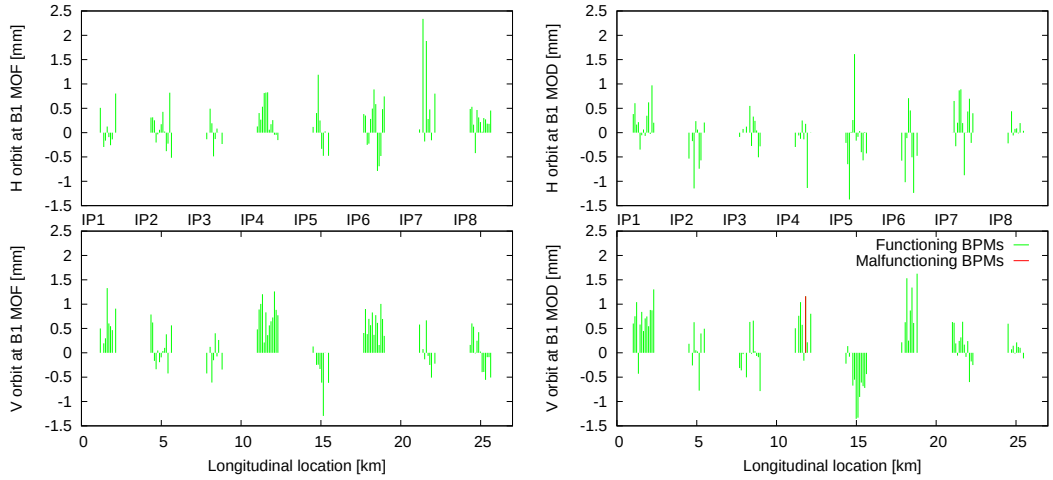

Figure 5.25: Example of orbit data for Beam 1 as logged by YASP during the dedicated chromaticity measurements (Section 5.2.3). Corrections for the BPM alignments are applied.

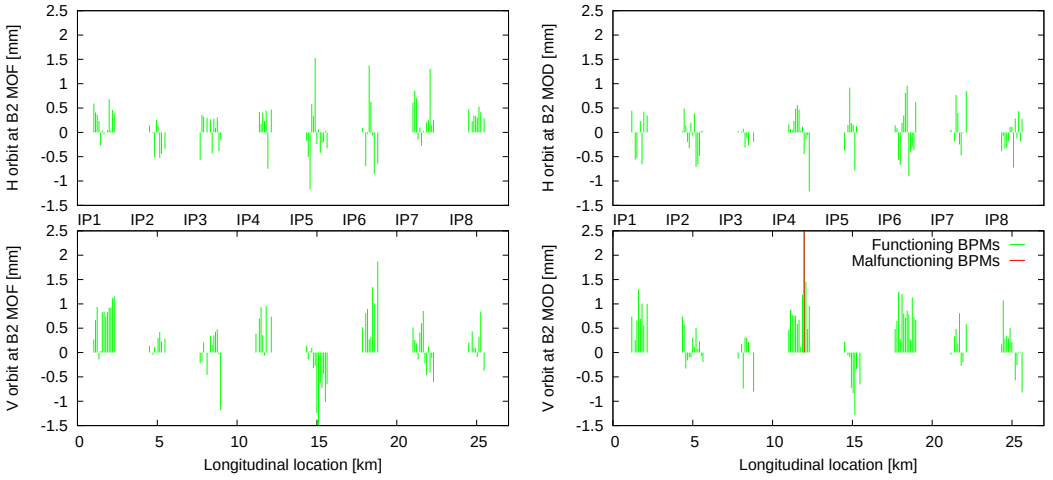

Figure 5.26: Example of orbit data for Beam 2 as logged by YASP during the dedicated chromaticity measurements (Section 5.2.3). Corrections for the BPM alignments are applied.

The systematic misalignment is clear as discussed in Section 5.3.3, however in several circumstances there are also considerable contributions arising from individual MO. The most prominent of these are a pair of logged orbits seen at $\sim 22\,\mathrm{km}$ in the Beam 1 horizontal orbit at the MOF. Corresponding to BPM.29R7.B1 and BPM.33R7.B1, both orbits are in excess of $2\,\mathrm{mm}$: a dramatic excursion for the LHC arcs. From simulation it is concluded that the orbit at these two MO alone accounts for $\sim 30\%$ of the total Beam 1 $\Delta Q'$. Consultation with the LHC operations group (OP) revealed that the dramatic misalignment in these Landau octupoles is the result of a broken orbit corrector in the arc right of point 7.

To first order in the octupole strength it is expected that feed-down of the MO to b_2 should influence the tune split. The Q'' generated by the Landau octupoles could generate a tune shift with MO powering due to a momentum offset of the beam, however this would also drive the tunes in separate directions. First order detuning with amplitude, due to any residual oscillation of the beam centroid, could give rise to a coherent tune shift with MO powering, however the amplitude required to generate the observed $\Delta Q_{x,y}$ is prohibitively large. The coherent nature of the tune shift in both planes may therefore suggest as a source, perturbations higher than first order in the multipole strength. For such higher order perturbations the local distribution of sources around the ring may be relevant. To examine this, misalignments of the MOF and MOD, corresponding to the closed orbit at neighbouring BPMs, were individually applied to each MO. Corrections were applied for the individual BPM alignments. The alignment errors of the Landau octupoles were also applied. In this way the closed orbit was modelled locally rather than systematically. The closed orbit logged at a specific instant during the dedicated chromaticity measurements was considered. This orbit was shown in Fig. 5.25 and 5.26.

Table 5.7 presents the shifts to tune, chromaticity and coupling on depowering the MO in the local model. Simulated shifts obtained using the corresponding systematic closed orbit are also shown. Note that as the systematic and local orbits at a specific instance have been considered, some differences are observed with respect to the shifts obtained from the mean systematic orbit (as calculated from the average of the YASP data for the entire chromaticity measurement) presented in Tab. 5.6. Table 5.7 is intended to illustrate differences in the simulation due to local and systematic modelling of the MO closed orbit, not to provide detailed quantitative predictions for direct comparison to observation.

Table 5.7: Q, Q' and $|C^-|$ shifts on depowering the Landau octupoles in a MAD-X model at Flattop ($I_{MOD:a12} = 450 \rightarrow 0\,[\mathrm{A}]$), with measured MO misalignments applied, and additional misalignments of the individual MO applied individually in order to simulate the effect of the local closed orbit. The local orbit data used to generate this model was logged by YASP at a specific instance during the dedicated chromaticity measurements (Section 5.2.3), and was shown in Fig. 5.25 and 5.26. The systematic closed orbit corresponding to this specific logged orbit has also been modelled and the resulting tune, coupling, and chromaticity shifts are detailed for comparison.

BEAM 1	Instantaneous systematic orbit	Instantaneous local orbit
$\Delta Q_x(\times 10^{-4})$	-10	1
$\Delta Q_y(\times 10^{-4})$	12	3
$\Delta Q'_x$	4.4	4.6
$\Delta Q'_y$	-1.0	-1.3
$\Delta\|C^-\|(\times 10^{-3})$	0.5	-0.4

Instantaneous systematic closed orbit from YASP + BPM alignment.

$\bar{\delta_x}\ MOF\ [\mathrm{mm}]$	0.20
$\bar{\delta_y}\ MOF\ [\mathrm{mm}]$	0.236
$\bar{\delta_x}\ MOD\ [\mathrm{mm}]$	-0.02
$\bar{\delta_y}\ MOD\ [\mathrm{mm}]$	0.188

BEAM 2	Instantaneous systematic orbit	Instantaneous local orbit
$\Delta Q_x(\times 10^{-4})$	-16	-11
$\Delta Q_y(\times 10^{-4})$	27	18
$\Delta Q'_x$	3.2	2.8
$\Delta Q'_y$	-1.3	-0.9
$\Delta\|C^-\|(\times 10^{-3})$	0.7	-0.2

Instantaneous systematic closed orbit from YASP + BPM alignment.

$\bar{\delta_x}\ MOF\ [\mathrm{mm}]$	0.12
$\bar{\delta_y}\ MOF\ [\mathrm{mm}]$	0.213
$\bar{\delta_x}\ MOD\ [\mathrm{mm}]$	-0.02
$\bar{\delta_y}\ MOD\ [\mathrm{mm}]$	0.306

Small variations of the chromaticity shift were observed between the local and systematic techniques, up to the level of $\delta(\Delta Q'_{x,y}) \sim 0.4$. Variations on this scale may define an uncertainty on the chromaticity shift obtained from the mean systematic orbit. The coupling variation, while also significantly influenced by the local orbit, is inconsistent with the BBQ based observations.

The tune shifts in Beam 1 changed substantially. In contrast to the systematic model, applying the closed-orbit locally generated a coherent positive tune shift in both planes with the expected order of magnitude. Reversing the polarity of the Landau octupoles in the model reversed the sign of the tune shift in the Beam 1 simulation, consistent with the observations. Modelling the closed orbit locally did not, however, substantially alter the tune shifts of Beam 2. This is not necessarily surprising: a simplified model of the LHC has been utilized for these studies, the local orbit at only one instant has been considered which may have been distorted by the RF trims used to measure chromaticity, and if the tune shifts are the result of perturbations higher than first order in the multipole strength the distribution of various sources around the ring may be relevant. For example, upon introducing a closed orbit into the Beam 2 systematic model, which did not significantly impact upon the systematic closed orbit at the MO, a positive tune shift was obtained in both planes. Similarly, varying the momentum offset (within the level defined by the chromaticity measurement trims) was seen to influence the tune shift of the local model on the relevant scale.

Local simulation of the closed orbit in the Landau octupoles did produce tune shifts qualitatively similar to the observations. The LHC Beam 2 local model did not differ significantly from the systematic case, but inclusion of a closed orbit into the systematic model was seen to generate a positive shift in both planes. It should be emphasised however, that these results do not constitute a true understanding of the observed tune shifts, or the ability to predict or replicate them in simulation. They should be considered a demonstration that uncertainty in the simulation can encompass the observed behaviour of the machine. It is not necessarily required therefore, to try and seek further explanation of the tune observations through additional sources or artifacts in the measurement. Given the very small tune shifts under examination, for practical purposes this may be sufficient.

5.3.6 Magnetic errors

Another potential source of the dependence of tune, chromaticity and coupling on Landau octupole powering are magnetic errors in the MO. From magnetic measurements performed during LHC construction WISE generates 60 instances (*seeds*) of the likely LHC magnetic model, including normal and skew errors up to the 15$^{\text{th}}$ order. To assess the impact of the magnetic errors in the Landau octupoles on the tune, chromaticity, and coupling dependence, the WISE magnetic errors (excluding the $a1$ and $b1$ multipoles) in the MO were applied to a MAD-X model, which also included the geometric errors of the MO and the mean systematic orbit obtained from all YASP data during the dedicated chromaticity measurement (Section 5.2.3).

Table 5.8 details the shifts to Q, Q' and $|C^-|$ on depowering the Landau octupoles in this model. Measurements quoted in Tab. 5.8 are for studies performed at Flattop during the dedicated chromaticity measurements, this being the only occasion for which there are chromaticity measurements of both beams. Tune, chromaticity and coupling shifts generated in a MAD-X model including only the geometric errors and mean systematic closed orbit (equivalent to the results presented in Section 5.3.4, Tab. 5.6) are shown for comparison. The values and errors quoted for simulation including the WISE magnetic errors are the mean and standard deviation of the 60 WISE seeds.

Applying the magnetic errors to the Landau octupoles slightly improved the modelling of the Q' dependence, however the dominant source of the chromaticity shift remains feed-down due to closed orbit. Including the geometric errors, magnetic errors and systematic closed orbit of the MO in MAD-X generates a chromaticity dependence on Landau octupole powering which agrees within the measurement uncertainty in the horizontal plane of Beam 1 and both transverse planes of Beam 2. The agreement in the vertical plane of Beam 1 is within twice the measurement uncertainty. As highlighted in Section 5.3.5, differences in predictions for the local and systematic closed orbits implied an uncertainty of around ± 0.4 units of chromaticity in the modelled shifts. Taking this uncertainty into account the the modelled and measured $\Delta Q'_y$ in Beam 1 agree within overlapping errors.

Inclusion of b_2 errors in the Landau octupoles significantly enhanced the shift in the tune

Table 5.8: Q, Q' and $|C^-|$ shifts on depowering the Landau octupoles in a MAD-X model at Flattop ($I_{MOD:a12} = 450 \rightarrow 0\,[\mathrm{A}]$). Magnetic and alignment errors generated from measurements by WISE are applied to the MO, and additional misalignments are applied systematically to simulate the the closed orbit. The mean systematic closed orbit, from the average over all YASP data collected during the dedicated chromaticity measurements (Section 5.2.3) has been considered. The values and errors quoted are the mean and standard deviation of simulations with the 60 seeds of the LHC generated by WISE. Measurements quoted are for studies performed at Flattop during the dedicated chromaticity measurements, this being the only occasion for which there are chromaticity measurements of both beams. Predictions from simulation incorporating only alignment errors and the systematic closed orbit (corresponding to data presented in Tab. 5.6) are shown for comparison.

Beam 1	Model misalignments & mean systematic orbit	Model misalignments & mean systematic orbit & field errors	Measurement
$\Delta Q_x (\times 10^{-4})$	-9	-32.0 ± 0.3	5 ± 4
$\Delta Q_y (\times 10^{-4})$	12	33.0 ± 0.3	8 ± 1
$\Delta Q'_x$	5.3	5.575 ± 0.006	6.3 ± 0.8
$\Delta Q'_y$	-1.5	-1.487 ± 0.004	-2.3 ± 0.4
$\Delta \lvert C^- \rvert (\times 10^{-3})$	0.6	0.5734 ± 0.0006	-2.5 ± 0.5

Beam 2	Model misalignments & mean systematic orbit	Model misalignments & mean systematic orbit & field errors	Measurement
$\Delta Q_x (\times 10^{-4})$	-15	-35.3 ± 0.3	20 ± 6
$\Delta Q_y (\times 10^{-4})$	27	50.4 ± 0.3	8 ± 2
$\Delta Q'_x$	4.1	4.246 ± 0.006	4.7 ± 0.7
$\Delta Q'_y$	-1.6	-1.741 ± 0.004	-2.2 ± 0.6
$\Delta \lvert C^- \rvert (\times 10^{-3})$	0.8	0.7558 ± 0.0009	-3.5 ± 0.2

split upon changes in MO powering, further departing the model from the observations. Inclusion of the Landau octupole's magnetic errors in the local Beam 1 simulation considered in Section 5.3.5 was also seen to remove the coherent tune shifts of Beam 1. It was once more observed however, that inclusion of some local variation in the systematic model could generate tune shifts qualitatively consistent with the observations. The conclusions of Section 5.3.5 appear therefore to remain valid in-spite of the addition of the magnetic errors in the MO.

The modelled coupling shifts are inconsistent with measurements performed by the BBQ, and more closely reflect the observations of the resonance driving terms.

5.3.7 Linear coupling

Observations made by the LHC BBQ of shifts to linear coupling which were correlated with changes in Landau octupole powering are as yet unexplained. The simulations described in the preceding sections however, demonstrated coupling shifts more compatible with measurements of the resonance driving terms.

When the Landau octupoles are trimmed to towards $0\,\mathrm{A}$ a reduction in the coupling measured by the LHC BBQ is consistently observed. A reduction in the $|C^-|$ recorded by the BBQ occurs independent of the polarity of the Landau octupoles. Considering the full body of data collected no clear trend is seen in the $\Delta|C^-|$ dependent on the size of the Landau octupole trim. This is shown in Fig. 5.27.

The independence of the $\Delta|C^-|$ on MO polarity excludes the common sources of a linear coupling dependence on octupolar elements, namely feed-down and the field quality. As expected therefore, and in spite of successes with other main dynamical properties of the LHC, the modelling of these sources has failed to reproduce the BBQ observation. Measurements of the linear coupling resonance driving terms (f_{1001} and f_{1010}), from analysis of betatron oscillations induced with the LHC AC-dipole, were performed on two occasions when coupling drifts were seen by the BBQ. No corresponding shifts in the RDTs were observed. The quality of the RDT data and the size of the shift to $|C^-|$, particularly in the case of the MQY calibration studies (Section 5.2.4), are such that a shift in the driving terms should

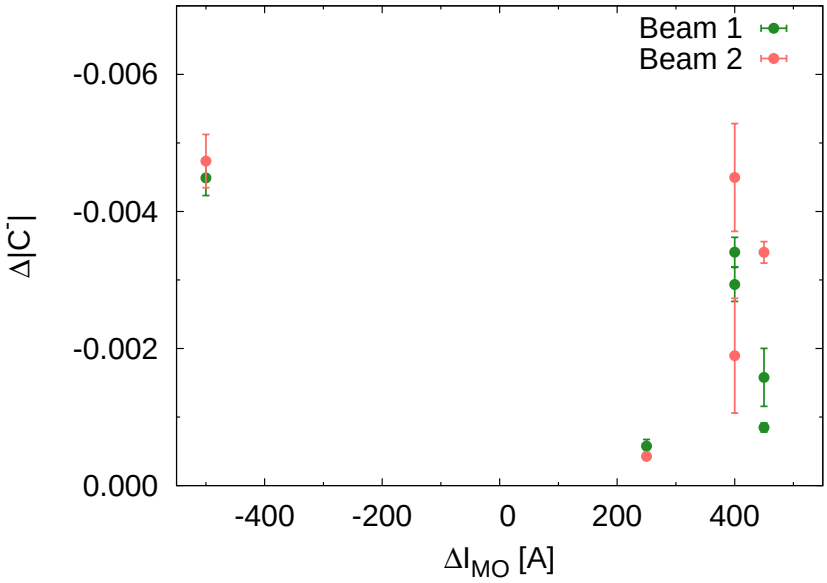

Figure 5.27: The shift to $|C^-|$ on depowering the Landau octupoles, as recorded by the LHC BBQ, plotted versus the change in Landau octupole current (as characterized by the ΔI_{MO} of the Arc12 MOD). The coupling shift appears to be independent of the polarity of the Landau octupoles.

have been clearly visible. The RDT approach to studying the coupling has been extremely well verified during the commissioning of the LHC. In regard to these measurements it is concluded therefore, that the linear coupling is not changing appreciably due to the Landau octupole powering. While the change in $|C^-|$ observed by the BBQ system on depowering the Landau octupoles is confidently identified as an artifact in the measurement, the mechanism which leads to such differing observations between the BBQ and spectral analysis of betatron oscillations is not understood.

Throughout 2012, BBQ and RDT based measurements of the coupling with the Landau octupoles off have generally been found to be consistent. Figure 5.28 shows the shifts to the $|C^-|$, as calculated from $|f_{1001}|$, on depowering the MO during the MQY calibration studies (Section 5.2.4), together with the corresponding BBQ data. Significantly the $|C^-|$ measured by the BBQ agrees well with the $|C^-|$ calculated from the f_{1001} when the MO are depowered. This is particularly true in the case of the higher quality Beam 1 data. The discrepancy between the BBQ and RDT observations of $\Delta|C^-|$ on depowering the MO appears, therefore, to arise from a discrepancy in the measured value with the MO powered.

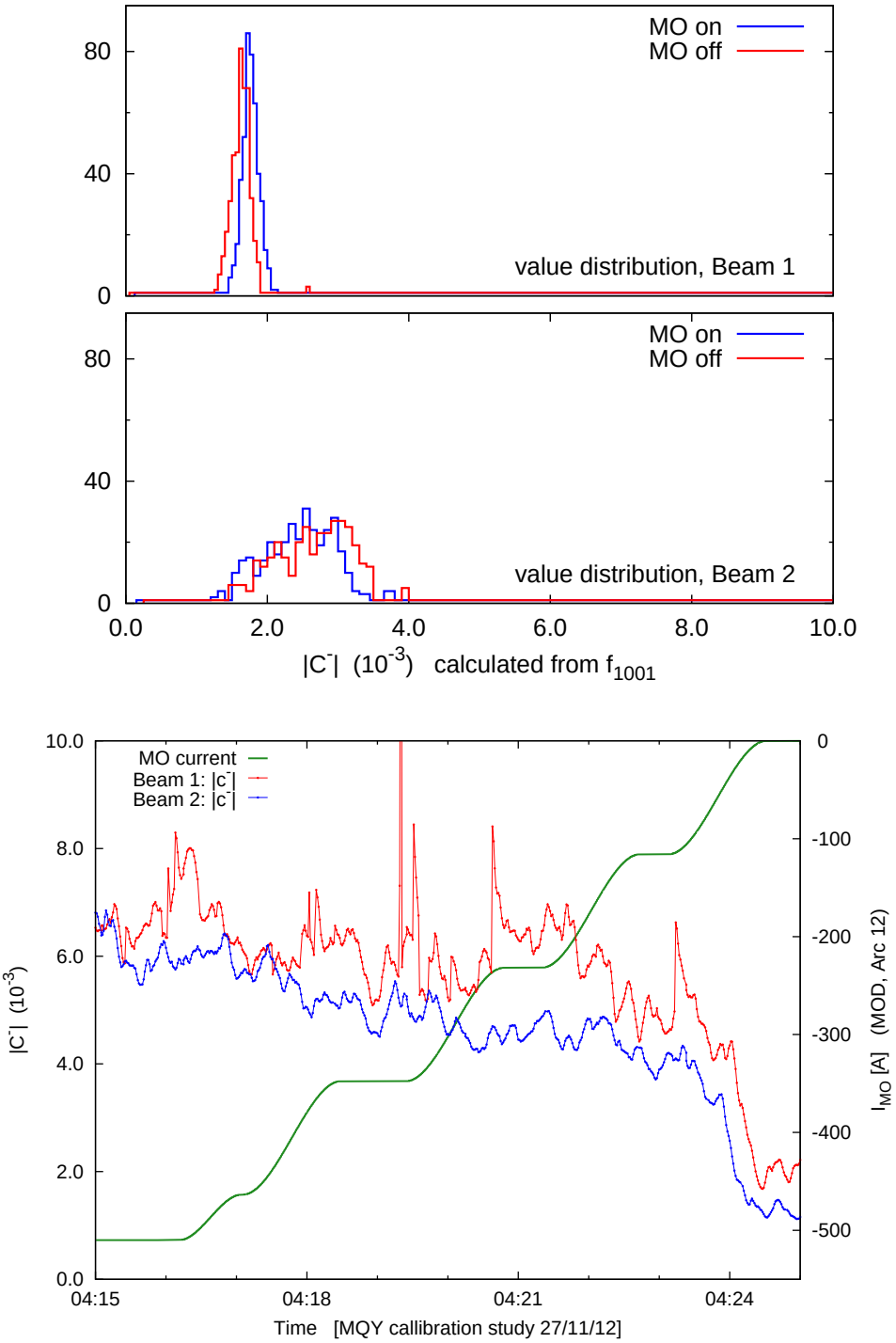

Figure 5.28: The value distribution of Beam 1 and Beam 2 $|C^-|$, as calculated from $|f_{1001}|$ data around the LHC ring (top and center), and the corresponding BBQ data (bottom). The $|C^-|$ measured by the BBQ agrees well with the $|C^-|$ calculated from the f_{1001} when the MO are depowered.

In light of these conclusions with respect to the RDT data, the $|C^-|$ with MO depowered may be regarded as the *'real'* coupling present in the LHC. Figure 5.29 plots the $|C^-|$ with Landau octupoles powered (as recorded by the LHC BBQ) versus the $|C^-|$ with Landau octupoles depowered (as recorded by the LHC BBQ), for all measurements considered in this analysis. Considering this data it may be inferred that with the Landau octupoles powered the linear coupling in the LHC is in reality both better corrected, and more stable, than implied by the BBQ $|C^-|$ measurement when MO are powered. It should be noted though that this is a limited sample of measurements, in which the MO are very strongly powered. In Chapter 4 at injection (where at that time the MO were powered to $K_4 = -3\,\mathrm{m}^{-4}$ as opposed to $K_4 = -23.4\,\mathrm{m}^{-4}$ at top energy) the BBQ and f_{1001} were seen to agree well.

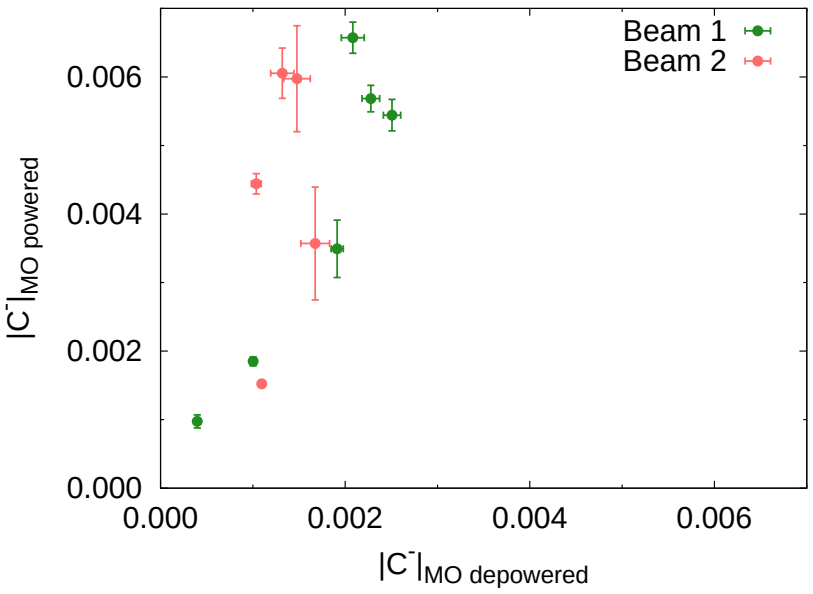

Figure 5.29: The $|C^-|$ with Landau octupoles powered (as recorded by the LHC BBQ) plotted versus the $|C^-|$ with Landau octupoles depowered (as recorded by the LHC BBQ) for all measurements considered in this analysis.

5.4 Analytical expression for first order chromaticity generated by octupolar feed down

The feed-down to chromaticity from the closed orbit is an important effect in the machine. While simulation in MAD-X is a viable solution to examine the Q' generated by octupole feed-down for specific instances, such as the analysis presented in the preceding sections, it may be impractical to rapidly examine large amounts of closed orbit data using this approach. It was desired therefore to derive an analytical expression for the Q' generated by an offset of the beam from the magnetic center of the Landau octupoles. This is not a significantly new result, and the linear variation of Q' with octupole misalignment is of course well known. In a quick review of the literature however, it was not possible to find an explicit equation for the $\Delta Q'$ in terms of the octupole powering and the offset of the beam from the magnetic center. The purpose of this section therefore, is to arrive at a relation for the $\Delta Q'$ in terms of the known parameters of the lattice and octupoles, and to obtain the correct constant factors in the expression. The relation is then verified by comparison to simulation.

From Eq.(1.15), the Hamiltonian for a normal octupole ($n = 4$) is given by Eq.(5.2), where B_4 is defined by Eq.(1.13).

$$\mathbf{N_4} = \frac{q}{p}\frac{1}{4}B_4\left(x^4 - 6x^2y^2 + y^4\right) \tag{5.2}$$

Following the approach in Wiedeman [25], the transformation $x \rightarrow x - \Delta x$ is made, where Δx represents the misalignment of the octupole from the orbit. A Taylor expansion is then performed about $\Delta x = 0$, the Hamiltonian is modified to:

$$\mathbf{N_{4,4\rightarrow 3,\ldots}}(\mathbf{\Delta x}) = \frac{q}{p}\frac{1}{4}B_4\left[(x^4 - 6x^2y^2 + y^4) - 4\Delta x(x^3 - 3xy^2) + \mathcal{O}(\Delta x^2)\right] \tag{5.3}$$

which may be expressed:

$$\mathbf{N_{4,4\rightarrow 3,\ldots}}(\mathbf{\Delta x}) = \mathbf{N_4} + \frac{q}{p}\frac{1}{4}B_4\left[-4\Delta x\,\mathrm{Re}\left[(x+iy)^3\right]\right] + \mathcal{O}(\Delta x^2) \tag{5.4}$$

From Eq.(1.19) it is found that $\mathbf{N_3} \propto \mathrm{Re}\left[(x+iy)^3\right]$, and it is clear that the first order horizontal feed-down of the normal octupole gives a normal sextupole-like term in the Hamil-

tonian. The higher order terms give quadrupole and dipole-like terms before the Taylor expansion terminates. The first order feed-down due to a vertical offset feeds down to a skew sextupole like perturbation.

Chromaticity is given by Eq.(5.5), where $\langle\rangle$ represents an average over the phase variables, and $\delta = \frac{p-p_0}{p_0}$ is the relative momentum offset.

$$Q'_{x,y} = \frac{\partial Q_{x,y}}{\partial \delta} = \frac{1}{2\pi}\left\langle \frac{\partial^2 \mathbf{H}}{\partial J_{x,y}\partial\delta}\right\rangle \tag{5.5}$$

Chromaticity is generated by normal sextupoles in a region of non-zero horizontal dispersion, and skew sextupoles in a region of non-zero vertical dispersion. By contrast normal sextupoles with vertical dispersion and skew sextupoles with horizontal dispersion generate chromatic coupling. In the LHC the vertical dispersion is negligible. Consequently it is the first order horizontal feed-down of normal octupoles, in regions of non-zero horizontal dispersion which is of relevance to the Q'. The chromaticity shift due to this term in the Hamiltonian is now derived.

$$Q'_{x,y} = \oint \mathrm{d}s \;\; \frac{1}{2\pi}\left\langle \frac{\partial^2}{\partial J_{x,y}\partial\delta} \;\; \frac{q}{p}\frac{1}{4}B_4\left[-4\Delta x(x^3 - 3xy^2)\right]\right\rangle \tag{5.6}$$

In a region of non-zero horizontal dispersion $x \to x + D_x\delta$.

$$\begin{aligned} Q'_{x,y} &= \oint \mathrm{d}s \;\; \frac{1}{2\pi}\left\langle \frac{\mathrm{d}^2}{\mathrm{d}J_{x,y}\mathrm{d}\delta} \;\; - \Delta x\frac{q}{p}B_4\left[(x+D_x\delta)^3 - 3(x+D_x\delta)y^2\right]\right\rangle \\ Q'_{x,y} &= \oint \mathrm{d}s \;\; \frac{1}{2\pi}\left\langle \frac{\mathrm{d}}{\mathrm{d}J_{x,y}} \;\; - 3D_x\Delta x\frac{q}{p}B_4\left[(x+D_x\delta)^2 - y^2\right]\right\rangle \end{aligned} \tag{5.7}$$

Expressing x and y in action angle coordinates ($x = \sqrt{2J_x\beta_x}\cos\phi_x$ and $y = \sqrt{2J_y\beta_y}\cos\phi_y$), and taking the differential with respect to the action provides expressions for Q'_x and Q'_y.

$$\begin{aligned} Q'_x &= \oint \mathrm{d}s \;\; \frac{1}{2\pi}\left\langle \;\; -3D_x\Delta x\frac{q}{p}B_4 2\beta_x(\cos^2\phi_x + \frac{1}{\sqrt{2J_x\beta_x}}D_x\cos\phi_x)\right\rangle \\ Q'_y &= \oint \mathrm{d}s \;\; \frac{1}{2\pi}\left\langle \;\; +3D_x\Delta x\frac{q}{p}B_4 2\beta_y\cos^2\phi_y\right\rangle \end{aligned} \tag{5.8}$$

Averaging over the phase variables yields

$$Q'_x = -\frac{3}{2\pi}\oint \mathrm{d}s\ \beta_x D_x \Delta x \frac{q}{p} B_4 \qquad\qquad Q'_y = \frac{3}{2\pi}\oint \mathrm{d}s\ \beta_y D_x \Delta x \frac{q}{p} B_4 \tag{5.9}$$

It is desired to convert from an expression in terms of B_4 to the octupole strength, K_4. For a normal multipole K_n is related to B_n by Eq.(5.10) [134].[3]

$$K_n = \frac{q}{p}(n-1)!B_n \tag{5.10}$$

Making this substitution yields:

$$Q'_x = -\frac{1}{4\pi}\oint \mathrm{d}s\ \beta_x D_x K_4 \Delta x \qquad\qquad Q'_y = \frac{1}{4\pi}\oint \mathrm{d}s\ \beta_y D_x K_4 \Delta x \tag{5.11}$$

Δx in these equations represents the offset of the Landau octupole from the ideal orbit. If an expression is desired for the $\Delta Q'$ caused by the closed orbit in an octupole, Δx should be replaced with $-CO$, the closed orbit in the octupole with the sign reversed. This is equivalent with the procedure used in the preceding sections to model the closed orbit as effective misalignments of the Landau octupoles in MAD-X.

Integrating around the entire ring, making use of the fact that the lattice functions are approximately identical in all the MOF and in all the MOD, gives an expression for the chromaticity shift due to the systematic misalignment and closed orbit of the Landau octupoles in the LHC,

$$\begin{aligned} Q'_x = +\frac{1}{4\pi}\Big(& N_{\text{MOF}}\ (\beta_x D_x)|_{\text{MOF}}\ K_4 L_{\text{MO}} (\overline{CO}_{\text{MOF}} - \overline{\Delta x}_{\text{MOF}}) \\ & + N_{\text{MOD}}\ (\beta_x D_x)|_{\text{MOD}}\ K_4 L_{\text{MO}} (\overline{CO}_{\text{MOD}} - \overline{\Delta x}_{\text{MOD}})\Big) \end{aligned} \tag{5.12}$$

$$\begin{aligned} Q'_y = -\frac{1}{4\pi}\Big(& N_{\text{MOF}}\ (\beta_y D_x)|_{\text{MOF}}\ K_4 L_{\text{MO}} (\overline{CO}_{\text{MOF}} - \overline{\Delta x}_{\text{MOF}}) \\ & + N_{\text{MOD}}\ (\beta_y D_x)|_{\text{MOD}}\ K_4 L_{\text{MO}} (\overline{CO}_{\text{MOD}} - \overline{\Delta x}_{\text{MOD}})\Big) \end{aligned} \tag{5.13}$$

[3] In the notation used here $n = 4$ indicates an octupole, it should be noted that in MAD-X the indices of the multipoles are one lower, thus the octupole strength in MAD-X is labelled as K_3, but is identical with the K_4 as defined here.

where N_{MOF} and N_{MOD} are the number of operational focusing and defocusing Landau octupoles (84 or 82 depending on the beam and family), $\overline{CO}$ is the systematic closed orbit in the MOF or MOD, and $\overline{\Delta x}$ is the systematic misalignment of the MOF or MOD. It has been assumed that K_4 is the same in all MO, as is normal for LHC operation. L_{MO} is the length of the Landau octupoles, and is the same for all magnets ($0.32\,\text{m}$). As the MOF are located at large β_x and small β_y they predominantly influence the Q'_x. This situation is reversed for the MOD. The nominal values of β and D_x in the LHC are: $\beta_x = 176\,\text{m}$, $\beta_y = 33.5\,\text{m}$ and $D_x = 2\,\text{m}$ in the MOF; and $\beta_x = 30\,\text{m}$, $\beta_y = 179\,\text{m}$ and $D_x = 1\,\text{m}$ in the MOD.

The validity of this expression may be assessed by comparison to simulation in MAD-X. Figure 5.30a and 5.30b compare the predictions of the analytical expression to simulation in MAD-X, for the horizontal misalignment of a single octupole, and for the systematic horizontal misalignment of all MOF (all MOF were misaligned with the same displacement in the simulation) respectively. The agreement between simulation and theory is good.

5.5 Implications for LHC operation

The analysis detailed in this chapter has a number of implications. The influence of Landau octupole powering on BBQ based measurement of $|C^-|$ means caution will have to be exercised when utilizing the BBQ for studies of the linear coupling when Landau octupoles are strongly powered. The most far reaching aspect of the analysis however, is the identification of a large influence on the LHC Q' of the systematic closed orbit in the Landau octupoles. The disruption to Q' caused by a single malfunctioning orbit corrector also came as somewhat of a surprise, and demonstrates that even such seemingly innocuous features of the machine may need to be accounted for in the LHC models [135].

The analysis of these effects is still ongoing. Software tools [136] were recently developed to determine the systematic closed orbits in the MOF and MOD from BPM orbit data extracted from the LHC logging database [137], and calculate the corresponding chromaticity shifts using the analytical expression derived in Section 5.4. These tools have facilitated analysis of the chromaticity shifts induced by the closed orbit throughout the 2012 LHC run (given the large volumes of data this entails simulation in MAD-X would have been computationally unfeasible, hence the use of the analytical expression). First results from the 2012

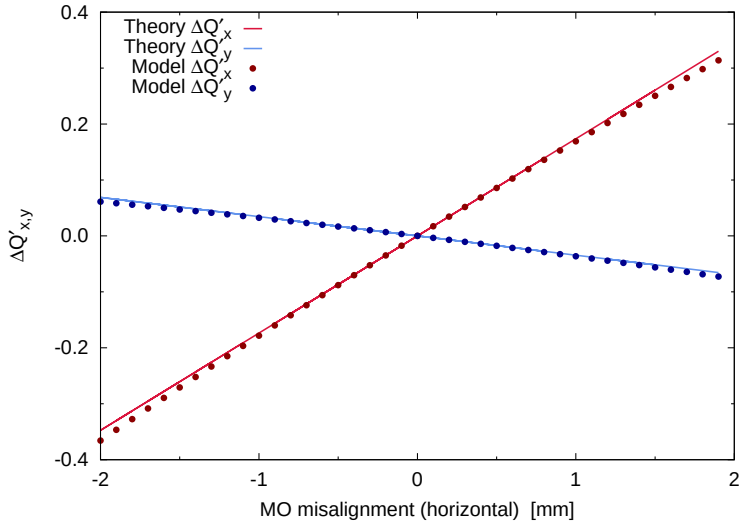

(a) Horizontal misalignment of a single octupole

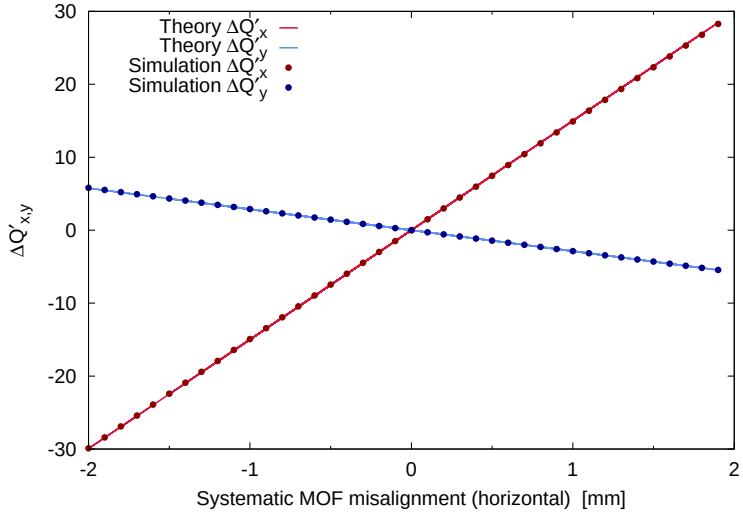

(b) Systematic horizontal misalignment of all MOF

Figure 5.30: Comparison to MAD-X simulation of the theoretical shift in Q' caused by Landau octupole misalignment in LHC Beam 1. Note that the horizontal axis plots the MOF misalignment, not the closed orbit.

run seemed to show large variations in the mean closed orbit in the MOF and MOD, both between fills and within single fills. An example is shown in Fig. 5.31 which plots the mean closed orbit from Flattop to the end of Stable Beams in the MOF of LHC Beam 2 during several fills.

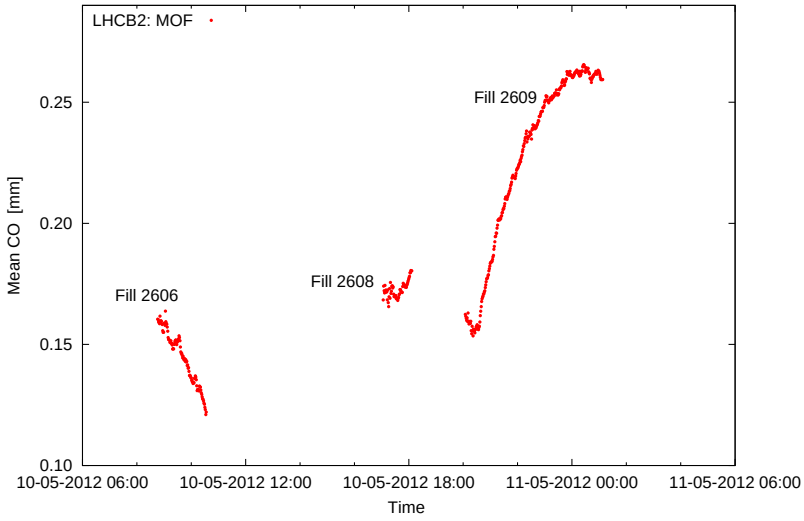

Figure 5.31: The variation of the systematic closed orbit in the LHC Beam 2 MOF, during Flattop, Squeeze, Adjust and Stable beams, for Fills 2606, 2608 and 2609.

Substantial shifts in the closed orbit are seen. Considering the Fill 2609 in Fig. 5.31, the change in systematic closed orbit in the B2 MOF is predicted to have led to a shift in chromaticity of $\Delta Q'_x = -1.6$ (shifts in the MOD were negligible in comparison). This is a substantial variation of the chromaticity, and depending on the initial Q' may have led to the chromaticity becoming negative. Large drifts in the chromaticity could result in instabilities developing in the beam motion. During 2012 most difficulties with instabilities developed during the squeeze, where the orbit is in general stable, and the analysis presented in this chapter allowed chromaticity shifts due to changes in the mean closed orbit at the Landau octupoles to be ruled out as a significant source of instabilities in the squeeze. The effect of the closed orbit during the remainder of the fill remains to be studied in detail.

Shifts to the chromaticity, either due to changes in the closed orbit or due to changes in the Landau octupole powering, also pose challenges operationally. The understanding of the chromaticity dependence on the MO gained through these studies should assist LHC

operations in regard to anticipating and correcting such variations in the Q'. At present there is a project underway at CERN to develop an online model of the LHC [138]. These studies will allow for the first order chromaticity dependence on Landau octupole powering to be included accurately in the LHC online model [138]. In a broader sense the applicability of the LHC model has also been expanded to include circumstances where the closed orbit or Landau octupole powering are not constant.

5.6 Conclusions

The chromaticity dependence of the LHC on Landau octupole powering is well understood. The dominant source is feed-down due to a systematic closed orbit in Landau octupoles, with an additional contribution from feed-down due to misalignments. Within the feed-down due to the closed orbit there are substantial contributions from a minority of octupoles with particularly substantial excursions, notably right of Point 7 where two octupoles contribute approximately 30% of the Beam 1 chromaticity dependence. This is the result of a malfunctioning orbit corrector. The magnetic errors in the MO play a small role in the observed chromaticity shifts. The identification of the closed orbit distortion as a significant source of chromaticity is significant. The closed orbit may vary substantially, both between and within LHC fills, and the resulting chromaticity shifts could lead to the growth of instabilities in the beam motion. The variation of chromaticity with Landau octupole powering can now be well reproduced in the LHC model.

The variation of tune with Landau octupole powering is small enough that its impact on LHC operation should be negligible. While the tune shifts are not definitively reproduced in the model, it has been shown that a qualitatively similar behaviour can be generated in the model when considering the local feed-down from the MO. The uncertainty in the simulation appears to encompass the observed behaviour, suggesting there is no clear requirement to search for additional sources of tune variation beyond those already included in the LHC model.

Coupling shifts dependent on the MO powering were observed by the LHC BBQ. This is in contradiction with measurements of the linear coupling resonance driving terms (RDTs) which showed no compatible shifts. Attempts to model the common sources of a linear

coupling dependence on octupolar elements (feed-down and field quality) failed to reproduce the BBQ observations, but were approximately consistent with the study of the RDTs. On the basis of the RDT measurements it has been concluded that there is no real change to the linear coupling dependent on the Landau octupole powering, that caution should be exercised in trusting the BBQ $|C^-|$ measurement when MO are strongly powered, and that the linear coupling in the LHC with Landau octupoles powered is in fact smaller and more stable than previously appreciated. The reason for the differing observations between the BBQ and spectral analysis of kicked beams is unknown.

An analytical expression for the Q' was obtained, and verified against simulation. This may be used to facilitate rapid analysis of LHC closed orbit data for its impact upon the first order chromaticity.

Chapter 6

Measurement and correction of non-linear errors in the LHC experimental insertions

Non-linear magnetic errors in low-β insertions can contribute significantly to the detuning with amplitude, the linear and non-linear chromaticity, and to the degradation of the dynamic aperture and beam lifetime of a particle collider. Through the application of closed orbit bumps it is possible to examine the non-linearities in such insertions via their feed-down to readily observed beam properties. Such beam-based studies allow for the verification and refinement of the magnetic model of the accelerator, and in conjunction with magnetic measurements allow for the commissioning of local corrections. In this chapter the application of such a method to the experimental insertions of the Large Hadron Collider is demonstrated, and results of the first measurements and corrections are presented.

6.1 Introduction

Non-linear errors at locations of large β can significantly influence the non-linear beam dynamics of an accelerator, contributing to detuning with amplitude, linear and non-linear chromaticity, and to the degradation of dynamic aperture and beam lifetime. The triplet arrangement of quadrupoles used to achieve a small β^* (and hence a high luminosity) in the ATLAS, ALICE, CMS, and LHCb experiments (IR1, IR2, IR5, and IR8 respectively) necessitates a substantial beta function in the triplet quadrupoles and neighbouring elements. This was illustrated in Section 2.1.2, Fig. 2.6, which plots the nominal beta function through IR1, for a β^* at the ATLAS interaction point (IP) of $0.6\,\mathrm{m}$ (the value for normal operation during 2012).

During its first operational run the contribution of magnetic errors in the low-β insertions to such non-linear phenomenology did not limit the LHC's performance. As more challenging regimes of operation are confronted however, correction of the IR non-linearity in the nominal LHC may become important for an optimized performance of the machine, and correction of the non-linear errors in the experimental insertions is expected to be essential [139] for operation after the High-Luminosity (HL) LHC upgrade [140]. Correction of non-linear errors in low-β insertions may also be relevant for potential future colliders.

As discussed in Section 2.1.2, to enable the correction of errors in the LHC IRs linear and non-linear corrector magnets are present in the insertions, distributed symmetrically about the Interaction Point (IP). Combined b_3 / b_6 correctors, and combined a_3 / b_4 / a_4 correctors are installed on the non-IP sides of the *Q3* triplet quadrupoles. A schematic of the corrector layout in the LHC experimental insertions was shown in Figure 2.7.

Two strategies have been proposed for the local correction of non-linear errors in the LHC experimental IRs. The first method compensates for the magnetic errors in IR elements via the local minimization of selected resonance driving terms between the *D1* separation dipoles left and right of the IP [86]. The second method is based upon a compensation of the multipoles locally either side of the IP [141]. Both strategies require an accurate magnetic model of the LHC insertion regions from which to calculate corrections. Magnetic measurements performed on the LHC magnets during construction provide a foundation for

such a model, but must be verified and refined though beam-based studies of the non-linear dynamics. Any corrections determined using these methods must also be commissioned with beam-based measurements at safe intensities prior to their inclusion in operation for luminosity production.

This chapter is concerned with the beam-based study of non-linear errors in the LHC experimental insertions, and the resulting effort to simulate and correct the observed errors. Section 6.2 introduces the method used to perform the beam-based measurements, Section 6.3 then provides details of the model to which these measurements are compared. Section 6.4 presents the results of parasitic studies performed on IR2, which demonstrated the validity of this method in the LHC, and Section 6.5 presents the results of the first dedicated studies of the IR non-linearity performed in IR1 and IR5, including the results of the first attempt at local corrections of the errors in IR1.

6.2 Beam-based study of IR non-linearity

Beam-based study of non-linear magnetic errors can be performed by examining feed-down [25] to easily observed beam properties. Such a strategy was employed with some success at RHIC, where an attempt was made to correct non-linear errors in the RHIC IRs by minimizing tune shifts under the influence of selected closed orbit bumps [142]. Linear coupling was held constant in the RHIC method.

The non-linear errors in the LHC experimental insertions have also been studied though their feed-down, however the goal of the beam-based studies in this case is not, as attempted at RHIC, a direct compensation of the relevant shifts in beam properties, but rather the validation and refinement of the LHC magnetic model in the insertions. It is from this model that eventual corrections may be calculated. This is considered to be a safer technique, as the risk of incorrectly compensating a shift to the beam properties with the wrong multipole (and so inadvertently increasing the non-linearity, while appearing to correct the machine) is reduced.

In contrast to the method employed at RHIC, in the LHC non-linear multipoles in the IRs have been examined through their feed-down to both unconstrained (*'free'*) tune ($Q_{x,y}$)

and unconstrained (*'free'*) linear coupling ($|C^-|$). This method has a number of advantages with respect to the examination of feed-down to tune with controlled coupling: all multipoles may be examined simultaneously and the studies may be performed parasitically; however it also introduces complications: notably the possibility for large changes in linear coupling to drive shifts in the observed tune split, and the introduction of additional complexities in the simulation effort.

Table 6.1 summarizes the feed-down of normal and skew non-linear multipoles, due to horizontal or vertical displacement from the magnetic axis, generating shifts in tune (ΔQ) and linear coupling ($\Delta|C^-|$). The variation of the tune and coupling is dependent on the order of the feed-down: a first order feed-down ($\Delta n = 1$: for example a normal sextupole, $n = 3$, feeding down to a normal quadrupole, $n = 2$, resulting in a tune shift) will exhibit a linear variation with the amplitude of the displacement, a second order feed-down ($\Delta n = 2$: for example a normal octupole, $n = 4$, feeding down to a normal quadrupole, $n = 2$, resulting in a tune shift) will exhibit a quadratic variation with the amplitude of displacement, and so forth. In principle this allows for the identification of a multipole from the observed change in tune and coupling upon the application of varying amplitude closed orbit bumps through the IR.

Table 6.1: Feed-down to tune (ΔQ) and coupling ($\Delta|C^-|$) from non-linear multipoles, due to horizontal or vertical displacement from the magnetic axis. In this notation b_3 is a normal sextupole, a_3 a skew sextupole, similarly for higher orders. The order of the feed-down to tune/coupling is indicated.

	1st order		2nd order		3rd order		4th order	
Feed-down order								
Multipole	$\mathbf{b}_3$	$\mathbf{a}_3$	$\mathbf{b}_4$	$\mathbf{a}_4$	$\mathbf{b}_5$	$\mathbf{a}_5$	$\mathbf{b}_6$	...
Horizontal displacement	ΔQ	$\Delta\|C^-\|$	ΔQ	$\Delta\|C^-\|$	ΔQ	$\Delta\|C^-\|$	ΔQ	...
Vertical displacement	$\Delta\|C^-\|$	ΔQ	ΔQ	$\Delta\|C^-\|$	$\Delta\|C^-\|$	ΔQ	ΔQ	...

For the closed orbit bumps considered in these studies, the value of the crossing angle at the interaction point (defined in Section 2.1.2) may be taken as an appropriate figure of merit to characterize the amplitude of the bump through the insertion region. Indeed, during many of the studies presented in this chapter it was the dedicated crossing bumps which were varied in order to examine the feed-down.

Tune and linear coupling in the LHC may be measured by the Base-Band Tune (BBQ) system [97]. As described in Chapter 2.3, the BBQ provides passive, continuous monitoring of the beam spectra from turn-by-turn beam position data, recorded by a single BPM located in IR4. Values for the tune and linear coupling are logged in $0.5\,\mathrm{s}$ intervals. As the BBQ system utilizes only a single BPM it cannot distinguish the sum and difference coupling in the beam spectra, and in fact measures a mixture of C^+ and C^-. In practice the linear coupling in the LHC is dominated by the difference resonance and $|C_{BBQ}| \approx |C^-|$.

To study the feed-down from non-linear errors, closed orbit bumps through the IR were varied in a series of steps, pausing after each trim to collect data from the BBQ. Typically the length of such trim plateaus was of the order of 30 to 60 seconds. An example of raw tune and coupling data measured by the LHC BBQ during a parasitic study of the feed-down is shown in Fig. 6.1 as a function of time. Where necessary a manual cleaning of the BBQ data was performed, in order to assist with the removal of noise and spectral lines misidentified by the BBQ. In this manual cleaning procedure cuts were applied to the data within a given plateau, the mean and standard deviation of the retained BBQ data were taken as the value and uncertainty on the tune and coupling measurements. An example of the cleaning process is shown in Fig. 6.2.

Small transverse excitation may be applied to the LHC beams to improve the quality of the BBQ data (‘*chirping*’). When possible, such a chirp was applied during the studies presented in this chapter, however during parasitic studies it was not always possible to maintain the chirp. The significant reduction in data quality observed around $21{:}45$ in Fig. 6.1 corresponded to the deactivation of the chirp midway through the measurement. In this case manual cleaning was essential in order to retrieve worthwhile data from the BBQ.

The tunes and linear coupling determined by this method were examined for dependence on the applied crossing angle trim at an IP, the observed variations providing insights into the non-linear multipoles present in the insertion region.

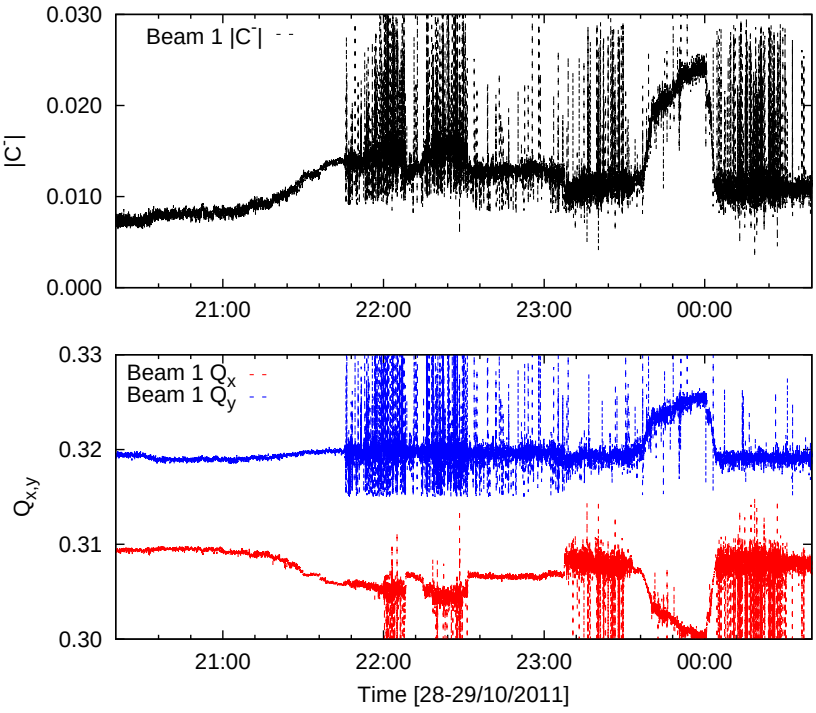

Figure 6.1: An example of raw coupling (top) and tune (bottom) data recorded by the LHC BBQ and plotted versus time.

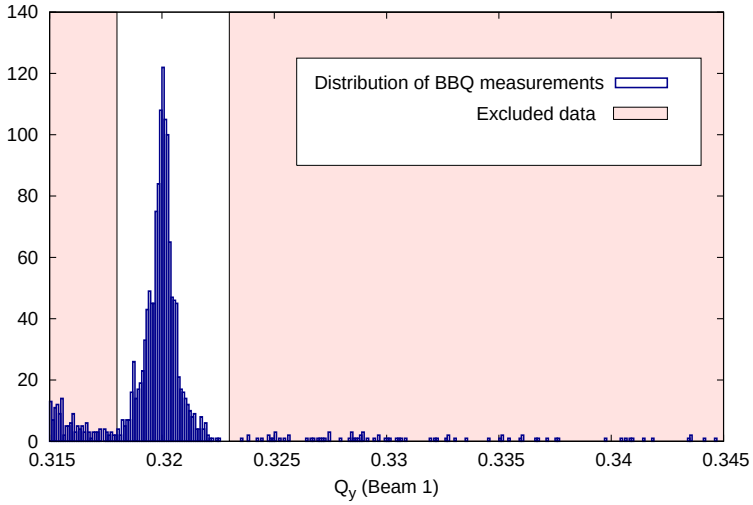

Figure 6.2: An example demonstrating the manual cleaning of BBQ data within a trim plateau.

6.3 Simulation of the IR non-linearity

As described in the preceding section, the goal of the beam-based measurements is the validation and refinement of the LHC magnetic model in the IRs. To this end it was necessary to compare the observed dependence of tune and linear coupling on crossing angle with the predictions of the LHC model.

Estimates of magnetic errors generated by WISE[1] [87, 89] (based on magnetic measurements performed on the LHC during construction) from order (b_3, a_3) to (b_{15}, a_{15}) were applied to the triplet quadrupoles ($Q_{1,2,3}$), the separation dipoles ($D_{1,2}$), and the matching quadrupoles ($Q_{4,5,6,7}$) in experimental insertions in a thin lattice MAD-X [48] model of the LHC. Closed orbit bumps, equivalent in terms of the applied magnetic trims to those implemented in the real machine, were applied to this model. Predictions of the variation in tune and linear coupling with crossing angle, as determined from these simulations, were then compared with observations. The coupling in the MAD-X model was examined by determining the minimum tune split in the model at each trim plateau. This determines the magnitude of the difference coupling coefficient which dominates the linear coupling in the LHC: $|\delta Q_{min}| = |C^-|$. The tunes and linear coupling at the start of the simulated crossing angle scan were matched in MAD-X to reproduce the initial conditions of the beam-based study. The necessity of both matching the coupling and determining the $|\delta Q_{min}|$ in the model made the use of a thick lattice model with PTC [50] impractical for these simulations, as the relevant procedures were too time consuming, forcing the use of the thin lattice model in MAD-X.

The matching of the simulated linear coupling to the initial conditions of the measurement is not necessarily straightforward. Linear coupling is driven by two resonance driving terms (RDTs): f_{1001} driving the difference coupling resonance, and f_{1010} driving the sum coupling resonance. Of relevance to the LHC is the f_{1001} RDT, related to the difference coupling coefficient though Eq.(6.1) [27], where $\overline{|f_{1001}|}$ is the mean amplitude of the f_{1001} RDT around the ring.

$$|C^-| \approx 4|Q_x - Q_y| \, \overline{|f_{1001}|} \tag{6.1}$$

[1] WISE, the Windows Interface to Simulation Errors, was introduced in Chapter 2.1.3.

Resonance driving terms are complex quantities. The coupling measurement obtained from the LHC BBQ provides $|C^-|$, but does not provide details of the phase of f_{1001}. Feed-down to a skew-quadrupole in the IR introduces a Δf_{1001}, which is summed with the initial f_{1001} of the machine. The observed change in $|C^-|$ depends therefore on the relative phase of Δf_{1001} to the initial f_{1001}. While the magnitude of the initial f_{1001} may be known, this ambiguity in the phase may result in an ambiguity of the simulated evolution of $|C^-|$ with changing crossing angle. This may be overcome in two ways. The amplitude and phase of the f_{1001} may be measured around the LHC ring by performing a spectral analysis of betatron oscillations excited by an AC-dipole [57]. Preferably, if the initial coupling is small the question of the RDT phase is rendered moot, and the simulated coupling can be matched to zero at the crossing angle corresponding to the observed minimum. It is in any case worth ensuring the linear coupling is well corrected prior to measurements as this also reduces the chance of a growth in $|C^-|$ affecting the measured tunes.

6.4 Parasitic demonstration in IR2

IR2 houses the Alice experiment, which during normal operation for proton-proton (**p-p**) collisions does not run with tightly squeezed beams at the IP ($\beta^* = 3\,\mathrm{m}$ during 2012 **p-p** luminosity production). During operation for heavy ion collisions (**Pb-Pb** or **p-Pb**) however, the beta function at the IP is significantly reduced ($\beta^* = 0.8\,\mathrm{m}$ during 2013 **p-Pb** luminosity production). As a consequence, correction of the non-linear errors in IR2 is of particular interest for heavy ion operation.

To demonstrate, as described in Sections 6.2 and 6.3, that the non-linear beam dynamics of the LHC experimental insertions could be examined via feed-down under the influence of varying closed orbit bumps through the IRs, parasitic studies were performed in IR2 at $\beta^*_{IP2} = 1\,\mathrm{m}$. Two opportunities arose to perform these studies during the 2011 commissioning of the LHC for heavy ion collisions: firstly during a test for the reversal of the Alice dipole-spectrometer polarity, and then during local measurements of the mechanical aperture in IR2.

6.4.1 Parasitic study during Alice dipole-spectrometer polarity reversal at $\beta^*_{IP2} = 1\,\mathrm{m}$

In IR2 the Alice detector's dipole-spectrometer generates a so-called *'internal'* crossing angle of $\pm 140\,\mu\mathrm{rad}$ in the vertical plane, dependent on the spectrometer polarity. The internal crossing angle is partially compensated through the application of a vertical closed orbit bump through the IR, generating a so-called *'external'* crossing angle of $\mp 80\,\mu\mathrm{rad}$. Collision data is collected for both polarities of the dipole-spectrometer, the reversal of the polarity requiring a reversal of the sign of the external crossing angle. As the pre-collision LHC optics are optimized for the $-80\,\mu\mathrm{rad}$ configuration, the reversal of the external crossing angle is performed following the squeezing of the β^* to their operation values. Figure 6.3 shows the simulated orbit through IR2 with internal ($+140\,\mu\mathrm{rad}$) and internal+external ($+140 - 80\,\mu\mathrm{rad}$) crossing angle bumps applied.

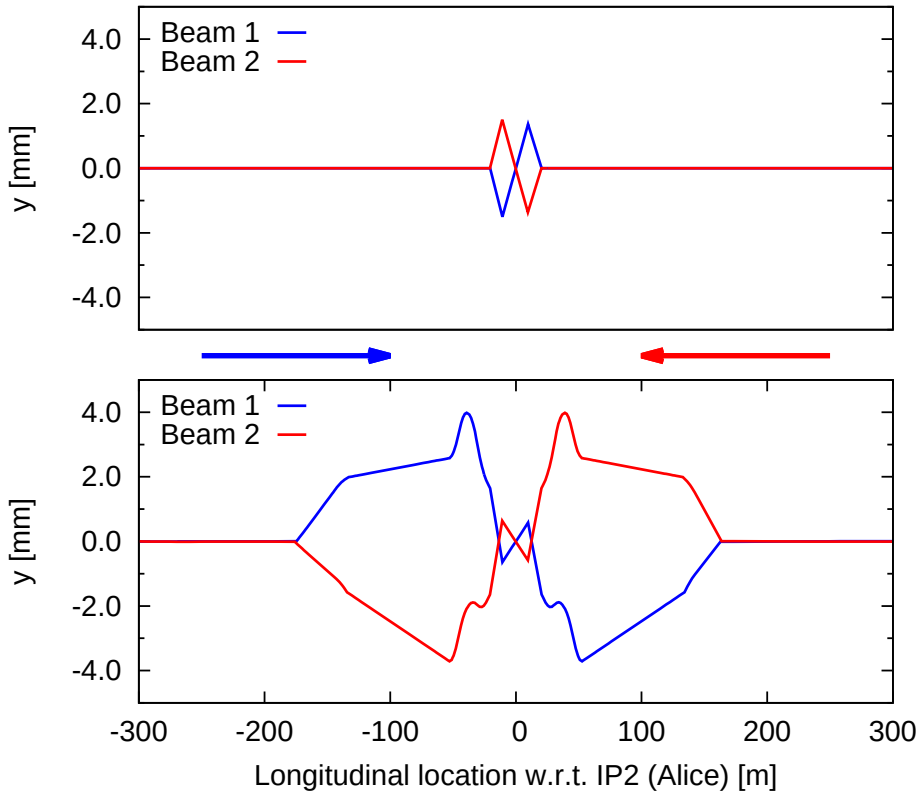

Figure 6.3: Simulated orbit in IR2 with internal ($+140\,\mu\mathrm{rad}$) and internal+external ($+140 - 80\,\mu\mathrm{rad}$) crossing angle bumps applied.

The procedure for reversal of the external crossing angle was commissioned with proton beams during an end-of-fill study, prior to the 2011 **Pb-Pb** run [143]. The external crossing angle was varied from $-80\,\mu\mathrm{rad}$ to $+80\,\mu\mathrm{rad}$ in a series of small steps, allowing a pause following each change in the crossing angle. Consequently, the tune and coupling data measured by the BBQ during the reversal of the crossing angle could be used to study feed-down from non-linear errors in the IR2 magnets. As the study was performed at end-of-fill, a large number of high intensity bunches (compared to typical optics measurement conditions) were present in the machine. The raw BBQ data was therefore of a very high quality and no manual cleaning was performed. The chirp was depowered during most of the scan.

Figures 6.4 and 6.5 show the simulated and measured tunes and coupling during the scan of the IR2 external crossing angle in LHC Beam 1 and Beam 2 respectively. Linear coupling has been matched to zero at the crossing angle corresponding to its projected minima ($-80\,\mu\mathrm{rad}$ in Beam 1 and $-30\,\mu\mathrm{rad}$ in Beam 2).

Shifts to the tune and coupling are dominated by a linear variation of the $|C^-|$, corresponding to feed down from b_3. The simulated variation of the coupling shows an excellent agreement with the observations, with the exception of a brief jump between $-40\,\mu\mathrm{rad}$ and $-20\,\mu\mathrm{rad}$. This departure and return of the measured data to the simulation corresponded to the powering, then depowering, of the chirp excitation. Such an influence of the chirp upon the BBQ measurement is not generally observed in the LHC, and its appearance in this data is not understood. Nonetheless the observed discrepancy at the three affected data points is not believed to significantly impact upon the conclusion that the measured and simulated coupling are in good agreement.

Variations of the tunes are significantly smaller than of the coupling (by a factor of ~ 3). In the horizontal plane the tune is roughly consistent with the predictions of the magnetic model. In the vertical plane the general trend of the tune shift is consistent with expectations from the model, however the measured value appears to oscillate about the prediction from simulation with an amplitude $\sim 3 \times 10^{-4}$. Such a variation is deemed to be negligible.

During reversal of the external crossing angle no measurement of f_{1001} was possible for reasons of machine protection. This was not significant as the initial $|C^-|$ was small compared to that generated by the feed-down, and it was possible to match the coupling of

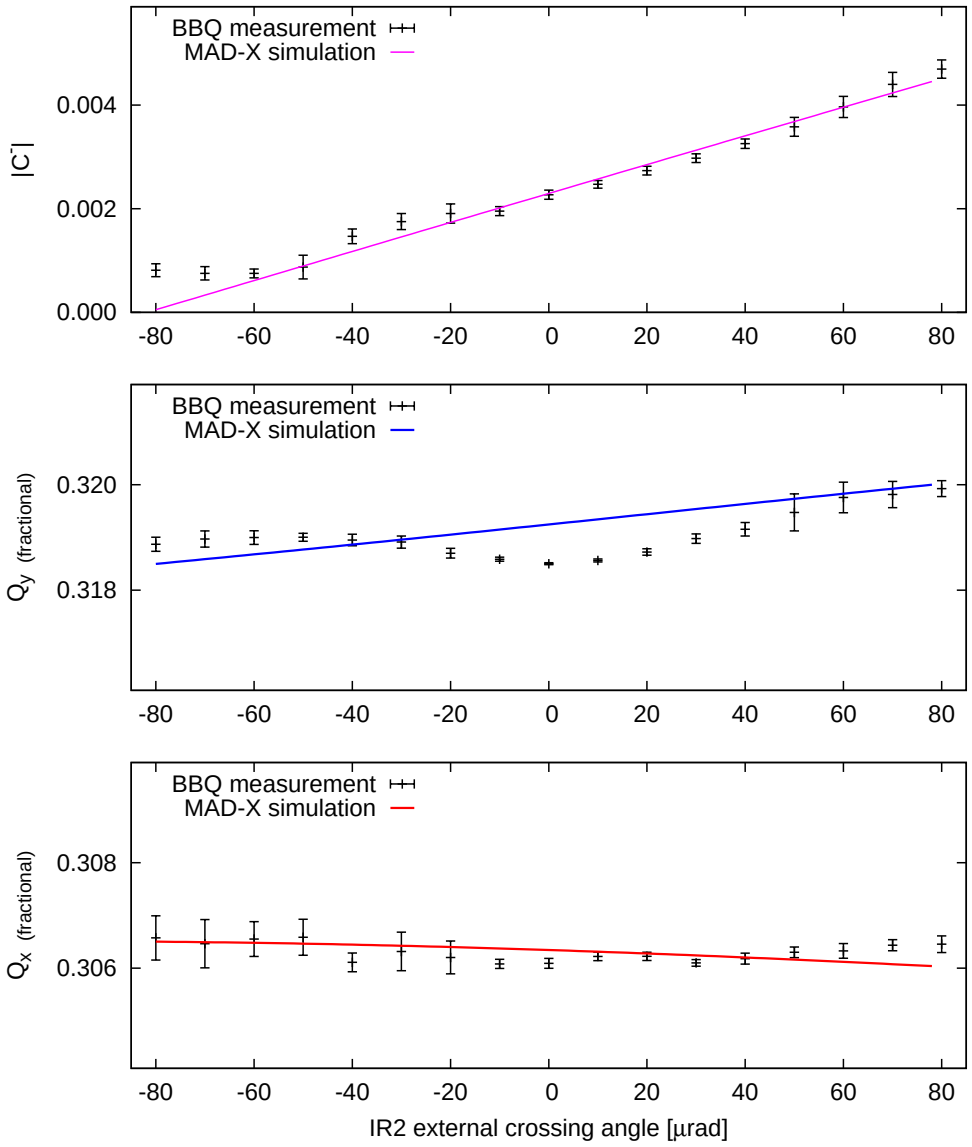

Figure 6.4: Modelled and measured tunes and coupling of LHC Beam 1, plotted versus the external crossing angle. The model has been matched to produce zero coupling at the crossing angles corresponding with the projected minima of the observed $|C^-|$ variation.

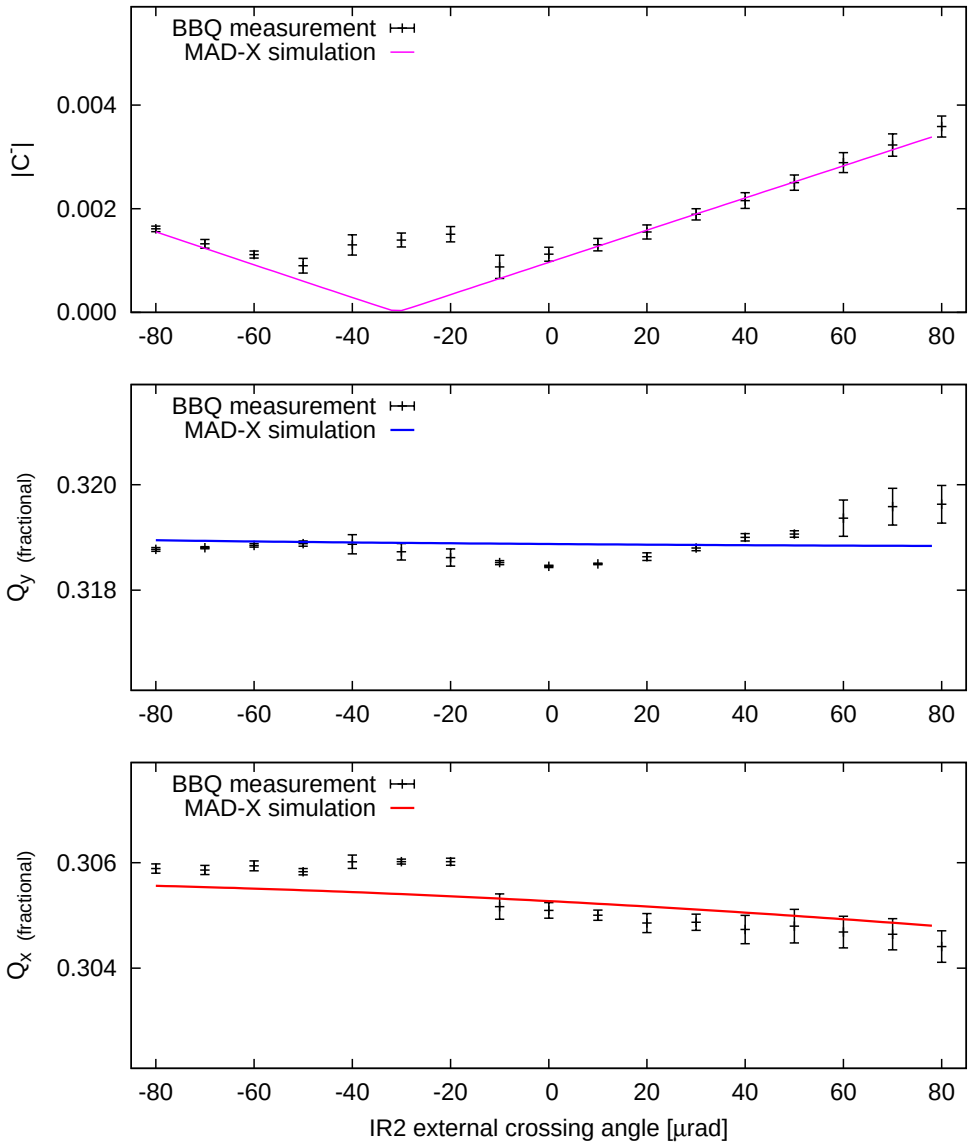

Figure 6.5: Modelled and measured tunes and coupling of LHC Beam 2, plotted versus the external crossing angle. The model has been matched to produce zero coupling at the crossing angles corresponding with the projected minima of the observed $|C^-|$ variation.

the model to zero. Figure 6.6 however, illustrates that given an appropriate phase of f_{1001} the model reproduces the observed variation irrespective of the matching point. In Fig. 6.6 the f_{1001} of both beams was matched to reproduce the measured $|C^-|$ at the beginning of the scan ($-80\,\mu\mathrm{rad}$), the phase of the f_{1001} was then selected to reproduce the observed variation of $|C^-|$. This demonstrates that if the initial phase of the f_{1001} is known it is possible to make an accurate prediction of the variation of $|C^-|$, even if the magnitude of the initial $|C^-|$ is not negligible compared to that generated through feed-down.

Variations in the simulation between the sixty instances of the LHC defined by the WISE seeds were negligible for this configuration of the optics in IR2.

6.4.2 Parasitic study during local aperture measurements in IR2 at $\beta^*_{IP2} = 1\,\mathrm{m}$

In preparation for the 2011 **Pb-Pb** run it was necessary to commission a new optics of the LHC, with the β^* in IP2 squeezed to $1\,\mathrm{m}$ (during the preceding **p-p** run IP2 operated at $\beta^* = 10\,\mathrm{m}$). Local measurements of the physical aperture in IR2 were a necessary component of the commissioning effort, allowing determination of the available parameter space in β^* and crossing angle. Measurements of the local aperture were performed on the $\beta^*_{IP2} = 1\,\mathrm{m}$ optics with depowered Landau octupoles, using a method based on the application of closed orbit bumps through the IR [144]. The measurements were performed with proton beams. The variation of the closed orbit bumps during these measurements allowed for parasitic studies of the feed-down from non-linear errors to free tune and free linear coupling.

During the aperture study several different closed orbit bumps were applied. The initial state of the machine was defined by the (vertical) internal dipole-spectrometer bump and the (vertical) external crossing angle, together with the (horizontal) separation bump. Throughout the measurement the external crossing angle and separation bump were held constant at $-80\,\mu\mathrm{rad}$ and $0.7\,\mathrm{mm}$ respectively. The IR2 luminosity optimization knobs[2] (known as *Lumiscan* or *Anglescan* knobs) were then used to apply additional closed orbit bumps on top of the nominal crossing and separation. The Lumiscan knobs lacked sufficient strength to reach the aperture, and in the vertical plane two further knobs: *APERT* and *APERSCAN*,

[2] A *'knob'* is a set of magnet trims designed to generate a specific shift in the beam properties.

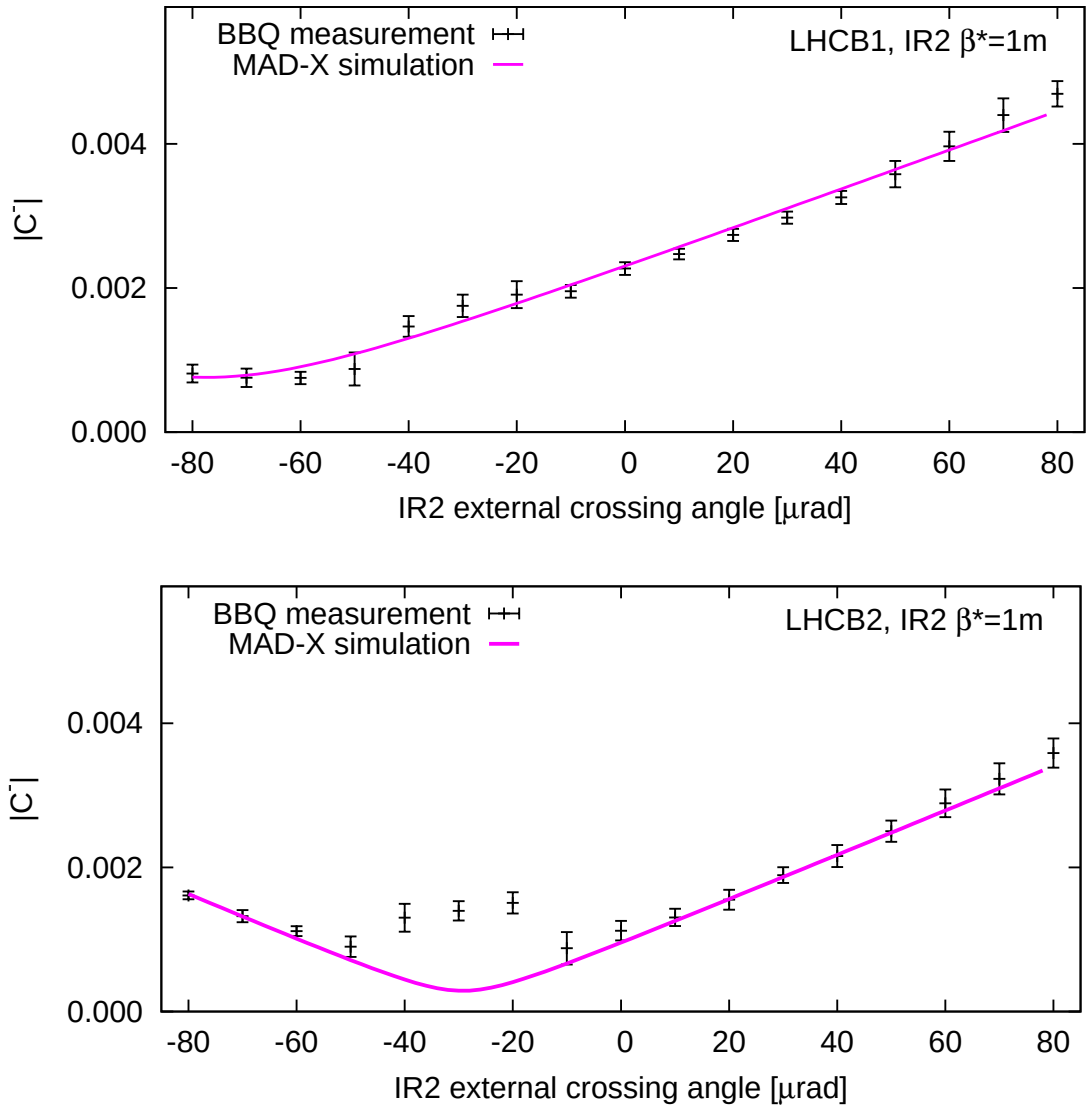

Figure 6.6: Modelled and measured coupling plotted versus the external crossing angle. $|f_{1001}|$ in the model was matched to reproduce the measured amplitude of $|C^-|$ at the beginning of the scan ($-80\,\mu$rad). The phase of f_{1001} was selected to give agreement with the observed data. Data is shown for Beam 1 (top) and Beam 2 (bottom).

were used to reach higher excursions. Figure 6.7 shows MAD-X simulations of how the final closed orbit bump in the vertical plane was built up from its component knobs. Initially only the effect of the spectrometer bump is shown (Fig. 6.7a). Figure 6.7b shows the effect of adding the crossing and separation bumps on top of that generated by the spectrometer. Figures 6.7c, 6.7d and 6.7e show the effect of the maximum trim of the Lumiscan knob, then adding the APERT and finally the APERSCAN knobs.

As described in Section 6.3, simulations of the feed-down to tune and coupling have been performed using a thin lattice model in MAD-X . In the case of the LHC knobs used to generate the external crossing angle and the separation bump re-matched versions exist which reproduce the applied crossing angle in the thin lattice. No such re-matched versions of the Lumiscan, APERSCAN, and APERT knobs exist, and the knob definitions applied in simulation are identical to those applied in the real machine. To assess the size of the error introduced into the model due to the use of the thin lattice together with the real knob definitions, the total crossing angle in the model was compared to the theoretical expectation for the trims applied during the aperture measurement. Figure 6.8 plots the difference between the simulated crossing angle (defined by the ratio of the transverse momenta to the references momenta) and the expected value. The discrepancy in a thick lattice MAD-X model is also shown for comparison. The error introduced by using the thin lattice model is deemed to be small, and may be neglected.

During the aperture measurements tune and coupling data was initially of a high quality. As the aperture was approached however it was necessary to remove the chirp from the beam to avoid interference with the loss measurements, and the quality of the data dropped correspondingly. The BBQ data shown previously in Fig. 6.1 correspond to these measurements. Manual cleaning of the BBQ data was therefore essential for study of the feed-down. Figure 6.9 demonstrates the improvement in data quality achieved for LHC Beam 2. Similar improvements were gained in the Beam 1 data.

The manual cleaning was highly effective. Most noise in the BBQ data arose from a minority of misidentified spectral lines which were straightforward to exclude, though some of the data at large crossing angles had to be excluded as the tunes passed outwith the frequency search window applied by the BBQ. Cleaning revealed a small difference in the Beam 2 $|C^-|$

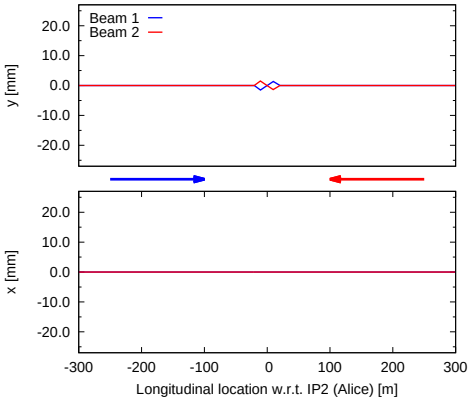

(a) Spectrometer bump.

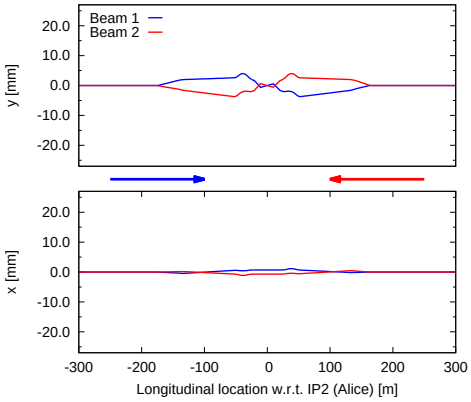

(b) Spectrometer bump + nominal external crossing angle and separation bumps.

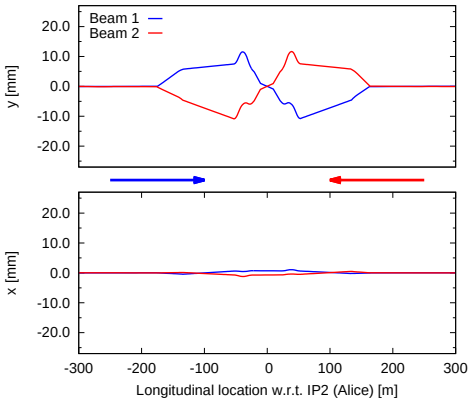

(c) Spectrometer, crossing, and separation bumps + maximum vertical trim of the Lumiscan knobs.

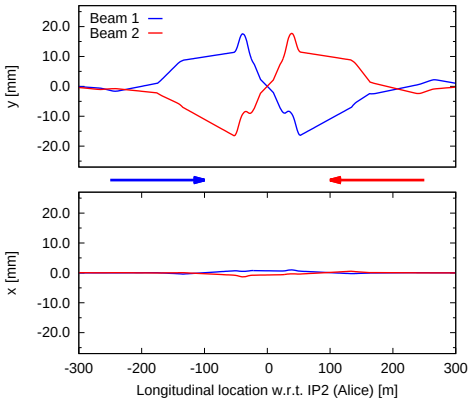

(d) Spectrometer, crossing/separation and Lumiscan bumps + maximum vertical trim of the APERT knob.

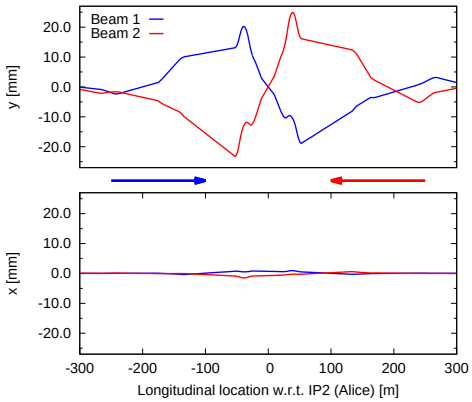

(e) Spectrometer, crossing/separation, Lumiscan and APERT bumps + maximum vertical trims of the APERSCAN knobs.

Figure 6.7: Simulated orbit through IR2, for maximum trims of the closed orbit bumps used during the vertical aperture studies.

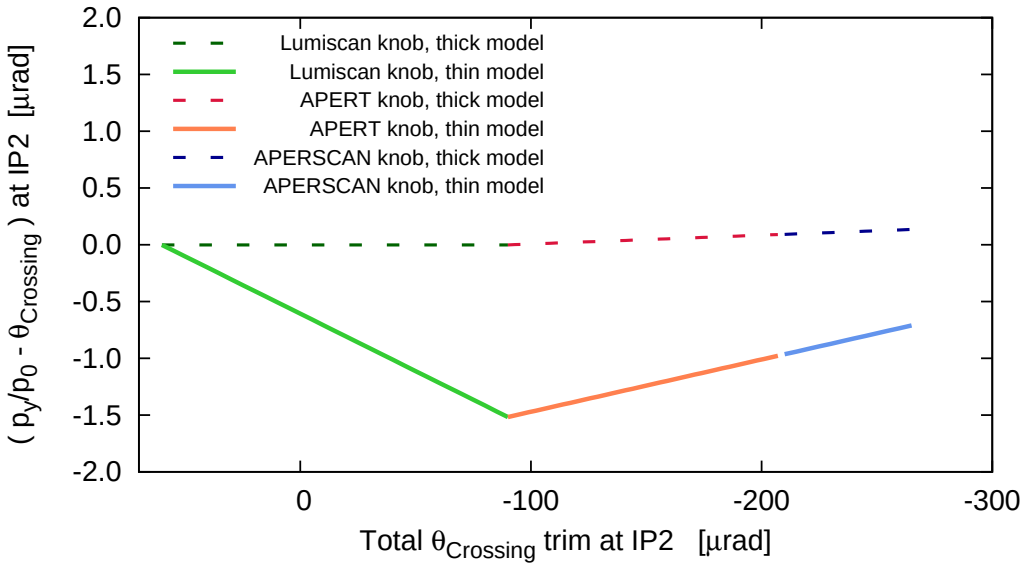

Figure 6.8: Comparison of the modelled and expected crossing angles in IP2, for trims of the Lumiscan, APERT, and APERSCAN knobs used during local IR2 aperture measurements in 2011. Results are shown for both thick and thin lattice models. Both models used the basic LHC lattice with no magnetic errors applied.

data between the APERT and APERSCAN knobs where the measurements overlap. A corresponding shift was not observed in Beam 1. It is possible that different types of orbit bump may reveal differing aspects of the non-linear errors, however significant conclusions cannot be reached from this data, as the raw measurement was of a low quality and there was a delay in the implementation of the APERSCAN knob upon completion of the APERT knob scan, therefore the discrepancy may just reflect a drift in the coupling.

Unlike the measurements presented in Section 6.4.1 the initial coupling of LHC during the aperture measurements was not small in comparison to the coupling generated through feed-down, and the simulated coupling could not be matched to zero. As part of the commissioning procedure however, linear optics measurements had been performed on the $\beta^*_{IP2} = 1\,\mathrm{m}$ configuration during the LHC fill immediately prior to that used for study of the aperture. The phase of f_{1001} in BPMs adjacent to the IR2 separation dipoles, measured during the linear optics studies, was therefore used as a constraint for the matching to initial conditions in the MAD-X simulation of the aperture measurement. Figures 6.10 and 6.11 present comparisons of cleaned BBQ data to the MAD-X simulation in Beam 1 and Beam 2 respectively.

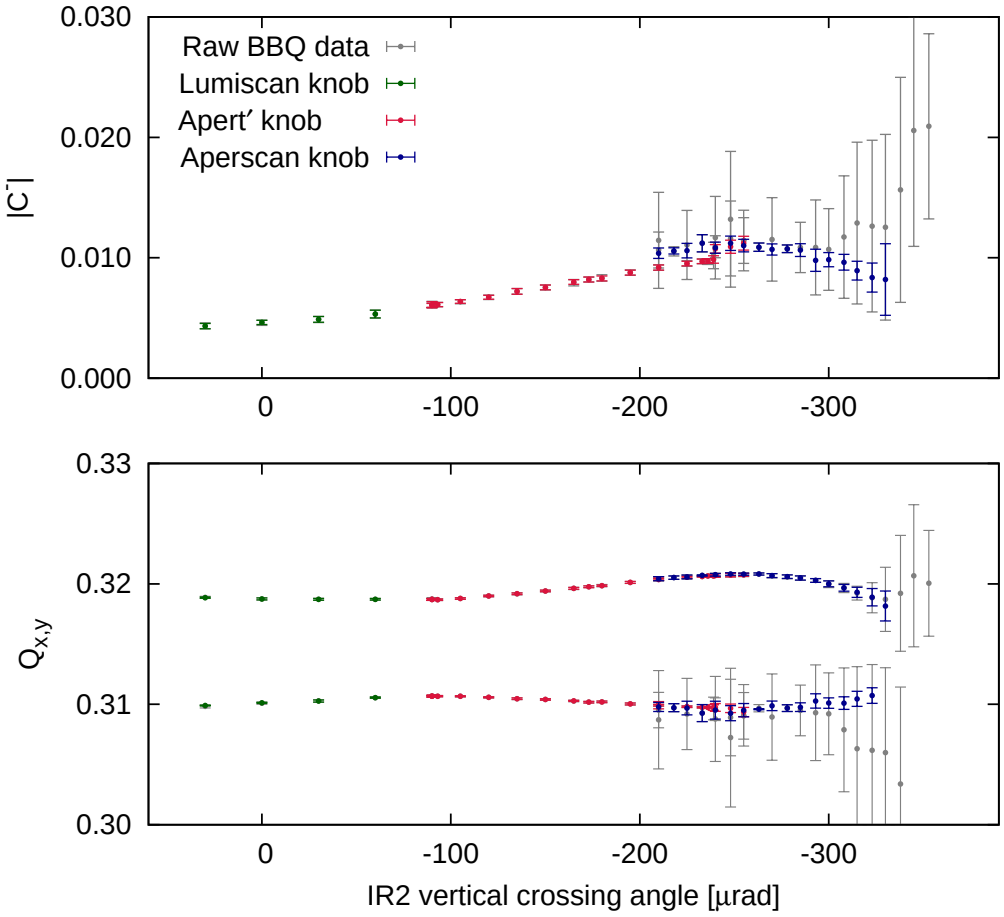

Figure 6.9: Manual cleaning of Beam 2 BBQ data obtained during local aperture measurements in IR2. Uncleaned BBQ data is plotted in grey, cleaned data in colour.

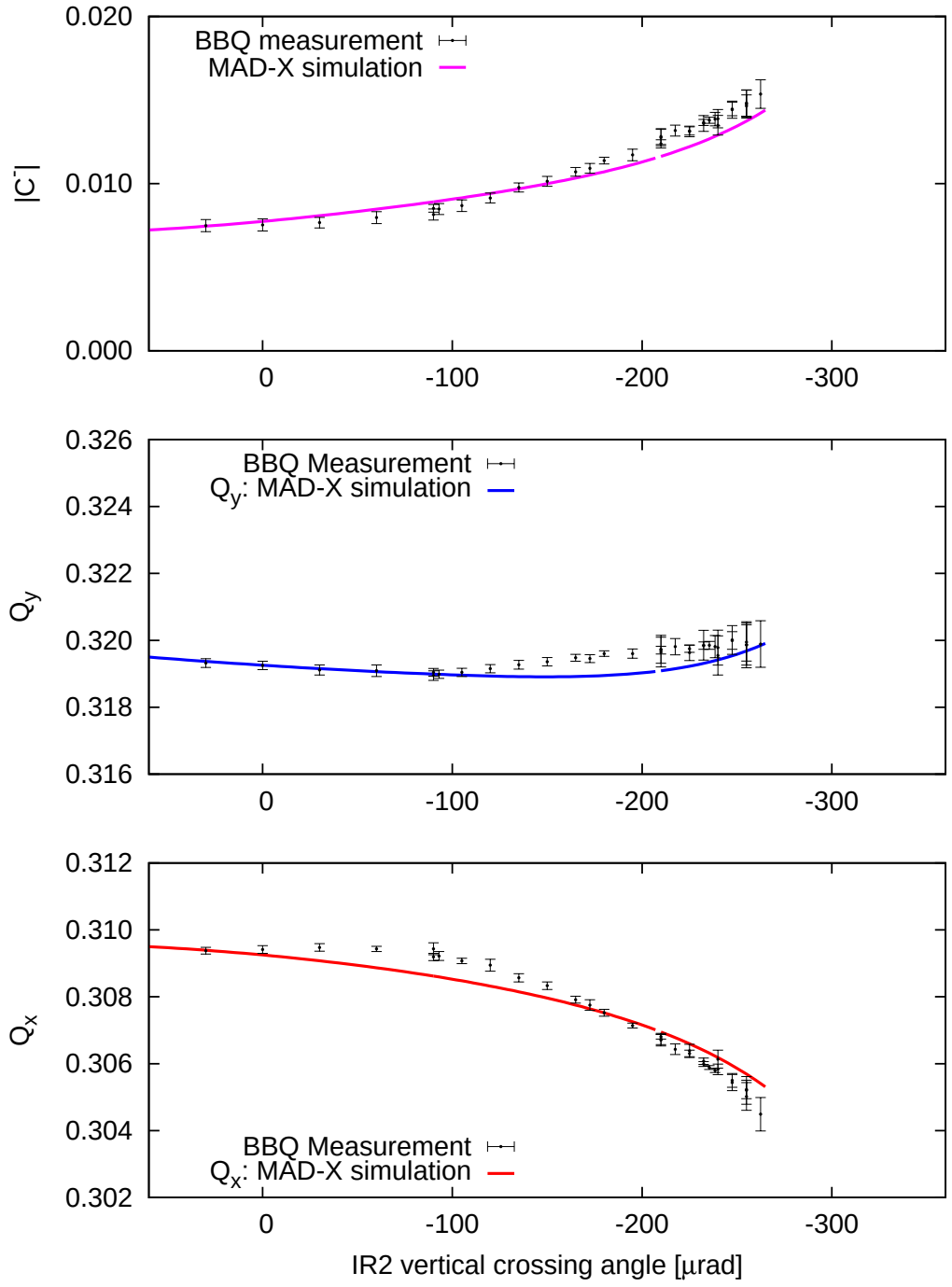

Figure 6.10: Modelled and measured tune and coupling of LHC Beam 1, plotted versus the total crossing angle at IP2 during local aperture measurements of IR2 in 2011.

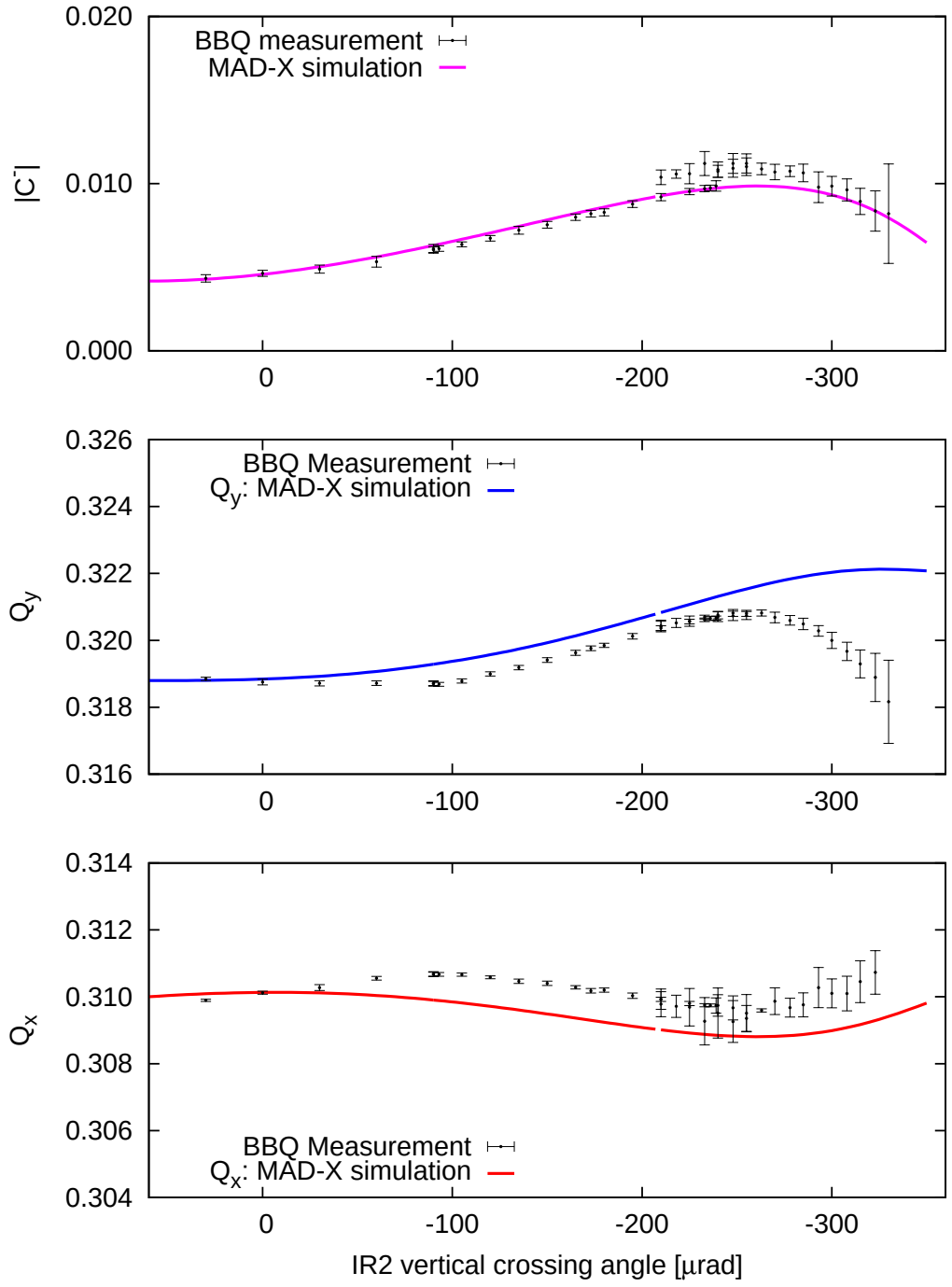

Figure 6.11: Modelled and measured tune and coupling of LHC Beam 2, plotted versus the total crossing angle at IP2 during local aperture measurements of IR2 in 2011.

Clear shifts to the coupling and tune were seen during the aperture measurement. In particular feed-down to coupling was observed from multipoles of order higher than b_3, which it had not been possible to observe during the study of crossing angle reversal. The relatively poor quality of the linear coupling correction at the start of the study complicates the interpretation of the available tune data, as the δQ_{min} defined by the growing $|C^-|$ appears to have perturbed the tunes. A good agreement is seen between the observations and the predictions of the magnetic model for the coupling data. As found in Section 6.4.1 the feed-down is dominated by the b_3 component of the separation dipoles. The agreement in the tune data is less precise, though the general trends appear consistent and as previously mentioned the situation is complicated by the impact of the coupling on the tune split. Discrepancies between the modelled and measured tunes are particularly apparent in LHC Beam 2 at very large crossing angles, potentially indicating a discrepancy with the model in the higher order multipoles. Limitations from the aperture prevented Beam 1 reaching amplitudes where the Beam 2 discrepancy became significant. Variations between the WISE seeds were negligible.

6.4.3 Proof of principle: measurement and correction of non-linear errors in the LHC experimental insertions

The parasitic studies performed on IR2 during 2011 demonstrated that it was possible to examine non-linear errors in low-β insertions of the LHC, using a method based upon the feed-down to both free tune and free linear coupling under the influence of varying closed orbit bumps. Feed-down from high order multipoles was observed in both the coupling and the tune. Magnetic measurements of the dominant non-linear errors in IR2, namely the b_3 component of the *D1* separation dipoles, were verified with beam based studies.

In light of the excellent agreement of the observed b_3 errors with the magnetic model, correction of these errors should be possible. Table 6.2 presents corrections for b_3 errors, calculated from the magnetic model at $\beta^*_{IP2} = 1\,\mathrm{m}$ and $3.5\,\mathrm{TeV}$, using the method of local compensation of the dominant normal sextupole RDTs with correctors either side of the IP. The required trims were well within the capacity of the correctors. Figure 6.12 illustrates the predicted effect of the correction on the feed-down to free linear coupling. Unfortunately, during the LHC's first operational run (*'Run 1'*) several non-linear correctors on one side of

IP2 were out of commission, including those for b_3. Local correction of the b_3 errors on one side of the IR is still feasible, however due to the unavailability of the correctors, and a lack of beam time, no attempt was made to perform corrections for the non-linear errors in IR2 during Run 1.

Table 6.2: Corrections for the b_3 errors in IR2. Corrections were calculated in MAD-X using magnetic measurement data verified with beam-based studies. These corrections were determined for $\beta^*_{IP2} = 1\,\mathrm{m}$ at $3.5\,\mathrm{TeV}$.

Corrector	Strength k $[\mathrm{m}^{-3}]$	Strength $[\%_{max}]$
KCSX.L2	-0.00482	-57.41
KCSX.R2	0.00085	10.15

A number of discrepancies with the magnetic model were also identified during the parasitic studies of IR2. These effects were either small or only became apparent at large amplitudes, however further study may be of interest once the dominant errors are corrected.

6.5 Dedicated measurement and correction of non-linear errors in IR1 and IR5

The success of the parasitic studies performed on IR2 led to dedicated studies of the feed-down from the non-linear errors in IR1 and IR5, which house the ATLAS and CMS experiments respectively. First dedicated measurements of the errors in IR1 were undertaken at the end of a linear optics study, performed on a new machine configuration with $\beta^* = 0.4\,\mathrm{m}$ in IP1 and IP5. This was followed shortly after by dedicated measurement of the errors in IR5 at the nominal optics ($\beta^* = 0.6\,\mathrm{m}$ in IP1 and IP5), together with a first attempt at correction of the errors in IR1.

6.5.1 Measurement of non-linear errors in IR1 at $\beta^*_{IP1} = 0.4\,\mathrm{m}$

In 2012 an exploratory study of the linear optics was performed on the LHC at $\beta^* = 0.4\,\mathrm{m}$ in IP1 and IP5. At the end of the optics measurements a scan was performed of the vertical

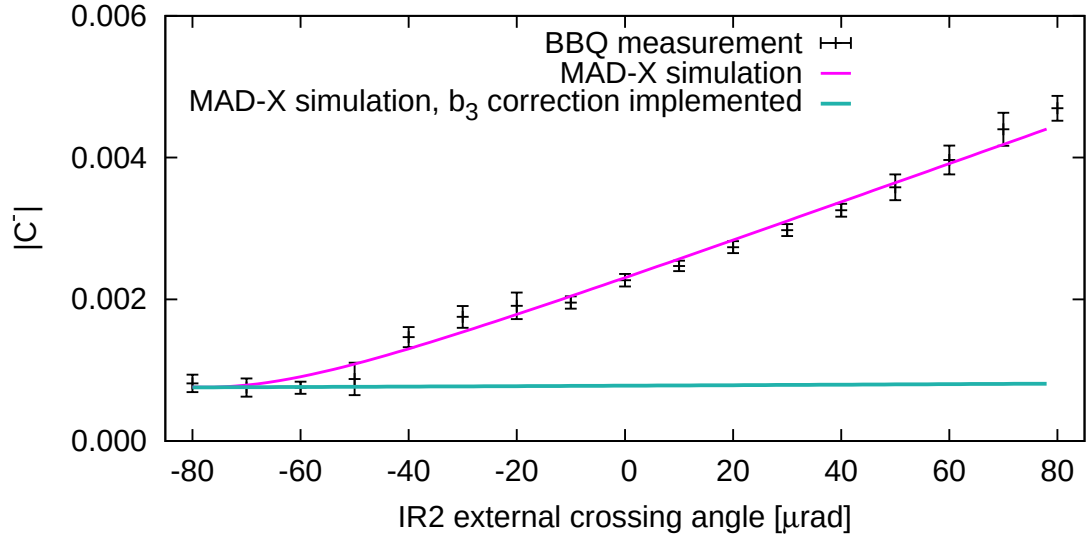

(a) Beam 1

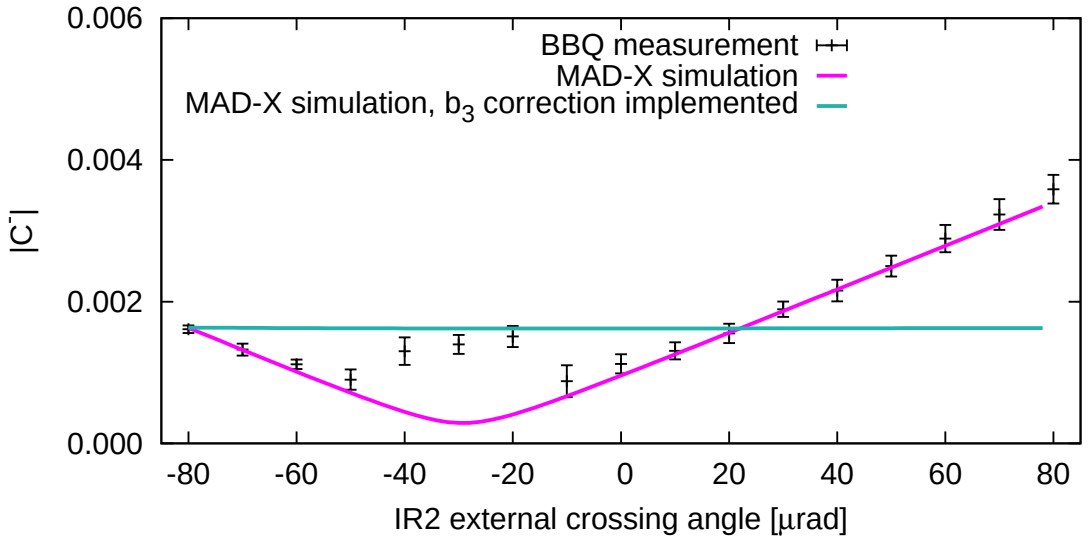

(b) Beam 2

Figure 6.12: Simulated variation of the coupling with IR2 external crossing angle, with and without corrections applied for the b_3 multipole errors in the IR.

crossing angle in IR1 (time was only available to study a single plane of one IP). Feed-down to tune and linear coupling was observed in order to examine the non-linear errors in the insertion. The raw BBQ data obtained throughout the crossing angle scan was of a low quality. Beam 1 data was unusable, however a respectable quality of data was obtained for Beam 2 following manual removal of a number of regularly misidentified spectral lines.

As with the parasitic studies performed for IR2, the feed-down to tune and free coupling were simulated in MAD-X allowing for comparison between the observations and predictions from the magnetic measurements. Initial conditions for the simulation were matched at $0\,\mu\mathrm{rad}$. Tunes and $|C^-|$ were matched to the values obtained from the BBQ, while the phase of the f_{1001} was matched to measurements, obtained immediately prior to the crossing angle scan, at BPMs adjacent to IP1. Figure 6.13 plots the measured and simulated tune and coupling shifts for the scan of the vertical crossing angle in IP1 at $\beta^* = 0.4\,\mathrm{m}$. All sixty WISE seeds are plotted individually. Unlike the studies of IP2 at $\beta^* = 1\,\mathrm{m}$, the variation between seeds is not negligible.

Substantial feed-down is observed to the linear coupling. The measurements and simulation agree, and appear to indicate that the errors in the machine lie towards the extrema of the uncertainty in the magnetic measurements. This should allow for a refinement of the non-linear model of IR1. The feed-down to coupling shows significant contributions from both b_3 and a_4 multipoles. Figure 6.14 demonstrates the effect in simulation of removing the b_3 and the $b_3 + a_4$ errors. WISE seed 4 was utilized for this simulation as it showed a good agreement with the measured coupling.

Correction of b_3 alone still leaves a very substantial coupling variation with crossing angle in the machine at $0.4\,\mathrm{m}$, however during Run 1 the skew octupolar corrector left of point one was out of commission. It is unclear at what point the malfunctioning a_4 corrector may become available, however if it remains out of use local correction of a_4 right of IP1 may be a worthwhile consideration during the LHC's second operational run. The simulation shown in Fig. 6.14 demonstrates that perfect correction of b_3 and a_4 errors should significantly reduce the feed-down to coupling, though some does remain.

As regards the tune, variation of Q_y with the crossing angle shows a good agreement with the observations, though a small discrepancy does seem to appear in the higher order

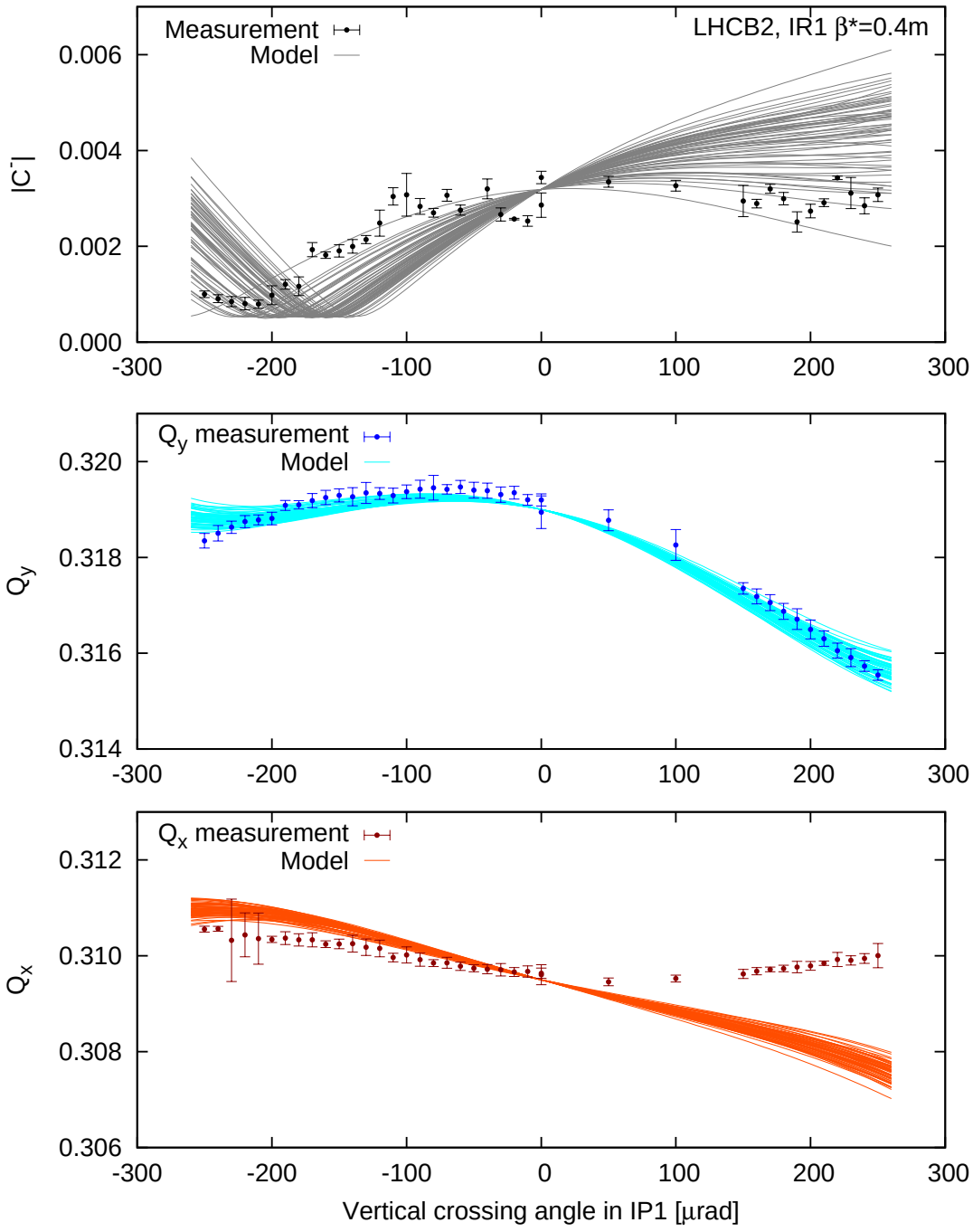

Figure 6.13: Measured and modelled variation of free tune and coupling in LHC Beam 2, during a scan of the (vertical) crossing angle in IR1 at $\beta^* = 0.4\,\mathrm{m}$.

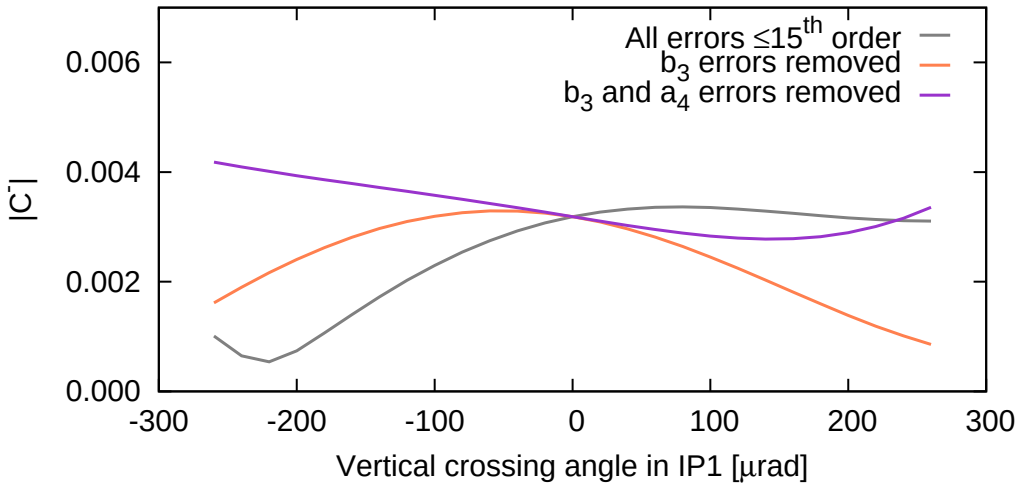

Figure 6.14: Simulated effect in Beam 2 of removing b_3 and $b_3 + a_4$ errors in IR1 at $\beta^* = 0.4\,\mathrm{m}$. The simulation was performed for WISE Seed 4, which showed good agreement with measured coupling shifts.

terms at crossing angles $> 200\,\mu\mathrm{rad}$. The difference between the feed-down to tune of the WISE seeds is significantly smaller for the tune than for the linear coupling, therefore no refinement of the model is possible from this Q_y data.

In the horizontal plane a sizable discrepancy is observed between the measured feed-down and the predictions of the magnetic model. The discrepancy between model and measurement shows both a linear (corresponding to a discrepancy in the a_3 errors) and higher order variation with crossing angle. Polynomial fits to the difference between the modelled and measured change in Q_x with crossing angle were unable to convincingly distinguish between polynomials with $(1^{st} + 2^{nd})$, $(1^{st} + 3^{rd} + 4^{th})$, and $(1^{st} + 2^{nd} + 3^{rd} + 4^{th})$ order terms. The challenge in understanding the errors in IR1 therefore seems to lie firstly in reducing the number of possible combinations of multipoles which may give rise to the observed discrepancy in Q_x. Studies of the feed-down in the horizontal plane may assist in this regard by exchanging sources of odd order variations of tune and coupling (as seen in Tab. 6.1). Studies of the feed-down at different optics or over different ranges of amplitudes should also assist in distinguishing sources of lower and higher order.

With respect to location of the error, that the discrepancy appears only in the horizontal plane suggests it may lie at a location of significantly larger β_x than β_y (though the possibility

of cancellation between different sources of ΔQ_y cannot be ruled out). If the data were available analysis of the Beam 1 tune shifts may assist in the localization of the source, however further studies using different types of orbit bump through the IR may also aid in localization.

During construction measurements were performed of magnet alignments within the LHC. In addition to generating estimates of magnetic errors, WISE may also produce estimates of the geometric errors in the LHC lattice from these measurements [88]. In response to the observed discrepancy in Q_x, geometric errors were incorporated into the MAD-X simulation. As expected the effect of the alignment errors in the IR was negligible, several orders of magnitude below the observed discrepancy, and offers no explanation for the difference between model and measurement.

6.5.2 Correction of non-linear errors in IR1 at $\beta^*_{IP1} = 0.6\,\mathrm{m}$

Shortly after the dedicated study of the non-linear errors in IP1 at $\beta^* = 0.4\,\mathrm{m}$, an opportunity arose to perform a second set of dedicated measurements at $\beta^* = 0.6\,\mathrm{m}$. Due to the brief interlude between the measurements the data obtained during the $0.4\,\mathrm{m}$ study had not been analysed, however it was considered important to make a first attempt at correction of the non-linear errors, prior to the LHC's first long shutdown for maintenance and upgrades, in order to gain experience in preparation for its second operational run. Two scans were therefore performed of the vertical crossing angle in IR1, firstly with corrections for the $a_3 + b_3$ errors applied, then with corrections for the $a_3 + b_3 + b_4$ errors implemented. The corrections were calculated from the magnetic model, using WISE seed 1[3]. A scan of the virgin LHC (the LHC with no corrections applied for the IR non-linearity) was not performed, as data had been collected for the virgin machine at $\beta^*_{IP1} = 0.4\,\mathrm{m}$ the previous day, and beam time was extremely limited.

The data obtained from the BBQ was once more of a low quality. Coupling data was unusable and the quality of the b_3 correction may not be assessed, however after manual cleaning it was possible to examine the feed-down to tune of both LHC beams. Figure 6.15

[3]Seed 1 was chosen arbitrarily, as detailed analysis of the $\beta^*_{IP1} = 0.4\,\mathrm{m}$ measurement had not been performed at the time of the $\beta^*_{IP1} = 0.6\,\mathrm{m}$ measurement.

plots the measured tune of LHC Beam 2 as a function of the vertical crossing angle trim for the scans. The predictions of the MAD-X model at $0.6\,\mathrm{m}$ are shown for all sixty WISE seeds. The upper plot compares the scan with $a_3 + b_3$ corrections implemented, and the lower plot with $a_3 + b_3 + b_4$ corrections.

Results for LHC Beam 2 show a good agreement between the measured feed down and the predictions from simulations. Considering primarily the Q_y data both the a_3 and b_4 corrections appear to have functioned roughly as expected. The upper plot does seem to indicate there may have been a slight overcompensation of the a_3 errors which could be addressed in future corrections. With regard to Q_x it is interesting to observe that the substantial discrepancy between the model and measurement observed at $\beta^* = 0.4\,\mathrm{m}$ is not apparent. A discrepancy does exist, but it is not so pronounced. More detailed analysis of this feature may help shed light on the relevant sources. In spite of the discrepancies however, the application of a_3 and b_4 corrections calculated from the magnetic model did manage to considerably reduce the feed-down to tune. The first attempt at correction of the non-linear errors in the LHC insertions seems to have been broadly successful in LHC Beam 2.

Figure 6.16 shows the result of the crossing angle scans for LHC Beam 1. As with LHC Beam 2 the a_3 correction (Fig. 6.16, top) appears to have functioned roughly as expected, though the overcompensation of a_3 appears to be slightly more pronounced in Beam 1. Of much greater concern however, is that upon application of the corrections for b_4 (Fig. 6.16, bottom) a sizable linear feed-down to tune appears to have been introduced. b_4 errors should generate a quadratic variation of the tune, therefore this cannot be due to a simple mispowering of the corrector. Rather the linear variation of the tune (which may be expected to correspond with an a_3-like perturbation), introduced on powering the b_4 circuits, implies a vertical misalignment of the b_4 correctors with respect to the b_4 sources. The relevant magnets in the IR are common to both beams; that the linear variation was introduced only for LHC Beam 1 implies that the feed-down from b_4 to a_3 is not the result of physical misalignments within the IR, but rather due to a deviation of the Beam 1 orbit through the IR.

It was determined from simulation (taking into account the linear discrepancy identified in the first scan) that a $2.5\,\mathrm{mm}$ misalignment of the the octupolar corrector left of IP1 would

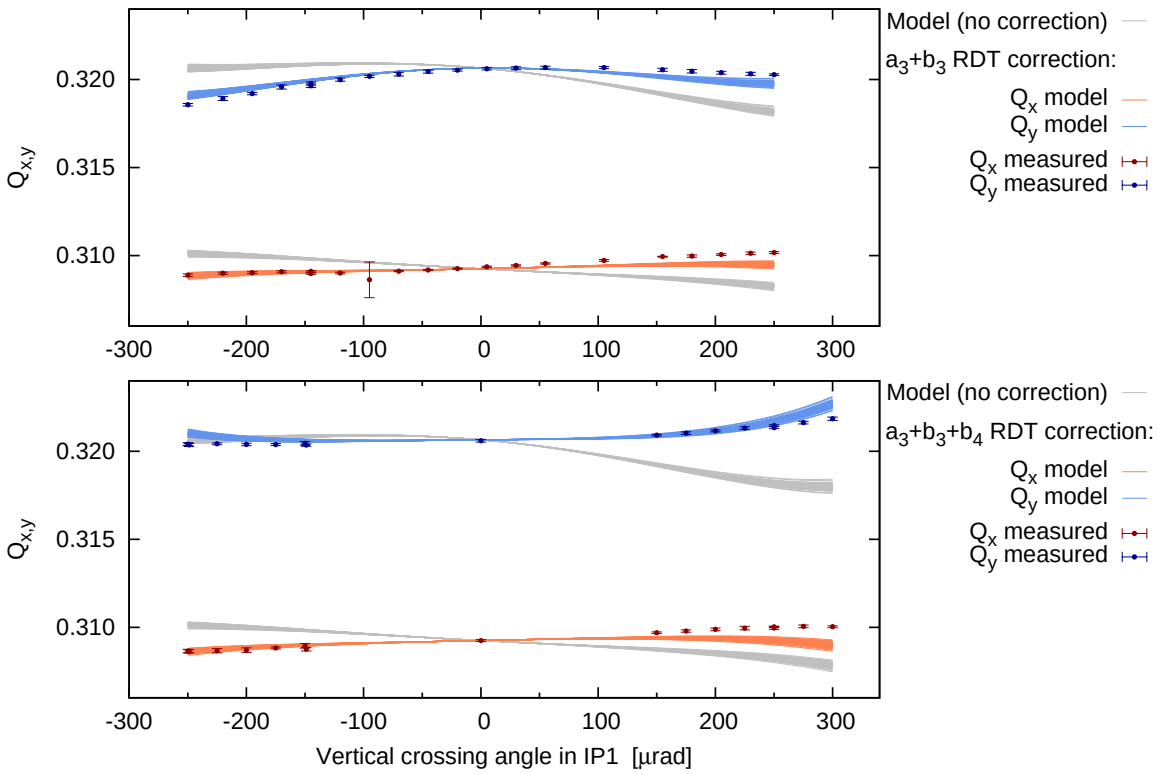

Figure 6.15: Measured and simulated variation of tune with (vertical) IP1 crossing angle in LHC Beam 2 at $\beta^* = 0.6\,\mathrm{m}$. Two scans were performed: with a_3 and b_3 corrections implemented in IR1 (top) and then on addition of b_4 corrections (bottom).

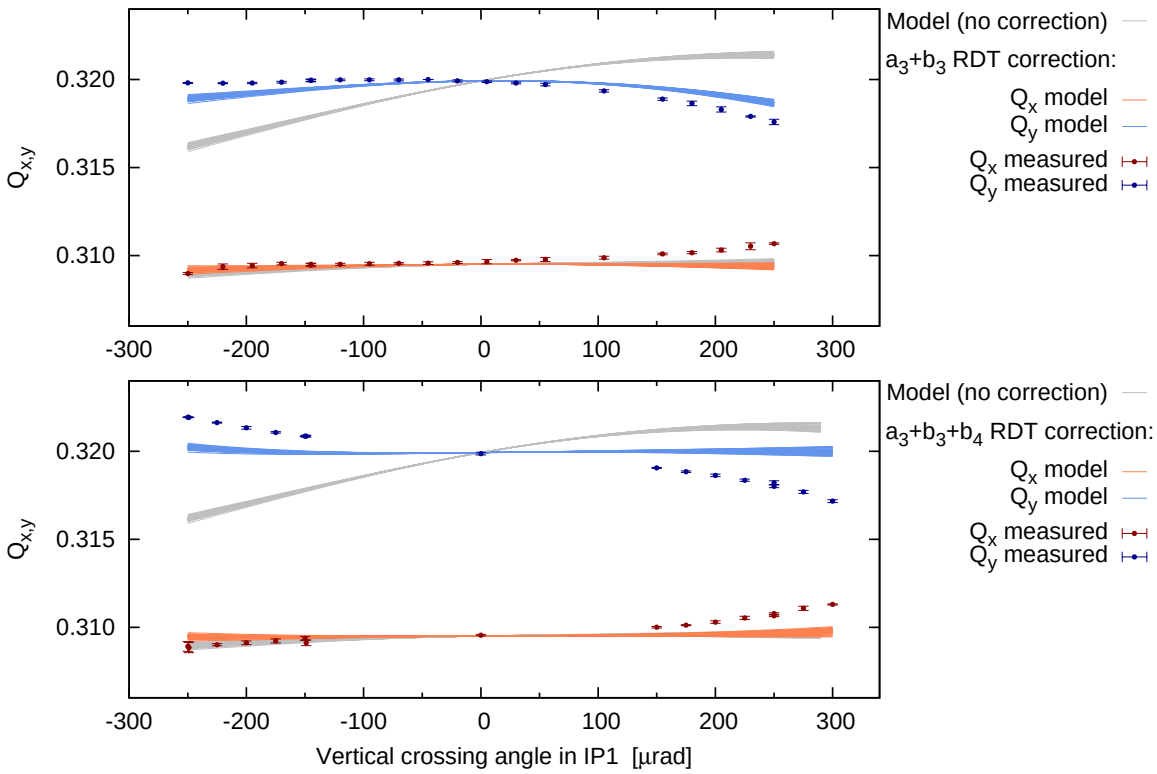

Figure 6.16: Measured and simulated variation of tune with (vertical) IP1 crossing angle in LHC Beam 1 at $\beta^* = 0.6\,\mathrm{m}$. Two scans were performed: with a_3 and b_3 corrections implemented in IR1 (top) and then on addition of b_4 corrections (bottom).

reproduce the additional linear variation of the tune following powering of the b_4 corrector. This serves to characterize the scale of the feed-down, and should not be taken as an assertion that the particular corrector examined is the source of the linear variation. It should also be clear that in the simulation this misalignment represents an assumed orbit discrepancy. An offset of the beam in the b_4 corrector with respect to the b_4 sources to the order of several millimeters is large but not unfeasible. This is particularly true if the alignment is distributed between both corrector and source, possibly on both sides of the IP.

As regards correction of the b_4, this effect will need to be carefully considered. The non-linear corrector circuits in the IRs are common to both beams, and it may be difficult to correct the a_3 error introduced in Beam 1 by the b_4 correction, without detrimentally affecting the quality of the correction in Beam 2. A first consideration may be to determine if this is a permanent feature of the IR, or if it varies between fills. Significantly however, this demonstrates the importance of commissioning the corrections order-by-order. Had the a_3 and b_4 corrections been applied simultaneously, without first verifying the quality of the sextupolar compensation, the most obvious conclusion would have been failure of the a_3 correction, which may have resulted in an incorrect strategy being adopted.

6.5.3 Measurement of non-linear errors in IR5 at $\beta^*_{IP5} = 0.6\,\mathrm{m}$

A study of the non-linear errors in IR5 at $\beta^* = 0.6\,\mathrm{m}$ was performed by scanning the horizontal crossing angle at IP5. No corrections for the non-linear errors in the insertion were applied. As with the $\beta^* = 0.6\,\mathrm{m}$ studies performed on IR1 the BBQ data was of a low quality, and the coupling measurement unusable. After manual cleaning however, tune data was obtained for both LHC Beams. Figures 6.17a and 6.17b plot the observed variation of the tune in Beam 1 and Beam 2 respectively, together with the predictions from simulation.

Considerable discrepancies are observed between simulation and measurement, well outwith the uncertainty in the magnetic model. The effect of alignment errors in the IR was verified to be negligible by incorporating WISE estimates of geometric errors into the simulation, however a possible explanation does lie with the coupling. As no data was available for $|C^-|$ during these scans the coupling in the simulation was held constant at $|C^-| \sim 0.0015$. Predictions of the model therefore reflect the variation of the tune in the absence of any per-

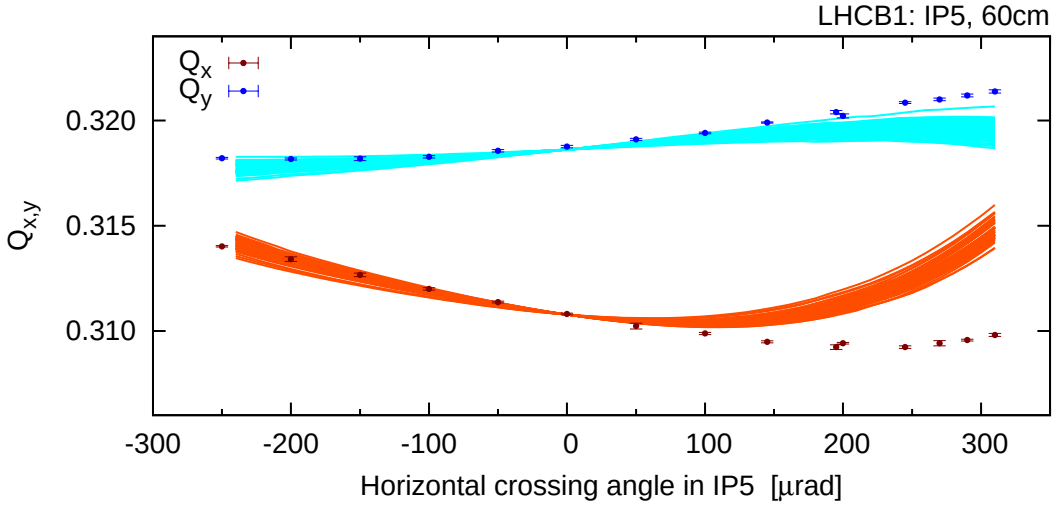

(a) Beam 1

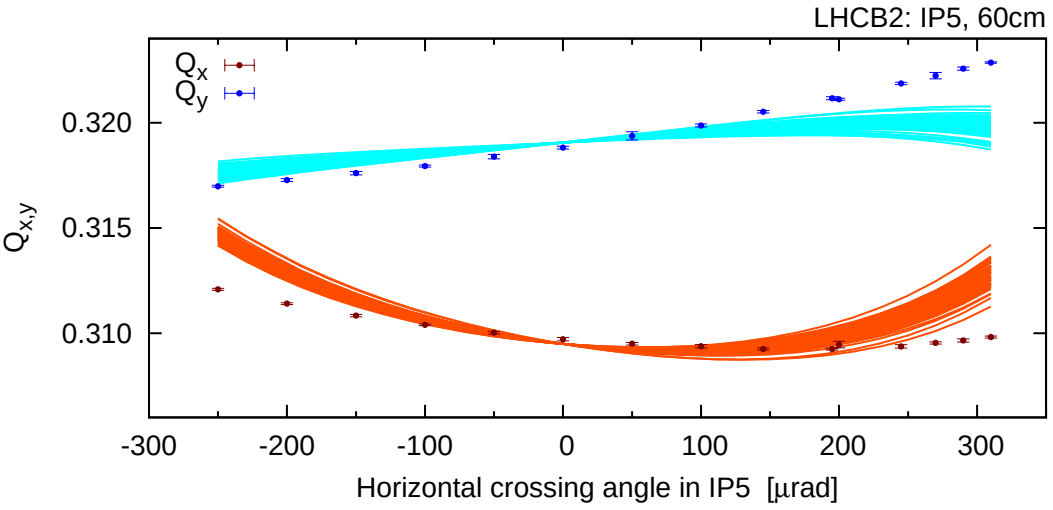

(b) Beam 2

Figure 6.17: Measured and modelled variation of the virgin LHC tune with (horizontal) crossing angle in IP5, at $\beta^*_{IP5} = 0.6\,\mathrm{m}$.

turbation from $|C^-|$. If the coupling increased substantially during the scan, the growth of δQ_{min} may have forced the observed tunes apart, contributing to the smaller tune split in the model. The tune split (particularly at large positive crossing angle trims) was substantial however, and the coupling would need to be large to explain the observations. Upon examining the simulated feed-down to coupling no comparable change is predicted, therefore even if coupling was the source of the tune discrepancy it would still indicate a considerable difference of the real machine with respect to the magnetic model. Without measured data however, it is only possible to speculate on any influence the coupling may have exerted.

Another potential cause of the discrepancy was orbit leakage into the LHC arcs, due to incomplete closure of the crossing angle bumps. A systematic horizontal closed orbit at normal multipoles in the arcs generates feed-down to the tune. Figure 6.18 shows how the Beam 1 orbit in the arcs varied during the IP5 scan. Changes in the mean and RMS orbit were comparable for Beam 2.

Changes in the RMS orbit in the LHC arcs become apparent as the crossing angles shift to the side opposite from that used in regular operation, however shifts to the mean closed orbit are small. To eliminate orbit leakage as a source of the discrepancy, the observed orbit at the end of the IP5 scan (the worst case in regard to the RMS orbit) was reproduced in MAD-X. The simulation included non-linear errors and magnets in the arcs. Orbit leakage was generated in the model by matching small trims of a horizontal orbit corrector in IR5 to replicate the closed orbit wave around the ring. Settings of the crossing angle knob in the model were adjusted to keep the crossing angle at the IP constant. No errors were included in the IRs to avoid changes in the IR orbit generating feed-down which could be misinterpreted as coming from the arcs. Figure 6.19 shows the closed orbit in the Beam 1 arcs measured at the end of the IP5 scan, together with the simulated orbit. The quality of the matched orbit is respectable, erring on the side of an overestimation.

The tune shifts generated in this model on the introduction of the closed orbit wave were of order 10^{-4} and 10^{-5} in the horizontal and vertical planes respectively. This is at least an order of magnitude less than the observed discrepancy. Orbit leakage into the arcs has therefore been discounted as a possible explanation for the observed difference between the measured and modelled feed-down to tune during the IP5 scan.

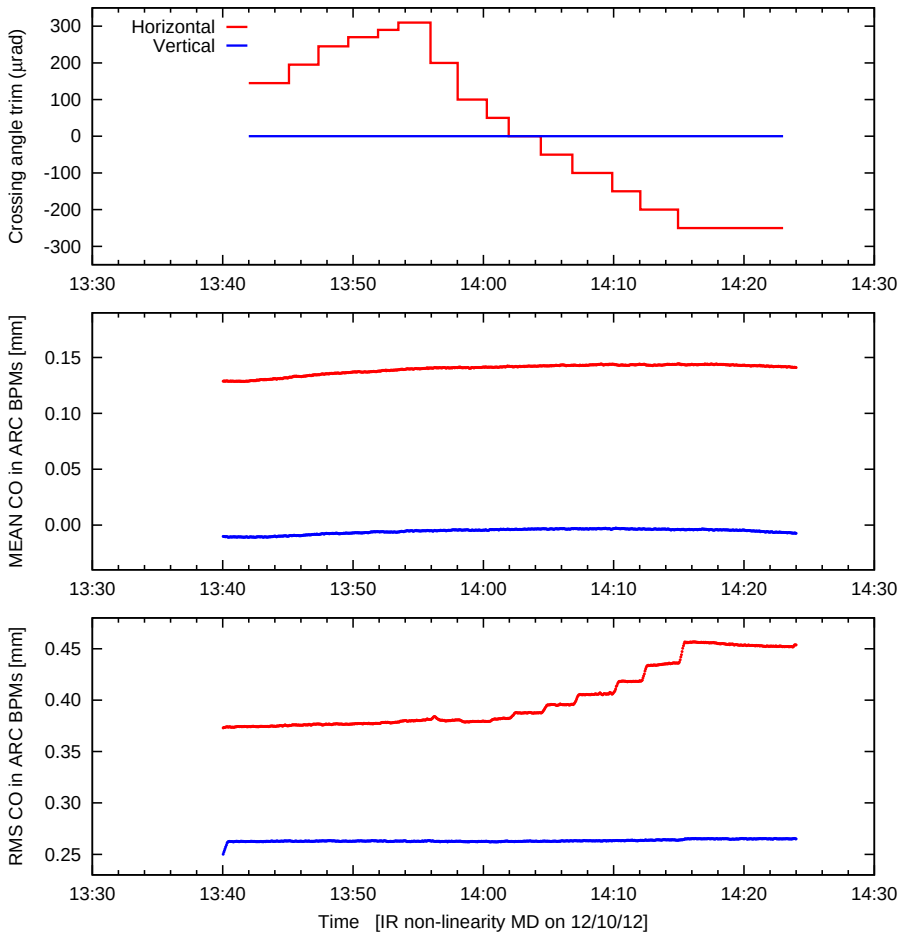

Figure 6.18: Variation with time of the Beam 1 closed orbit in the LHC arcs during a scan of the horizontal crossing angle in IP5, with virgin optics. The applied crossing angle trim is also shown. Similar results were obtained for Beam 2.

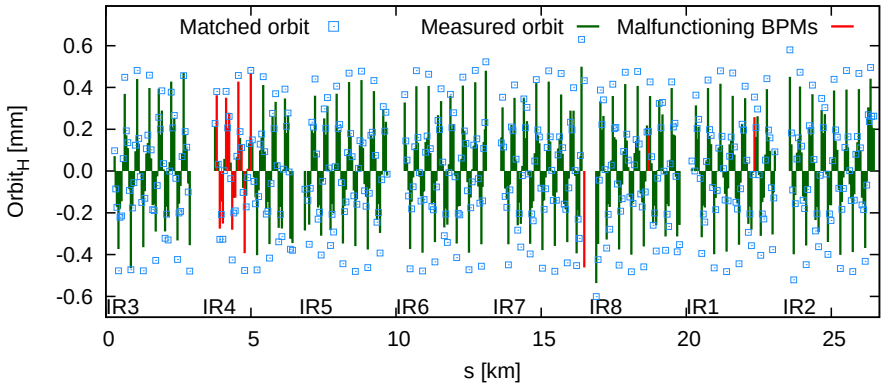

Figure 6.19: Measured and matched closed orbit through the LHC Beam 1 arcs, for the orbit logged by YASP at the end of the IP5 crossing angle scan.

A further possibility considered was that the real IR5 closed orbit bump may have differed from the nominal expectation present in the model, leading to the observed discrepancy. Several BPMs are present in the LHC IRs (their location may be seen in Fig. 2.7 as vertical grey lines), however there are known to be significant distortions in the measured beam position due to an incomplete compensation of the non-linear responses of the IR BPMs [93, 95], in addition to questions over their alignment. Use of the measured beam position data in the IR for comparison to the model is therefore hesitant at best, and these uncertainties should be born strongly in mind in the following discussion. Figure 6.20 compares the orbit measured in several pairs of BPMs in IR5, to the expectation from the MAD-X simulation.

Fig. 6.20 (top) compares the measured crossing angle in Beam 1 and Beam 2 to the applied crossing angle trim present in the machine. The crossing angle was determined from BPM data, using the measured orbits in BPMs immediately left and right of the IP together with their known separation. Discrepancies are observed, however it is emphasised again that the orbit in the BPMs, and hence the crossing angle calculated from these quantities, suffers from known issues with regard to uncompensated non-linear responses of the BPMs.

Figure 6.21 re-plots the measured variation of the tune as a function of the crossing angle, accounting for the measured discrepancies observed in Fig. 6.20 (top). The initial conditions of the simulation were re-matched to the new values and are shown alongside. Use of the measured crossing angle does not significantly affect the agreement between model and measurement of LHC Beam 1. In LHC Beam 2 the agreement between model and measurement shows some improvement on one side (crossing angles $< 0\,\mu\mathrm{rad}$), and becomes more akin to that of Beam 1. Clearly however, a disparity between the expected and measured crossing angles does not explain the bulk of the disagreement between model and measurement.

To consider possible discrepancies in the closed orbit bumps further from the IP, the orbit logged at BPMs adjacent to the D1 separation dipoles was also compared to the expectations from the model. The results of this comparison are shown in Fig. 6.20 for LHC Beam 1 (center) and Beam 2 (bottom). Discrepancies are observed in the orbit at these BPMs for negative, but not for positive, crossing angles. These variations of the orbit cannot, therefore, explain the observed discrepancies in the tune. Alignments of the D1 dipoles, arranged to

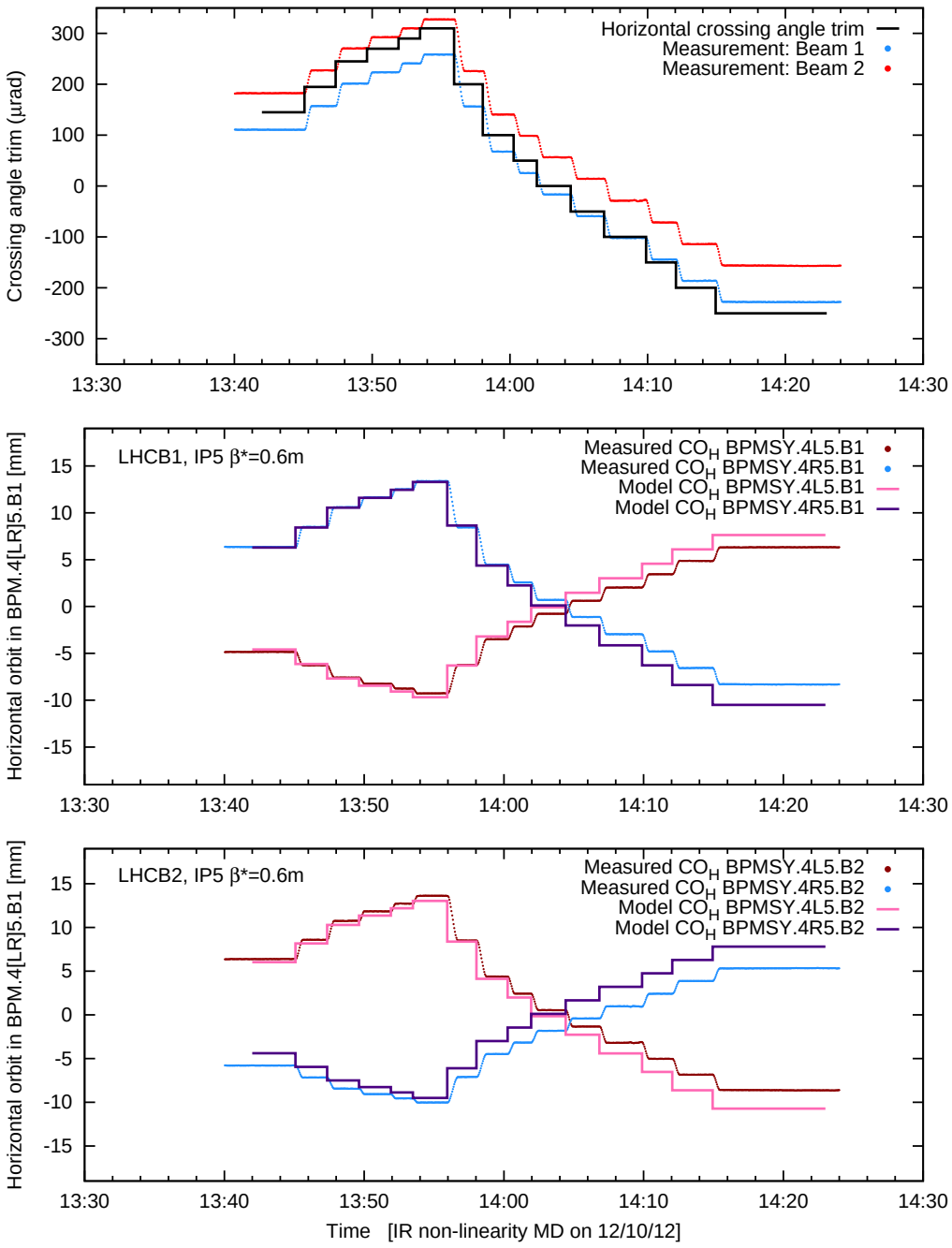

Figure 6.20: Variation with time of closed orbit in IR5. The upper plot shows the applied crossing angle trim in the IR, together with the measured crossing angles of Beam 1 and Beam 2, determined from the orbit recorded at BPMs immediately left and right of the IP. The center and bottom plots show the variation of the orbit at logged in BPMs adjacent to the D1 separation dipoles, together with the expectations from the model, for Beam 1 (center) and Beam 2 (bottom).

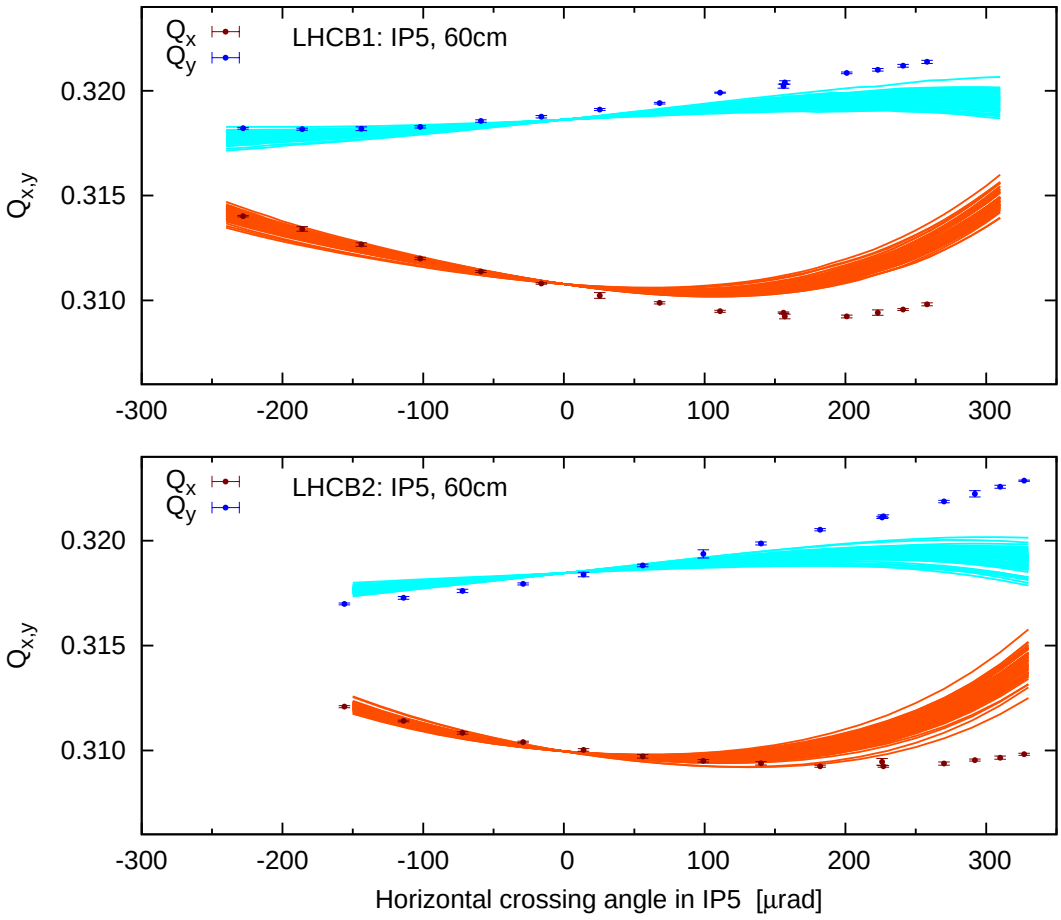

Figure 6.21: Measured and simulated variation of the tune in LHC Beam 1 (top) and Beam 2 (bottom) as a function of the horizontal crossing angle in IP5, at $\beta^*_{IP5} = 0.6\,\mathrm{m}$. Adjustments were applied to the measured tune data to reflect the crossing angle determined from measured orbit data, rather than the applied crossing angle trim. The simulation was re-matched to initial conditions using the measured crossing angles.

reproduce the observed offset of the beam through these elements, were applied in the MAD-X model, and the impact on the tune found to be negligible ($\Delta Q_{x,y} \sim 1 \times 10^{-4}$).

In the LHC's second operational run it is hoped that improved compensation of the BPM non-linearity will allow the use of measured orbit data with greater confidence than the discussion presented here; however, in light of the comparisons between the measured and expected crossing angles, and of the orbit at the separation dipoles, it is concluded that while deviation of the real machine orbit from its nominal trajectory has the potential to explain some of the observed tune discrepancy (namely that of LHC Beam 2 at negative crossing angles), it does not seem able to explain the majority of the difference between the observed and simulated tune variations. It seems increasing likely therefore that the substantial differences between the observed and predicted feed-down to tune in IR5 are the result of a discrepancy of the magnetic model of the LHC with the real machine. Further studies of the non-linear feed-down in IR5 will therefore be essential before correction can be attempted.

6.6 Conclusions

As the LHC progresses to more demanding regimes of operation, correction of non-linear errors in the low-β insertions will become important for an optimized performance of the accelerator. In the HL-LHC, correction of the non-linear errors in the experimental insertions will be essential for operation of the machine. A method to study these errors, based on examination of feed-down to unconstrained tune and unconstrained linear coupling, has been demonstrated to be effective in the LHC. First results from the study of the non-linear errors have been obtained.

The method was initially demonstrated parasitically in IR2 at $\beta^*_{IP2} = 1\,\mathrm{m}$. It was shown that it was possible to study feed-down to both unconstrained tune and unconstrained linear coupling from non-linear errors of sextupole and higher order. From the observations made it was possible to determine that the non-linear errors in IR2 are well understood in the $\beta^*_{IP2} = 1\,\mathrm{m}$ regime, and are dominated by b_3 component of the D1 separation dipoles. A number of the non-linear correctors in IR2 were out of commission, and no correction was attempted. Given the good understanding of the dominant b_3 errors, local correction on the functional side should still be feasible in future operation of the LHC. Several small

discrepancies were identified between the beam-based and magnetic measurements which may warrant further examination.

Following on from the success of parasitic studies in IR2, dedicated measurements were performed on IR1 and IR5. Non-linear errors in IR1 appear to be partially understood. Studies of feed-down to linear coupling and Q_y in LHC Beam 2 at $\beta^* = 0.4\,\mathrm{m}$ showed a good agreement between measurement and simulation, and a refinement of the magnetic model should be possible from the obtained coupling data. Feed-down to Q_x showed a sizable discrepancy with the predictions of the magnetic model, and will need to be studied further. Nonetheless, first corrections of the non-linear errors in IR1, performed at $\beta^* = 0.6\,\mathrm{m}$, appear to have been broadly successful. The discrepancy in Q_x was not apparent at the larger β^*, and correction of a_3 behaved roughly as expected (a slight overcompensation was observed). Correction of b_4 was successful in Beam 2, but introduced a sizable a_3-like perturbation in Beam 1. Given the success of the Beam 2 correction it seems likely this is the result of feed-down due to deviation of the Beam 1 orbit from its nominal trajectory. This represents a clear demonstration of the need for commissioning of the non-linear errors to progress on an order-by-order basis.

In IR5 sizable discrepancies were observed between the beam-based studies and the predictions of the magnetic model. Leakage of the closed orbit into the LHC arcs and deviation of the real orbit in the IR from its nominal path have been ruled out as significant sources of the discrepancy. Shifts in the linear coupling could offer an explanation, but would need to be exceptionally large. Further study of the non-linear errors in IR5 will be required before any attempt at correction can be made.

Chapter 7

Conclusions

The Large Hadron Collider (LHC) at CERN is arguably the most complicated and advanced particle accelerator constructed to date. It represents a new and exciting dynamical system, in which study of the non-linear beam dynamics lies on the frontier of accelerator science. This thesis set out to quantify for the first time the non-linear dynamics of the Large Hadron Collider through direct beam-based measurement, and to further develop the understanding of, and ability to correct, the non-linear phenomenology of the accelerator. Highlights of the research presented in this thesis have included: a record breaking quality of linear optics correction; the simultaneous correction of non-linear chromaticity, detuning with amplitude, and dynamic aperture; first observations of non-linear coupling, a new feature in the phenomenology of the LHC optics; detailed analysis, leading to an understanding, of the influence of the LHC Landau octupoles on first order chromaticity; and the demonstration of a method to study and correct non-linear errors in the LHC experimental insertion regions. More detailed summaries of the results from the four analyses presented in this thesis are given below.

In Chapter 3 the linear dynamics of the LHC was addressed, firstly as an important prerequisite to study of the non-linear beam dynamics, but also as a significant issue in its own right. Measurements of the beta-beating around the LHC ring at $3.5\,\mathrm{TeV}$, $\beta^* = 3.5\,\mathrm{m}$, after correction of local errors in the insertion regions, were compared to predictions of LHC models including the best available knowledge of geometric and magnetic errors in the arcs. The global scale of the simulated beta-beat agreed well with observation. Local variation of the beta-beat was significantly influenced by the uncertainty in the b_2 errors of the Main Quadrupoles in the arcs, which limits the understanding of the linear dynamics. Results from

the 2012 commissioning of the LHC optics for proton-proton operation at $\beta^* = 0.6\,\mathrm{m}$, $4\,\mathrm{TeV}$ (including commissioning of the injection optics) were then presented. An excellent quality of linear optics correction was achieved, with peak and RMS beta beats of $7 \pm 4\,\%$ and $2\,\%$ at $\beta^* = 0.6\,\mathrm{m}$, and comparable results at injection. This set a new record for hadron colliders, and equalled the record for lepton colliders held by CESR. The good understanding of the linear dynamics, together with the excellent quality of linear optics corrections, paved the way for study of the non-linear dynamics.

Chapter 4 considered the non-linear dynamics of the LHC at injection optics. Initial studies focused on measurement of the non-linear chromaticity. Measurements of second and third order chromaticity at injection, with Landau octupoles powered off, revealed a substantial non-linear chromaticity. This indicated significant discrepancies of the magnetic model of the LHC with respect to the real machine. Through simulation it was determined that hysteresis in octupolar spool piece correctors was a significant source of the discrepancy between model and measurement. Limits were also placed on the allowed feed-down to second order chromaticity from decapolar spool piece correctors in the arcs, which could make at most a small contribution to the discrepancy. Hysteresis of the octupole spool pieces, together with feed-down from the decapole spool pieces, could explain the majority of the difference between the modelled and measured second order chromaticity in the vertical plane, however a significant discrepancy remained in the horizontal. Correction of the second and third order chromaticity was demonstrated in LHC Beam 2 at injection optics, with depowered Landau octupoles. Correction significantly reduced both orders, and was observed to compensate detuning with amplitude and reduce the decoherence of kicked beams.

Initial studies of the second and third order chromaticity were also performed at nominal injection optics, including the nominal powering of the Landau octupoles. The change in second order chromaticity upon powering of the Landau octupoles indicated a correction functioning of these elements. Detailed studies of the non-linear dynamics were later performed at nominal injection optics using kicked beams. First and second order detuning with amplitude and the dynamic aperture were measured. Comparison to simulations, incorporating the experience from previous non-linear dynamics studies, demonstrated a good agreement between measurement and the model at nominal injection optics. In addition to amplitude detuning and dynamic aperture, first observations of non-linear coupling in the

LHC optics were made. Measurements were reproduced in the model. Observation of the non-linear coupling opens a new avenue for study of the LHC beam dynamics, and further studies of this aspect of the non-linear phenomenology have been launched as a result. The ability of the LHC model to reproduce the non-linear phenomenology of the accelerator at nominal injection optics allowed its use for examination of optical configurations which had not been measured directly.

It was demonstrated, using corrections for non-linear chromaticity, determined in 2011, that it was possible to increase the dynamic aperture of the LHC through the minimization of readily observed properties of the non-linear beam dynamics. That corrections found in 2011 remained valid a year later is also a significant indication of the stability of the non-linear dynamics in the LHC. The corrected configuration of the LHC was not modelled directly, due both to the departure of corrector circuits from their nominal cycles and to the residual discrepancy in the second order chromaticity, however by matching to measured values of non-linear observables an effective model was developed. The effective model was observed to reproduce the dynamic aperture of the LHC in the diagonal plane (horizontal and vertical planes were limited by the physical aperture).

In Chapter 5 observations of significant shifts to the first order chromaticity upon changes in Landau octupole powering at top energy ($4\,\mathrm{TeV}$) in the LHC were reported. Variations of the chromaticity were explained through feed-down due to systematic misalignment errors, and systematic closed orbit, in the Landau octupoles, together with a small contribution from magnetic errors in these elements. Inclusion of these effects in the LHC model reproduced the observed changes in the first order chromaticity. An analytic expression for the chromaticity shift due to Landau octupole feed-down was provided, to facilitate the rapid analysis of large quantities of closed orbit data.

Substantial changes in the linear coupling measured by the LHC Band Based Tune (BBQ) measurement system were also observed. These were not reproduced in the LHC model and conflicting results were obtained from analysis of the linear coupling resonance driving terms measured with kicked beams. Furthermore, the change in linear coupling reported by the BBQ was independent of the Landau octupole polarity, excluding feed-down and magnetic errors as the source. It was concluded that the shift in linear coupling upon changes in

Landau octupole powering, reported by the BBQ, was an artifact of the measurement. The reason for the differing observations between the BBQ and spectral analysis of kicked beams are not understood.

Finally, in Chapter 6 a method to study the non-linear errors in the LHC experimental insertions was demonstrated. The technique, based upon the study of feed down to unconstrained tune and unconstrained linear coupling under the influence of varying closed orbit bumps, was demonstrated parasitically in IR2 at $\beta^* = 1\,\mathrm{m}$. A good agreement of the magnetic model to the real LHC was found, with the non-linear errors being dominated by the b_3 component of the D1 separation dipoles. Dedicated studies were then performed of the non-linear errors in IR1 at $\beta^* = 0.4\,\mathrm{m}$ which indicated the non-linear errors were partially understood. Some refinement of the magnetic model should be possible from the feed-down to linear coupling in this regime. First attempts at correction of the errors in IR1 were performed at $\beta^* = 0.6\,\mathrm{m}$. These were successful for Beam 2, however compensation of the normal octupole errors introduced a sizable feed-down in Beam 1. This demonstrated the importance of commissioning these corrections on an order-by-order basis. Measurements were also performed in IR5, however in this case substantial deviations of the measurements from predictions of the magnetic model were observed. Potential sources relating to the reproduction of the relevant closed orbit bumps in the model were examined, and were ruled out as significant sources of the discrepancy. Further study of IR5 will be required before correction may be attempted, however compensation of certain non-linear errors in IR1 and IR2 should now be possible in future LHC operation.

Collectively, the studies presented in this thesis represent a significant improvement in the understanding, simulation, and correction of the non-linear beam dynamics in the Large Hadron Collider.

Bibliography

[1] C. Alabau Pons, E.H. Maclean, F. Schmidt & R. Tomás. "Beta-beating in the effective model of the LHC using PTC" (2011). CERN-ATS-Note-2011-096 TECH.
https://cds.cern.ch/record/1397343?ln

[2] C. Alabau Pons, E.H. Maclean, F. Schmidt & R. Tomás. "Beta-beating in the effective model of the LHC using PTC". In "Proceedings of IPAC 2011", WEPCO79 (2011).
http://accelconf.web.cern.ch/accelconf/IPAC2011/papers/wepc079.pdf

[3] E.H. Maclean. "First optics measurments 2012". Presentation to CERN LHC Beam Operation Committee (LBOC) (2012).
http://lhc-beam-operation-committee.web.cern.ch/lhc-beam-operation-committee/

[4] R. Tomás, R. Calaga, A. Langner, Y.I. Levinsen, E.H. Maclean, T.H.B. Persson, P.K. Skowronski, M. Stzelczyk, G. Vanbavinckhove & R. Miyamoto. "Record low β-beating in the LHC.", Phys. Rev. ST. AB, **15**, 091001.
http://prst-ab.aps.org/abstract/PRSTAB/v15/i9/e091001

[5] M. Albert, G. Crockford, S. Fartoukh, M. Giovannozzi, E.H. Maclean, A. MacPherson, R. Miyamoto, L. Ponce, S. Redaelli, F. Roncarolo, F. Schmidt, R. Steinhagen, E. Todesco, R. Tomás, G. Vanbavinckhove & W. Venturini Delsolaro. "Non-linear beam dynamics tests in the LHC" (2011). CERN-ATS-Note-2011-052 MD.
http://cds.cern.ch/record/1366082?ln

[6] E.H. Maclean, F. Schmidt, R. Tomás, R. Bartolini, E. Todesco, R. Steinhagen, G. Vanbavinckhove & M. Giovannozzi. "Non-linear chromaticity studies of the LHC at Injection". In "Proceedings of IPAC 2011", WEPCO78 (2011).
http://accelconf.web.cern.ch/accelconf/IPAC2011/papers/wepc078.pdf

[7] E.H. Maclean, S. Moeckel, T.H.B. Persson, S. Redaelli, F. Schmidt, R. Tomás & J. Uythoven. "Non-linear beam dynamics tests in the LHC: LHC dynamic aperture MD on Beam 2 (24th of June 2012)" (2013). CERN-ATS-Note-2013-022 MD.
https://cds.cern.ch/record/1541980?ln

[8] E.H. Maclean, R. Tomás, F. Schmidt & T.H.B. Persson. “Measurement of LHC nonlinear observables using kicked beams”, Phys. Rev. Spec. Top. Accel. Beams, **17**, 081002. https://journals.aps.org/prstab/abstract/10.1103/PhysRevSTAB.17.081002

[9] E.H. Maclean. “Non-linear modelling and machine set-up”. Presentation at LHC OMC review (2013). http://indico.cern.ch/getFile.py/access?contribId=5&sessionId=0&resId=1&materialId=slides&confId=246159

[10] E.H. Maclean, M. Giovannozzi, T.H.B. Persson, R. Tomás & J. Wenninger. “Understanding the tune, coupling, and chromaticity dependence of the LHC on Landau octupole powering.” (2013). CERN-ATS-Note-2013-023 TECH. https://cds.cern.ch/record/1541981?ln

[11] E.H. Maclean, M. Giovannozzi, W. Herr, Y.I. Levinsen, G. Papotti, T.H.B. Persson, P.K. Skowronski, R. Tomás & J. Wenninger. “Understanding the tune, coupling, and chromaticity dependence of the LHC on Landau octupole powering”. In “Proceedings of IPAC 2013”, TUPWO048 (2013). http://accelconf.web.cern.ch/AccelConf/IPAC2013/papers/tupwo048.pdf

[12] E. Wilson. “An introduction to particle accelerators”, Chapter 13: Applications of accelerators. Oxford University Press (2006).

[13] S.Y. Lee. “Accelerator Physics”, Chapter 1, III Accelerator Applications. World Scientific, third edition edition.

[14] Webpage of the Office of Naval Research. http://www.onr.navy.mil/Media-Center/Fact-Sheets/Free-Electron-Laser.aspx

[15] Ronald O’Rourke. “Navy Shipboard Lasers for Surface, Air, and Missile Defense: Background and Issues for Congress”. http://www.fas.org/sgp/crs/weapons/R41526.pdf

[16] E. Bains et al. “Towards an alternative nuclear future” (2009). http://epubs.cclrc.ac.uk/bitstream/5179/ThoreaReportFinal.pdf

[17] “CAS: Fifth advanced accelerator physics school (Rhodes 1993)”. CERN (1995). CERN 95-06. https://cds.cern.ch/record/254747/

[18] E. Wilson. “An introduction to particle accelerators”, Chapter 2.3.3: Alternating-gradient focusing. Oxford University Press (2006).

[19] S. Russenschuck. “Design of accelerator magnets”. In “CERN Accelerator School: Basic Course on General Accelerator Physics, Greece, 2000”, CERN. https://cds.cern.ch/record/865932?ln

[20] E. Wilson. “An introduction to particle accelerators”, Chapter 8. Oxford University Press (2006).

[21] A. Bazanni, E. Todesco & G. Turchetti. “A normal form approach to the theory of nonlinear betatronic motion.”, CERN, **94**, 02.
http://cds.cern.ch/record/262179?ln

[22] E. Wilson. “An introduction to particle accelerators”, Chapter 2.2: Bending magnets and magnetic rigidity. Oxford University Press (2006).

[23] E. Wilson. “An introduction to particle accelerators”, Chapter 5.2: The effect of momentum spread on transverse dynamics - dispersion. Oxford University Press (2006).

[24] R. Tomás. “Direct Measurement of Resonance Driving Terms in the Super Proton Synchrotron (SPS) of CERN using Beam Position Monitors”. Ph.D. thesis, Universitat de València (2003).
http://cds.cern.ch/record/615164?ln

[25] H. Wiedemann. “Particle Accelerator Physics”, Chapter 12.1: Magnet field and alignment errors. Springer, third edition edition.

[26] E. Forest. “A Hamiltonian free description of single particle dynamics for hopelessly complex periodic systems”, J. Math. Phys, **31**, 1133.
http://dx.doi.org/10.1063/1.528795

[27] A. Franchi. “Studies and Measurements of Linear Coupling and Nonlinearities in Hadron Circular Accelerators”. Ph.D. thesis, Universität Frankfurt (2006).
http://www.gsi.de/en/start/beschleuniger/fachabteilungen/accelerator_physics/phd_thesis.htm

[28] R. Bartolini & F. Schmidt. “Normal form via tracking or beam data”, Part. Accel., **59**, 93-106.
http://cds.cern.ch/record/333077

[29] J. Bengtsson. “Non-linear transverse dynamics for storage rings with applications to the low-energy antiproton ring (LEAR) at CERN”. Ph.D. thesis, Lund University (1988).
http://cds.cern.ch/record/190442

[30] G. Ripken. “Non-linear canonical equations of coupled synchro-betatron motion and their solution within the framework of a non-linear 6-dimensional (symplectic) tracking program for ultra-relativistic protons”, DESY pre-print, **85**, 084.
http://cds.cern.ch/record/162762?ln

[31] R. Jones. “Commissioning and first performance of the LHC beam instrumentation” (2010). CERN-BE-2010-007.
https://cds.cern.ch/record/1267394?ln

[32] E. Wilson. “An introduction to particle accelerators”, Chapter 7.4.1: Slow extraction using the third-order resonance. Oxford University Press (2006).

[33] R. Cappi & M. Giovannozzi. “Multiturn extraction and injection by means of adiabatic capture in stable islands of phase space”, Phys. Rev. Spec. Top. Accel. Beams, **7**, 024001.
http://cds.cern.ch/record/846139?ln

[34] M. Giovannozzi & J. Morel. “Principle and Analysis of Multiturn Injection Using Stable Islands of Transverse Phase Space”, Phys. Rev. Spec. Top. Accel. Beams, **10**, 034001.
http://cds.cern.ch/record/1035231?ln

[35] M. Giovannozzi. “Manipulation of transverse beam distribution in circular accelerators: beam splitting by particles trapping into resonance islands”. Lecture to the John Adams Institute for Accelerator Science (2013).
http://www.adams-institute.ac.uk/lectures

[36] E. Wilson. “An introduction to particle accelerators”, Chapter 7: Non-linearities and resonances. Oxford University Press (2006).

[37] S.Y. Lee. “Accelerator Physics”, Chapter 2.VII: Nonlinear Resonances. World Scientific, third edition.

[38] H. Wiedemann. “Particle Accelerator Physics”, Chapter 13: Hamiltonian Resonance Theory. Springer, third edition.

[39] R. Cappi & M. Giovannozzi. “Adiabatic Capture of Charged Particles in Islands of Phase Space : a New Method for Multiturn Extraction”. Proceedings of EPAC (2002).
http://cds.cern.ch/record/557704?ln

[40] “Dynamic aperture”. In “CAS: Third advanced accelerator physics school”, CERN 90-04 (1989).
https://cds.cern.ch/record/115975/files/CERN-90-04.pdf

[41] “Dynamic aperture”. In “CAS: Fifth advanced accelerator physics school”, CERN 95-06 (1995).
https://cds.cern.ch/record/254747?ln

[42] M. Boge & F. Schmidt. “Estimates for LongTerm Stability for the LHC” (1997). CERN-LHC-PROJECT-Report-114.
http://cds.cern.ch/record/327774?ln

[43] “SixTrack - 6D Tracking Code”.
http://sixtrack-ng.web.cern.ch/sixtrack-ng/

[44] J. Laskar. “Secular evolution of the solar system over 10 million years”, Astron. Astrophys., **198**, 314-362.
http://adsabs.harvard.edu/abs/1988A%26A...198..341L

[45] H.S. Dumas & J. Laskar. “Global dynamics and long-time stability in Hamiltonian systems via numerical frequency analysis”, Phys. Rev. Lett., **70**, 2975.
https://journals.aps.org/prl/abstract/10.1103/PhysRevLett.70.2975

[46] J. Laskar. “Frequency map analysis and particle accelerators”. In “Proceedings of 2003 Particle Accelerator Conference”, (2003).
http://www.toddsatogata.net/2013-USPAS/Laskar.pdf

[47] L.C.Teng. “Concerning n-dimensional coupled motions” (1971). FN-229.
http://lss.fnal.gov/archive/fn/FN-0229.pdf

[48] “MAD - Methodical Accelerator Design”.
http://mad.web.cern.ch/mad/

[49] F. Willeke & G. Ripken. “Methods of beam optics” (1988). DESY 88-114.
https://cds.cern.ch/record/194174/

[50] É. Forest, F. Schmidt & E. McIntosh. “Introduction to the Polymorphic Tracking Code” (2002). CERN-SL-2002-044 (AP).
http://cds.cern.ch/record/573082/files/sl-2002-044.pdf

[51] V.A. Lebedev & S.A. Bogacz. “Betatron motion with coupling of horizontal and vertical degrees of freedom”, JINST, **5**, P10010. FERMILAB-PUB-10-383-AD.
http://iopscience.iop.org/1748-0221/5/10/P10010/

[52] Y. Alexahain, E. Gianfelice-Wendt, V. Kapin & F. Schmidt. “Coupled optics reconstruction from TBT data using MAD-X”. In “Proceedings of PAC07”, THPAN104 (2007).
http://accelconf.web.cern.ch/AccelConf/p07/PAPERS/THPAN104.PDF

[53] G. Guignard. “Betatron coupling and related impact of radiation”, Phys. Rev. E, **51**, 6.
https://cds.cern.ch/record/300856?ln

[54] H. Wiedemann. “Particle Accelerator Physics”, Chapter 17: Dynamics of Coupled Motion. Springer, third edition.

[55] G. Vanbavinckhove. “Optics measurements and corrections for colliders and other storage rings”. Ph.D. thesis, Universiteit van Amsterdam (2012).
https://cds.cern.ch/record/1533084?ln

[56] J. Serrano & M. Cattin. “The LHC AC Dipole system: an introduction” (2010). CERN-BE-Note-2010-014.
http://cds.cern.ch/record/1263248?ln

[57] R. Miyamoto, R. Calaga, M. Aiba, R. Tomás & G. Vanbavinckhove. “Measurement of coupling resonance driving terms in the LHC with AC Dipoles” (2011). CERN-ATS-2011-158.
https://cds.cern.ch/record/1382073/files/?ln

[58] R. Tomás. “Optimizing the global coupling knobs for the LHC” (2012). CERN-ATS-Note-2012-019 MD.
http://cds.cern.ch/record/1422434?ln

[59] W. Herr & B. Muratori. “Concept of Luminosity”. In “CERN Accelerator School”, CERN (2003).
http://cds.cern.ch/record/941318/

[60] W. Herr. Presentation to CAS (2010).
http://cas.web.cern.ch/cas/Bulgaria-2010/Talks-web/Herr-1-web.pdf

[61] M.A. Furman. “The Møller Luminosity Factor” (2003). LBNL-53553, CBP Note-543.
https://publications.lbl.gov/islandora/object/ir%3A121871

[62] M. Hostettler & G. Papotti. “LHC Luminosity Lifetime: Measurement, comparison between fills, high bandwidth ADT effects”. Presentation to CERN LHC Beam Operation Committee (LBOC) (2012).
http://lhc-beam-operation-committee.web.cern.ch/lhc-beam-operation-committee/

[63] “ATLAS collaboration homepage”.
http://cds.cern.ch/collection/LHC%20Experiments?ln

[64] “CERN Document Server: ATLAS”.
url=http://cds.cern.ch/collection/ATLAS?ln

[65] “CERN LHCf webpage”.
http://home.web.cern.ch/about/experiments/lhcf

[66] “CERN Document Server: LHCf”.
http://cds.cern.ch/collection/LHCf?ln

[67] “Alice collaboration homepage”.
http://aliceinfo.cern.ch/Public/Welcome.html

[68] “CERN Document Server: Alice”.
http://cds.cern.ch/collection/ALICE?ln

[69] “CMS collaboration homepage”.
http://cms.web.cern.ch/

[70] “CERN Document Server: CMS”.
http://cds.cern.ch/collection/CMS?ln

[71] “TOTEM collaboration homepage”.
http://totem.web.cern.ch/Totem/

[72] “CERN Document Server: TOTEM”.
http://cds.cern.ch/collection/TOTEM?ln

[73] “LHCb collaboration homepage”.
http://lhcb.web.cern.ch/lhcb/

[74] “CERN Document Server: LHCb”.
http://cds.cern.ch/collection/LHCb?ln

[75] “MoEDAL collaboration homepage”.
http://moedal.web.cern.ch/

[76] CERN BE dept. “LHC Design Report v.1: the LHC Main Ring.” CERN (2004).
https://cds.cern.ch/record/782076?ln

[77] CERN BE dept. “LHC Design Report v.2: the LHC Infrastructure and General Services.” CERN (2004).
https://cds.cern.ch/record/815187?ln

[78] CERN BE dept. “LHC Design Report v.3: the LHC Injector Chain.” CERN (2004).
https://cds.cern.ch/record/823808?ln

[79] CERN BE dept. “LHC Design Report v.1: the LHC Main Ring”, Chapter 3: Layout and performance. CERN.
https://cds.cern.ch/record/782076/

[80] Image.
http://cds.cern.ch/record/40524?ln

[81] L. Deniau. “Magnetic model of Main Dipoles” (2009).
https://lhc-div-mms.web.cern.ch/lhc-div-mms/tests/MAG/Fidel/

[82] Image.
http://cds.cern.ch/record/841485/files/

[83] L. Deniau. “Magnetic model of Main Quadrupoles” (2009).
https://lhc-div-mms.web.cern.ch/lhc-div-mms/tests/MAG/Fidel/

[84] “CERN FiDel report on LHC magnetic model: Part III: Superconducting correctors in the arc”.
https://lhc-div-mms.web.cern.ch/lhc-div-mms/tests/MAG/Fidel/

[85] M. Haverkamp. “Decay and Snapback in Superconducting Accelerator Magnets”. Ph.D. thesis, University of Twente (2003).
http://cds.cern.ch/record/677979?ln

[86] O. Bruning, S. Fartoukh, M. Giovannozzi & T. Risselada. “Dynamic Aperture Studies for the LHC Separation Dipoles” (2004). LHC Project Note 349.
https://cds.cern.ch/record/742967?ln

[87] “WISE homepage”.
http://wise.web.cern.ch/WISE/

[88] “WISE geometry page”.
http://wise.web.cern.ch/WISE/Other/Geometry/

[89] P. Hagen. “WISE - user guide and implementation notes”.
http://wise.web.cern.ch/WISE/Doc/lhc-project-report-wise.pdf

[90] L. Bottura, M. Lamont, E. Todesco, W. Venturini Delsolaro & R. Wolf. “Pre-cycles of the LHC magnets during operation” (2010). CERN/ATS 2010-174.
cds.cern.ch/record/1283477?ln

[91] R. Alemany, M. Lamont & S. Page. “Functional specification: LHC MODES” (2007). LHC-OP-ES-0005 rev 1.0.
https://lhc-commissioning.web.cern.ch/lhc-commissioning/systems/data-exchange/doc/LHC-OP-ES-0005-10-00.pdf

[92] S.B. Pedersen, A. Boccardi, E. Bravin, G. Burtin, S. Burger, B. Dehning, J. Emery, A. Fisher, A. Guerrero, A. Jeff, J. Koopman, T. Lefevre, Aurelie Rabiller & Federico Roncarolo. “Profile monitors, injection matching monitor and synchrotron light monitor”. In “Proceedings of the Evian Workshop on LHC Commissioning”, (2010).
http://cds.cern.ch/record/1281646?ln

[93] E. Calvo, C. Boccard, L. Jensen, R. Jones, T. Lefevre, A. Margiolakis & A. Nosych. “BPM system upgrades and temperature regulation”. Presentation at LHC OMC review (2013).
https://indico.cern.ch/event/246159/session/1/contribution/11/material/slides/3.pptx

[94] P. Kowina P. Forck & D. Liakin. “Beam Position Monitors”. In “CERN Accelerator School”, CERN.
http://www-bd.gsi.de/uploads/paper/cas_bpm_main.pdf

[95] A. Nosych. “Geometrical non-linearity correction procedure of LHC beam position monitors” (2014). 1342295.
https://edms.cern.ch/document/1342295/1

[96] A. Boccardi, M. Gasior, R. Jones & R.J. Steinhagen. “An overview of the LHC Transverse Diagnostics Systems” (2009). LHC Project Report 1166.
http://cds.cern.ch/record/1156346?ln

[97] A. Boccardi, M. Gasior, O.R. Jones, P. Karlsson & R.J. Steinhagen. “First Results from the LHC BBQ Tune and Chromaticity Systems” (2009). CERN-LHC-Performance-Note-007.
http://cds.cern.ch/record/1156349?ln

[98] M. Gasior & R. Jones. “The principle and first results of betatron tune measurement by direct diode detection” (2005). LHC-Project-Report 853.
http://cds.cern.ch/record/883298?ln

[99] R. Jones, P. Cameron & Y. Luo. “Towards a Robust Phase Locked Loop Tune Feedback System” (2005). C-A/AP/#204.
http://cds.cern.ch/record/895167?ln

[100] R.A. Barlow, E. Carlier, J.P. Pianfetti, V. Senaj & M. Cattin. “Control of the MKQA tuning and aperture kickers of the LHC” (2010). CERN-TE-Note-2010-001.
https://cds.cern.ch/record/1232062?ln

[101] E. Carlier, L. Ducimetiere & E. Vossenberg. “A Kicker Pulse Generator for Measurement of the Tune and Dynamic Aperture in the LHC”. In “Conference record of the twenty seventh international power modulator symposium”, (2006).
http://ieeexplore.ieee.org/xpls/abs_all.jsp?arnumber=4216236

[102] F. Schmidt. “Dynamic aperture and non-linear measurements with the MKA” (2012).
http://cern.ch/Frank.Schmidt/report/MD2012_MKA_DA.docx

[103] R. Tomás. “Adiabaticity of the ramping process of an ac dipole”, Phys. Rev. ST. AB, **8**, 024401.
http://prst-ab.aps.org/abstract/PRSTAB/v8/i2/e024401

[104] R. Miyamoto, M. Cattin, J. Serrano & R. Tomás. “Signal quality of the LHC AC dipoles and its impact on beam dynamics”. In “Proceedings of IPAC 10”, THPE083 (2010).
https://accelconf.web.cern.ch/accelconf/IPAC10/papers/thpe083.pdf

[105] S. White, E. Maclean & R. Tomás. “Direct amplitude detuning measurement with ac dipole”, Phys. Rev. ST. AB, **16**, 071002.
http://prst-ab.aps.org/abstract/PRSTAB/v16/i7/e071002

[106] M. Aiba, S. Fartoukh, A. Franchi, M. Giovannozzi, V. Kain, M. Lamont, R. Tomás, G. Vanbavinckhove, J. Wenninger, F. Zimmermann, R. Calaga & A. Morita. “First β-beating measurement and optics analysis for the CERN Large Hadron Collider”, Phys. Rev. ST. AB, **12**, 081002.
http://prst-ab.aps.org/abstract/PRSTAB/v12/i8/e081002

[107] R. Tomás, O. Bruning, M. Giovannozzi, P. Hagen, M. Lamont, F. Schmidt, G. Vanbavinckhove, M. Aiba, R. Calaga & R. Miyamoto. "CERN Large Hadron Collider optics model, measurements, and corrections", Phys. Rev. ST. AB, **13**, 121004.
http://prst-ab.aps.org/abstract/PRSTAB/v13/i12/e121004

[108] O. Bruning & S. Fartoukh. "Field Quality Specification for the LHC Main Dipole Magnets" (2001). CERN-LHC-Project-Report-501.
https://cds.cern.ch/record/522049

[109] R. Calaga, R. Tomás & F. Zimmerman. "BPM calibration independent LHC optics correction" (2007). CERN-LHC-PROJECT-Report-1039.
http://cds.cern.ch/record/1058520?ln

[110] CERN BE dept. "LHC Design Report v.1: the LHC Main Ring", Chapter CHAPTER 13: Beam Instrumentation, 13.1: Beam position measurmement. CERN.
https://cds.cern.ch/record/782076/

[111] R. Tomás & R. Calaga. "Statistical analysis of RHIC beam position monitors performance", Phys. Rev. ST. AB, **7**, 042801.
http://journals.aps.org/prstab/abstract/10.1103/PhysRevSTAB.7.042801

[112] R. Bartolini & F. Schmidt. "SUSSIX: a computer code for frequency analysis of non-linear betatron motion" (2010). CERN SL/Note 98-017 (AP).
https://cds.cern.ch/record/702438/files/

[113] T. Bach & R. Tomás. "Improvements for Optics Measurement and Corrections software" (2013). CERN-ACC-NOTE-2013-0010.
https://cds.cern.ch/record/1595800?ln

[114] P. Castro. "Luminosity and beta function measurement at the electron-positron collider ring LEP". Ph.D. thesis, University of Valencia (1996).
http://cds.cern.ch/record/316609?ln

[115] R. Tomás, O. Bruning, S. Fartoukh, M. Giovannozzi, Y. Papaphilippou, F. Zimmermann, R. Calaga, S. Peggs & A. Franchi. "Procedures and accuracy estimates for beta-beat correction in the LHC". In "Proceedings of EPAC", WEPCH047 (2006).
http://cds.cern.ch/record/972668?ln

[116] "MAD - Methodical Accelerator Design".
http://mad.web.cern.ch/mad/

[117] T. Bach, P. Hagen, A. Langner, Y.I. Levinsen, M. McAteer, E.H. Maclean, T. Persson, P. Skowronski, R. Tomás, E. Todesco & S. White. "MQY 1% calibration errors" (2013). CERN-ATS-Note-2013-029 MD.
https://cds.cern.ch/record/1545888/files/?ln

[118] D. Sagan, R. Meller, R. Littauer & D. Rubin. “Betatron phase and coupling measurements at the Cornell Electron /Positron Storage Ring”, Phys. Rev. ST. AB, **3**, 092801.
http://journals.aps.org/prstab/abstract/10.1103/PhysRevSTAB.3.092801

[119] T.H.B. Persson, Y.I. Levinsen, R. Tomás & E.H. Maclean. “Chromatic Coupling Correction in the Large Hadron Collider”, Phys. Rev. ST. AB, **16**, 081003.
http://prst-ab.aps.org/abstract/PRSTAB/v16/i8/e081003

[120] G. Vanbavinckhove, M. Aiba, R. Bartolini, R. Calaga, M. Giovannozzi, E.H. Maclean, R. Miyamoto, F. Schmidt & R. Tomás. “First measurements of higher order optics parameters in the LHC”. In “Proceedings of IPAC 2011”, WEPCO32 (2011).
http://accelconf.web.cern.ch/accelconf/IPAC2011/papers/wepc032.pdf

[121] M.G. Minty & F. Zimmermann. “Beam Techniques - Beam Control and Manipulation”, Chapter 5: Longitudinal Optics - Measurement and Correction. Proceedings of US accelerator school (1999).
http://www.slac.stanford.edu/cgi-wrap/getdoc/slac-r-621.pdf

[122] J. Uythoven (CERN TE-ABT-BTP). personal communication (2013).

[123] A. Sherman. “Improvements in the error calculation of the action of a kicked beam” (2013). CERN-STUDENTS-Note-2013-215.
http://cds.cern.ch/record/1602304?ln

[124] L. Drosdal, K. Cornelis, B. Goddard, V. Kain, M. Meddahi, O. Mete, B. Salvachua, G.Valentino & E. Veyrunes. “SPS Scraping and LHC Transverse Tails”. In “Proceedings of IPAC 2013”, MOPWO032 (2013).
https://accelconf.web.cern.ch/accelconf/IPAC2013/papers/mopwo032.pdf

[125] S. Fartoukh. “Chromatic coupling induced by skew sextupolar field errors in the LHC main dipoles and its correction” (1998). LHC Project Report 278.
http://cds.cern.ch/record/383926/files/lhc-project-report-278.pdf

[126] E. Todesco. personal communication (2012).

[127] S. Cettour Cave, R. De Maria, M. Giovannozzi, M. Ludwig, A. MacPherson, S. Redaelli, F. Roncarolo, M. Solfaroli Camillocci & W. Venturini Delsolaro. “Non-linear beam dynamics tests in the LHC: measurement of intensity decay for probing dynamic aperture at injection” (2013). CERN-ATS-Note-2013-025 MD.
https://cds.cern.ch/record/1543434?ln

[128] R. Tomás. “Optimizing the global coupling knobs for the LHC.” (2012). CERN-ATS-Note-2012-019 MD.
https://cds.cern.ch/record/1422434

[129] E.H. Maclean (for the LHC OMC team). “LHC Commissioning: First Optics Measurements - 2012”. Presentation to LHC Beam Operation Committee, 27 March 2012.
https://lhc-beam-operation-committee.web.cern.ch/lhc-beam-operation-committee/

[130] N. Mounet, Y.Le Borgne, X. Buffat, A. Burov, G. Hemelsoet, E. Metral, G. Papotti, T. Pieloni, M. Pojer, B. Salvant & G. Trad. “Single-beam measurements of LHC instability threshold in terms of octupole current” (2012). CERN-ATS-Note-2012-073 MD.
https://cds.cern.ch/record/1478165?ln

[131] G. Papotti, W. Herr, E. Maclean, E. Metral, N. Mounet, R. Tomás Garcia & J. Wenninger. “Chromaticity dependence on octupole strength” (2012). CERN-ATS-Note-2012-072 MD.
https://cds.cern.ch/record/1477917?ln

[132] “LHC V6.503 as-built sequence”.
/afs/cern.ch/eng/lhc/optics/V6.503/as-built/V6.5.2012.02.seq

[133] J. Wenninger. “YASP Steering Program User Guide”.
http://jwenning.web.cern.ch/jwenning/documents/YASP/YASP-user-guide.pdf

[134] R. Wolf. “Field error naming conventions for LHC magnets” (2001). LHC-M-ES-0001 rev 3.0.
https://lhc-div-mms.web.cern.ch/lhc-div-mms/tests/MAG/Fidel/

[135] G. Arduini. “Closeout of the 2013 OMC review”. Presentation at LHC OMC review (2013).
http://indico.cern.ch/conferenceDisplay.py?confId=246159

[136] N. Anders. “CERN BE deptartment Summer student program work report for N. Anders”. Supervisor: R. Tomás.

[137] “LHC Logging Project”.
http://lhc-logging.web.cern.ch/lhc-logging/software/default.htm

[138] G. Roy. “Online model”. Presentation at LHC OMC review (2013).
http://indico.cern.ch/conferenceDisplay.py?confId=246159

[139] M. Giovannozzi, S. Fartoukh & R. de Maria. “Triplet correctors specifications”. Presentation at 3rd Joint HiLumi LHC-LARP Annual meeting.
https://indico.cern.ch/event/257368/session/5/contribution/24/material/slides/1.pdf

[140] L. Rossi. “LHC upgrade plans: options and strategy”. In “Proceedings of IPAC 2011”, TUYA02 (2011).
http://accelconf.web.cern.ch/AccelConf/IPAC2011/papers/tuya02.pdf

[141] R. Tomás, M. Giovannozzi & R. de Maria. “Nonlinear correction schemes for the phase 1 LHC insertion region upgrade and dynamic aperture studies”,

Phys. Rev. Spec. Top. Accel. Beams, **12**, 011002.
https://cds.cern.ch/record/1159657

[142] F. Pilat, Y. Luo, N. Malitsky & V.Ptitsyn. “Beam-based non-linear optics corrections in colliders”. In “Proceedings of 2005 PAC”, (2005).
https://cds.cern.ch/record/928146?ln

[143] R. Alemany-Fernandez, G.H. Hemelsoet, J.M. Jowett, M. Lamont, D. Manglunki, S. Redaelli, M. Schaumann, R. Versteegen & J. Wenninger. “ALICE spectrometer polarity reversal” (2012). ATS/Note/2012/039 MD.
https://cds.cern.ch/record/1441694?ln

[144] C. Alabau Pons, G. Arduini, R.W. Assmann, R. Bruce, M. Giovannozzi, J.M. Jowett, E.H. Maclean, G. Müeller, S. Redaelli, R. Tomás, G. Valentino & J. Wenninger. “IR2 aperture measurements at 3.5 TeV” (2012). CERN-ATS-Note-2012-017 MD.
https://cds.cern.ch/record/1421274?ln

[145] CERN BE dept. “LHC Design Report v.1: the LHC Main Ring”, Chapter 2: Beam parameters and definitions. CERN.
https://cds.cern.ch/record/782076/

Appendix A

Appendices pertaining to Chapter 3: Modelling and correction of the linear optics

Chapter 3 presented results from the highly successful 2012 linear optics commissioning. Local and global corrections were applied to the LHC which reduced the beta-beat to record levels. This appendix provides details of the specific corrections applied in order to achieve the performance described in Chapter 3. Appendix A.1 shows the global corrections applied at injection optics. Appendices A.2 and A.3 show the respective local and global corrections applied at $4\,\mathrm{TeV}$.

A.1 Global correction trims at injection during 2012 commissioning

Global correction of linear optics was described in Section 3.2.2. Figure A.1 plots the correction trims around the LHC rings determined by this method at injection optics during 2012 commissioning.

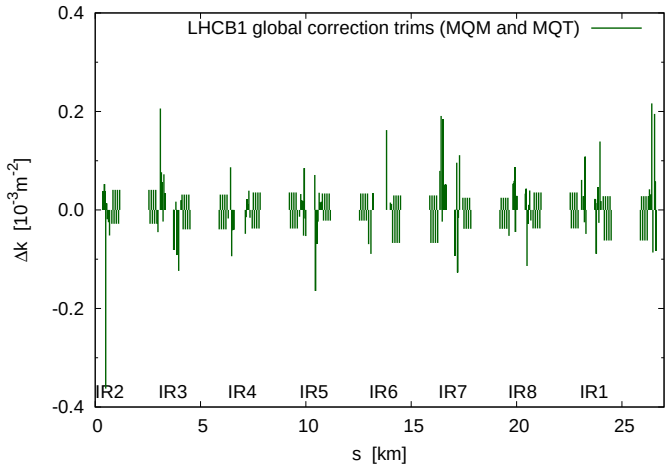

(a) Beam 1

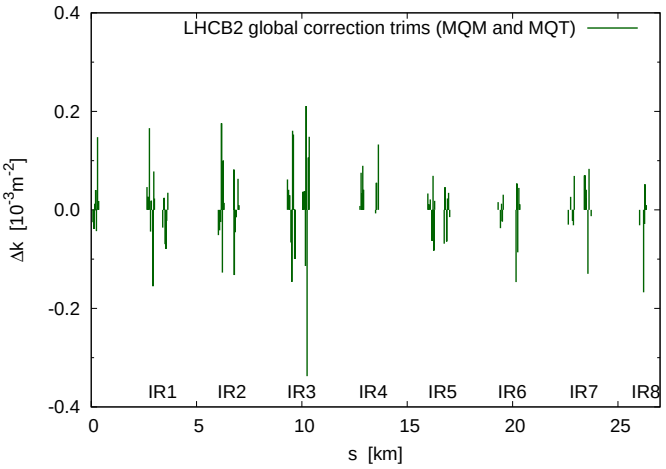

(b) Beam 2

Figure A.1: Global correction for phase advance and normalized horizontal dispersion at injection. Correction was performed independently for Beam 1 and Beam 2 using trims of MQM and MQT magnets.

A.2 Local optics correction at $4\,\mathrm{TeV}$ during 2012 commissioning

The segment-by-segment method for local correction of the linear optics in the LHC was described in Section 3.2.2. The corrections obtained using this method at $4\,\mathrm{TeV}$ during 2012 commissioning are shown in Table A.1. Figures A.2 to A.5 show the corresponding error reconstructions at $\beta^* = 0.6\,\mathrm{m}$ in the relevant IRs.

Table A.1: Local correction trims for IR1, IR5, IR6 and IR8 determined during 2012 optics commissioning. This table has been adapted from that presented in [4].

Insertion	Element	Δk $[10^{-5}\mathrm{m}^{-2}]$	[%]
IR1	ktqx2.r1	-1.4	0.16
	ktqx2.l1	1.0	0.11
	ktqx1.r1	1.0	0.11
	kq9.l1b1	1.5	0.23
	kq4.l1b2	-0.5	0.13
IR5	ktqx2.r5	1.05	0.12
	ktqx2.l5	0.70	0.08
	kq4.l5b2	3.80	1.00
IR6	kq5.l6b1	-3.9	0.6
	kq5.r6b1	0.9	0.1
	kq5.l6b2	4.8	0.7
	kq5.r6b2	1.0	0.1
IR8	kq4.l8b1	4.0	1.0
	kq5.r8b1	8.0	2.7
	kq6.l8b1	2.0	0.4
	kq4.r8b2	-10.0	2.4
	kq5.r8b2	-3.0	0.8
	kq6.l8b2	-3.0	0.5

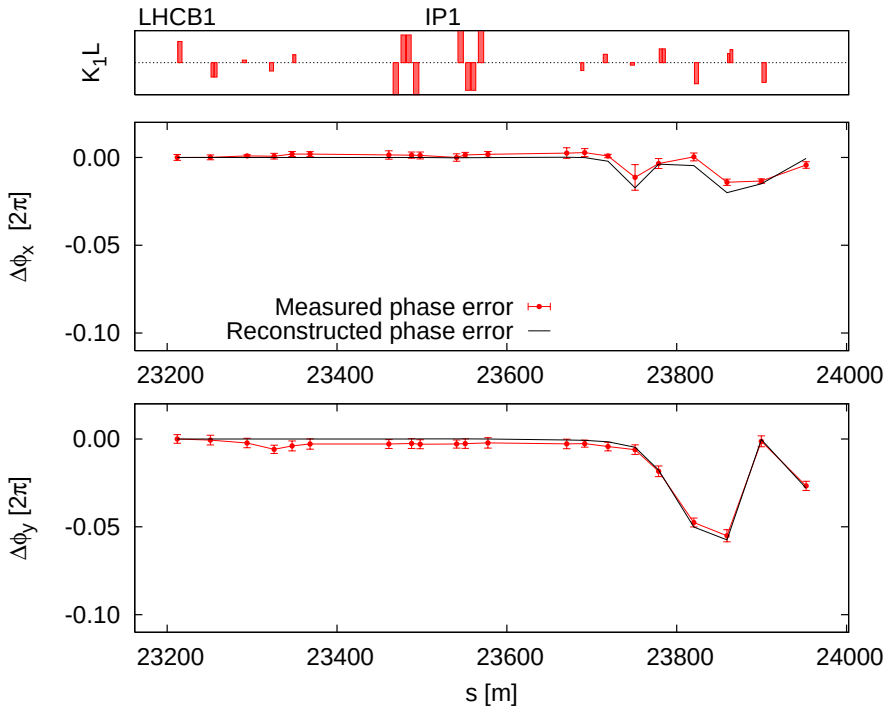

(a) Beam 1

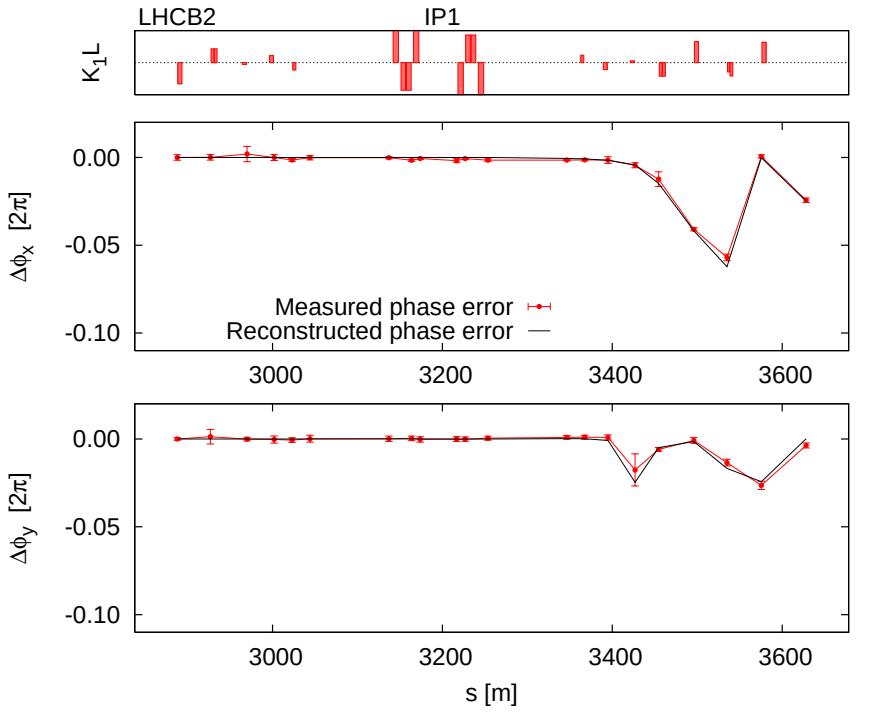

(b) Beam 2

Figure A.2: Local optics correction in IR1 at $\beta^* = 0.6\,\mathrm{m}$

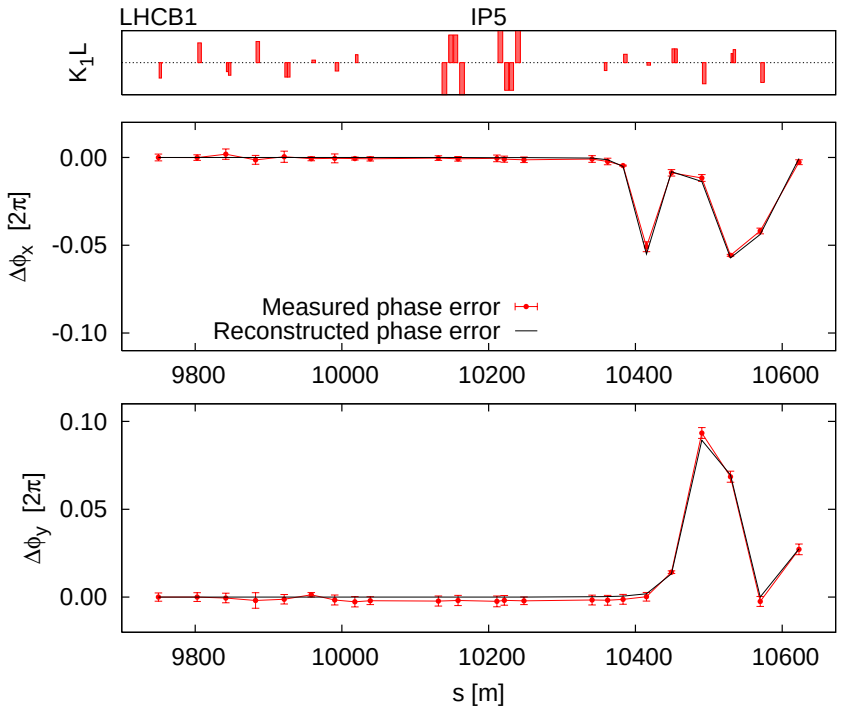

(a) Beam 1

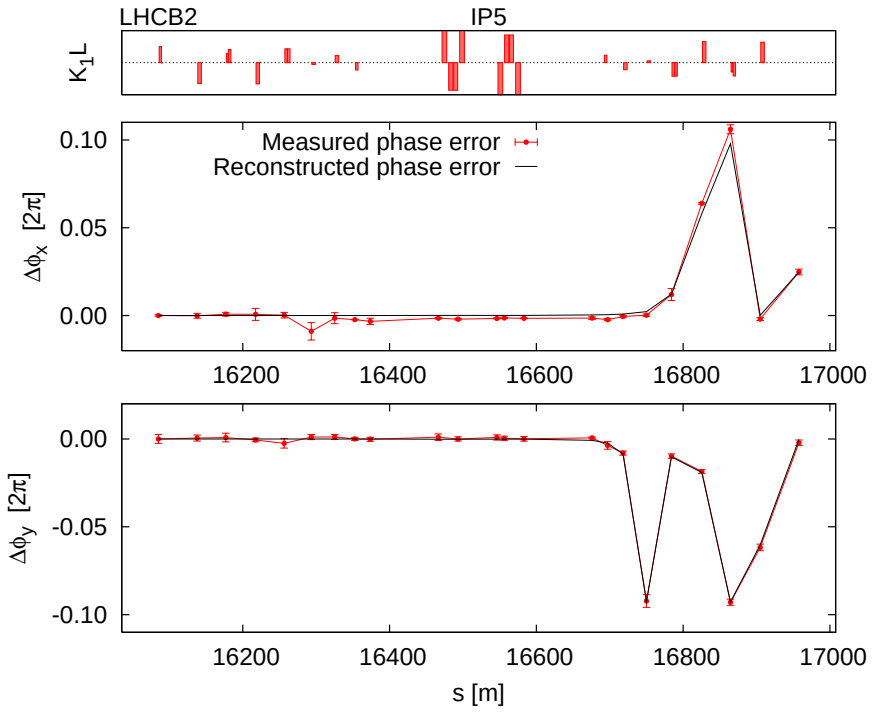

(b) Beam 2

Figure A.3: Local optics correction in IR5 at $\beta^* = 0.6\,\mathrm{m}$

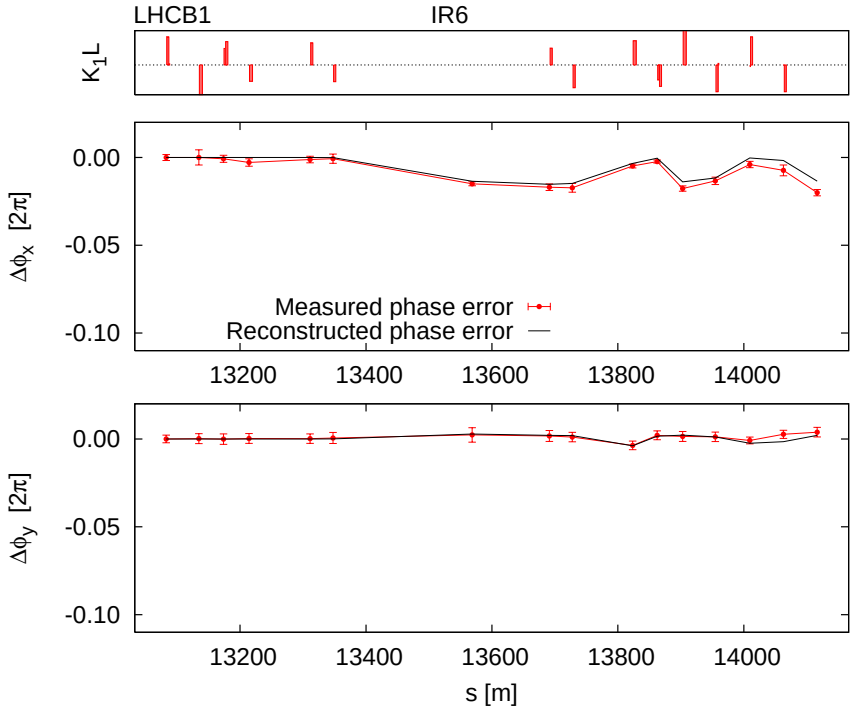

(a) Beam 1

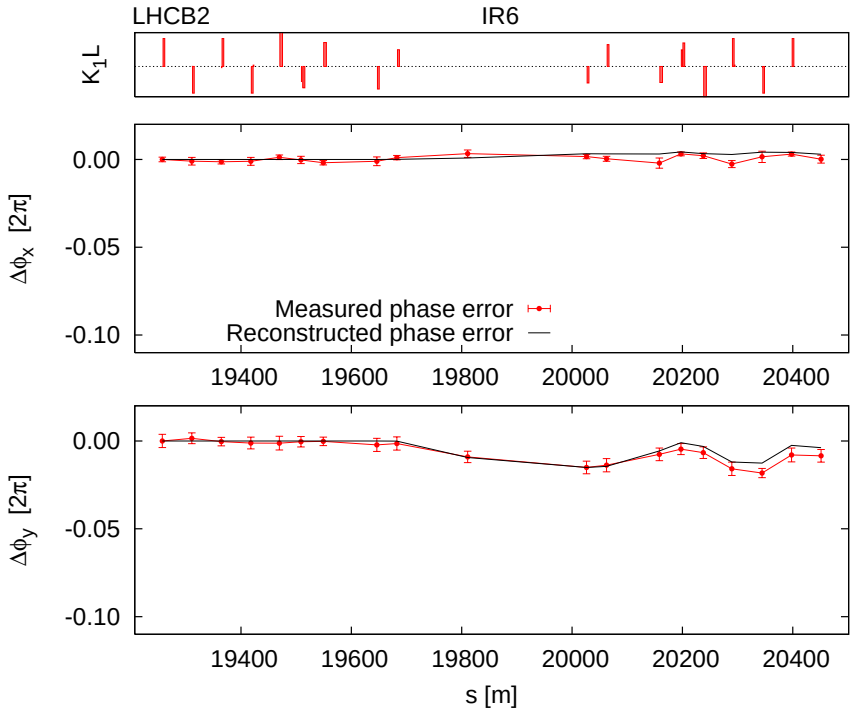

(b) Beam 2

Figure A.4: Local optics correction in IR6 at $\beta^* = 0.6\,\mathrm{m}$

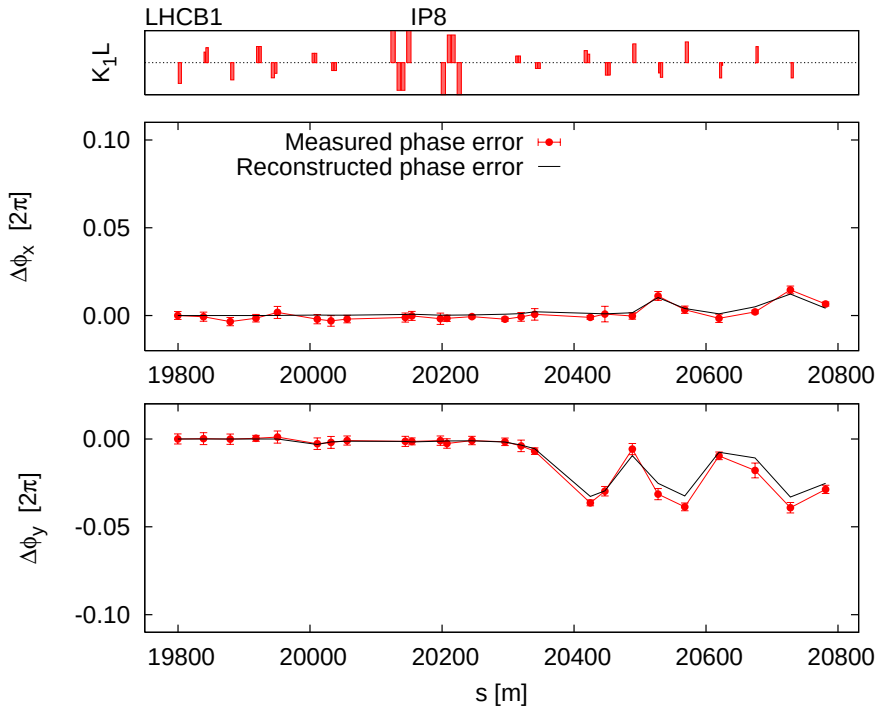

(a) Beam 1

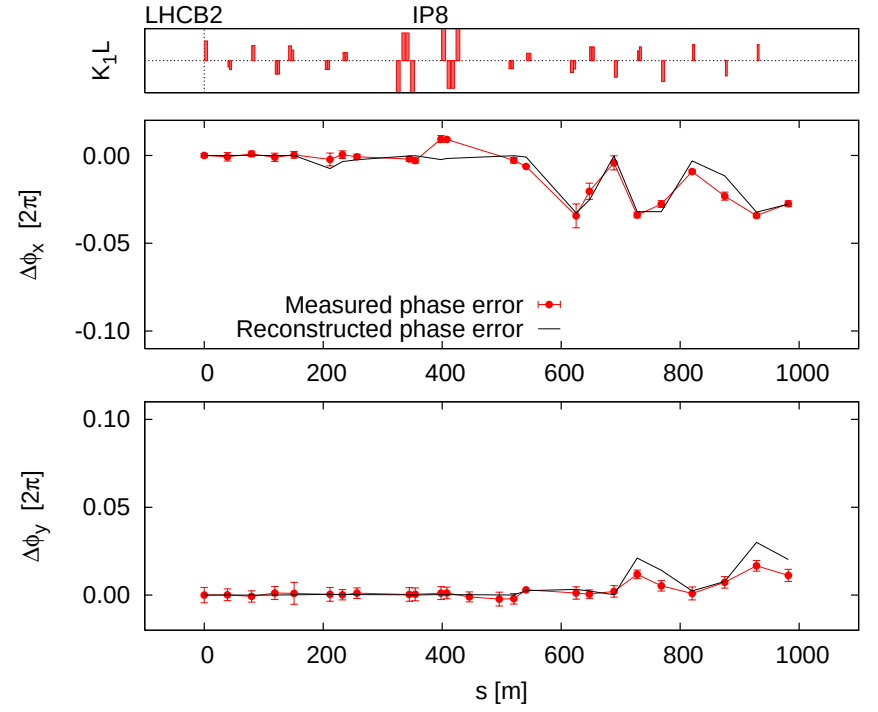

(b) Beam 2

Figure A.5: Local optics correction in IR8 at $\beta^* = 0.6\,\mathrm{m}$

A.3 Global correction trims at $4\,\mathrm{TeV}$ during 2012 commissioning

Following the application of the local corrections described in the preceding section, global corrections were applied at $4\,\mathrm{TeV}$ to further reduce the beta-beat. Figure A.6 plots these global correction trims around the LHC ring for both beams.

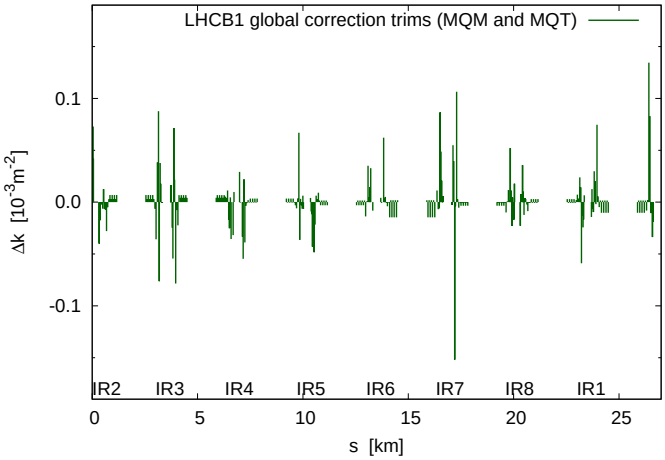

(a) Beam 1

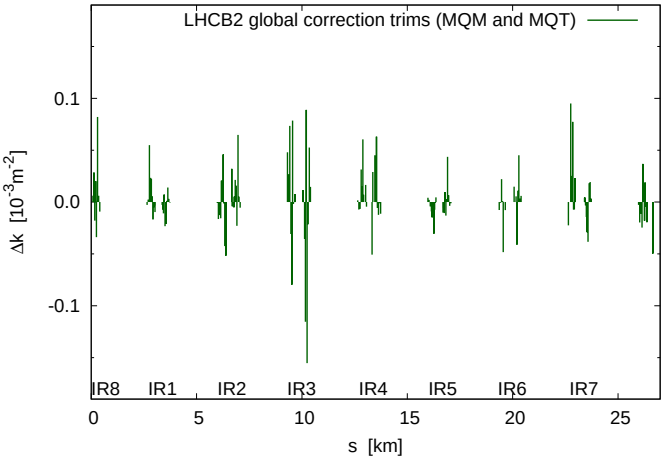

(b) Beam 2

Figure A.6: Global correction for phase advance and normalized horizontal dispersion at $4\,\mathrm{TeV}$. Correction was performed independently for Beam 1 and Beam 2 using trims of MQM and MQT magnets, after local correction in IR1, IR5, IR6 and IR8.

Appendix B

Appendices pertaining to Chapter 4: Measurement and correction of non-linear observables in the LHC at injection

Chapter 4 considered the non-linear dynamics of the LHC at injection optics. This Appendix includes tables of data and aspects of the analysis from the 2011 and 2012 measurements which may assist in future analysis, but were not included in the main chapter. Appendix B.1 provides details of the non-linear chromaticity correction knobs used in 2011. Appendix B.2 summarizes the three states of the machine examined in 2012. Appendix B.3 summarizes the kicks performed throughout the 2012 experiment. Appendix B.4 presents the derivation of Eq.(4.10) used in the determination of the dynamic aperture, together with its double Gaussian equivalent.

B.1 Correction knobs for Q'' and Q''' at injection during 2011

For studies of non-linear chromaticity at injection in 2011, correction knobs for Q'' and Q''' were determined from simulation. The knobs were applied to compensate the observed non-linear chromaticity at injection optics with depowered Landau octupoles. The correction was highly effective. The trims of the knobs applied in 2011 were $+1200$ and $+160$ units of the Q'' and Q''' knobs respectively. The 2011 knob definitions are provided in Tab. B.1. The currents in the MCDO circuits before and after correction are shown in Tab. B.2.

Table B.1: Knob definitions for the Q'' and Q''' determined simulation of MCO and MCD trims in MAD-X and PTC. The knobs were defined against trims of $\Delta Q''_x = +1$ and $\Delta Q'''_x = +10000$ respectively.

Q'' knob		Q''' knob	
Circuit	$\Delta K\ [m^{-4}]$	Circuit	$\Delta K\ [m^{-5}]$
RCO.A12B2	$+0.00189$	RCD.A12B2	$+8.3525$
RCO.A23B2	$+0.00189$	RCD.A32B2	$+8.3525$
RCO.A34B2	$+0.00189$	RCD.A43B2	$+8.3525$
RCO.A45B2	$+0.00189$	RCD.A54B2	$+8.3525$
RCO.A56B2	$+0.00189$	RCD.A65B2	$+8.3525$
RCO.A67B2	$+0.00189$	RCD.A76B2	$+8.3525$
RCO.A78B2	0	RCD.A87B2	$+8.3525$
RCO.A81B2	0	RCD.A81B2	$+8.3525$

Table B.2: Octupole (MCO) and decapole (MCD) spool piece settings in LHC Beam 2 before and after Q'' and Q''' correction.

	MCO		MCD	
	I_{before} [A]	I_{after} [A]	I_{before} [A]	I_{after} [A]
Arc 12	3.00	9.41	-120.10	-85.41
Arc 23	-3.00	3.41	-120.10	-85.41
Arc 34	-3.00	3.41	-128.83	-94.14
Arc 45	-3.00	3.41	-122.75	-88.05
Arc 56	3.00	9.41	-110.29	-75.6
Arc 67	3.00	9.41	-134.91	-100.22
Arc 78	0	0	-184.54	-149.85
Arc 81	0	0	-145.57	-110.88

B.2 Currents in the Landau octupoles and $b4, 5$ correctors for optics studied during 2012 measurements of non-linear observables with kicked beams

Table B.3: Measured currents in the Landau octupole (MOF and MOD), and the octupolar and decapolar spool pieces (arc correctors: MCO and MCD), for the machine states measured during the experiment. State 1 is nominal injection optics. State 2 is as state 1 but with Landau octupoles powered to zero and the residual field of the MCO zeroed. In State 3 corrections to State 2 have been applied for the second and third order chromaticities using the MCO and MCD.

Power converter circuit	State 1: I_{meas}[A] Nominal injection	State 2: I_{meas}[A] MO off, MCO residual field zeroed	State 3: I_{meas}[A] Non-linear chromaticity corrected
ROF A12	-6.5	0	0
ROF A23	-6.5	0	0
ROF A34	-6.5	0	0
ROF A45	-6.5	0	0
ROF A56	-6.5	0	0
ROF A67	-6.5	0	0
ROF A78	-6.5	0	0
ROF A81	-6.5	0	0
ROD A12	+6.5	0	0
ROD A23	+6.5	0	0
ROD A34	+6.5	0	0
ROD A45	+6.5	0	0
ROD A56	+6.5	0	0
ROD A67	+6.5	0	0
ROD A78	+6.5	0	0
ROD A81	+6.5	0	0
RCO A12	0	0	0
RCO A23	3.417	-3	4.692
RCO A34	3.375	-3	4.692
RCO A45	2.957	-3	4.692
RCO A56	-3.473	3	10.693
RCO A67	-4.752	3	10.693
RCO A78	0	0	0
RCO A81	-	-	-
RCD A12	-112.73	-112.73	-85.41
RCD A23	-127.74	-127.74	-100.43
RCD A34	-121.45	-121.45	-94.14
RCD A45	-115.37	-115.37	-88.05
RCD A56	-102.92	-102.92	-75.60
RCD A67	-127.54	-127.54	-100.22
RCD A78	-177.17	-177.17	-149.85
RCD A81	-138.20	-138.20	-110.88

B.3 Measured amplitudes of MKA excitations performed during the MD

The actions ($2J_{x,y}$) of kicks performed during measurements of non-linear observables in 2012 were calculated from Turn-by-Turn BPM data as described in Section 4.2.2. For the estimates of the kick amplitude in $[\sigma_{\mathrm{nominal}}]$, a normalized emittance of $3.75\mu\mathrm{m}$ [145] at $450\,\mathrm{GeV}$ is assumed. This gives a nominal physical emittance of $\epsilon_{nominal\ (physical)} = \epsilon^{*}_{nominal}/(\beta\gamma) = 0.0078$, where $\beta \sim 1$ and $\gamma \sim 479.6$. Estimates of the excitation in beam sigmas were calculated using the physical emittance measured by the LHC wirescanners. Where no wirescan was performed the most recent profile data was used. Expected kick amplitudes in $[\sigma_{nominal}]$ were calculated from MKA settings in the control room assuming a calibration factor of $(+1\sigma_x, +1\sigma_y) \approx (+7\%, +6\%)$. Errors on the kick amplitude in units of $[\sigma_{beam}]$ were calculated using Eq.(B.1), where $\Delta\epsilon_{x,y}$ is the standard deviation of the emittances determined from the *IN* and *OUT* wirescans. For calculation in units of $[\sigma_{nominal}]$, $\Delta\epsilon_{x,y}$ is zero by definition.

$$\Delta N\sigma = \frac{N\sigma}{2}\sqrt{\left(\frac{\Delta(2J_{x,y})}{2J_{x,y}}\right)^2 + \left(\frac{\Delta\epsilon_{x,y}}{\epsilon_{x,y}}\right)^2} \tag{B.1}$$

Table B.4: Amplitudes of MKA excitations performed during the MD, as calculated from BPM and wirescanner data.

Time	MKA (H) MKA (V) [%]	$N\sigma_{x\ Expected}$ $N\sigma_{y\ Expected}$ $[\sigma_{nom}]$	$2J_x$ $2J_y$ [μm]	$N\sigma_x$=$\sqrt{\frac{2J_x}{\epsilon_{x\ phys\ (meas)}}}$ $N\sigma_y$=$\sqrt{\frac{2J_y}{\epsilon_{y\ phys\ (meas)}}}$ $[\sigma_{beam}]$	$N\sigma_x$=$\sqrt{\frac{2J_x}{\epsilon_{x\ phys\ (nominal)}}}$ $N\sigma_y$=$\sqrt{\frac{2J_y}{\epsilon_{y\ phys\ (nominal)}}}$ $[\sigma_{nominal}]$
LHC at nominal injection settings.					
00:36:59	56	8	0.42 ± 0.04	11.0 ± 0.9	7.3 ± 0.4
	6	1	0.007 ± 0.002	1.3 ± 0.2	1.0 ± 0.1
01:03:25	7	1	0.04 ± 0.006	3.4 ± 0.4	2.3 ± 0.2
	48	8	0.31 ± 0.03	8.8 ± 0.4	6.3 ± 0.3
01:12:51	63	9	0.52 ± 0.06	12.2 ± 1.1	8.2 ± 0.5
	6	1	0.003 ± 0.001	0.9 ± 0.2	0.6 ± 0.1
01:17:56	7	1	0.12 ± 0.01	5.9 ± 0.5	3.9 ± 0.2
	54	9	0.37 ± 0.04	9.6 ± 0.5	6.9 ± 0.4
01:24:12	unknown	–	0.33 ± 0.03	9.7 ± 0.8	6.5 ± 0.3
	unknown	–	0.21 ± 0.02	7.2 ± 0.3	5.2 ± 0.2

...continued on next page.

σ_{kick} of MKA excitations ...continued from previous page.

Time	MKA (H) MKA (V) [%]	$N\sigma_{x\ Expected}$ $N\sigma_{y\ Expected}$ [σ_{nom}]	$2J_x$ $2J_y$ [μm]	$N\sigma_x$=$\sqrt{\frac{2J_x}{\epsilon_{x\ phys\ (meas)}}}$ $N\sigma_y$=$\sqrt{\frac{2J_y}{\epsilon_{y\ phys\ (meas)}}}$ [σ_{beam}]	$N\sigma_x$=$\sqrt{\frac{2J_x}{\epsilon_{x\ phys\ (nominal)}}}$ $N\sigma_y$=$\sqrt{\frac{2J_y}{\epsilon_{y\ phys\ (nominal)}}}$ [$\sigma_{nominal}$]
01:29:34	49	7	0.33 ± 0.03	9.7 ± 0.8	6.5 ± 0.3
	6	1	0.044 ± 0.005	3.3 ± 0.2	2.4 ± 0.2
01:39:06	7	1	0.014 ± 0.003	2.0 ± 0.3	1.3 ± 0.1
	42	7	0.24 ± 0.02	7.7 ± 0.3	5.5 ± 0.2
01:43:00	28	4	0.107 ± 0.008	5.5 ± 0.4	3.7 ± 0.1
	6	1	0.033 ± 0.004	2.9 ± 0.2	2.1 ± 0.1
01:47:00	7	1	0.021 ± 0.002	2.4 ± 0.2	1.6 ± 0.1
	24	4	0.074 ± 0.007	4.3 ± 0.2	3.1 ± 0.1
01:51:11	14	2	0.027 ± 0.002	2.8 ± 0.2	1.9 ± 0.1
	6	1	0.039 ± 0.004	3.1 ± 0.2	2.2 ± 0.1
01:55:26	7	1	0.019 ± 0.002	2.3 ± 0.2	1.6 ± 0.1
	12	2	0.017 ± 0.002	2.1 ± 0.1	1.5 ± 0.1
MO powered to zero & zeroing of MCO residual field.					
02:22:15	14	2	0.026 ± 0.002	2.7 ± 0.2	1.8 ± 0.1
	12	2	0.017 ± 0.002	2.1 ± 0.1	1.5 ± 0.1
NL chroma correction applied.					
03:07:03	14	2	0.027 ± 0.002	2.8 ± 0.2	1.86 ± 0.07
	12	2	0.017 ± 0.002	2.1 ± 0.1	1.48 ± 0.09
03:13:11	56	8	0.44 ± 0.03	11.2 ± 0.9	7.5 ± 0.3
	6	1	0.005 ± 0.002	1.1 ± 0.2	0.8 ± 0.2
03:19:31	63	9	0.55 ± 0.04	12.5 ± 1.0	8.4 ± 0.3
	6	1	0.0014 ± 0.0008	0.6 ± 0.2	0.4 ± 0.1
03:54:37	42	6	0.25 ± 0.02	7.9 ± 0.3	5.7 ± 0.2
	6	1	0.003 ± 0.001	0.9 ± 0.1	0.6 ± 0.1
03:59:05	7	1	0.13 ± 0.01	6.6 ± 0.3	4.1 ± 0.2
	36	6	0.18 ± 0.02	6.3 ± 0.5	4.8 ± 0.3
04:06:06	29	4.14	0.13 ± 0.02	6.6 ± 0.5	4.4 ± 0.3
	25	4.16	0.083 ± 0.009	4.6 ± 0.2	3.3 ± 0.2
04:09:38	28	4	0.11 ± 0.01	6.1 ± 0.3	3.8 ± 0.2
	6	1	0.0033 ± 0.0009	1.0 ± 0.1	0.65 ± 0.09
04:12:58	7	1	0.008 ± 0.001	1.6 ± 0.1	1.01 ± 0.06
	24	4	0.078 ± 0.006	4.4 ± 0.2	3.2 ± 0.1
04:16:17	20	2.86	0.058 ± 0.005	4.4 ± 0.2	2.7 ± 0.1
	17	2.83	0.037 ± 0.004	2.7 ± 0.1	2.2 ± 0.1
04:19:27	14	2	0.026 ± 0.003	2.9 ± 0.2	1.8 ± 0.1
	6	1	0.0051 ± 0.0007	1.13 ± 0.08	0.81 ± 0.06
04:23:09	7	1	0.007 ± 0.006	1.5 ± 0.7	0.9 ± 0.4
	12	2	0.018 ± 0.001	2.12 ± 0.06	1.52 ± 0.04
04:25:56	10	1.43	0.013 ± 0.001	2.08 ± 0.08	1.29 ± 0.05
	8	1.33	0.007 ± 0.0008	1.32 ± 0.08	0.95 ± 0.05

...continued on next page.

σ_{kick} of MKA excitations ...continued from previous page.

Time	MKA (H) MKA (V) [%]	$N\sigma_{x\ Expected}$ $N\sigma_{y\ Expected}$ [σ_{nom}]	$2J_x$ $2J_y$ [μm]	$N\sigma_x$=$\sqrt{\frac{2J_x}{\epsilon_{x\ phys\ (meas)}}}$ $N\sigma_y$=$\sqrt{\frac{2J_y}{\epsilon_{y\ phys\ (meas)}}}$ [σ_{beam}]	$N\sigma_x$=$\sqrt{\frac{2J_x}{\epsilon_{x\ phys\ (nominal)}}}$ $N\sigma_y$=$\sqrt{\frac{2J_y}{\epsilon_{y\ phys\ (nominal)}}}$ [$\sigma_{nominal}$]
04:29:36	56 6	8 1	0.44 ± 0.03 0.003 ± 0.002	12.1 ± 0.4 0.9 ± 0.3	7.5 ± 0.3 0.6 ± 0.2
04:40:36	7 48	1 8	0.061 ± 0.007 0.32 ± 0.07	4.5 ± 0.3 8.0 ± 0.9	2.8 ± 0.2 6.4 ± 0.7
04:46:25	7 54	1 9	0.013 ± 0.003 0.41 ± 0.04	2.1 ± 0.2 10.1 ± 0.5	1.3 ± 0.1 7.3 ± 0.4
04:53:44	7 60	1 10	0.015 ± 0.004 0.5 ± 0.05	2.2 ± 0.3 10.5 ± 0.8	1.4 ± 0.2 8.0 ± 0.4
04:59:06	7 63	1 10.5	0.016 ± 0.004 0.55 ± 0.05	2.1 ± 0.3 10.5 ± 0.5	1.4 ± 0.2 8.4 ± 0.4
05:02:48	7 66	1 11	0.017 ± 0.005 0.6 ± 0.05	2.4 ± 0.4 12.2 ± 0.5	1.5 ± 0.2 8.8 ± 0.4
05:11:33	7 69	1 11.5	0.019 ± 0.005 0.65 ± 0.05	2.5 ± 0.3 13.6 ± 1.1	1.6 ± 0.2 9.1 ± 0.4
05:19:43	7 72	1 12	0.02 ± 0.005 0.7 ± 0.06	2.6 ± 0.3 13.2 ± 0.6	1.6 ± 0.2 9.5 ± 0.4
05:25:13	39 34	5.57 5.67	0.24 ± 0.04 0.2 ± 0.02	8.9 ± 0.7 6.3 ± 0.3	5.5 ± 0.5 5.1 ± 0.3
05:30:55	44 38	6.29 6.33	0.3 ± 0.02 0.19 ± 0.02	11.0 ± 1.2 7.4 ± 0.7	6.2 ± 0.2 4.9 ± 0.3
05:36:40	49 42	7 7	0.37 ± 0.03 0.23 ± 0.03	11.1 ± 0.5 7.1 ± 0.6	6.9 ± 0.3 5.4 ± 0.5
05:44:50	51 44	7.29 7.33	0.4 ± 0.03 0.25 ± 0.02	11.5 ± 0.4 7.5 ± 0.5	7.2 ± 0.3 5.7 ± 0.2
05:49:40	54 46	7.71 7.67	0.45 ± 0.03 0.29 ± 0.03	12.2 ± 0.4 8.5 ± 0.4	7.6 ± 0.3 6.1 ± 0.3
05:55:09	56 48	8 8	0.48 ± 0.04 0.3 ± 0.03	12.6 ± 0.5 8.7 ± 0.4	7.8 ± 0.3 6.2 ± 0.3
06:00:22	59 51	8.43 8.5	0.53 ± 0.04 0.33 ± 0.03	13.3 ± 0.5 8.1 ± 0.4	8.2 ± 0.3 6.5 ± 0.3
06:03:04	56 6	8 1	0.45 ± 0.04 0.017 ± 0.004	12.2 ± 0.5 1.8 ± 0.2	7.6 ± 0.3 1.5 ± 0.2
06:08:16	60 6	8.57 1	0.51 ± 0.04 0.002 ± 0.001	12.1 ± 1.0 0.6 ± 0.2	8.1 ± 0.3 0.5 ± 0.1
06:12:38	70 6	10 1	0.68 ± 0.05 0.003 ± 0.002	15.4 ± 0.6 0.8 ± 0.3	9.3 ± 0.3 0.6 ± 0.2
06:16:38	77 6	11 1	0.81 ± 0.06 0.004 ± 0.002	15.2 ± 1.2 0.9 ± 0.2	10.2 ± 0.4 0.7 ± 0.2
06:20:38	74 6	10.57 1	0.76 ± 0.06 0.003 ± 0.002	15.9 ± 0.6 0.9 ± 0.3	9.9 ± 0.4 0.6 ± 0.2

B.4 Calculation of $DA - KICK$ from measured beam loss

During the LHC non-linear MD in summer 2012, the beam was excited by large amplitude kicks with the MKA. In order to determine the dynamic aperture from these measurements, it is necessary to determine both the kick amplitude and the distance of the kick from the DA. As described in Section 4.2.2, the kick amplitude was determined from the turn-by-turn betatron oscillation data. The distance between the kick amplitude and the dynamic aperture was determined using the measured beam losses following the kicks. This section summarizes the derivation of the relation used to determine the distance of the DA from the kick amplitude.

B.4.1 Derivation for a Gaussian charge distribution

It was assumed that losses only occurred in the plane of the kick. Effectively this is makes the assumption that the beam is small in comparison to the DA, such that the eventual integrations over phase space may be performed between $\pm\infty$ in the plane perpendicular to the kick (which will considerably simplify the derivation). If the amplitude of the kick ($KICK$) was equal to the dynamic aperture after a specific number of turns (DA) it could be expected that about half the beam would have been lost. All kicks showed less than 50% losses so it is reasonable to assume that the DA must be greater than about $8\,\sigma_{\mathrm{nominal}}$, or $11\,\sigma_{\mathrm{measured}}$. It aught to be reasonable therefore to ignore losses from the plane perpendicular to the kick.

Let z represent the position amplitude in the plane of the kick, let z' represent the angle amplitude in the plane of the kick. Assume a Gaussian charge distribution, then express in terms of σ_{beam}.

$$\rho(z, z') = e^{-\frac{1}{2}\left(\frac{z^2}{\sigma_z^2}+\frac{z'^2}{\sigma_{z'}^2}\right)} \tag{B.2}$$

$$\rho(N, N') = e^{-\frac{1}{2}\left(N^2+N'^2\right)} \quad \text{where} \quad N = \frac{z}{\sigma_z} \text{ and } N' = \frac{z'}{\sigma_{z'}} \tag{B.3}$$

N have the units of $[\sigma_{beam}]$. ρ is then normalized to the total charge, I.

$$I = \int_{-\infty}^{+\infty}\int_{-\infty}^{+\infty} e^{-\frac{1}{2}\left(N^2+N'^2\right)}\,\mathrm{d}N\mathrm{d}N' = 2\pi \tag{B.4}$$

$$\rho(N, N') = \frac{1}{2\pi}e^{-\frac{1}{2}\left(N^2+N'^2\right)} \tag{B.5}$$

The MKA kick shifts the beam to large amplitude z'. The proportion of the beam which lies outside the DA for this kick amplitude is lost. This was illustrated schematically in Fig. 4.1.Having normalized ρ to the total charge, the fractional beam loss is given by the

integral over the charge distribution outwith the DA. To simplify the integration it is assumed that the beam size is small compared with the DA, and the boundary for the integration may be taken as the tangent to the arc of the DA at $z = 0$. The integration may then be performed over N from $-\infty$ to $+\infty$, and over N' from $DA - KICK$ to ∞.

$$\frac{\Delta I}{I} = \frac{1}{2\pi} \int_{-\infty}^{+\infty} e^{-\frac{1}{2}N^2} \, \mathrm{d}N \int_{DA-KICK}^{+\infty} e^{-\frac{1}{2}N'^2} \, \mathrm{d}N' \tag{B.6}$$

Making use of the well known Gaussian integral:

$$\int_{-\infty}^{+\infty} ae^{-bx} \, \mathrm{d}x = a\sqrt{\frac{\pi}{b}} \tag{B.7}$$

the integral over N is removed.

$$\frac{\Delta I}{I} = \frac{1}{2\pi}\sqrt{2\pi} \int_{DA-KICK}^{+\infty} e^{-\frac{1}{2}N'^2} \, \mathrm{d}N' \tag{B.8}$$

(B.9)

$$\frac{\Delta I}{I} = \frac{1}{\sqrt{2\pi}} \int_{DA-KICK}^{+\infty} e^{-\frac{1}{2}N'^2} \, \mathrm{d}N'$$

In the special case that $KICK = DA$, Eq.(B.10) has a particularly simple solution, which is consistent with expected beam loss given the assumptions made.

$$\frac{\Delta I}{I} = \frac{1}{\sqrt{2\pi}} \int_{0}^{+\infty} e^{-\frac{1}{2}N'^2} \, \mathrm{d}N' \tag{B.10}$$

$$= \frac{1}{\sqrt{2\pi}} \frac{1}{2} \int_{-\infty}^{+\infty} e^{-\frac{1}{2}N'^2} \, \mathrm{d}N' \tag{B.11}$$

$$= \frac{1}{2} \tag{B.12}$$

To determine the dynamic aperture it was desired re-express Eq.(B.10) for the DA, in terms of the beam loss. The integral in Eq.(B.10) takes a similar from to the complementary error function, $[1 - \mathbf{erf}]$, defined in Eq.(B.13).

$$\int_{p}^{\infty} e^{-t^2} \, \mathrm{d}t = \frac{\sqrt{\pi}}{2} \left[1 - \mathbf{erf}(p)\right] \tag{B.13}$$

Making the change of variables $t^2 = \frac{1}{2}N'^2$, $\mathrm{d}t = \frac{1}{\sqrt{2}}\mathrm{d}N'$, the integral in Eq.(B.10) may be put in the form of Eq.(B.13).

$$\int_{N'=DA-KICK}^{\infty} e^{-\frac{1}{2}N'^2} \, \mathrm{d}N' = \sqrt{2} \int_{t=\frac{DA-KICK}{\sqrt{2}}}^{\infty} e^{-t^2} \, \mathrm{d}t \tag{B.14}$$

The distance of the MKA excitation from the dynamic aperture may therefore be expressed in terms of the beam loss, where it should be noted that the expression is still in terms of σ_{beam}

$$\frac{\Delta I}{I} = \frac{1}{2}\left(1 - \mathbf{erf}\left[\frac{DA - KICK}{\sqrt{2}}\right]\right) \tag{B.15}$$

$$\frac{DA - KICK}{\sqrt{2}} = \mathbf{erf}^{-1}\left[1 - 2\frac{\Delta I}{I}\right] \tag{B.16}$$

The error function and its inverse may be obtained using a wide variety of software. It should be noted that in the approximation that the beam size is small in comparison to the DA, that the DA does not fluctuate wildly with angle, and that the horizontal and vertical emittances are equal, the above relation still holds for kicks at all angles in the (x', y') plane.

B.4.2 Double Gaussian distribution

The probe beams used in the non-linear dynamics measurements in the LHC do not undergo scraping in the SPS to remove transverse tails in the charge distribution. Measurements of unscraped beams in 2012, based on incremental scraping with the LHC collimators, showed a charge distribution with substantially overpopulated transverse tails relative to a single Gaussian. A double Gaussian was determined to better describe the scraping measurements [124]. The derivation of the previous section may be applied to a double Gaussian ρ.

$$\rho(N, N', N_2, N_2') = A_1 e^{-\frac{1}{2}\left(N^2 + N'^2\right)} + A_2 e^{-\frac{1}{2}\left(N_2^2 + N_2'^2\right)} \tag{B.17}$$

$$\rho(N, N') = A_1 e^{-\frac{1}{2}\left(N^2 + N'^2\right)} + A_2 e^{-\frac{1}{2}\frac{\sigma_1^2}{\sigma_2^2}\left(N^2 + N'^2\right)} \tag{B.18}$$

$$I = 2\pi A_1 + 2\pi \frac{\sigma_2^2}{\sigma_1^2} A_2 \tag{B.19}$$

Following the method of the previous section the fractional beam loss may be related to the dynamic aperture.

$$\frac{\Delta I}{I} = \frac{1}{2\pi A_1 + 2\pi \frac{\sigma_2^2}{\sigma_1^2} A_2} \frac{1}{2}\left[2\pi A_1 \left(1 - \mathbf{erf}\left(\frac{DA - KICK}{\sqrt{2}}\right)\right) + 2\pi \frac{\sigma_2^2}{\sigma_1^2} A_2 \left(1 - \mathbf{erf}\left(\frac{DA - KICK}{\sqrt{2}} \frac{\sigma_1}{\sigma_2}\right)\right)\right] \tag{B.20}$$

Eq.(B.20) cannot be simply re-expressed for the dynamic aperture. Using the ratios of A_1 to A_2, and σ_1 to σ_2 determined during the LHC transverse beam tails studies, it is possible

to check the value of the DA determined in the single Gaussian approximation from only the highest amplitude kicks (only the highest amplitude kicks were used with the single Gaussian equation in order to limit the impact of the overpopulated transverse tails on the calculation) against all the measured losses. This is shown in Fig. B.1 for the horizontal kicks before and after correction of the non-linearities in the LHC at injection.

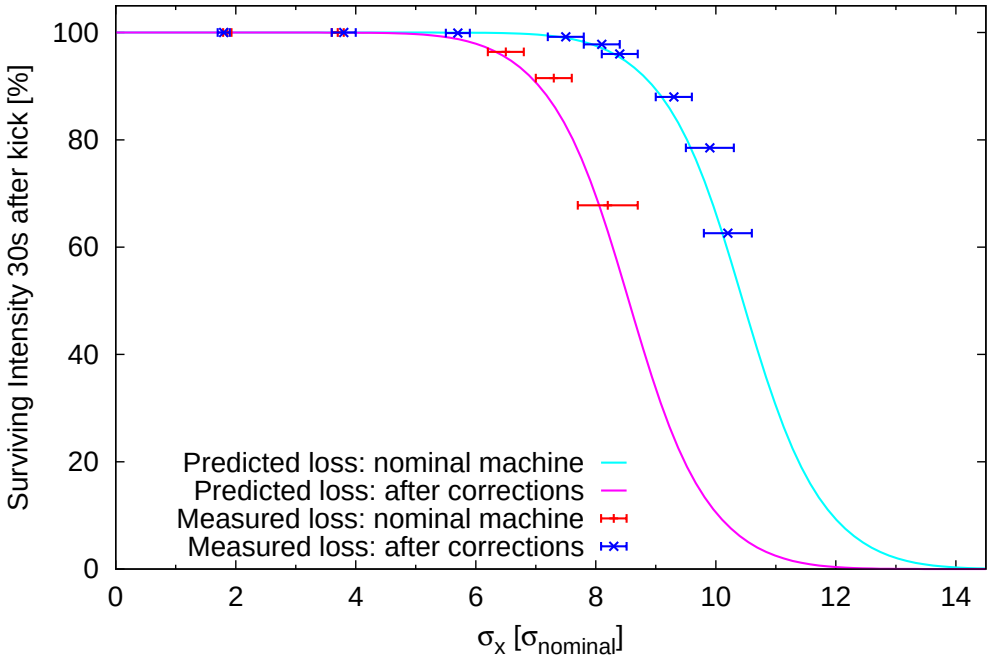

Figure B.1: Measured beam losses following horizontal excitations with the MKA, compared to expectations for the double Gaussian charge distribution determined from scraping studies, for the DA calculated using the highest amplitude kicks in the single Gaussian approximation.

The agreement between measurement and the predictions is good, though the best fit of the double Gaussian ρ predicts a slightly higher DA ($\sim 0.1\,\sigma_{\mathrm{nominal}}$) than was obtained in the single Gaussian approximation.